

# Applications of Wavelet Analysis in System Identification

(Anwendungen der Wavelet-Transformation  
in der Systemidentifikation)

DISSERTATION

zur Erlangung des akademischen Grades  
Doktor-Ingenieur (Dr.-Ing.)  
an der Fakultät Bauingenieurwesen  
der  
Bauhaus-Universität Weimar

vorgelegt von  
Dipl.-Ing. Volkmar Zabel  
geb. am 26. November 1968 in Potsdam

Weimar, November 2002

Gutachter:

1. Prof. Dr. Christian Bucher, Bauhaus-Universität Weimar
2. Prof. Dr. Guido De Roeck, Katholieke Universiteit Leuven (Belgien)
3. Prof. Dr.rer.nat.habil. Klaus Gürlebeck, Bauhaus-Universität Weimar

Disputation am 15. April 2003

Meinen Eltern Ingeborg und Albrecht Zabel

# Vorwort

Die vorliegende Dissertation entstand während meiner Tätigkeit als wissenschaftlicher Mitarbeiter am Institut für Strukturmechanik der Bauhaus-Universität Weimar. Die dokumentierten Forschungsergebnisse wurden im Rahmen des von der Deutschen Forschungsgemeinschaft geförderten Sonderforschungsbereichs SFB 524 “Werkstoffe und Konstruktionen für die Revitalisierung von Bauwerken” erarbeitet.

Mein besonderer Dank gilt Herrn Professor Cristian Bucher für die hervorragende fachliche und persönlich sehr angenehme Betreuung der Arbeit. Außerordentlich wertvoll waren die Hinweise und Ratschläge von Herrn Professor Guido De Roeck. Ihm und Herrn Professor Klaus Gürlebeck danke ich für die Bereitschaft zur Begutachtung meiner Dissertation.

Unvergessen bleiben die fachlichen Diskussionen mit meinem Kollegen Doktor Klaus Markwardt bei der Erarbeitung der mathematischen Grundlagen für die vorliegende Arbeit. Für die hilfreiche Unterstützung bei der Implementierung der numerischen Werkzeuge in das Programm SLang danke ich Herrn Jörg Riedel, Herrn Thomas Most und Herrn Doktor Michael Macke.

Ohne die engagierte Zusammenarbeit mit den Kollegen der Versuchstechnischen Einrichtung der Fakultät Bauingenieurwesen der Bauhaus-Universität Weimar bei der Vorbereitung und Durchführung der experimentellen Untersuchungen hätten wesentliche Bestandteile der vorliegenden Arbeit nicht durchgeführt werden können. In diesem Zusammenhang wird besonders Herrn Wolf-Dieter Vogler, Herrn Aribert Jahn und Herrn Heiner Schuhmann gedankt. Herrn Doktor Matthias Ebert danke ich für die Kooperation bei den Versuchen mit einem Stahlbetonbalken.

# Abstract

Most traditional methods in system identification are based on the analysis of measured data in either the time or frequency domain. In recent years some procedures were developed that apply wavelet analysis in the context of system identification.

The purpose of this study was to develop an algorithm that allows for identifying the parameters of a finite element model that describes a tested mechanical system. A method has been derived that determines the desired parameters by solving a system of equations of motion in the time-scale domain. By using this representation, problems that are caused by noise contamination of the measured data can be reduced. The results of numerical simulations and an experimental study confirmed the benefits of applying wavelet analysis in the proposed way.

A second emphasis was put on investigations with respect to a wavelet-based first level damage indicator. Considerations of the impulse response wavelet coefficients' energy components led to a damage indicator for reinforced concrete structures. The findings of an experimental study suggest a relatively high sensitivity of this indicator.

# Kurzfassung

Die meisten traditionellen Methoden der Systemidentifikation beruhen auf der Abbildung der Meßwerte entweder im Zeit- oder im Frequenzbereich. In jüngerer Zeit wurden im Zusammenhang mit der Systemidentifikation Verfahren entwickelt, die auf der Anwendung der Wavelet-Transformation beruhen.

Das Ziel dieser Arbeit war, einen Algorithmus zu entwickeln, der die Identifikation von Parametern eines Finite-Elemente-Modells, das ein experimentell untersuchtes mechanisches System beschreibt, ermöglicht. Es wurde eine Methode erarbeitet, mit deren Hilfe die gesuchten Parameter durch Lösen eines Systems von Bewegungsgleichungen im Zeit-Skalen-Bereich ermittelt werden. Durch die Anwendung dieser Darstellung können Probleme, die durch Rauschanteile in den Meßdaten entstehen, reduziert werden. Die Ergebnisse numerischer Simulationen und einer experimentellen Studie bestätigen die Vorteile einer Anwendung der Wavelet-Transformation in der vorgeschlagenen Weise.

Ein zweiter Schwerpunkt wurde auf Untersuchungen hinsichtlich eines auf der Wavelet-Transformation basierenden Indikators zur Schadenserkennung gelegt. Betrachtungen der Energie-Komponenten von Wavelet-Koeffizienten einer Impulsreaktion führten zu einem Schädigungsindikator für Stahlbetontragwerke. Die Resultate einer experimentellen Untersuchung lassen auf eine relativ hohe Empfindlichkeit dieses Indikators schließen.

# Contents

<b>Abstract</b>	<b>i</b>
<b>Kurzfassung</b>	<b>ii</b>
<b>Notation</b>	<b>vii</b>
<b>Introduction</b>	<b>1</b>
<b>1 Fundamentals of Wavelet Analysis</b>	<b>4</b>
1.1 Fourier Transform, Windowed Fourier Transform . . . . .	4
1.2 Introduction to Wavelet Analysis . . . . .	7
1.3 The Continuous Wavelet Analysis . . . . .	9
1.3.1 Examples of Wavelets . . . . .	10
The Haar Wavelet . . . . .	10
The Gaussian Family . . . . .	10
The Morlet Wavelet . . . . .	11
1.4 The Discrete Wavelet Transformation . . . . .	11
1.4.1 The Orthogonal Wavelet Transformation, Multi-Scale Analysis . . . . .	13

The Daubechies Wavelets . . . . .	19
1.4.2 The Fast Wavelet Transformation . . . . .	21
<b>2 Wavelets in System Identification – a Review</b>	<b>25</b>
2.1 Identification of Modal Parameters . . . . .	25
2.1.1 Methods Based on Continuous Wavelet Analysis . . . . .	26
2.1.2 Methods Based on Discrete Wavelet Analysis . . . . .	28
2.2 Identification of Time-Varying Systems . . . . .	31
2.2.1 Methods Based on Continuous Wavelet Analysis . . . . .	31
2.2.2 Approaches Based on Discrete Wavelet Analysis . . . . .	33
2.3 Damage Detection . . . . .	36
2.3.1 Presence and Occurrence of Damage . . . . .	36
2.3.2 Wavelet-Based Damage Indicators . . . . .	38
<b>3 De-noising by Selective Wavelet Reconstruction</b>	<b>42</b>
3.1 Selective Wavelet Reconstruction . . . . .	42
3.2 Estimation of Thresholds and Implementation . . . . .	44
3.2.1 Definition of Thresholds . . . . .	44
VisuShrink . . . . .	45
RiskShrink . . . . .	45
SUREShrink . . . . .	45
HybridShrink . . . . .	47
3.2.2 Implementation . . . . .	47
3.3 Enhanced De-noising Algorithms . . . . .	54

<b>4</b>	<b>Derivatives and Integrals in Wavelet Analysis</b>	<b>56</b>
4.1	Continuous Wavelet Transforms . . . . .	56
4.2	Discrete Wavelet Calculus, Connection Coefficients . . . . .	60
4.2.1	Orthogonal Wavelets and Linear Operators . . . . .	60
	Relations between Translation and Dilation . . . . .	60
	Differential and Integral Operators . . . . .	62
4.2.2	Connection Coefficients . . . . .	64
4.2.3	Application of Connection Coefficients . . . . .	66
4.2.4	Implementation of the Concept of Connection Coefficients . . . . .	69
<b>5</b>	<b>Direct Parameter Estimation</b>	<b>70</b>
5.1	Continuous Wavelet Analysis Approach . . . . .	71
5.2	Discrete Wavelet Analysis Approach . . . . .	77
5.2.1	Derivation of the Approach . . . . .	77
5.2.2	Solution Methods . . . . .	80
5.2.3	Verification . . . . .	82
<b>6</b>	<b>Assessment of Progressive Damage</b>	<b>97</b>
6.1	Signal Energy-Based Damage Assessment . . . . .	97
6.2	Description of the Tests . . . . .	99
6.3	Assessment of the Test Results . . . . .	100
	<b>Conclusions</b>	<b>108</b>
	<b>Bibliography</b>	<b>111</b>



<b>A SLang Commands Related to Wavelet Analysis</b>	<b>120</b>
<b>B Wavelet Connection Coefficients</b>	<b>122</b>
<b>C Examples – Differentiation and Integration</b>	<b>131</b>
<b>D Examples – Direct Parameter Estimation</b>	<b>154</b>
D.1 Example 5.1 – Diagrams . . . . .	154
D.2 Example 5.2 – Diagrams and Tables . . . . .	159
<b>E Progressive Damage – Experiments</b>	<b>164</b>
E.1 Description of progressive damage . . . . .	164
<b>Zusammenfassung in Deutsch</b>	<b>169</b>

# Notation

## General Terms and Symbols

$\mathbb{H}_\lambda$	class of linear operators
$\mathbb{N}$	set of all non-negative integers
$\mathbb{N}_+$	set of all positive integers
$\mathbb{R}$	set of all real numbers
$\mathbb{R}_+$	set of all positive real numbers
$\mathbb{Z}$	set of all integers
$\mathcal{D}^\lambda$	differential operator of $\lambda$ th order
$\mathcal{I}^\lambda$	integral operator of $\lambda$ th order
$\mathcal{K}$	linear operator
$[\cdot]$	matrix
$\{\cdot\}$	vector
$[\cdot]^T$	transpose of a matrix
$\{\cdot\}^T$	transpose of a vector
$[\cdot]^{-1}$	inverse of a matrix
$[\cdot]^+$	generalised / pseudo inverse of a matrix
$\ \cdot\ $	norm of a function, vector or matrix
$(\cdot)^*$	complex conjugate
$\overline{(\cdot)}$	mean value
$\langle f, g \rangle$	general inner product of $f$ and $g$

**Latin Letters**

$A$	lower bound of a wavelet frame
$A_m$	series of scaling coefficients at scale $m$ of an orthogonal wavelet decomposition (approximation)
$a$	scaling parameter in continuous wavelet analysis
$a_{m,k}$	$k$ th scaling coefficient at scale $m$ of an orthogonal wavelet decomposition
$B$	upper bound of a wavelet frame
$b$	translation parameter in continuous wavelet analysis
$c$	viscous damping parameter
$[C]$	viscous damping matrix
$C_\psi$	admissibility constant for a wavelet $\psi$
$d_{m,k}$	$k$ th wavelet coefficient at scale $m$ of an orthogonal wavelet decomposition
$D(s)$	operator of normalised dilation
$\bar{D}$	adjoint operator of $D$
$D_m$	series of wavelet coefficients at scale $m$ of an orthogonal wavelet decomposition (details)
$E$	expectation value
$E$	Young's modulus
$E_{i,j}$	wavelet coefficients' energy component
$e$	Euler number $\approx 2.718282$
$F$	force
$f, g$	function
$f$	frequency [ $Hz$ ]
$f_n$	natural frequency [ $Hz$ ]
$f_{m,n}$	wavelet coefficient of an excitation series

$f(t)$	general function of time (signal)
$f(t)$	time series of excitation
$f_w(t)$	windowed signal
$\hat{f}(\omega)$	Fourier transform of a function $f$
$f^m$	projection of a function $f$ onto a linear subspace $V_m$
$G$	projection operator of the wavelet in discrete wavelet analysis
$\bar{G}$	adjoint operator of $G$
$G_{AA}$	auto spectral density
$g$	order of a wavelet
$g_n$	coefficient of a wavelet in discrete wavelet analysis
$\tilde{g}_n$	normalised coefficient of a wavelet in discrete wavelet analysis
$H$	projection operator of the scaling function in discrete wavelet analysis
$\bar{H}$	adjoint operator of $H$
$H(\omega)$	frequency response function (FRF)
$h_n$	coefficient of a scaling function in discrete wavelet analysis
$h_{m,n}$	wavelet coefficient of an impulse response function
$\tilde{h}_n$	normalised coefficient of a scaling function in discrete wavelet analysis
$h(\Theta)$	impulse response function (IRF)
$I$	geometrical moment of inertia
$i$	imaginary unit $\sqrt{-1}$
$i, j, k, l, m, n$	indices, integers
$k$	stiffness parameter
$[K]$	stiffness matrix
$L^n(\mathbb{R})$	space of real functions with $\int_{\mathbb{R}}  f(t) ^n dt < \infty$
$M$	integer, max. wavelet decomposition level

$m$	mass
$[M]$	mass matrix
$P_m, Q_m$	projection operator of a multi-scale analysis
$R$	risk measure
$s$	scale parameter
$T(\tau)$	operator of translation
$\bar{T}(\tau)$	adjoint operator of $T$
$t$	time variable
$u_m$	weighting coefficient
$V_m, W_m$	subspaces of a multi-scale analysis
$W_\psi^f(a, b)$	continuous wavelet transform with respect to a wavelet $\psi$
$w(\cdot)$	window function
$w^{\omega, \tau}(t)$	basic function of a windowed Fourier transformation
$x(t), \dot{x}(t), \ddot{x}(t)$	time series of displacements, velocities, accelerations
$z_\psi$	normalisation coefficient
$z_{j,k}$	wavelet coefficients of noise in a signal

### Greek Letters

$\alpha_\nu$	normalised autocorrelation coefficient of the scaling function's coefficients
$\beta_{k,\nu}$	parameter for the calculation of connection coefficients
$\Gamma_{i,j}^{k,l}(f, g)$	connection coefficient
$\Delta t$	time sampling rate
$\Delta f, \Delta \omega$	frequency sampling rate
$\delta_j$	modal logarithmic decrement
$\delta_{i,j}$	Kronecker symbol
$\zeta_j$	modal damping ratio
$\eta_j$	threshold operator for wavelet shrinkage

$\Theta$	time interval between instants of response and excitation, resp.
$\Theta_{j,k}$	wavelet coefficients of a noise-free signal
$\lambda$	threshold for wavelet shrinkage
$\lambda$	integer indicating order of differentiation or integration
$\lambda_A$	eigenvalue of a matrix $[A]$
$\nu$	integer
$\rho$	mass density
$\tau$	time parameter
$\sigma$	standard deviation
$[\Phi]$	eigenvector matrix
$\phi$	scaling function
$\phi_{m,n}$	dilated and translated scaling function
$\psi(\cdot), \psi$	mother wavelet
$\psi^{a,b}$	dilated and translated wavelet in continuous wavelet analysis
$\psi_{m,n}$	dilated and translated wavelet in discrete wavelet analysis
$\omega$	frequency $[\frac{rad}{s}]$
$\omega_n$	natural frequency $[\frac{rad}{s}]$



# Introduction

A typical engineering task in the design phase of buildings and civil engineering structures is the prediction of the structure's response to an external loading. Usually, a numerical model of the structural system is used in this context. Consequently, the quality of the predictions depends to a great extent on the model's quality.

The subject of system identification is the solution of the inverse problem, i.e. the identification of a system that describes the relation between an input and a known output (figure 1). That means, the aim of system identification is the description of an existing structural system by a model, based on experimentally obtained data. This data is often obtained from dynamic tests of the structure.

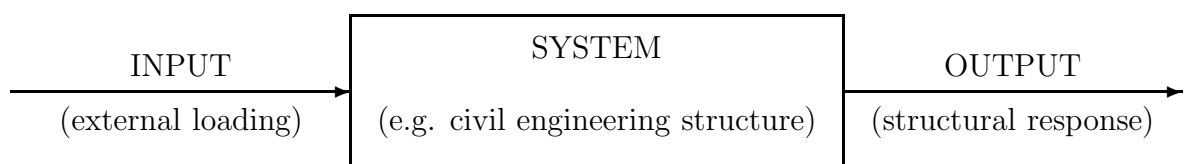


Figure 1: Schematic representation of input-output relation of a structural system

Often it is desired to detect irregularities or changes of the considered structural system's properties that were caused by structural damage. The field of damage detection (or damage identification) includes the following objectives:

1. Detection of presence of damage,



2. Localisation of damage,
3. Severity assessment of damage (quantification) and
4. Prediction of structural safety.

If damage is regarded as a modification of the system's parameters, the first three of these four levels are related to system identification.

Traditionally, most approaches in system identification are based on the analysis of the measured data either in the time or in the frequency domain. While frequency domain approaches are not well suited to the consideration of a system's properties with respect to time, time domain methods are often very sensitive to noise in the data since all frequency components present in the data are included into the analysis.

In order to overcome these disadvantages, several methods, that use time-frequency or time-scale domain analysis, were developed in recent years. A considerable number of these approaches is based on wavelet analysis. The objective of these developments range from the extraction of signal feature in the context of damage detection over modal parameter identification to the estimation of structural system parameters. In many cases only comparatively simple systems are considered (single, two or three degree of freedom systems). With respect to experimental applications, only very few examples are reported, particularly in the context of civil engineering structures.

During tests on civil engineering structures, the structural response is usually measured in the form of accelerations. However, often estimations of displacements or velocities are required. An integration of measured accelerations can result in considerable errors due to the presence of noise in the data.

Concerning structural health monitoring of civil engineering structures, the definition of a sensitive and reliable indicator for first level damage detection is still the subject of current research.

The objectives of this dissertation can be summarised as follows:

- Development of a methodology for a wavelet-based direct system parameter estimation that uses solely measured accelerations and applied forces,
- Investigation of this method's applicability to more complex systems and of its accuracy with respect to the data's noise content,
- Application of the derived method to data generated in dynamic tests on an existing structural system,
- Investigations concerning a sensitive and applicable wavelet-based indicator for first level damage detection in reinforced concrete structures.

Specific emphasis is put on the application of discrete wavelet analysis in order to benefit from the advantages of the respective fast algorithms.

The theoretical background of wavelet analysis is explained in chapter 1. A number of recent applications of wavelet analysis in system identification are summarised in chapter 2. De-noising by selective wavelet reconstruction, an important application in signal processing, is described and applied to structural dynamics-related problems in chapter 3. In chapter 4 relations for the representation of derivatives and integrals in both continuous and discrete time-scale domain are derived. These relations are applied to the identification of a system's parameters in chapter 5. A proposal for a wavelet-based indicator for first level damage detection on reinforced concrete structures is made in chapter 6.

The intention of the presented study is to contribute to the developments of wavelet-based approaches in system identification. These techniques should combine the advantages of fast numerical algorithms with those of time-scale domain representations.

# Chapter 1

## Fundamentals of Wavelet Analysis

In this chapter a brief introduction to wavelet analysis is given. The starting point is the Fourier transform and the windowed Fourier transform. Following the reflections on these methods, that are extensively utilised for analysing signals in the frequency and time-frequency domain, respectively, wavelet analysis is introduced. First the continuous wavelet transform is described before passing on to the discrete wavelet transform. The multi-scale analysis, that the fast wavelet transformation algorithms are based on, is explained.

The descriptions in this chapter are restricted to the one-dimensional wavelet transformation. For detailed derivations and further descriptions refer to the literature (e.g. [14] [17], [34], [40]).

### 1.1 The Fourier Transform and the Windowed Fourier Transform

As in other engineering disciplines, an important part of structural dynamics is the identification of certain properties of time-variable processes. In this context measured signals,

that can be interpreted as functions with respect to time, are often transferred into another domain.

The most commonly used transformation method in signal analysis is the Fourier transformation. The basic idea of the Fourier analysis is to describe a signal by means of an infinite series of harmonic functions. The Fourier transform of a function  $f(t)$  is defined as:

$$\hat{f}(\omega) = \frac{1}{\sqrt{2\pi}} \int_{-\infty}^{\infty} f(t) e^{-i\omega t} dt . \quad (1.1)$$

Its inverse is given by:

$$f(t) = \frac{1}{\sqrt{2\pi}} \int_{-\infty}^{\infty} \hat{f}(\omega) e^{i\omega t} d\omega . \quad (1.2)$$

The Fourier transform is defined for real functions that are square-integrable. A function  $f(t)$  belongs to the space  $L^2(\mathbb{R})$ ,  $\mathbb{R} := (-\infty; +\infty)$  if

$$\int_{\mathbb{R}} f^2(t) dt < \infty . \quad (1.3)$$

If the condition in equation 1.3 is satisfied and with the normalisation used in equations (1.1) and (1.2) one has (e.g. [34])

$$\|\hat{f}(\omega)\|_{L^2} = \|f\|_{L^2} , \quad (1.4)$$

with

$$\|f\|_{L^2} = \left[ \int |f(t)|^2 \right]^{\frac{1}{2}} . \quad (1.5)$$

The application of the Fourier analysis has become very popular since the introduction of the Fast Fourier Transform method (FFT). Usually the Fourier analysis is applied to finite time series assuming that the signals are periodically continuing outside the observation interval. The Fourier transform does not give information about how the frequency contents of a signal behave with respect to time. Therefore the Fourier analysis is not particularly appropriate for the investigation of non-linear and non-stationary problems.

The first important step in the analysis of signals in the time-frequency domain was the introduction of the windowed Fourier transform. Basically, with the windowed Fourier

transform the frequency contents of a signal within a time window are analysed. The window is of constant length and is translated along the time axis. That means, the Fourier analysis is only applied to a section of the entire signal. Within each of these sections the signal is assumed to be stationary. Such a section is called windowed signal:

$$f_w(t) = w(t) f(t) . \quad (1.6)$$

The window function  $w(t)$  must be square-integrable [34] and the product  $f(t) w(t)$  has to be an element of  $L^2(\mathbb{R})$  as well.

By moving the window along the time axis, the complete time domain is covered. Consequently the windowed signal  $f_w(t)$  depends both on the time  $t$  and the windows position  $\tau$ :

$$f_w(t, \tau) = w(t - \tau) f(t) . \quad (1.7)$$

By applying the Fourier transformation on such a windowed signal, one obtains the windowed Fourier transform as a function of the frequency  $\omega$  and the window's position  $\tau$ :

$$\hat{f}_w(\omega, \tau) = \frac{1}{\sqrt{2\pi}} \int_{-\infty}^{\infty} w(t - \tau) f(t) e^{-i\omega t} dt . \quad (1.8)$$

If the Fourier transform  $\hat{w}(\omega)$  of the window function  $w(t)$  is also a window function ( $\hat{w}(\omega) \in L^2(\mathbb{R}), \omega \hat{w}(\omega) \in L^2(\mathbb{R})$ ), then equation (1.8) is called the short time Fourier transform.

The resolutions in the frequency and time domains are generally different. They are governed by the length and the frequency band width of the utilised window function. For an ‘‘optimal’’ localisation in the time-frequency domain, the application of a function proportional to the Gaussian function is recommended (e.g. [60], [40], [51], [13], [14]):

$$w = g_\alpha = \frac{1}{2\sqrt{\pi\alpha}} e^{-\frac{t^2}{4\alpha}} , \quad (1.9)$$

where  $\alpha > 0$  is a constant. The respective windowed Fourier transform is also called the Gabor transform [27].

Fourier analysis decomposes a signal by means of elementary harmonic functions. For the windowed Fourier transformation the decomposition is carried out partially. The basic

functions usually are decaying harmonic functions of constant duration. The number of oscillations within a window varies.

## 1.2 Introduction to Wavelet Analysis

Similar to the windowed Fourier transformation, the one-dimensional wavelet transformation projects a signal into a two-dimensional space. Analogous to equation (1.8) the wavelet transform of a signal  $f(t)$  is defined as:

$$W_{\psi}^f(a, b) = |a|^{-\frac{1}{2}} \int_{-\infty}^{\infty} f(t) \psi^* \left( \frac{t-b}{a} \right) dt, \quad (1.10)$$

where  $\psi^*(\cdot)$  denotes the complex conjugate of  $\psi(\cdot)$ . It is assumed that the mean value of the function  $\psi$  vanishes (e.g. [40]):

$$\int_{-\infty}^{\infty} \psi(t) dt = 0. \quad (1.11)$$

Both in the windowed Fourier transformation and in the wavelet transformation the signal  $f(t)$  is multiplied by a function of two variables. In the case of the windowed Fourier transform this is the function

$$w^{\omega, \tau}(t) = \frac{1}{\sqrt{2\pi}} w(t - \tau) e^{-i\omega t}. \quad (1.12)$$

The respective function for the wavelet transformation is

$$\psi^{a,b}(t) = |a|^{-\frac{1}{2}} \psi^* \left( \frac{t-b}{a} \right). \quad (1.13)$$

The functions  $\psi^{a,b}$  are called wavelets. They are dilated and translated versions of the mother wavelet  $\psi$ . As the basic functions of the windowed Fourier transformation, wavelets are usually oscillating, rapidly decaying functions. However, in contrast to the functions  $w^{\omega, \tau}(t)$ , the number of oscillations of the functions  $\psi^{a,b}(t)$  remains constant with the changing width of the window. This means a wavelet is “stretched” or “squeezed”

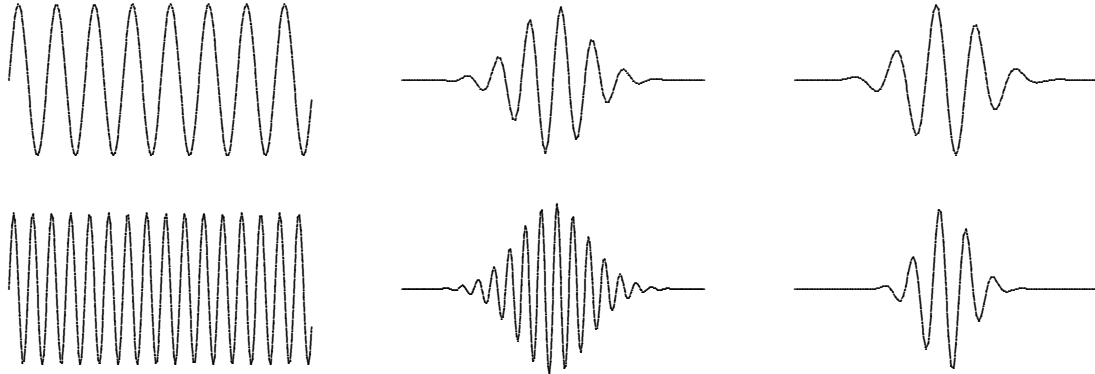


Figure 1.1: Illustration of the basic functions for the Fourier transformation (left), the windowed Fourier transformation (centre) and the wavelet transformation (right)

(dilated) along the time axis. For the windowed Fourier transformation the size of the window remains constant while the number of oscillations changes. This principle is illustrated in figure 1.1.

A typical example for a wavelet is the so-called “Mexican hat”:

$$\psi(t) = (1 - t^2) e^{-\frac{t^2}{2}},$$

the second derivative of the Gaussian function. The condition of equation (1.11) is satisfied for the “Mexican hat”.

Large values of the scaling parameter  $a$  correspond with small frequencies. A change of the parameter  $b$  results in a translation of the localisation point. Each  $\psi^{a,b}(t)$  is located at  $t = b$ .

It can be shown (e.g. [14], [60]) that the wavelet transform of a function  $f(t)$  can be calculated by means of the Fourier transforms of this function,  $\hat{f}(\omega)$  and of the dilated wavelet,  $\hat{\psi}(a\omega)$ . Equation (1.10) becomes then:

$$W_{\psi}^f(a, b) = \frac{\sqrt{a}}{2\pi} \int_{-\infty}^{\infty} \hat{f}(\omega) \hat{\psi}^*(a\omega) e^{i\omega b} d\omega. \quad (1.14)$$

Generally two types of the wavelet transformation can be distinguished:

- the continuous wavelet transformation and
- the discrete wavelet transformation.

Their basic properties are briefly described in the following sections and verified by examples.

### 1.3 The Continuous Wavelet Analysis

For the continuous wavelet transformation, the wavelet  $\psi^{a,b}$  can always be described by an analytical function. Both the scaling parameter  $a$  and the translation parameter  $b$  change continuously over  $\mathbb{R}$ . It is excluded that  $a$  vanishes ( $a \neq 0$ ). The continuous wavelet transform is defined by equation (1.10). If  $\psi\left(\frac{t-b}{a}\right)$  is a real function, equation (1.10) becomes:

$$W_{\psi}^f(a, b) = |a|^{-\frac{1}{2}} \int_{-\infty}^{\infty} f(t) \psi\left(\frac{t-b}{a}\right) dt. \quad (1.15)$$

Beside the assumption of the vanishing mean value (equation (1.11)), a wavelet must satisfy the admissibility condition:

$$C_{\psi} = 2\pi \int_{-\infty}^{\infty} \frac{|\hat{\psi}(\omega)|^2}{|\omega|} d\omega < \infty. \quad (1.16)$$

Here  $\hat{\psi}(\omega)$  denotes the Fourier transform of  $\psi(t)$ . The inverse of the continuous wavelet transform is given by

$$f(t) = \frac{1}{C_{\psi}} \int_{-\infty}^{\infty} \int_{-\infty}^{\infty} \frac{1}{\sqrt{|a|}} W_{\psi}^f(a, b) \psi^*\left(\frac{t-b}{a}\right) \frac{da db}{a^2}. \quad (1.17)$$

For real wavelets equation (1.17) becomes

$$f(t) = \frac{1}{C_{\psi}} \int_{-\infty}^{\infty} \int_{-\infty}^{\infty} \frac{1}{\sqrt{|a|}} W_{\psi}^f(a, b) \psi\left(\frac{t-b}{a}\right) \frac{da db}{a^2}. \quad (1.18)$$



A wavelet  $\psi$  is called of order  $g \in \mathbb{N}$  [40] if its mean value and the first  $g - 1$  moments vanish:

$$\int_{-\infty}^{\infty} t^k \psi(t) dt = 0, \quad k = 0, 1, 2, \dots, g - 1 \quad (1.19)$$

and if the  $g$ th moment is finite and non-zero:

$$\int_{-\infty}^{\infty} t^g \psi(t) dt \neq 0, \quad . \quad (1.20)$$

Some examples for often applied wavelets are given in the following paragraphs.

### 1.3.1 Examples of Wavelets

#### The Haar Wavelet

The Haar wavelet has been known since 1910 [17]. It is defined by:

$$\psi(t) = \begin{cases} 1 & \text{for } 0 \leq t < \frac{1}{2} \\ -1 & \text{for } \frac{1}{2} \leq t < 1 \\ 0 & \text{elsewhere} \end{cases} \quad (1.21)$$

Its Fourier transform is given by:

$$\hat{\psi}(\omega) = 2 \frac{i}{\sqrt{2\pi}} e^{-\frac{i\omega}{2}} \frac{1 - \cos\left(\frac{\omega}{2}\right)}{\omega} \quad (1.22)$$

The Fourier transform of the Haar wavelet decays relatively slowly, as can be seen in figure 1.2. Accordingly, the Haar wavelet does not localise well with respect to frequency. However, it forms the simplest orthogonal base and can be easily applied as a wavelet for the discrete wavelet transformation (section 1.4.)

#### The Gaussian Family

The wavelets of the Gaussian family are formed by the  $n$ th derivatives of the Gaussian distribution function  $g(t) = e^{-\frac{t^2}{2}}$ . Each wavelet of this family is defined by:

$$\psi(t) = (-1)^n \frac{d^n}{dt^n} e^{-\frac{t^2}{2}}, \quad n \in \mathbb{N} \quad (1.23)$$

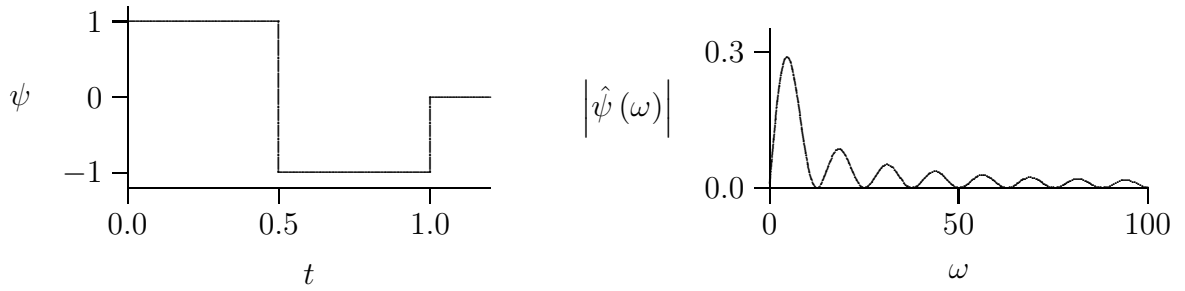


Figure 1.2: The Haar wavelet (left) and the magnitude of its Fourier transform (right)

The respective Fourier transforms are:

$$\hat{\psi}(\omega) = (-i\omega)^n e^{-\frac{\omega^2}{2}}. \quad (1.24)$$

The earlier mentioned “Mexican hat” also belongs to this family. The first three wavelets of the Gaussian family are shown in figure 1.3. The localisation properties improve with increasing order  $n$ .

### The Morlet Wavelet

All the wavelets that have been introduced so far are real functions. One of the most often applied complex valued wavelets is the Morlet wavelet. It is defined as the product of a complex exponential function and the Gaussian function:

$$\psi(t) = e^{i\omega_\psi t} e^{-\frac{|t|^2}{2}}. \quad (1.25)$$

The Fourier transform is then

$$\hat{\psi}(\omega) = e^{-\frac{(\omega - \omega_\psi)^2}{2}}. \quad (1.26)$$

The wavelet transform is a complex valued function which is represented either by its real and imaginary parts or by the modulus and phase.

## 1.4 The Discrete Wavelet Transformation

The continuous wavelet transformation, as introduced in section 1.3, projects a one-dimensional signal  $f(t)$  into the continuous time-scale domain. For most of the applied

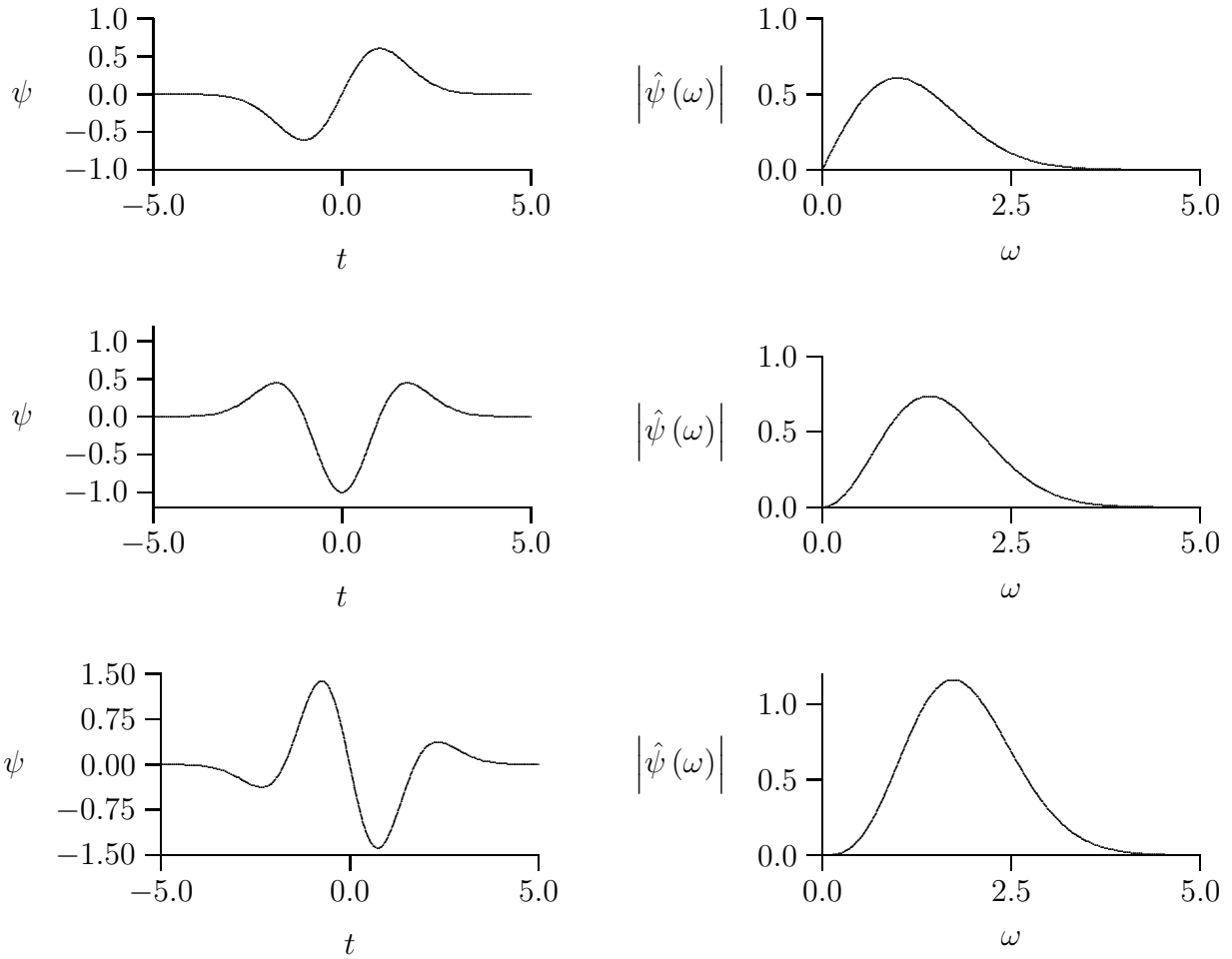


Figure 1.3: The first, second and third derivatives (from top to bottom) of the Gaussian function (left) and their Fourier transforms (right),

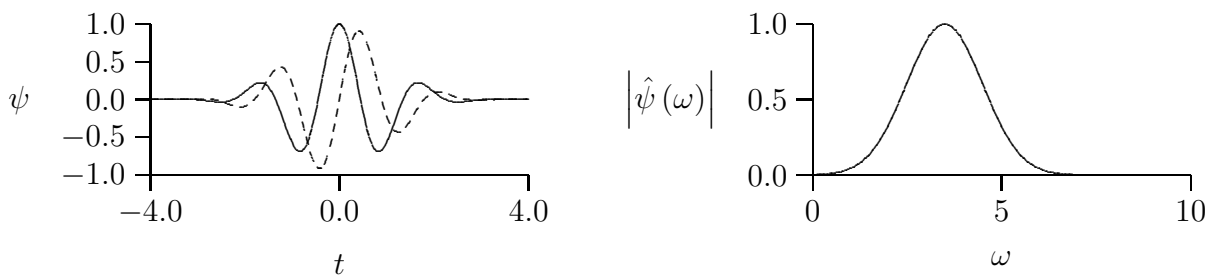


Figure 1.4: The Morlet wavelet (left), the real part (solid) and the imaginary part (dashed), and the magnitude of its Fourier transform (right)

wavelets, this leads to a redundancy of information in the wavelet transform and requires a considerable number of numerical operations.

For the continuous wavelet analysis, the wavelets (equation 1.13)

$$\psi^{a,b}(t) = |a|^{-\frac{1}{2}} \psi\left(\frac{t-b}{a}\right)$$

are used. Here are  $b \in \mathbb{R}$  and  $a \in \mathbb{R}$  with  $a \neq 0$ . The wavelet  $\psi$  must satisfy the admissibility condition (1.16). In signal analysis it is sensible to restrict the scaling parameter to positive real numbers ( $a \in \mathbb{R}_+$ ). As a consequence the admissibility condition (1.16) can be modified to [17]:

$$C_\psi = \int_0^\infty \frac{|\hat{\psi}(\omega)|^2}{|\omega|} d\omega = \int_{-\infty}^0 \frac{|\hat{\psi}(\omega)|^2}{|\omega|} d\omega < \infty. \quad (1.27)$$

For the discrete wavelet transform the parameters  $a$  and  $b$  become discrete values. The scaling parameter  $a$  is chosen to be a power of a constant  $a_0$ . The translation parameter  $b$  is also determined based on a constant  $b_0$ . The parameters  $a$  and  $b$  are formed as:

$$a_m = a_0^m \quad b_{m,n} = n b_0 a_0^m. \quad (1.28)$$

with  $m, n \in \mathbb{Z}$  and  $a_0 > 1, b_0 > 0$  [17]. The choice of the constants  $a_0, b_0$  depends on the wavelet  $\psi$ :

$$\psi_{m,n}(t) = a_0^{-\frac{m}{2}} \psi\left(\frac{t - n b_0 a_0^m}{a_0^m}\right) = a_0^{-\frac{m}{2}} \psi(a_0^{-m}t - n b_0). \quad (1.29)$$

The system of functions  $\{\psi_{m,n}(t); m, n \in \mathbb{Z}\}$  in equation (1.29) forms a wavelet frame, if

$$A \|f\|^2 \leq \sum_m \sum_n |\langle f, \psi_{m,n} \rangle|^2 \leq B \|f\|^2 \quad \forall f \in L^2(\mathbb{R}), \quad (1.30)$$

where  $A$  and  $B$  are constants with  $A > 0$  and  $B < \infty$ . The constants  $A$  and  $B$  are called the frame bounds. If  $A = B$ , a frame is called a tight frame [17], [40].

### 1.4.1 The Orthogonal Wavelet Transformation, Multi-Scale Analysis

If  $\psi_{m,n}(t)$  forms a tight frame with the bounds  $A = B = 1$  and if  $\psi_{m,n}$  is normalised such that  $\|\psi_{m,n}\| = 1$ , then  $\psi_{m,n}$  forms an orthonormal base. That means one obtains, for

arbitrarily chosen  $i, j, k, l$ :

$$\langle \psi_{i,j}, \psi_{k,l} \rangle = \begin{cases} 1 & \text{for } i = j \text{ and } k = l \\ 0 & \text{elsewhere} \end{cases} . \quad (1.31)$$

A well known group of discrete wavelets is given by the dyadic wavelets. They are formed if  $a_0 = 2$  and  $b_0 = 1$ . With these parameters, equation (1.29) becomes

$$\psi_{m,n}(t) = 2^{-\frac{m}{2}} \psi(2^{-m}t - n) . \quad (1.32)$$

From equation (1.28) one can conclude that the dyadic wavelet transformation is a projection onto a dyadic grid:

$$a = 2^m \quad b = n 2^m . \quad (1.33)$$

Such a dyadic grid is illustrated in figure 1.5. It can be easily deduced from figure 1.5 that the discrete scales can be interpreted as frequency bands. The discrete scales are also referred as levels. The levels' bandwidths of a dyadic wavelet transform are octaves. A broader band width corresponds with a finer resolution in time.

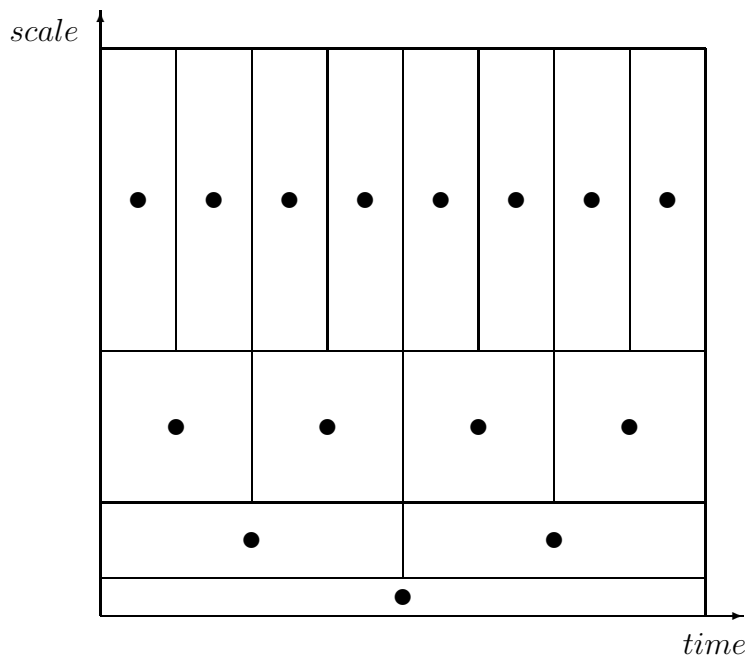


Figure 1.5: Dyadic wavelet grid

Typically the data for a signal analysis is provided in digital form. That means,  $f(t)$  is a series of discrete values that has been sampled with a sampling rate  $\Delta t$ . These time series may become very long, which sometimes results in a considerable amount of data that has to be analysed. Consequently a fast numerical algorithm is required. With respect to the discrete wavelet transformation, such an algorithm is usually based on a multi-scale analysis.

The basic idea of a multi-scale analysis is that a signal  $f(t)$  with a total length  $T = 1$ , which has been sampled at a rate of  $\Delta t = 2^{-n}$ , is decomposed into series at different scales with a bandwidth of  $2^{-m}$ ,  $m \in \mathbb{Z}$ . Each of these scales corresponds to a subspace  $V_m$  in  $L^2(\mathbb{R})$ :

$$\{0\} \subset \dots \subset V_2 \subset V_1 \subset V_0 \subset V_{-1} \subset V_{-2} \subset \dots \subset L^2(\mathbb{R}) . \quad (1.34)$$

This decomposition is schematically illustrated in figure 1.6. A signal  $f$  in the subspace

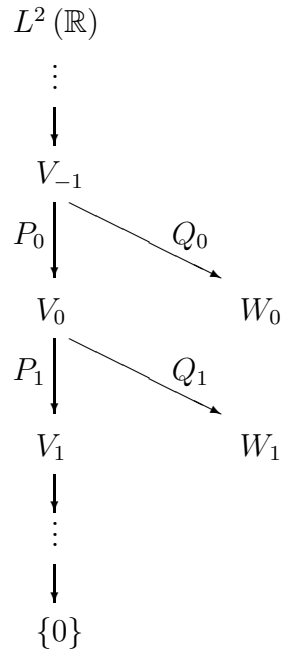


Figure 1.6: Scheme of a multi-scale analysis

$V_{-1}$  in  $L^2(\mathbb{R})$  is split into a high frequency part and a low frequency part. The low

frequency part is described by an orthogonal projection  $P_0 f$  onto the subspace  $V_0$  in  $V_{-1}$ . The subspace  $W_0$  in  $V_{-1}$  contains the high frequency parts of  $f$ . The orthogonal projection of  $f$  in  $V_{-1}$  onto  $W_0$  is  $Q_0 f$ . That means:

$$\begin{aligned} f &= P_0 f + Q_0 f, \\ V_{-1} &= V_0 \oplus W_0. \end{aligned} \quad (1.35)$$

If one follows the diagram in figure 1.6 it becomes apparent that

$$f = P_1 f + Q_1 f \quad (1.36)$$

and in consequence

$$f = P_1 f + Q_1 f + Q_0 f. \quad (1.37)$$

Therefore a signal  $f$  in  $L^2(\mathbb{R})$  ( $m \rightarrow -\infty$ ;  $P_m f \rightarrow f$ ) can be described by the following decomposition until a scale  $M$ :

$$f = P_M f + \sum_{k=-\infty}^M Q_k f, f \in L^2(\mathbb{R}). \quad (1.38)$$

Hence, one obtains for the orthogonal decomposition of  $L^2(\mathbb{R})$ :

$$L^2(\mathbb{R}) = V_M \oplus \bigoplus_{k=-\infty}^M W_k. \quad (1.39)$$

If a signal  $f$  belongs to a subspace  $V_m$ , equations (1.38) and (1.39) become:

$$f^m = P_m f = P_M f + \sum_{k=m+1}^M Q_k f, M > m, \quad (1.40)$$

$$V_m = V_M \oplus \bigoplus_{k=m+1}^M W_k, M > m. \quad (1.41)$$

The multi-scale analysis in the context of the orthogonal wavelet transformation assumes the existence of a scaling function  $\phi$ , such that the subspace  $V_m$  is formed by the functions

$$\{\phi_{m,n}(t) := 2^{-\frac{m}{2}} \phi(2^{-m}t - n), n \in \mathbb{Z}\}, \quad (1.42)$$

$$V_m = \left\{ f = \sum_{n \in \mathbb{Z}} a_{m,n} \phi_{m,n}, \|f\|^2 = \sum_{n \in \mathbb{Z}} |a_{m,n}|^2 < \infty \right\}. \quad (1.43)$$

The system of functions  $\{\phi_{m,n}, n \in \mathbb{Z}\}$  forms an orthonormal base of  $V_m$ .

$P_m f = f^m$  can be developed by means of the base:

$$f^m = P_m f = \sum_{n \in \mathbb{Z}} a_{m,n} \phi_{m,n}. \quad (1.44)$$

The scaling function  $\phi$  satisfies the scaling condition:

$$\phi(t) = \sqrt{2} \sum_{n \in \mathbb{Z}} h_n \phi(2t - n), \quad h_n \in \mathbb{R}. \quad (1.45)$$

It has the properties

$$\int_{-\infty}^{\infty} \phi(t) dt = 1 \quad (1.46)$$

and

$$\sum_{n \in \mathbb{Z}} h_n = \sqrt{2}, \quad \sum_{n \in \mathbb{Z}} (-1)^n h_n = 0. \quad (1.47)$$

Based on such a scaling function  $\phi$  a mother wavelet  $\psi$  can be built:

$$\psi(t) = \sqrt{2} \sum_{n \in \mathbb{Z}} g_n \phi(2t - n), \quad (1.48)$$

where

$$g_n = \langle \psi, \phi_{-1,n} \rangle = (-1)^n h_{1-n}. \quad (1.49)$$

With equation (1.11) one obtains for a wavelet of an orthogonal wavelet transformation the property:

$$\int_{-\infty}^{\infty} \psi(t) dt = \frac{1}{\sqrt{2}} \sum_{n \in \mathbb{Z}} g_n = 0. \quad (1.50)$$

The admissibility condition for a wavelet (1.16) is satisfied as well:

$$C_\psi = 2\pi \int_{-\infty}^{\infty} \frac{|\hat{\psi}(\omega)|^2}{|\omega|} d\omega = 2 \ln 2 < \infty. \quad (1.51)$$

The dilated and translated version of  $\psi$ :

$$\psi_{m,n}(t) = 2^{-\frac{m}{2}} \psi(2^{-m}t - n), \quad m, n \in \mathbb{Z} \quad (1.52)$$

is an orthonormal base for the subspace  $W_m$ .



If  $m = -1$  is chosen, equation (1.42) becomes

$$\phi_{-1,n}(t) = \sqrt{2} \phi(2t - n) . \quad (1.53)$$

Consequently, equation (1.48) can be re-written as

$$\psi(t) = \sum_{n \in \mathbb{Z}} g_n \phi(2t - n) . \quad (1.54)$$

Equation (1.32) can be re-arranged according to the following scheme [17]:

$$\begin{array}{l} \psi_{m,k}(t) = 2^{-\frac{m}{2}} \psi(2^{-m}t - k) \\ \left\{ \begin{array}{l} \longleftarrow \psi(2^{-m}t - k) = 2^{\frac{1}{2}} \sum_{n \in \mathbb{Z}} g_n \phi(2^{-m+1}t - 2k - n) \\ \longleftarrow \phi_{m-1,sk+n}(t) = 2^{-\frac{m+1}{2}} \phi(2^{-m+1}t - 2k - n) \end{array} \right. \\ \downarrow \\ \psi_{m,k}(t) = \sum_{n \in \mathbb{Z}} g_n \phi_{m-1,2k+n}(t) = \sum_{n \in \mathbb{Z}} g_{n-2k} \phi_{m-1,n}(t) \end{array} \quad (1.55)$$

Similarly it can be derived from equations (1.42) and (1.45):

$$\phi_{m,k}(t) = 2^{-\frac{m}{2}} \phi(2^{-m}t - k) = \sum_{n \in \mathbb{Z}} h_{n-2k} \phi_{m-1,n}(t) . \quad (1.56)$$

If the wavelet  $\psi$  and its respective scaling function  $\phi$  form an orthonormal system the following relations are satisfied ([53]):

$$\langle \phi_{i,k}, \phi_{i,l} \rangle = \delta_{k,l} , \quad (1.57)$$

$$\langle \phi_{i,k}, \psi_{j,l} \rangle = 0 \text{ for } i \geq j , \quad (1.58)$$

$$\langle \psi_{i,k}, \psi_{j,l} \rangle = \delta_{i,j} \delta_{k,l} , \quad (1.59)$$

$$\|\phi_{i,k}\| = \|\psi_{i,k}\| = 1 , \quad (1.60)$$

where  $\delta_{i,j}$  denotes the Kronecker delta.

Often used orthogonal wavelets are those of the Daubechies wavelets family [17]. There exist numerous other orthogonal wavelets, such as the Meyer wavelet, the so-called Coiflets, the Symmlets or spline wavelets. The description of these wavelets is beyond the scope of this work. Only some remarks on the Daubechies wavelets are made in the following section.

### The Daubechies Wavelets

For the sake of enhanced clarity it is useful to normalise the coefficients of the scaling function and the wavelet, respectively:

$$\tilde{h}_n = \sqrt{2} h_n \text{ and } \tilde{g}_n = \sqrt{2} g_n . \quad (1.61)$$

The number of non-zero coefficients  $h_n$  and  $g_n$ , respectively, is  $2g$ , where  $g \in \mathbb{N}_+$  denotes the order of the respective Daubechies wavelet. Accordingly, equations (1.45) and (1.48) become:

$$\phi(t) = \sum_{n=0}^{2g-1} \tilde{h}_n \phi(2t - n) , \quad (1.62)$$

$$\psi(t) = \sum_{n=0}^{2g-1} \tilde{g}_n \phi(2t - n) = \sum_{n=0}^{2g-1} (-1)^n \tilde{h}_{2g-1-n} \phi(2t - n) . \quad (1.63)$$

A Daubechies wavelet of order  $g$  always satisfies the following conditions:

- It is compactly supported in the interval  $[0, 2g - 1]$ ,
- $\psi(t)$  has  $g$  vanishing moments:

$$\int_{-\infty}^{\infty} t^m \psi^g(t) dt , \quad m = 0, \dots, g - 1 . \quad (1.64)$$

With an increasing number of vanishing moments, i.e. with higher order  $g$ ,  $\psi(t)$  becomes smoother.

In the following paragraphs it is described how the scaling functions of the Daubechies wavelets can be calculated. However, first some properties of the scaling functions, or rather their coefficients  $\tilde{h}_n$ , are summarised.

It follows from equations (1.47) and (1.61) that

$$\sum_{n=0}^{2g-1} \tilde{h}_n = 2. \quad (1.65)$$

Two further conditions that have to be satisfied by the coefficients  $\tilde{h}_n$  [60], [49] are the condition of accuracy

$$\sum_{n=0}^{2g-1} (-1)^n n^m \tilde{h}_n = 0, \quad m = 0, 1, 2, \dots, g-1 \quad (1.66)$$

and the condition of orthogonality

$$\sum_{n=0}^{(2g-1-2m)} \tilde{h}_n \tilde{h}_{n+2m} = 0, \quad m = 1, 2, \dots, g-1. \quad (1.67)$$

Furthermore, the orthogonality of the scaling function results in [49]:

$$\sum_{n=0}^{2g-1} \tilde{h}_n^2 = 2. \quad (1.68)$$

The coefficients  $\tilde{h}_n$  of the scaling function of a Daubechies wavelet of order  $g$  can be calculated utilising equations (1.65) to (1.68).

For further properties of the Daubechies wavelets and their scaling functions, refer to the literature (e.g.[17], [49], [40], [34]).

**Example 1.1.** *It is shown how the scaling function's coefficients  $\tilde{h}_n$  of the Daubechies wavelet D3 (order  $g = 3$ ) are calculated: (1.65):*

$$\tilde{h}_0 + \tilde{h}_1 + \tilde{h}_2 + \tilde{h}_3 + \tilde{h}_4 + \tilde{h}_5 = 2 \quad (1.69)$$

(1.66):

$$\tilde{h}_0 - \tilde{h}_1 + \tilde{h}_2 - \tilde{h}_3 + \tilde{h}_4 - \tilde{h}_5 = 0 \quad (1.70)$$

$$\tilde{h}_0 - \tilde{h}_1 + 2\tilde{h}_2 - 3\tilde{h}_3 + 4\tilde{h}_4 - 5\tilde{h}_5 = 0 \quad (1.71)$$

$$\tilde{h}_0 - \tilde{h}_1 + 4\tilde{h}_2 - 9\tilde{h}_3 + 16\tilde{h}_4 - 25\tilde{h}_5 = 0 \quad (1.72)$$

(1.67):

$$\tilde{h}_0 \tilde{h}_2 + \tilde{h}_1 \tilde{h}_3 + \tilde{h}_2 \tilde{h}_4 + \tilde{h}_3 \tilde{h}_5 = 0 \quad (1.73)$$

$$\tilde{h}_0 \tilde{h}_4 + \tilde{h}_1 \tilde{h}_5 = 0 \quad (1.74)$$

(1.68):

$$\tilde{h}_0^2 + \tilde{h}_1^2 + \tilde{h}_2^2 + \tilde{h}_3^2 + \tilde{h}_4^2 + \tilde{h}_5^2 = 1 \quad (1.75)$$

The solution of equations (1.69) to (1.75) is

$$\begin{aligned} \tilde{h}_0 &= \frac{1 + \sqrt{10} + s}{16} & \tilde{h}_1 &= \frac{5 + \sqrt{10} + 3s}{16} & \tilde{h}_2 &= \frac{5 - \sqrt{10} + s}{8} \\ \tilde{h}_3 &= \frac{5 - \sqrt{10} - s}{8} & \tilde{h}_4 &= \frac{5 + \sqrt{10} - 3s}{16} & \tilde{h}_5 &= \frac{1 + \sqrt{10} - s}{16} \end{aligned}$$

with  $s = \sqrt{5 + 2\sqrt{10}}$ .

The coefficients  $\tilde{h}_n$  of the scaling functions of further Daubechies wavelets are given in the literature (e.g. [17], [40], [49]).

With given coefficients  $\tilde{h}_n$ , the respective scaling function can be generated from the dilation equations. One can start from a box function  $\{\phi_0(t) = 1, 0 \leq t < 1, \phi_0(t) = 0 \text{ elsewhere}\}$ . The  $j$ th approximation of the scaling function is calculated from the result of the previous step in an iteration that follows from the basic dilation equation (1.62):

$$\phi^j(t) = \sum_{n=0}^{2^j-1} \tilde{h}_n \phi^{j-1}(2t - n) . \quad (1.76)$$

This iteration is repeated until the difference between the functions  $\phi^j(t)$  and  $\phi^{j-1}(t)$  is sufficiently small. In figure 1.7 the iteration is illustrated for the scaling function of the  $D2$  wavelet. The lines are drawn darker with converging results.

## 1.4.2 The Fast Wavelet Transformation

In section 1.4.1 the multi-scale analysis has been explained. It was shown, how a signal  $f$  in a subspace  $V_m$  can be described by projections of  $f$  onto the subspaces of  $V_m$  (equations (1.40), (1.41)). The dilated and translated scaling functions  $\phi_{m,n}$  form an orthonormal base of a subspace  $V_m$  while the dilated and translated wavelets  $\psi_{m,n}$  are an orthonormal

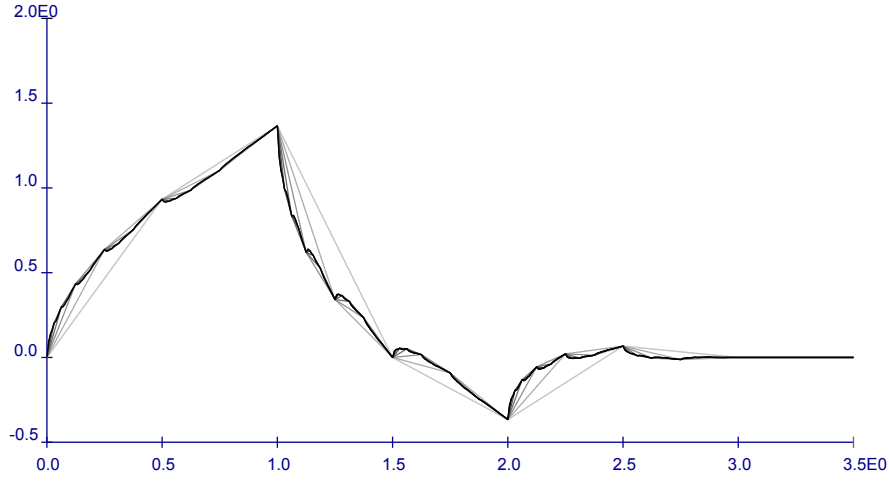


Figure 1.7: Iteration of the scaling function of the  $D2$  wavelet

base of the subspace  $W_m$ . Hence, a discrete series  $f$  in the fundamental space  $V_0$  can be described by means of projections based on scaling functions and wavelets. It can be derived from equation (1.40):

$$f(t) = P_0 f(t) = \sum_k f \phi_{0,k}(t) = \sum_k a_{M,k} \phi_{M,k}(t) + \sum_{m=1}^M \sum_k d_{m,k} \psi_{m,k}(t) . \quad (1.77)$$

Consequently, a discrete series  $f(t) = \langle f, \phi_{0,k} \rangle$  in  $V_0$  can be decomposed into a low frequency part  $\langle f, \phi_{1,k} \rangle$  and a high frequency part  $\langle f, \psi_{1,k} \rangle$ . This decomposition can be continued as a multi-scale analysis up to a level  $M$ . A discrete series  $A_m = \langle f, \phi_{m,k} \rangle$  that one obtains at a level  $m$  of a multi-scale analysis is an approximation of the series  $A_{m-1} = \langle f, \phi_{m-1,k} \rangle$ , while the series  $D_m = \langle f, \psi_{m,k} \rangle$  contains the details of  $A_{m-1}$ .

With equations (1.55) and (1.56) follows:

$$\langle f, \psi_{m,k} \rangle = \sum_{n \in \mathbb{Z}} g_n \langle f, \phi_{m-1,2k+n} \rangle = \sum_{n \in \mathbb{Z}} g_{n-2k} \langle f, \phi_{m-1,n} \rangle \quad (1.78)$$

and

$$\langle f, \phi_{m,k} \rangle = \sum_{n \in \mathbb{Z}} h_n \langle f, \phi_{m-1,2k+n} \rangle = \sum_{n \in \mathbb{Z}} h_{n-2k} \langle f, \phi_{m-1,n} \rangle . \quad (1.79)$$

Hence, the inner product  $\langle f, \psi_{m,n} \rangle$  can be obtained by a discrete convolution of  $\langle f, \phi_{m-1,n} \rangle$  and the series of the wavelet's coefficients  $g_n$ , taking only every other sample into account

(down-sampling). Respectively, equation (1.79) describes how the inner product  $\langle f, \phi_{m,n} \rangle$  is generated based on the scaling coefficients  $h_n$  and the series  $\langle f, \phi_{m-1,n} \rangle$ . Accordingly the approximations  $A_m$  (scaling coefficients  $a_{m,k}$ ) and the details  $D_m$  (wavelet coefficients  $d_{m,k}$ ) at a scale  $m$  and instant  $k$  can be calculated as:

$$a_{m,k} = \sum_{n \in \mathbb{Z}} h_{n-2k} a_{m-1,k}, \quad d_{m,k} = \sum_{n \in \mathbb{Z}} g_{n-2k} a_{m-1,k}. \quad (1.80)$$

That means, only the scaling function's coefficients  $h_n$  and the wavelet's coefficients  $g_n$  are required for the projection of a signal  $f$  onto the scales of an orthogonal wavelet transform. In compact form equation (1.80) can be written as:

$$a_{m,k} = H a_{m-1,k}, \quad d_{m,k} = G a_{m-1,k}. \quad (1.81)$$

The decomposition operators  $H$  and  $G$  are also called quadrature mirror filters.  $H$  is a low-pass filter,  $G$  is a high-pass filter.

The algorithm of the fast wavelet transformation that was developed by Mallat [44] is given schematically in figure 1.8. In inverse direction the series  $A_0 = f$  can be reconstructed

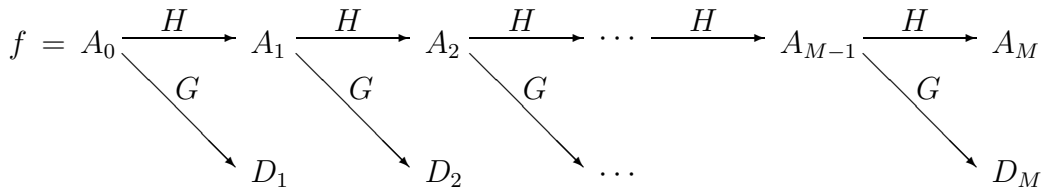


Figure 1.8: Scheme of the decomposition of a series  $f$  by means of Mallat's algorithm

from the approximation  $A_M$  and all details  $D_m$ ,  $m = 1, \dots, M$ . For the reconstruction the adjoint operators  $\bar{H}$  and  $\bar{G}$  of  $H$  and  $G$ , respectively, are applied. The reconstruction of a signal is illustrated in figure 1.9.

Since in practice one usually has finite series to analyse, there arises the question about the treatment of the signal's borders. Often the implemented algorithms assume a periodisation of the signal. In other cases it is supposed that the signal continues outside the observation interval as a constant (e.g. zero or the value at the borders), linearly with

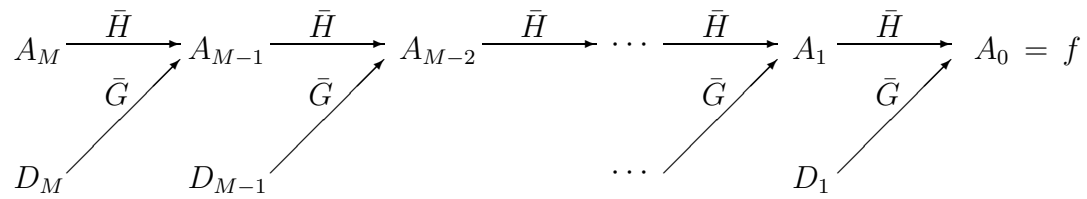


Figure 1.9: Scheme of the reconstruction of a series  $f$  from the details and the approximation of the last decomposition level by means of Mallat's algorithm

the slope at the respective border, or symmetrically to the respective signal's border. Further investigations about the topic of border distortions and respective algorithms can be found in the literature, (e.g. [64], [46], [15]).

The algorithms that are implemented into the software package SLang [5] offer the choice between the periodic assumption (circulant filter) and zero-padding (extended filter).

# Chapter 2

## Wavelets in System Identification – a Review

Wavelet analysis has been employed to numerous problems that belong to the general field of system identification in recent years. In this chapter a brief overview is given about some respective approaches, without being exhausting.

The following sections are organised with respect to the identification of modal parameters of linear time-invariant systems, the investigation of time-varying systems and the detection of structural damage by dynamic tests. Methods that are based on both continuous and discrete wavelet analysis are presented.

### 2.1 Identification of Modal Parameters

Several attempts have been made in recent years to employ wavelet analysis for the extraction of modal parameters of linear time-invariant systems from measured data. In section 2.1.1 methods that are based on continuous wavelet transforms are summarised while section 2.1.2 is concentrated on approaches that use discrete wavelet decompositions.



### 2.1.1 Methods Based on Continuous Wavelet Analysis

An approach for the identification of natural frequencies and modal damping ratios by means of wavelet transforms of free vibration response data with respect to the complex Morlet wavelet  $\psi(t) = e^{i\omega_\psi t} e^{-\frac{t^2}{2}}$  (section 1.3) was proposed in [61], [56] and [60]. As is common in modal analysis (e.g. [26], [43], [33], [31], [61]), it is assumed that the system's free vibration response can be decoupled into contributions of  $N$  single modes  $j$ :

$$x(t) = \sum_{j=1}^N A_j e^{-\zeta_j \omega_{n_j} t} \sin\left(\sqrt{1 - \zeta_j^2} \omega_{n_j} t + \phi_j\right), \quad (2.1)$$

where  $A_j$  is the residue amplitude,  $\zeta_j$  denotes the modal damping ratio and  $\omega_{n_j}$  and  $\phi_j$  refer to the undamped natural frequency and phase lag, respectively. The wavelet transform of equation (2.1) for  $\phi_j = 0$  with respect to the Morlet wavelet is [56]:

$$W_\psi^x(a, b) = \sqrt{a} \sum_{j=1}^N A_j e^{-\zeta_j \omega_{n_j} t} e^{-(a\sqrt{1 - \zeta_j^2} \omega_{n_j} - \omega_\psi)^2} e^{i\sqrt{1 - \zeta_j^2} \omega_{n_j} b}. \quad (2.2)$$

Depending on the wavelet's frequency  $\omega_\psi$ , each scaling parameter  $a_j$  is related to the signal's frequency  $\omega_j$  by

$$a_j = \frac{\omega_\psi}{\omega_j}, \quad (2.3)$$

assuming that both the signal and the analysing wavelet are sampled with the same frequency. For a fixed  $a_j$ , that is related to a frequency  $\omega_{d_j} = \sqrt{1 - \zeta_j^2} \omega_{n_j}$ , equation (2.2) becomes

$$W_\psi^x(a_j, b) = \sqrt{a_j} A_j e^{-\zeta_j \omega_{n_j} t} e^{-(a\omega_{d_j} - \omega_\psi)^2} e^{i\omega_{d_j} b} = A_j e^{-\zeta_j \omega_{n_j} t} e^{i\omega_{d_j} b}. \quad (2.4)$$

For a previously chosen  $a_j$  (i.e.  $\omega_{d_j}$ ) the respective modal damping ratio is determined from the plot of the envelope in the semi-logarithmic scale.

A method for the estimation of the mode shapes by means of wavelet transforms with respect to the Morlet wavelet is given in [52]. If  $W_\psi^{x_k}(a, b)$  and  $W_\psi^{x_{ref}}(a, b)$  respectively denote the wavelet transforms of the signals at point  $k$  and at a reference point, their ratio at scale  $a_j$

$$\frac{W_\psi^{x_k}(a_j, b)}{W_\psi^{x_{ref}}(a_j, b)} = \phi_{k,j} \quad (2.5)$$

is the  $k$ th component of the  $j$ th complex eigenvector. Theoretically, the quantity  $\phi_{k,j} = r_{k,j} + i s_{k,j}$  should be constant for all  $b$ . However, for the application to real data it is suggested in [52] to estimate the components of the eigenvectors as

$$r_{k,j} = \frac{\sum_{l=1}^N \operatorname{Re} [W_{\psi}^{x_k}(a_j, b_l)] \operatorname{Re} [W_{\psi}^{x_{ref}}(a_j, b_l)]}{\sum_{l=1}^N \operatorname{Re}^2 [W_{\psi}^{x_{ref}}(a_j, b_l)]}, \quad (2.6)$$

$$s_{k,j} = \frac{\sum_{l=1}^N \operatorname{Re} [W_{\psi}^{x_k}(a_j, b_l)] \operatorname{Im} [W_{\psi}^{x_{ref}}(a_j, b_l)]}{\sum_{l=1}^N \operatorname{Im}^2 [W_{\psi}^{x_{ref}}(a_j, b_l)]}. \quad (2.7)$$

A modal ‘quality index’ is introduced for the assessment of the reliability of the estimated components of the  $j$ th mode shape vector  $\phi_j$ :

$$c_{k,j} = \frac{\sigma_{W_{\psi}^{x_k} W_{\psi}^{x_{ref}}}^2}{\sigma_{W_{\psi}^{x_k}} \sigma_{W_{\psi}^{x_{ref}}}}, \quad (2.8)$$

where  $\sigma_{W_{\psi}^{x_k}}$  and  $\sigma_{W_{\psi}^{x_{ref}}}$  denote the standard deviations of  $W_{\psi}^{x_k}(a_j, b)$  and  $W_{\psi}^{x_{ref}}(a_j, b)$ , respectively, and  $\sigma_{W_{\psi}^{x_k} W_{\psi}^{x_{ref}}}^2$  refers to their covariance. If  $|c_{k,j}|$  is close to 1, a high reliability for the estimation of  $\phi_{k,j}$  is indicated.

In [4] a technique for the identification of natural frequencies and modal damping ratios from a continuous wavelet analysis of the frequency response function (FRF) is proposed. The complex function  $\psi(\omega) = \frac{1}{(\omega-1)^2}$  is chosen as analysing wavelet. Since the wavelet transform is applied to the frequency response function  $H(\omega)$ , the wavelet is given as a function of frequency rather than of time, in this case. It is shown, that the real and imaginary parts of the respective wavelet transforms are related to each other by

$$\begin{aligned} \operatorname{Re} [W_{\psi}^H(a, b)] &= 2 W_{\operatorname{Re}[\psi]}^{\operatorname{Re}[H]}(a, b) \\ &= 2 W_{\operatorname{Im}[\psi]}^{\operatorname{Im}[H]}(a, b) \end{aligned} \quad (2.9)$$

and

$$\begin{aligned} \operatorname{Im} [W_{\psi}^H(a, b)] &= 2 W_{\operatorname{Re}[\psi]}^{\operatorname{Im}[H]}(a, b) \\ &= -2 W_{\operatorname{Im}[\psi]}^{\operatorname{Re}[H]}(a, b). \end{aligned} \quad (2.10)$$

It is postulated and verified by two numerical examples that the natural frequencies and modal damping ratios can be estimated from the coordinates of the maxima of

$\text{Im} [W_{\psi}^H(a, b)]$ ,  $a_{max_j}$  and  $b_{max_j}$ :

$$\omega_{n,j} = \sqrt{a_{max_j} + b_{max_j}}, \quad (2.11)$$

$$\zeta_j = \frac{a_{max_j}}{\omega_{n,j}}. \quad (2.12)$$

### 2.1.2 Methods Based on Discrete Wavelet Analysis

A wavelet-based approach for damping identification is proposed in [38]. Similar to the logarithmic decrement that can be deduced from a free vibration  $x(t)$  of an SDOF system

$$\delta = \frac{1}{nT} \ln \left| \frac{x(t)}{x(t+nT)} \right|. \quad (2.13)$$

a wavelet-logarithmic decrement formula is derived:

$$\delta_j \simeq \frac{1}{(m-n)T} \ln \left| \frac{W_{\psi}^x(a_j, nT)}{W_{\psi}^x(a_j, mT)} \right|, m > n, \quad (2.14)$$

where  $j$  refers to the  $j$ th mode with a natural frequency  $\omega_{n_j}$  that corresponds to the scale  $a_j$ .

For the identification of damping from the scaling coefficients obtained by a discrete wavelet decomposition of free vibration data with  $2^M$  samples, that has been mapped to an interval  $[0, 1]$ , a discrete wavelet-logarithmic decrement is given in [38]:

$$\delta_j \simeq \frac{2^{(M-j)}}{k-l} \ln \left| \frac{a_{j,l}}{a_{j,k}} \right|, k > l. \quad (2.15)$$

In equation (2.15) the terms  $a_{i,l}$  and  $a_{i,k}$  refer to two maximal scaling coefficients at decomposition level  $j$ , that means equation (2.15) can be interpreted as the classical logarithmic decrement formula (2.13) applied to an approximation of the original signal at level  $j$ , i.e. a filtered and down-sampled version of  $x(t)$ .

In order to improve the localisation of the extreme scaling coefficients a so-called ‘‘super-abundant wavelet analysis’’ was applied. By means of this method the scaling coefficients are mapped onto an equidistant, rather than on a dyadic, grid. The result is a constant resolution at all decomposition levels, similar to the continuous wavelet transform.

The proposed procedure was verified by a numerical simulation in [38] and applied to data obtained from tests of an eight-storey building [30]. Since the method is based on the assumption of an SDOF system, mode decoupling is necessary that was obtained by a selective wavelet reconstruction, an approach that might be applicable if the data does not contain significant contributions of close modes.

The response of a linear system  $x(t)$  due to a given excitation  $f(t)$  can be calculated by means of the convolution integral

$$x(t) = \int_{-\infty}^t h(t - \tau) f(\tau) d\tau, \quad (2.16)$$

or with  $\Theta = t - \tau$ ,  $\tau = t - \Theta$ :

$$x(t) = \int_0^{\infty} h(\Theta) f(t - \Theta) d\Theta, \quad (2.17)$$

where  $h(\Theta)$  is the system's impulse response function ( $h(\Theta) = 0$  for  $\Theta \geq 0$ ). It was derived in [49], that the convolution in equation (2.17) can be completely replaced for discrete response series with  $2^J$  samples by

$$x(t_n) = \{h_{j,k}\}^T \{f_{j,k}\}. \quad (2.18)$$

The vectors  $\{h_{j,k}\}$  and  $\{f_{j,k}\}$  in equation (2.18) contain the coefficients obtained from a wavelet decomposition of the impulse response function (IRF) and the excitation:

$$\begin{aligned} \{h_{j,k}\}^T &= \left\{ \frac{1}{2^{J-1}} \{d_{1,1}(h), d_{1,2}(h), \dots, d_{1,2^{J-1}}(h)\}, \dots, \right. \\ &\quad \frac{1}{2^{J-M}} \{d_{M,1}(h), d_{M,2}(h), \dots, d_{M,2^{J-M}}(h)\}, \\ &\quad \left. \frac{1}{2^{J-M}} \{a_{M,1}(h), a_{M,2}(h), \dots, a_{M,2^{J-M}}(h)\} \right\} \\ \{f_{j,k}\}^T &= \left\{ \{d_{1,1}(f), d_{1,2}(f), \dots, d_{1,2^{J-1}}(f)\}, \dots, \right. \\ &\quad \{d_{M,1}(f), d_{M,2}(f), \dots, d_{M,2^{J-M}}(f)\}, \\ &\quad \left. \{a_{M,1}(f), a_{M,2}(f), \dots, a_{M,2^{J-M}}(f)\} \right\} \end{aligned} \quad (2.19)$$

In [54] an approach is suggested for the estimation of the discrete IRF of a system, also known as Markov parameters [31]. For the entire response data equation (2.18) can be extended as:

$$[x]_{m \times s} = [h_{j,k}]_{m \times rl} [f_{j,k}]_{rl \times s} . \quad (2.20)$$

Here  $m$ ,  $r$ ,  $s$  and  $l$  refer to the number of measured response series, the number of input signals, the number of measured samples and the number of considered wavelet coefficients, respectively. Equation (2.20) can be solved for  $[h_{j,k}]$  as

$$[h_{j,k}] = [x] [f_{j,k}]^T \left( [f_{j,k}] [f_{m,n}]^T \right)^{-1} . \quad (2.21)$$

The impulse response functions with respect to time are eventually obtained by wavelet reconstruction of the respective row vectors in  $[h_{m,n}]$ . From equation (2.18) it becomes obvious that the inverse dyadic coefficients in equation (2.19) can be applied to the wavelet coefficients of either the IRF or the excitation. Accordingly, it can be decided by the analyser if pre-processing of  $[f_{m,n}]$  or post-processing of  $[h_{m,n}]$  is preferred.

The proposed method for the identification of impulse response functions is verified in [54] by means of numerical examples. In [55] these impulse response functions are used for the identification of state space models. The respective mode shapes, natural frequencies and damping ratios of the system are derived from the state space representation [3].

In order to improve frequency response functions (FRF), that were extracted from measured data, a wavelet-based method is proposed in [8] and [7]. According to [8], the FRF is first estimated based on measured input and output data either as  $H(\omega) = \frac{\hat{x}(\omega)}{\hat{f}(\omega)}$  or  $H(\omega) = \frac{\hat{x}(\omega)\hat{f}^*(\omega)}{|\hat{f}(\omega)|^2}$ . Then both the real and imaginary parts of  $H(\omega)$  are smoothed by means of a selective wavelet reconstruction, in this case by soft thresholding (chapter 3). This procedure is slightly modified in [7] where an estimated FRF is first smoothed using a Hanning window before wavelet shrinkage is carried out.

## 2.2 Identification of Time-Varying Systems

Both continuous wavelet transforms and wavelet coefficients of a discrete wavelet decomposition represent the characteristics of a signal in the time-scale domain. This feature is obviously very stimulating if systems with time-varying properties are considered. Some examples for the application of wavelet analysis with respect to the identification of non-linear and linear time-varying systems are given in the following sections.

### 2.2.1 Methods Based on Continuous Wavelet Analysis

From the graphic representation of a continuous wavelet transform, it can be deduced how the energy density of a signal is distributed with respect to time and scale (or frequency). In [4] an example of a simulated free vibration response of an SDOF system is presented. The ridge of the corresponding wavelet transform [12], [65] clearly shows a frequency shift with respect to time, that indicates a non-linearity of the system.

A more detailed investigation of the impulse response of a non-linear system based on wavelet analysis with respect to the Morlet wavelet and a method for the identification of the system's parameters are described in [58] and [60].

In modal analysis it is common to represent the impulse response of an MDOF system by a modal superposition, as given in equation (2.1). The wavelet transform of the linear combination (2.1) can be written as

$$W_{\psi}^{x(t)}(a, b) = W_{\psi}^{\sum x_j}(a, b) = \sqrt{a} \sum_{j=1}^N \int_{\omega_{n_j} - \frac{\Delta\omega_{\psi}}{a}}^{\omega_{n_j} + \frac{\Delta\omega_{\psi}}{a}} \hat{x}(\omega) \hat{\psi}^*(a\omega) e^{i\omega_{n_j}b} d\omega. \quad (2.22)$$

The wavelet transform in equation (2.22) is represented using the Fourier transforms of  $x(t)$  and  $\psi(t)$ , as in equation (1.14). The ratio between the bandwidth of the basic wavelet function  $\Delta\omega_{\psi}$  and the scale parameter  $a$  gives the bandwidth of the dilated wavelet at scale  $a$ .

Relation (2.22) shows that the wavelet transform allows for a modal decoupling. The identification approach suggested in [58] proposes the extraction of the ridge, skeleton and backbone from the mode decoupled wavelet transform. The ridge is a curve that connects the local extrema in the time-scale plane. The values of the wavelet transform along the ridge form the respective skeleton. The projection of the skeleton's envelope, as a function of vibration amplitudes versus scale, is called the backbone curve.

According to [58] the system's parameters can be estimated by calculating the instantaneous properties along the ridges and the application of curve fitting to both the skeleton's envelope and the backbone curve. The proposed method is applied in [58] to an SDOF system with Coulomb friction and cubic stiffness contribution and to a 2-DOF system with cubic stiffness non-linearity.

In order to describe the input-output relation of a system in the time-scale domain, the ratio of the wavelet transform of the system's response to that of the excitation is introduced in [62] as the wavelet-based frequency response function ( $H_W(a, b)$ ) or scale-translation response function (STRF), as it is called in [37]:

$$H_W(a, b) = \frac{W_\psi^x(a, b)}{W_\psi^f(a, b)}. \quad (2.23)$$

The similarity between equation (2.23) and the definition of the FRF for a linear system is obvious. The important difference is, that the wavelet-based FRF is capable of describing non-linearities and non-stationary processes. For the practical calculation, equation (2.23) is modified to:

$$H_W(a, b) = \frac{W_\psi^x(a, b) W_\psi^{f*}(a, b)}{W_\psi^f(a, b) W_\psi^{f*}(a, b)}, \quad (2.24)$$

which is very similar to a form of calculation of the classical FRF in modal analysis that is known as  $H_1(\omega)$  (e.g. [26], [31]):

$$H_1(\omega) = \frac{\hat{x}(\omega) \hat{f}^*(\omega)}{\hat{f}(\omega) \hat{f}^*(\omega)}. \quad (2.25)$$

In [62] the wavelet-based FRF is employed for the investigation of the non-linear behaviour of an automobile seat-passenger system under real service conditions. The wavelet-based

FRF is used in the sense of a transmissibility function, i.e. as a relation between the accelerations measured at a mounting bolt of the seat and those at the seat/person interface. Two resonances were deduced from the ridges of this transmissibility function. The frequencies of these resonances varied significantly over the observation interval which is interpreted as an indicator for non-linearities in the behaviour of the considered system.

An alternative method for the description of input-output relations in the time-scale domain is introduced in [37], the cross wavelet transform:

$$W_{\psi}^{fx}(a, b) = W_{\psi}^{f*}(a, b) W_{\psi}^x(a, b) . \quad (2.26)$$

The cross wavelet transform displays the similarities of the input  $f$  with a projection of the output  $x$  at scale  $a$  and translation  $b$ . High values of the cross wavelet transform indicate a vigorous response of the system to an input with corresponding scale at the respective time instant. It is demonstrated in an example with an SDOF Duffing oscillator, that is excited by a sweep force, how non-linearities of a system can be retrieved by comparing the wavelet transform of the response with the cross wavelet transform.

An extension of the cross wavelet analysis technique for the assessment of MDOF systems is presented in [59] by means of a 3-DOF system with cubic stiffness non-linearity.

### 2.2.2 Approaches Based on Discrete Wavelet Analysis

Assuming that the displacements  $x(t)$  due to a measured excitation  $f(t)$  are known from a test, the equation of motion for a linear SDOF system with viscous damping can be expressed as [28]:

$$m_l \sum_k a_{j,k}(x) \Gamma_{j,k}^{j,l(2)} + c_l \sum_k a_{j,k}(x) \Gamma_{j,k}^{j,l(1)} + k_l a_{j,l}(x) = a_{j,l}(f) , \quad (2.27)$$

where  $a_{j,k}(x)$ ,  $a_{j,l}(x)$  and  $a_{j,l}(f)$  respectively refer to the scaling coefficients of the displacements and of the excitation at the discrete translations  $k$  and  $l$  at level  $j$ . The  $\Gamma_{j,k}^{j,l(n)}$  denote the connection coefficients of the  $n$ th derivative with respect to a certain wavelet



at level  $j$ . More detailed descriptions about these connection coefficients are given in section 4.2.

Accordingly, equation (2.27) represents the equation of motion for a linear, viscously damped system using scaling coefficients of response and excitation rather than the respective time series. The scaling coefficients can be interpreted as a low-pass filtered and down-sampled version of the respective time series. As a result of the application of appropriate connection coefficients, the response in equation (2.27) is completely described by scaling coefficients of the displacements.

The formulation of the equation of motion (2.27) is the core of an identification procedure that is presented in [28]. For noise corrupted data, a pre-processing of the measured series by means of a selective wavelet reconstruction, applying hard thresholding (chapter 3), is suggested. For MDOF systems, equation (2.27) can be extended to matrix–vector relations in the same way as in the time domain.

In a second step, equation (2.27) is rearranged such that the system’s parameters to be identified are collected in a vector  $\{P\}$  while the scaling coefficients of the response are assembled in a matrix. Provided that the system’s mass is known, one obtains

$$\left[ \left[ \sum_k a_{j,k}(x) \Gamma_{j,k}^{j,l(1)} \right] [a_{j,l}(x)] \right] \{P\} = \left\{ a_{j,l}(f) - [M] \left\{ \sum_k a_{j,k}(x) \Gamma_{j,k}^{j,l(2)} \right\} \right\} . \quad (2.28)$$

If a sufficient number of scaling coefficients is taken into account, the solution of the system of equations (2.28) yields the system’s parameters.

The performance of this method is demonstrated for an SDOF system and for a 2-DOF system. The capability of identifying linear parameters, that show different kinds of time-variance, is reported. The behaviour of the algorithm in the case of noise contamination of the measured data was also tested.

The procedure introduced in [28] is extended for non-linear systems in [29]. The equation of motion for a non-linear SDOF system is given by

$$m\ddot{x} + c\dot{x} + kx + g(x, \dot{x}) = f , \quad (2.29)$$

where  $g(x, \dot{x})$  denotes a non-linear force that depends on displacements and velocities. The approximation of the accelerations and velocities are represented in the same way as in equation (2.27). It is shown for the assumption that

$$g(x, \dot{x}) = dx \dot{x} , \quad (2.30)$$

the product  $(x \dot{x})$  can be approximated at level  $j$  by

$$\sum_m \sum_k a_{j,m}(x) a_{j,k}(x) \Omega_{j,k,l}^{j,m,m(1,0)} , \quad (2.31)$$

with the 3-term connection coefficients of the differential operator

$$\Omega_{j,k,l}^{j,m,m(1,0)} = \int_0^{2^n-m} \phi(\tau-m) \dot{\phi}(\tau-k) \phi(\tau-l) d\tau .$$

With the assumption (2.30) one can re-formulate equation (2.29) in a similar form to equation (2.27):

$$\begin{aligned} m \sum_k a_{j,k}(x) \Gamma_{j,k}^{j,l(2)} + c \sum_k a_{j,k}(x) \Gamma_{j,k}^{j,l(1)} + k a_{j,k}(x) \\ + d \sum_m \sum_k a_{j,m}(x) a_{j,k}(x) \Omega_{j,k,l}^{j,m,m(1,0)} = a_{j,k}(f) . \end{aligned} \quad (2.32)$$

The parameters  $m$ ,  $c$ ,  $k$  and  $d$  are obtained as the solution of a respective system of equations pertinent to equation (2.28).

Even though derived and tested for a numerical simulation for an SDOF system described by equations (2.29) and (2.30), this approach is not further developed. Instead it is proposed in [29] to approximate the non-linearity as

$$g(x, \dot{x}) = d \langle b_{j,k}, \phi_{j,l} \rangle . \quad (2.33)$$

The scaling coefficients  $b_{j,k}$  have to be calculated based on prior knowledge of  $x$  and  $\dot{x}$ . Numerical tests are described in [29] for an SDOF system with different types of non-linearities using the assumption of equation (2.33). For the identification of an unknown non-linearity it is suggested to try different types of non-linearity and to detect the model that results in the closest calculated response due to the experimental excitation compared

with the measured values. The proposed procedure is verified by means of simulated tests of SDOF and 2-DOF systems without considering noise contamination of the data.

All methods, mentioned so far, used the wavelet transformation more or less as a signal processing tool. In [35] a procedure is submitted that uses a wavelet decomposition in order to estimate a time-varying tangent stiffness of a system. The method is tested for a 5-DOF system using both simulated and experimental data. However, no results about the identified time-varying system's parameters are reported.

Several attempts for the application of discrete wavelet analysis in the context of the identification of time-varying systems are described in the literature. The examples mentioned are limited to comparatively simple systems. Furthermore, the proposed procedures are based on scaling coefficients (i.e. approximations) rather than on wavelet coefficients (i.e. details).

## 2.3 Damage Detection

There is a great variety of problems that are included within the wide subject of damage detection. The intentions strongly depend on the applications. They range from the detection of the presence of a certain kind of damage inside a mechanical system, over the observation of damage occurrence, up to the assessment of a structure's condition by certain indicators in the context of long time health monitoring.

This section is divided into two parts. The first part is concerned with the identification of the occurrence or presence of damage, using wavelet analysis, while the second subsection is devoted to wavelet-based damage indicators.

### 2.3.1 Presence and Occurrence of Damage

The detection of existing defects by means of efficient and non-destructive techniques is of particular interest in context with rotating machinery parts such as gearboxes or ball

bearings. The application of wavelet shrinkage (chapter 3) for the identification of rubbing in a mechanical system, that results from some structural fault, is proposed in [23]. The approach is based on the assumption that rubbing produces features in a measured signal that result in very large wavelet coefficients at a certain level. Contributions related to the defect are retained in the signal by applying an appropriate threshold. The presence of such features in the de-noised signal are interpreted as an indicator for present rubbing. The suggested method was implemented and integrated in an on-line condition monitoring system for respective machinery.

The basic idea of the previously described technique is that of the detection of certain features in a response signal. A related methodology is suggested in [60] for fault detection in gearboxes. Here, the damage is detected by the assessment of certain patterns in the plots of both the modulus and phase of the continuous wavelet transforms of the response data with respect to the Morlet wavelet. Rather sophisticated algorithms for the extraction of patterns are presented. These techniques are applied to the so-called scalogram, a plot of the squared magnitudes of the continuous wavelet transform  $|W_{\psi}^x(a, b)^2|$ .

The methods proposed in [1], [32] and [2] are focused on the detection of the time instant when damage occurs in a structure as might be the case during a strong earthquake. In a numerical investigation of a linear SDOF system with viscous damping, in [1] damage was simulated by superimposing short impulses with a random excitation. The instants of occurrence of these simulated damage scenarios were detected as spikes in the wavelet coefficient series of the response at selected decomposition levels.

Similar investigations are described in [32]. However, there the damage is simulated by abrupt stiffness reductions of the SDOF system. The wavelet decomposition was applied to response data recorded in a building during an earthquake. It is reported that certain features in the wavelet coefficients coincide with observations of damage occurrence on site. It is concluded from an investigation of the influence of noise in the measured response data, that the detectability of damage, in terms of loss in stiffness, improves with increasing damage intensity and decreasing noise corruption.

Continuing the study in [32], the possibility of an improved detection of damage occurrence is investigated in [2]. It was observed that spikes in the wavelet coefficient series of the response due to an abrupt stiffness change are difficult to identify if the system was excited by a random force. Better results were obtained from the plots of continuous wavelet transforms with respect to the Morlet wavelet and of the windowed Fourier transform, that clearly show a concentration of energy at frequencies that coincide with the system's natural frequencies at the respective damage states. It is deduced from the example presented, that the continuous wavelet transform localises the system's changes better in time, while the windowed Fourier transform provides an enhanced frequency localisation.

### 2.3.2 Wavelet-Based Damage Indicators

The procedures summarised in the previous section deduced the presence or occurrence of damage directly from certain features of wavelet transforms of measured data. In the following examples either wavelet-based functions are proposed as a measure of damage severity or damage is quantified by identified changes of the system's parameters such as stiffness or damping.

The use of wavelet coefficients' statistics for damage identification is presented in [58], [60] and [10]. It is illustrated by means of tests on drilling equipment [58] that the signal-to-noise ratio ( $SNR$ ) of measured response data can be interpreted as an indicator of damage. Based on the assumption that the wavelet coefficients at the first  $k$  decomposition levels solely represent noise, the so-called wavelet-based statistics is defined:

$$S_m = \left( \frac{\sigma^2(d_{m,n})}{\sum_k \sigma^2(d_{k,n})} \right)^2, \quad (2.34)$$

where  $m$  denotes the respective decomposition level. It is indicated that a large value  $S_m$  refers to a high signal-to-noise ratio. In the example presented, transients in the signal, that are due to damage, produce the desired information and consequently a large  $S_m$  (or  $SNR$ ) denotes damage.

A damage indicator, that is based on wavelet variance characteristics, is defined in [58],

[10]:

$$\Delta_{x,\mu} = \{\{\bar{x}\} - \{\bar{\mu}\}\}^T \{\{\bar{x}\} - \{\bar{\mu}\}\} . \quad (2.35)$$

The vector  $\{\bar{\mu}\}$  contains the mean wavelet coefficient's variances at the respective decomposition level  $m$  from  $N$  data series measured in the initial (undamaged) state [58]:

$$\bar{\mu}(m) = \frac{1}{N} \sum_{i=1}^N \sigma_i^2(d_{m,n}) , \quad (2.36)$$

or using the logarithmic variances [10]

$$\bar{\mu}(m) = \frac{1}{N} \sum_{i=1}^N \log \sigma_i^2(d_{m,n}) . \quad (2.37)$$

The respective mean wavelet variances obtained from tests on the structure in a respective damaged condition are collected in the vector  $\{\bar{x}\}$ . The indicator defined in equation (2.35) is employed in tests of a progressively damaged aluminium plate excited by a random force.

A method that uses special wavelet filters in context with condition monitoring of rotating machinery is introduced in [41]. Measured response data is filtered such that only components of a single frequency, or of a number of selected frequencies, are retained. Special combination wavelets are designed for filtering. The condition of the considered system is then assessed by evaluating the filtered signals either in time or frequency domain (e.g. by power spectra peak ratio). An enhancement of the filtered data with respect to noise is obtained using autocorrelation.

A numerical simulation of an SDOF system excited by a random force is presented in [57]. The system's stiffness is changed abruptly. It is estimated from a slightly modified version of the equation of motion in the time-scale domain:

$$\frac{m}{k} W_{\psi}^{\ddot{x}}(a, b) + \frac{c}{k} W_{\psi}^{\dot{x}}(a, b) + W_{\psi}^x(a, b) = \frac{1}{k} W_{\psi}^f(a, b) + W_{\psi}^e(a, b) , \quad (2.38)$$

where  $W_{\psi}^e(a, b)$  is the wavelet transform of an error. It is reported that the parameters  $\frac{c}{k}$  and  $\frac{m}{k}$  are determined such that  $|W_{\psi}^e(a, b)|^2$  is minimised.

Furthermore, in [57] a formula is given for estimating the wavelet transform of the  $n$ th derivative of a given signal  $x(t)$ :

$$W_{\psi}^{x^{(n)}}(a, b) = (-1)^n \frac{1}{a^n \sqrt{a}} \int_{-\infty}^{\infty} x(t) \psi^{(n)*} \left( \frac{t-b}{a} \right) dt. \quad (2.39)$$

The derivation of equation (2.39) and further considerations about its application to finite signals are given in section 4.1. In [57] relation (2.39) is used for the calculation of the wavelet transforms of velocities and accelerations from observed displacements. It is mentioned that in the example presented, a Daubechies wavelet is used as the analysing wavelet for a continuous wavelet transformation.

Stiffness and damping coefficients of a 3-DOF lumped mass system are identified in [47]. It is assumed that accelerations were only measured at two degrees of freedom. In order to overcome this lack of information, a neural network approach is studied. As input for the neural network, formulations are used that were calculated by means of continuous wavelet transforms with respect to the Meyer wavelet. The wavelet transforms of the displacements and velocities are estimated from the simulated accelerations using the respective relations derived in section 4.1.

Two damage indices that are based on wavelet packet analysis are proposed in [63]. It is assumed that identical dynamic tests are carried out on a considered structure in an undamaged state and in the damaged conditions. Repetitive testing within a structural health monitoring scheme should then provide information about the structure's condition. The damage indicators are calculated according to the following steps:

1. Full wavelet packet decomposition of the measured response signal  $\longrightarrow$  wavelet packet components  $d_j^k(t)$ ,
2. Calculation of the wavelet packet component energies:

$$E_j^k = \int (d_j^k(t))^2 dt, \quad (2.40)$$

3. Extraction of the  $N$  largest  $E_j^k$ ,  $k = 1 \dots N$ ,

4. Calculation of the damage index, that is either the sum of absolute differences  $SAD$ :

$$SAD = \sum_{k=1}^N \left| E_j^k - \tilde{E}_j^k \right| \quad (2.41)$$

or the square sum of differences  $SSD$ :

$$SSD = \sum_{k=1}^N \left( E_j^k - \tilde{E}_j^k \right)^2, \quad (2.42)$$

where  $\tilde{E}_j^k$  refers to the wavelet packet component energies computed for the undamaged (reference) condition. For the calculation of the damage indices, the respective  $N$  largest differences are considered.

The structure's condition is then assessed by comparison of the respective damage indicator with a pre-defined threshold.

Discrete wavelet analysis is employed in [39] for crack location in a simply supported beam. However, not the response data with respect to time is decomposed, but the displacements at a certain time instant as a function of the beam's length. A discontinuity in the wavelet coefficient series at a certain level is interpreted as an indicator for the crack location. A numerical example with 1024 measurement points is presented. This seems to be rather impractical for a real test application.



## Chapter 3

# De-noising by Selective Wavelet Reconstruction

In signal analysis and image processing, smoothing of the original data is often desired. Since the original data is considered to be contaminated by noise, this smoothing is also called de-noising.

Very good results in the research on appropriate de-noising techniques were obtained with algorithms that are based on a selective wavelet reconstruction (e.g. [19], [22], [20], [21]). In the following paragraphs the basic concept of this approach is described. Some variations and enhanced algorithms are briefly explained.

### 3.1 Selective Wavelet Reconstruction

The concept of a selective wavelet reconstruction is basically that of a comparatively simple thresholding procedure consisting of three steps:

1. Decomposition of the original (noisy) data, applying an orthogonal wavelet transformation,

2. Application of thresholding to the resulting coefficients,
3. Reconstruction of an estimate of the noise-free data based on the thresholded coefficients.

It has to be mentioned, that thresholding is only applied to the detail coefficients. The approximation on the coarsest decomposition level remains unchanged as a basic structure of the processed data.

The assumption is that there is a given data series  $y$ , that has been observed over an interval  $(0, 1)$ :

$$y_i = f(t_i) + e_i, \quad i = 1 \dots n, \quad (3.1)$$

where  $e_i$  denotes independent, identically distributed Gaussian noise with the (known) standard deviation  $\sigma$ . The unknown function to be recovered is  $f(t)$ . Its estimate is denoted  $\tilde{f}(t)$ .

An orthogonal wavelet decomposition of  $y$  yields the detail coefficients

$$d_{j,k} = \Theta_{j,k} + \sigma z_{j,k}, \quad j = 1 \dots M, \quad k = 1 \dots 2^j. \quad (3.2)$$

Here  $\Theta_{j,k}$  are the wavelet coefficients corresponding to the noise-free signal  $f$  while  $z_{j,k}$  are those of the noise. The coefficients  $z_{j,k}$  are also independent and identically distributed.

The threshold rules are defined supposing that relatively few wavelet coefficients contribute contents to the signal  $f$ . According to the respective threshold rule, only coefficients of the observed data that exceed a multiple of the noise level are retained. This procedure is also called shrinkage.

Generally, one distinguishes between two thresholding operators; the so-called ‘hard’ threshold  $\eta_H$  and the ‘soft’ threshold  $\eta_S$ . Hard thresholding keeps the samples exceeding the positive threshold  $\lambda$ , the remaining coefficients are set to zero:

$$d_{j,k} \xrightarrow{\eta_H(d,\lambda)} \tilde{\Theta}_{j,k} = \begin{cases} d_{j,k} & \text{if } |d_{j,k}| > \lambda \\ 0 & \text{if } |d_{j,k}| \leq \lambda \end{cases}. \quad (3.3)$$

The application of soft thresholding reduces the absolute values of the respective samples by the threshold  $\lambda$ , provided this difference is positive. Otherwise the respective coefficient is set to zero:

$$d_{j,k} \xrightarrow{\eta_S(d,\lambda)} \tilde{\Theta}_{j,k} = \begin{cases} \operatorname{sgn}(d_{j,k}) (|d_{j,k}| - \lambda) & \text{if } (|d_{j,k}| - \lambda) > 0 \\ 0 & \text{if } (|d_{j,k}| - \lambda) \leq 0 \end{cases}. \quad (3.4)$$

Several models for the definition of the threshold  $\lambda$  were defined and are explained in detail in [20] and [21]. A selection of these models and their implementation is described in the consecutive section.

## 3.2 Estimation of Thresholds and Implementation

### 3.2.1 Definition of Thresholds

The estimation of the threshold, as introduced in the previous section, is based on the assumption that the noise level is known. However, for measured data this is generally not the case. Therefore the noise level has to be estimated first. In [22] and [20] it is suggested considering the wavelet coefficients at the finest scale as representing exclusively noise. According to this assumption, the standard deviation of the noise is approximated by the median of the absolute of the wavelet coefficients at that level divided by 0.6745:

$$\tilde{\sigma} = \frac{\operatorname{median}(|d_{j,k}|)}{0.6745}. \quad (3.5)$$

Following the descriptions and the terminology in [22], [20] and [21], three versions of how the thresholds  $\lambda$  can be determined, are mentioned here:

- *VisuShrink*,
- *RiskShrink*,
- *SUREShrink*,
- *HybridShrink*.

### VisuShrink

The threshold  $\lambda_n^V$  applied to a data set of  $n$  samples is defined as:

$$\lambda_n^V = \sigma \sqrt{2 \ln n}. \quad (3.6)$$

According to [20] a comparatively good visual appearance can be achieved by the application of this estimator.

### RiskShrink

In [20] a risk measure

$$R(\tilde{\Theta}, \Theta) = E \left\| \tilde{\Theta} - \Theta \right\|_{2,n}^s \quad (3.7)$$

was defined in order to assess the quality of the estimate. Depending on the number of coefficients  $n$ , the threshold is applied to, the minimax threshold  $\lambda_n^*$  was obeyed. With this threshold one obtains minimal risks  $R(\tilde{\Theta}, \Theta)$  for soft thresholding.

Table 3.1 gives the thresholds  $\lambda_n^V$  and  $\lambda_n^*$  with  $\sigma = 1$  for  $n = 2^j$ ,  $j = 6 \dots 16$ .

$n$	$2^6$	$2^7$	$2^8$	$2^9$	$2^{10}$	$2^{11}$	$2^{12}$	$2^{13}$	$2^{14}$	$2^{15}$	$2^{16}$
$\lambda_n^*$	1.474	1.669	1.860	2.048	2.232	2.414	2.584	2.773	2.952	3.131	3.310
$\lambda_n^V$	2.884	3.115	3.330	3.532	3.723	3.905	4.079	4.245	4.405	4.560	4.710

Table 3.1: Thresholds  $\lambda_n^*$  and  $\lambda_n^V$  depending on the number of samples, the threshold is applied on [20]

### SUREShrink

*SURE* refers to Stein's Unbiased Risk Estimate that is employed for the threshold's choice. The threshold  $\lambda_n^S$  is specified level-dependent, i.e.  $n$  in this case denotes the number of wavelet coefficients on a scale  $j$  rather than the number of data samples. An approximate risk for an estimate of the wavelet coefficients on a scale  $j$  is obtained by the

Stein's unbiased estimate of risk. The threshold  $\lambda_n^S$  for a level  $j$  can be concluded from the minimum of that risk. In fact, the threshold is selected from the wavelet coefficients at the respective scale. The algorithm consists of the following steps:

1. given: vector  $\{D_j\}_n = \{d_{j,1}, \dots, d_{j,n}\}^T$ ,
2. form a vector  $\{a\}_n$  that contains all  $(d_{j,k})^2$  in ascending order,
3. form a vector  $\{b\}_n$  containing the cumulative sums of the elements in  $\{a\}_n$ :

$$\{b\}_n = \begin{pmatrix} a_1 \\ a_1 + a_2 \\ \vdots \\ \sum_{k=1}^n a_k \end{pmatrix},$$

4. form a vector  $\{c\}_n = \{n-1, n-2, \dots, 1, 0\}^T$ ,
5. form a vector  $\{s\}_n$  that is obtained by the linear combination of the vector  $\{b\}_n$  with a vector that contains the products of the elements of  $\{a\}_n$  and  $\{c\}_n$ :

$$\{s\}_n = \begin{pmatrix} b_1 + a_1 c_1 \\ b_2 + a_2 c_2 \\ \vdots \\ b_n + a_n c_n \end{pmatrix},$$

6. estimate the risks:

$$\{R\}_n = \begin{pmatrix} \frac{n-2+s_1}{n} \\ \frac{n-4+s_2}{n} \\ \vdots \\ \frac{n-2n+s_n}{n} \end{pmatrix} = \begin{pmatrix} 1 + \frac{s_1-2}{n} \\ 1 + \frac{s_2-4}{n} \\ \vdots \\ 1 + \frac{s_n-2n}{n} \end{pmatrix},$$

7. determine the minimum of  $\{R\}_n$  and the index  $i$  of  $(\min \{R\}_n)$ ,
8. select the threshold  $\lambda_n^S = \sqrt{a_i}$ .

### HybridShrink

If only very few wavelet coefficients are nonzero, the application of the *SUREShrink* approach may result in a considerable loss of information in the estimate. Therefore, in [21] a hybrid scheme is proposed. According to a certain criterion, it is decided whether the threshold  $\lambda_n^S$  (*SUREShrink*) or the threshold  $\lambda_n^V$  (*VisuShrink*) should be applied to the coefficients at a respective scale:

$$\lambda_n^H = \begin{cases} \lambda_n^V & \text{if } \frac{|d_{j,k}|^2}{n} - 1 < \frac{(\frac{\log n}{\log 2})^{\frac{3}{2}}}{\sqrt{n}} \\ \min(\lambda_n^S, \lambda_n^V) & \text{if } \frac{|d_{j,k}|^2}{n} - 1 \geq \frac{(\frac{\log n}{\log 2})^{\frac{3}{2}}}{\sqrt{n}} \end{cases} \quad (3.8)$$

Notice that  $n$  denotes the number of wavelet coefficients at the respective scale rather than the number of all coefficients in equation (3.8).

### 3.2.2 Implementation

All described thresholds can be applied for both hard and soft thresholding. Algorithms for selective wavelet reconstruction based on the thresholds  $\lambda_n^*$ ,  $\lambda_n^V$ ,  $\lambda_n^S$  and  $\lambda_n^H$  are implemented in the MATLAB \*.m files that are available over the Internet (Wavelab library).

De-noising, as described above, is based on the assumption of independent and identically distributed noise. Apart from *SUREShrink* and the related *HybridShrink* approach, the presented algorithms estimate the noise level presuming that the wavelet coefficients at the finest scale contain only noise. Furthermore, wavelet shrinkage, according to the proposals explained above, is solely applied to the details at the finest scales  $1 \leq j \leq \max.j$  in order to preserve the basic low frequency characteristics of the original data. However, sometimes there is a particular demand to filter out only contributions to the signal that are represented by the wavelet coefficients at very few scales or low frequency contents. The latter may be true, e.g. if the measured signal shows comparatively strong low frequency features (nearly DC), that are not due to a mechanical motion, which should

be measured. In this case a treatment of the coefficients representing the low frequency contents of the signal is sensible.

Both the algorithms described, and a routine that allows for a selective filtering by setting all coefficients at certain levels to zero, were implemented in the SLang software package [5]. Two applications for the performance of these routines are given in examples 3.1 and 3.2.

### Example 3.1. De-noising of a numerically simulated signal

Figure 3.1 shows the curve of a structural response that was obeyed by a numerical simulation of a dynamic test with a sweep sine excitation and a signal obtained by superimposing the original data with a vector containing Gaussian white noise. The signal-to-noise ratio

$$SNR = \frac{\|signal\|}{\|noise\|} \quad (3.9)$$

for the noise corrupted data is 2.66. The thresholds according to the rules *VisuShrink*, *RiskShrink*, *SUREShrink* and *HybridShrink* were applied to the five finest scales of the decomposition of the data with respect to the Daubechies-8 wavelet. Both hard and soft thresholding were carried out. The resulting curves are given in figures 3.2 to 3.5. The original curves are drawn in each diagram as grey lines.

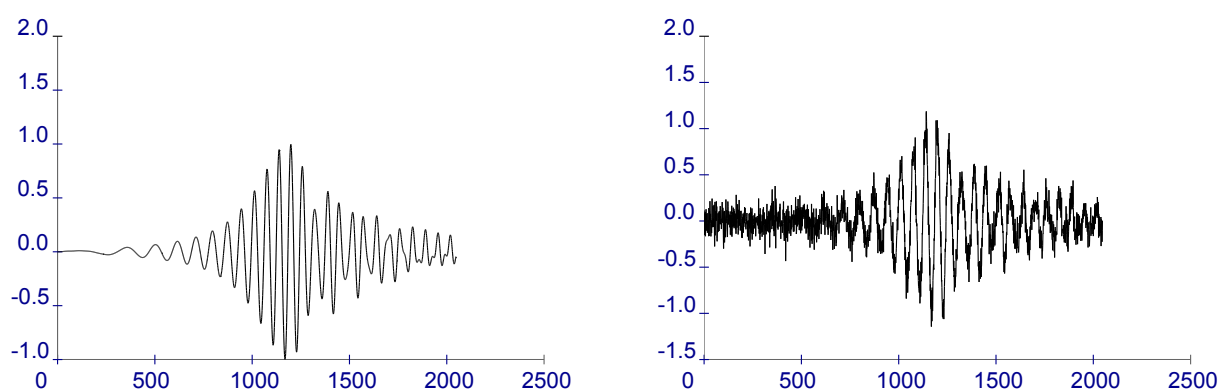


Figure 3.1: Numerically simulated structural response due to a sweep excitation (left) and noise corrupted version, signal-to-noise ratio = 2.66 (right)

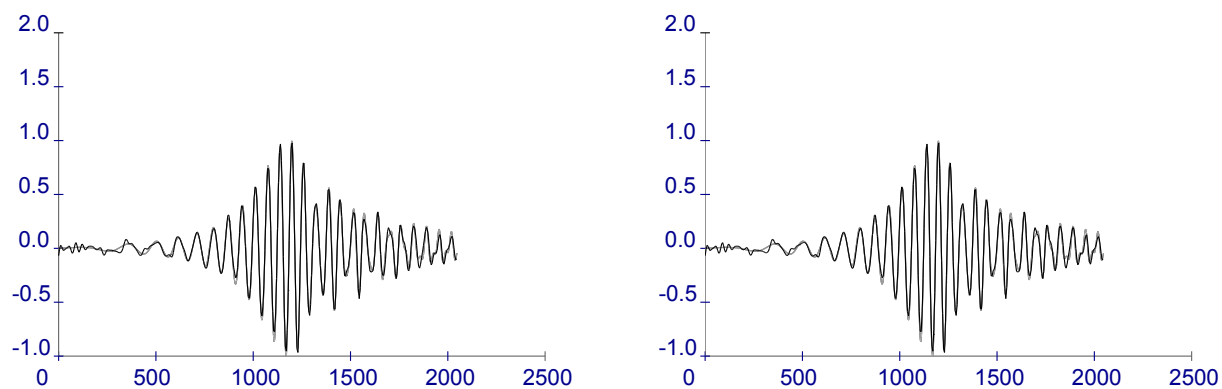


Figure 3.2: Data after hard (left) and soft (right) thresholding with respect to the threshold  $\lambda_n^V$

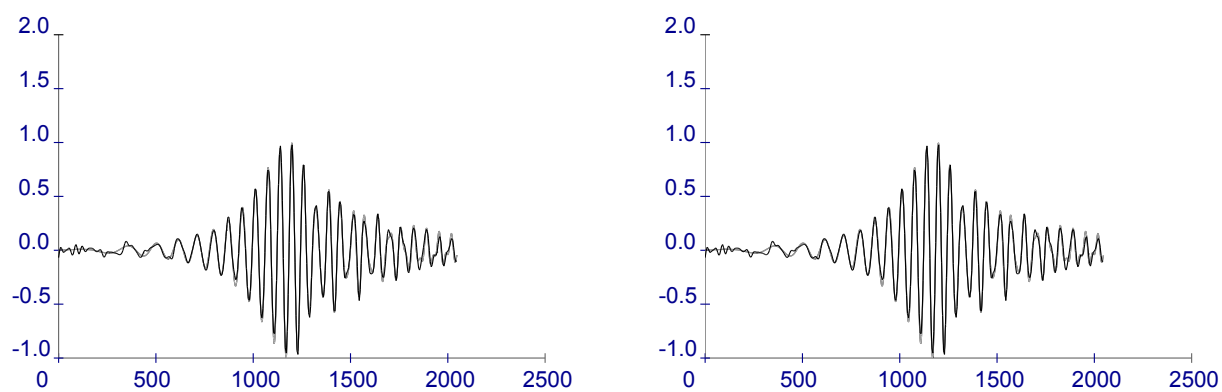


Figure 3.3: Data after hard (left) and soft (right) thresholding with respect to the threshold  $\lambda_n^*$



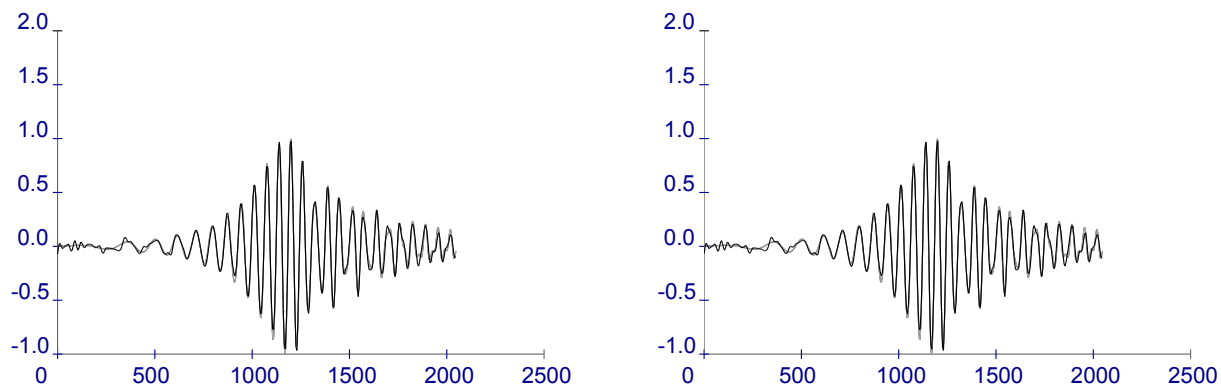


Figure 3.4: Data after hard (left) and soft (right) thresholding with respect to the threshold  $\lambda_n^S$

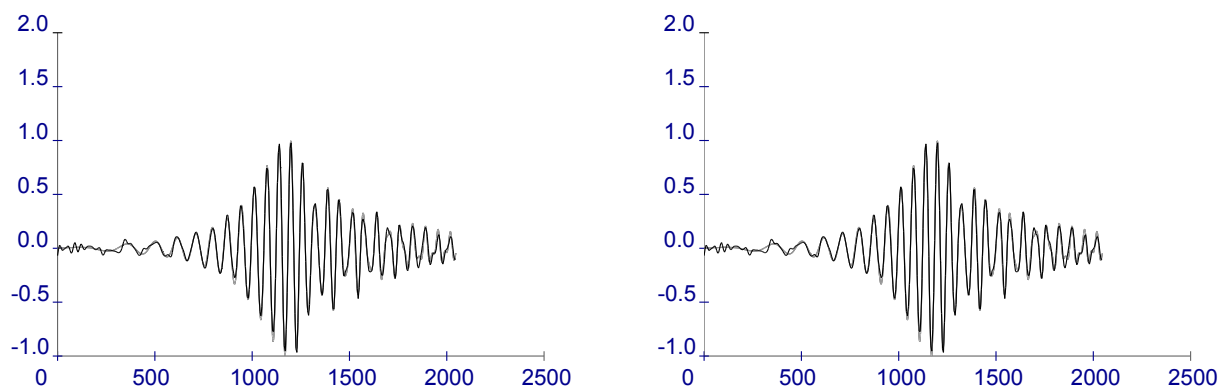


Figure 3.5: Data after hard (left) and soft (right) thresholding with respect to the threshold  $\lambda_n^H$

**Example 3.2. Low frequency calibration of an accelerometer**

*Manufacturers of accelerometers usually guarantee a constant sensitivity of their sensors within a certain frequency range. However, particularly for some civil engineering structures, it might be required to measure the structural response at frequencies below that range as well. Therefore calibration of an available piezoelectric accelerometer was carried out. The test setup is illustrated in figure 3.6.*

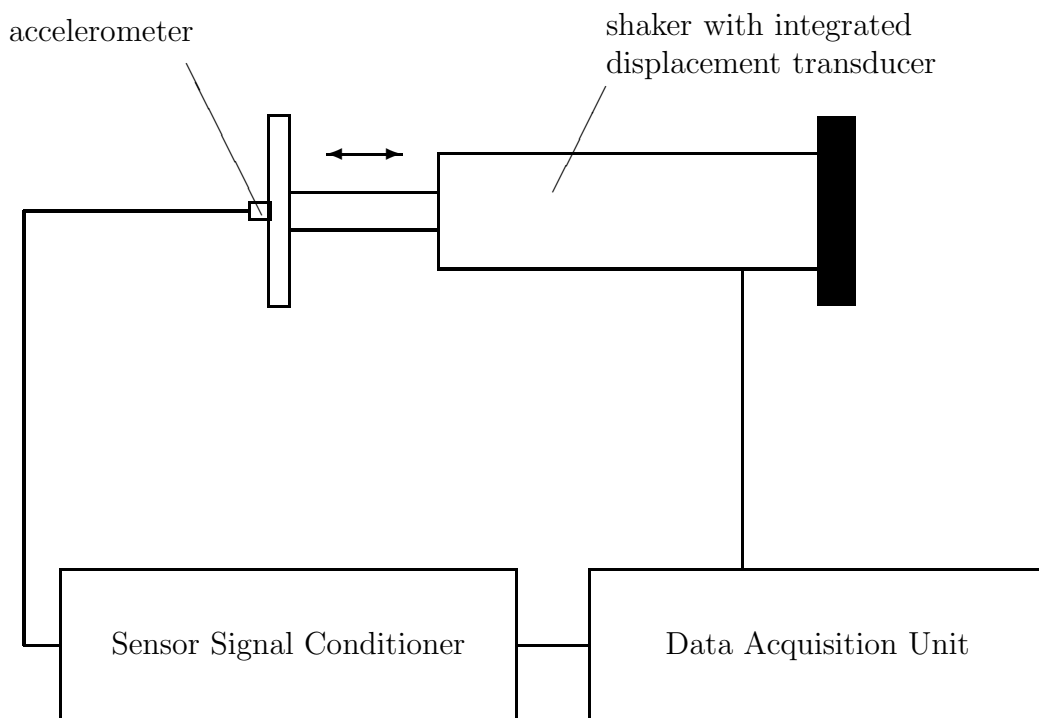


Figure 3.6: Test setup for the calibration of an ICP accelerometer

*The accelerometer was mounted on a servo-hydraulic shaker with an integrated displacement transducer. Both the displacements of the actuator and the accelerometer's signal were measured simultaneously. The shaker was driven in such a way that the amplitudes of the accelerations behaved approximately like a sweep function with constant amplitudes. The accelerometer's sensitivity, as a function of frequency, is obtained by setting the autospectra of the accelerometer's signal and of the actuator's accelerations, respectively, relative to each other. The latter can be derived from the measured displacements of the*

actuator.

$$H_{acc}(\omega) = \frac{G_{AA,acc}(\omega)}{G_{AA,shaker}(\omega)}. \quad (3.10)$$

The respective raw and de-noised autospectra are shown in figure 3.7 (grey curves). Figure 3.8 gives the wavelet transforms of the measured spectra with respect to the Daubechies-5 wavelet. Hard thresholding the wavelet coefficients of the measured autospectra, based on the threshold  $\lambda_n^*$ , yields the black curves in figure 3.7. The grey curve in figure 3.9 indicates the sensitivity function that is obtained from the raw spectra. The sensitivity derived from the de-noised autospectra is marked by the black line.

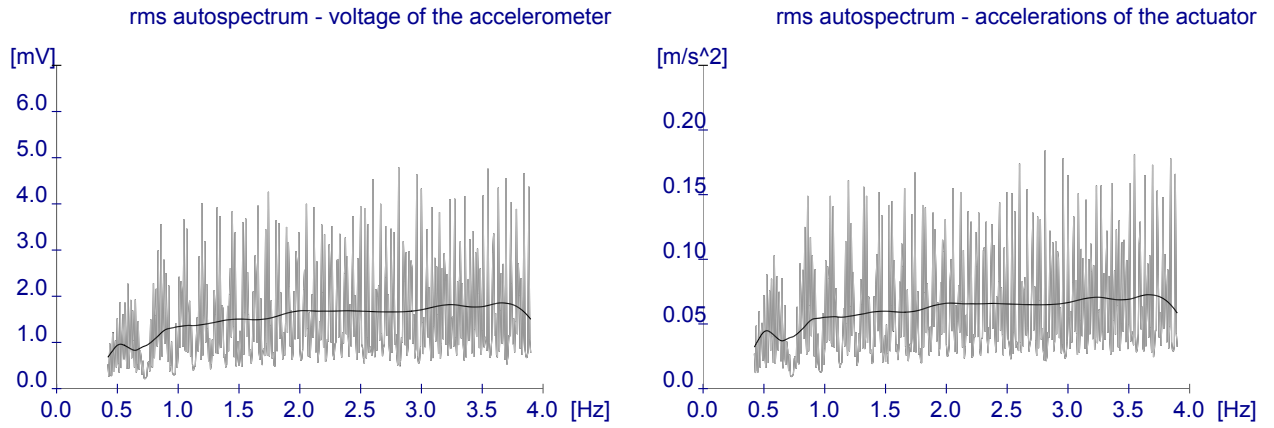


Figure 3.7: RMS autospectra of the accelerometer's voltage (left) and the actuator's acceleration (right): raw data (grey) and de-noised series (black), hard thresholding at the five finest scales (D6 wavelet) with respect to  $\lambda_n^*$

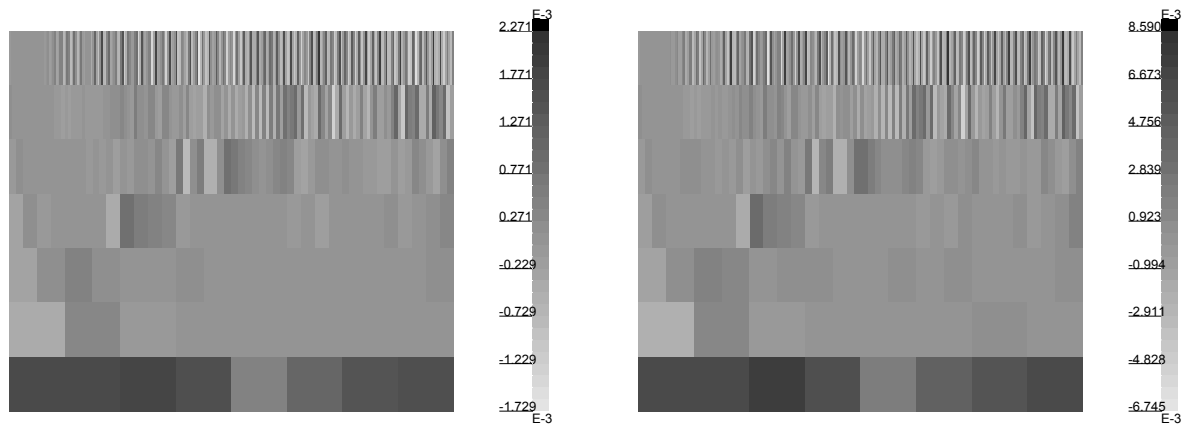


Figure 3.8: Wavelet coefficients of the RMS autospectra of the accelerometer's voltage (left) and the actuator's acceleration (right), decomposition with respect to the D6 wavelet

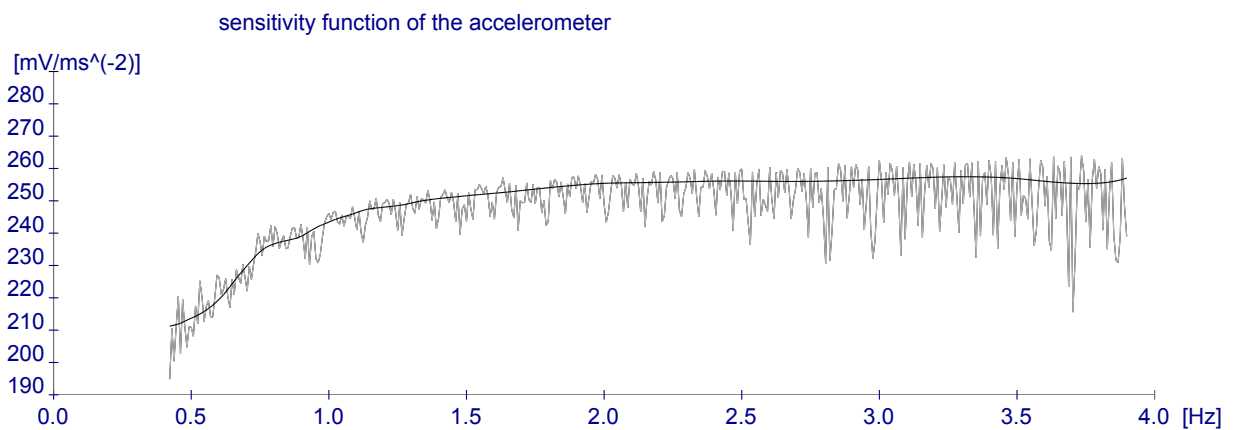


Figure 3.9: Sensitivity of the accelerometer with respect to frequency: function obtained from raw data (grey) and with de-noised series (black)

### 3.3 Enhanced De-noising Algorithms

The data that one obtains after the application of selective wavelet reconstruction may sometimes show distortions that are not due to noise corruption. These distortions are caused by a precise alignment between certain features in the signal and features of the analysing function [16]. In order to suppress such alignments, a method is proposed in [16] that shifts the signal, either in time or in frequency, prior to de-noising and re-shifting. Since signal shifting that avoids an alignment of respective features at one location may result in such an alignment at another sample, it is suggested analysing the whole range  $n$  of possible shifts and averaging the results:

$$\text{Average (Shift - De-noise - Unshift)}_n .$$

This procedure leads to a result that does not depend on a particular shift. It is therefore called translation-invariant de-noising or cycle-spinning.

Another approach for the improvement of the de-noising follows an iteration that is described in [48] and illustrated in figure 3.10. Selective wavelet reconstruction is not only applied to the signal but also to the difference  $\Delta$  between the original signal and the estimate  $\tilde{f}$ . The iteration is repeated until the standard deviation of the difference remains within a predefined range.

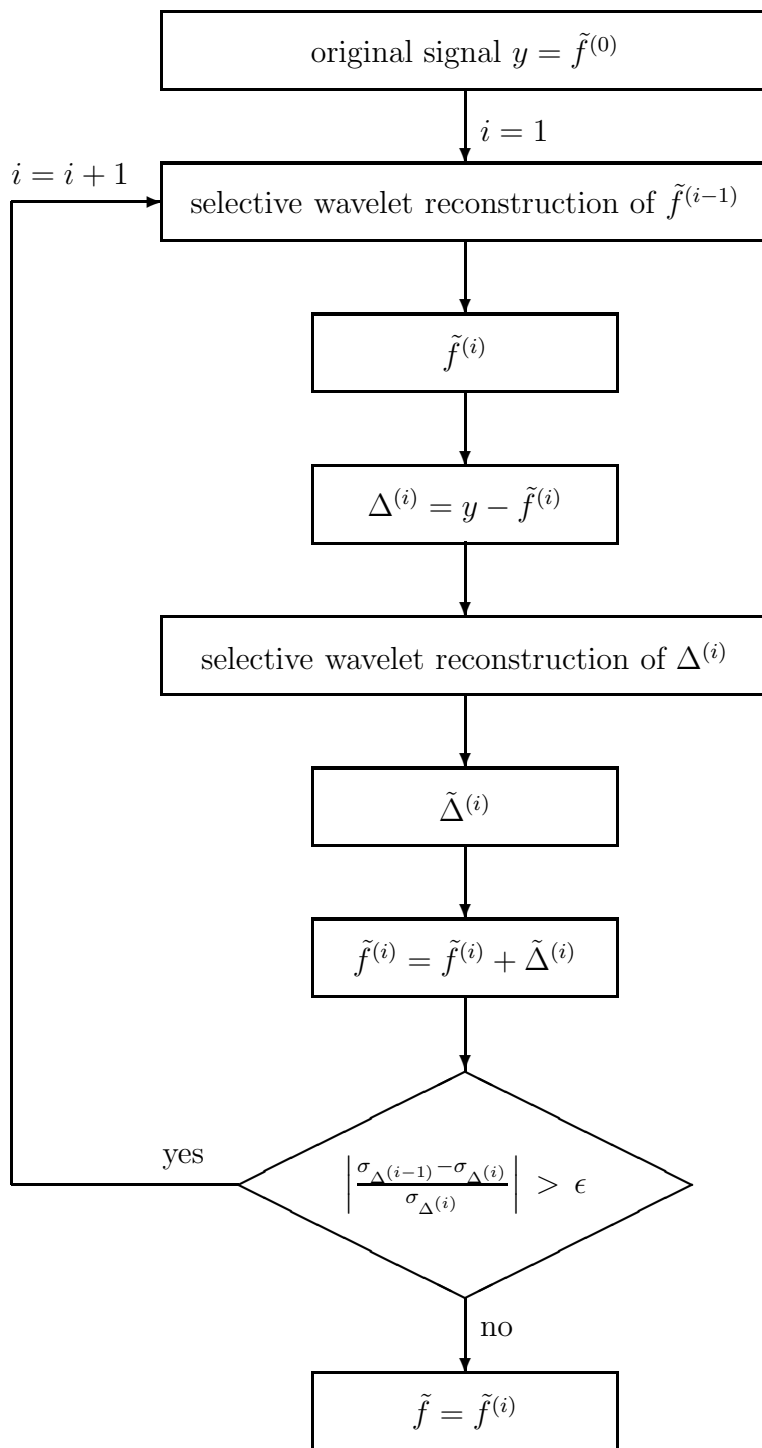


Figure 3.10: Flow diagram of the enhanced selective wavelet reconstruction according to [48]

# Chapter 4

## Derivatives and Integrals in Wavelet Analysis

In dynamic tests, the structural response is usually measured as either displacements, velocities or accelerations. In the case of tests on civil engineering structures, it is common to use accelerometers or geophones that measure vibration velocities. It is often desired to obtain derivatives or integrals of the measured signals.

This chapter is devoted to the topic of how the wavelet transforms of derivatives or integrals of a signal can be obtained directly. First the respective relations for the continuous wavelet transform are derived. In section 4.2, the concept of connection coefficients is described. It is shown how the details of the derivative or the integral of a signal can be calculated directly from an orthogonal wavelet decomposition of the signal. The relations that are derived in this chapter are verified by some examples in appendix C.

### 4.1 Continuous Wavelet Transforms

It is assumed that there were displacements measured in a test. The measured signals, the respective velocities and accelerations should be analysed in the continuous time-scale domain.

The starting point is the wavelet transform of the displacement series  $x(t)$  with respect to a real wavelet  $\psi''$ :

$$W_{\psi''}^x(a, b) = \frac{1}{\sqrt{a}} \int_{-\infty}^{\infty} x(t) \psi''\left(\frac{t-b}{a}\right) dt. \quad (4.1)$$

It is supposed that the wavelet  $\psi''$  is the second derivative of a wavelet  $\psi$ :

$$\psi'' = \frac{d^2\psi}{dt^2} = \frac{d\psi'}{dt}. \quad (4.2)$$

Provided that the function  $\psi$  is a wavelet and its first two derivatives exist, the functions  $\psi'$  and  $\psi''$  are also wavelets [40].

Integrating equation (4.1) by parts results in

$$W_{\psi''}^x(a, b) = \frac{a}{\sqrt{a}} \left( \underbrace{\left( x(t) \psi'\left(\frac{t-b}{a}\right) \right) \Big|_{-\infty}^{\infty}}_{=0} - \int_{-\infty}^{\infty} \dot{x}(t) \psi'\left(\frac{t-b}{a}\right) dt \right). \quad (4.3)$$

If  $\psi$ ,  $\psi'$  and  $\psi''$  are wavelets, it follows that  $\psi$  and  $\psi'$  are continuous functions and  $\psi', \psi'' \in L^2(\mathbb{R})$ . Accordingly,

$$\lim_{t \rightarrow \infty} \psi'(t) = \lim_{t \rightarrow -\infty} \psi'(t) = \lim_{t \rightarrow \infty} \psi(t) = \lim_{t \rightarrow -\infty} \psi(t) = 0. \quad (4.4)$$

Consequently, the underbraced term in equation (4.3) vanishes.

Partial integration of equation (4.3) gives:

$$W_{\psi''}^x(a, b) = \frac{a^2}{\sqrt{a}} \left( \underbrace{\left( \dot{x}(t) \psi\left(\frac{t-b}{a}\right) \right) \Big|_{-\infty}^{\infty}}_{=0} + \int_{-\infty}^{\infty} \ddot{x}(t) \psi\left(\frac{t-b}{a}\right) dt \right). \quad (4.5)$$

From equations (4.3) and (4.5) one can easily deduce that

$$W_{\psi''}^x(a, b) = -a W_{\psi'}^{\dot{x}}(a, b) = a^2 W_{\psi}^{\ddot{x}}(a, b). \quad (4.6)$$

Consequently, in the case that displacements were measured in a test, the wavelet transforms of the accelerations with respect to a wavelet  $\psi$  can be described similarly by a



wavelet transform of the displacements:

$$\begin{aligned}
W_{\psi}^{\ddot{x}}(a, b) &= \frac{1}{\sqrt{a}} \int_{-\infty}^{\infty} \ddot{x}(t) \psi''\left(\frac{t-b}{a}\right) dt \\
&= \frac{1}{a\sqrt{a}} \left( \underbrace{\left( \dot{x}(t) \psi\left(\frac{t-b}{a}\right) \right) \Big|_{-\infty}^{\infty}}_{=0} - \int_{-\infty}^{\infty} \dot{x}(t) \psi'\left(\frac{t-b}{a}\right) dt \right) \\
&= \frac{1}{a^2\sqrt{a}} \left( \underbrace{\left( x(t) \psi\left(\frac{t-b}{a}\right) \right) \Big|_{-\infty}^{\infty}}_{=0} + \int_{-\infty}^{\infty} x(t) \psi''\left(\frac{t-b}{a}\right) dt \right).
\end{aligned} \tag{4.7}$$

Hence

$$W_{\psi}^{\ddot{x}}(a, b) = -\frac{1}{a} W_{\psi'}^{\dot{x}}(a, b) = \frac{1}{a^2} W_{\psi''}^x(a, b). \tag{4.8}$$

measured quantity	WT of $x(t)$	WT of $\dot{x}(t)$	WT of $\ddot{x}(t)$
$x(t)$	$W_{\psi}^x(a, b)$	$-\frac{z_{\psi}}{a z_{\psi'}} W_{\psi'}^x(a, b)$	$\frac{z_{\psi}}{a^2 z_{\psi''}} W_{\psi''}^x(a, b)$
$\dot{x}(t)$	$-\frac{a z_{\psi}}{z_{\psi'}} W_{\psi}^{\dot{x}}(a, b)$	$W_{\psi'}^{\dot{x}}(a, b)$	$-\frac{z_{\psi'}}{a z_{\psi''}} W_{\psi''}^{\dot{x}}(a, b)$
$\ddot{x}(t)$	$\frac{a^2 z_{\psi}}{z_{\psi''}} W_{\psi}^{\ddot{x}}(a, b)$	$-\frac{a z_{\psi'}}{z_{\psi''}} W_{\psi'}^{\ddot{x}}(a, b)$	$W_{\psi''}^{\ddot{x}}(a, b)$

Table 4.1: Relations between the wavelet transforms of displacements, velocities and accelerations

In numerical algorithms for the calculation of the continuous wavelet transforms, in general normalised wavelets are applied. Therefore a normalisation coefficient  $z_{\psi}$  has to be introduced into equations (4.6) and (4.8). Table 4.1 gives the relations between the

wavelet transforms (WT) of  $x(t)$ ,  $\dot{x}(t)$  and  $\ddot{x}(t)$  dependent on the respective measured data, provided that the three functions  $\psi$ ,  $\psi'$  and  $\psi''$  are wavelets.

This condition is, for example, true if a derivative of the Gaussian function is chosen as the analysing wavelet  $\psi$ . The derivatives of the Gaussian function form a family of wavelets (section 1.3.1). If the wavelets are normalised such that  $\|\psi\|^2 = 1$ , as e.g. in the Wavelet Toolbox of the software package MATLAB [46] the normalisation coefficients for the first three derivatives of the Gaussian function become:

$$\begin{aligned} \psi &= t e^{-\frac{t^2}{2}} & \longrightarrow & z_\psi = -0.89324 \\ \psi' &= (t^2 - 1) e^{-\frac{t^2}{2}} & \longrightarrow & z_{\psi'} = 0.51571 \\ \psi'' &= (t^3 - 3t) e^{-\frac{t^2}{2}} & \longrightarrow & z_{\psi''} = 0.23063 \end{aligned} \quad (4.9)$$

Since measured time series are always finite, the integration can only be carried out over the finite observation interval ( $0 \leq t \leq T$ ). Accordingly equation (4.1) becomes

$$W_{\psi''}^x(a, b) = \frac{1}{\sqrt{a}} \int_0^T x(t) \psi''\left(\frac{t-b}{a}\right) dt. \quad (4.10)$$

Integrating equation (4.10) by parts twice one obtains

$$\begin{aligned} W_{\psi''}^x(a, b) &= \frac{a^2}{\sqrt{a}} \left( \left( x(t) \psi'\left(\frac{t-b}{a}\right) \right) \Big|_0^T - \int_{-\infty}^{\infty} \dot{x}(t) \psi'\left(\frac{t-b}{a}\right) dt \right) \\ &= \frac{a}{\sqrt{a}} \left[ \left( x(T) \psi'\left(\frac{T-b}{a}\right) - x(0) \psi'\left(-\frac{b}{a}\right) \right) \right. \\ &\quad \left. - a \left( \dot{x}(t) \psi\left(\frac{t-b}{a}\right) \right) \Big|_0^T + a \int_0^T \ddot{x}(t) \psi\left(\frac{t-b}{a}\right) dt \right] \\ &= a^2 \frac{z_\psi}{z_{\psi''}} W_{\psi}^{\ddot{x}}(a, b) \\ &\quad + \sqrt{a} \left[ x(T) \psi'\left(\frac{T-b}{a}\right) - x(0) \psi'\left(-\frac{b}{a}\right) \right. \\ &\quad \left. - a \left( \dot{x}(T) \psi\left(\frac{T-b}{a}\right) - \dot{x}(0) \psi\left(-\frac{b}{a}\right) \right) \right] \left. \vphantom{\frac{z_\psi}{z_{\psi''}}} \right\} = 0, \text{ if} \\ &\quad \left. \vphantom{\frac{z_\psi}{z_{\psi''}}} \right\} \begin{aligned} x(0) = x(T) = 0, \\ \dot{x}(0) = \dot{x}(T) = 0. \end{aligned} \end{aligned} \quad (4.11)$$

Provided that the system is in static equilibrium both at the beginning and at the end of the test ( $x(0) = x(T) = \dot{x}(0) = \dot{x}(T) = 0$ ), as it is approximately true for free vibration tests, the second term in equation (4.11) vanishes. If this condition cannot be completely satisfied, this term is still nearly zero for most  $(a, b)$  since the wavelets  $\psi$  and  $\psi'$  are usually rapidly decaying functions.

Some examples for the application of the derived relations are given in appendix C.

## 4.2 Discrete Wavelet Calculus and Connection Coefficients

The use of linear operators in context with discrete wavelet analysis, such as e.g. convolution operators [6] or differential operators [53], have been investigated in previous years. A more general approach is described in [45], where the derived relations are not limited to one particular type of operators but apply to a whole class of linear operators. The following sections are to a great extent based on [45].

### 4.2.1 Orthogonal Wavelets and Linear Operators

#### Relations between Translation and Dilation

First some general relations between a linear operator  $\mathcal{K}$  and both translations and normalised dilations are given. The group of translations with respect to a real parameter  $\tau$  is defined by:

$$T(\tau) = f(t) \rightarrow f(t - \tau), \quad t, \tau \in \mathbb{R}, \quad (4.12)$$

while

$$D(s) = f(t) \rightarrow \sqrt{s} f(st), \quad s > 0 \quad (4.13)$$

denotes the group of normalised dilations.

All  $\tau \in \mathbb{R}$  and  $s > 0$  satisfy the relations:

$$\begin{aligned} T(\tau_1 + \tau_2) &= T(\tau_1) T(\tau_2), \\ D(s_1 s_2) &= D(s_1) D(s_2), \end{aligned} \quad (4.14)$$

$$\begin{aligned} \bar{T}(\tau) &= T(-\tau), \\ \bar{D}(s) &= D(s^{-1}), \end{aligned} \quad (4.15)$$

where  $\bar{T}$  and  $\bar{D}$  are the adjoint operators of  $T$  and  $D$ , respectively.

The rule for the sequential exchange of translation and dilation is given by

$$T(\tau) D(s) = D(s) T(\tau s). \quad (4.16)$$

To the inner products of the translated and dilated versions of two functions  $f$  and  $g$  applies

$$\begin{aligned} \langle T(\tau) f, g \rangle &= \langle f, T(-\tau) g \rangle, \\ \langle D(s) f, g \rangle &= \langle f, D(s^{-1}) g \rangle \end{aligned} \quad (4.17)$$

and accordingly

$$\langle D(s) T(\tau) f, g \rangle = \langle f, T(-\tau) D(s^{-1}) g \rangle. \quad (4.18)$$

With the notation

$$D(s, \tau) = D(s) T(\tau) \quad (4.19)$$

one obtains

$$\bar{D}(s, \tau) = D\left(s^{-1}, -\frac{\tau}{s}\right), \quad (4.20)$$

$$D(s_1, \tau_1) D(s_2, \tau_2) = D(s_1 s_2, \tau_2 + s_2 \tau_1), \quad (4.21)$$

$$\langle D(s, \tau) f, g \rangle = \left\langle f, D\left(s^{-1}, -\frac{\tau}{s}\right) g \right\rangle \quad (4.22)$$

and consequently

$$\langle D(s_1, \tau_1) f, D(s_2, \tau_2) g \rangle = \left\langle f, D\left(\frac{s_2}{s_1}, \tau_2 - \frac{s_2}{s_1} \tau_1\right) g \right\rangle. \quad (4.23)$$

The dilated and translated versions of the scaling function and of the wavelet, respectively, as defined in equations (1.42) and (1.52), can be re-written in the form

$$\phi_{m,n} = D(2^{-m}, n) \phi, \quad (4.24)$$

$$\psi_{m,n} = D(2^{-m}, n) \psi. \quad (4.25)$$

The scaling function and the mother wavelet (equations (1.42) and (1.48)) in their normalised forms become

$$\phi(t) = \sum_{n=0}^{2g-1} h_n D(2, n) \phi, \quad (4.26)$$

$$\psi(t) = \sum_{n=0}^{2g-1} g_n D(2, n) \psi. \quad (4.27)$$

Hence

$$D(s, \tau) \phi = \sum_{n=0}^{2g-1} h_n D(2s, n + 2\tau) \phi, \quad (4.28)$$

$$D(s, \tau) \psi = \sum_{n=0}^{2g-1} g_n D(2s, n + 2\tau) \psi. \quad (4.29)$$

For  $s = 2^{-m}$  and  $\tau = k$  one obtains

$$D(2^{-m}, k) \phi = \phi_{m,k} = \sum_{n=0}^{2g-1} h_n \phi_{m-1, 2k+n} \quad (4.30)$$

and

$$D(2^{-m}, k) \psi = \psi_{m,k} = \sum_{n=0}^{2g-1} g_n \psi_{m-1, 2k+n} \quad (4.31)$$

that is equivalent to equations (1.55) and (1.56).

### Differential and Integral Operators

According to [45], a class of linear operators  $\mathbb{H}_\lambda$  can be defined. The differential operator  $\mathcal{D}^\lambda$  and the integral operator  $\mathcal{I}^\lambda$  belong to  $\mathbb{H}_\lambda$ :

$$\mathcal{D}^\lambda = \frac{d^\lambda}{dt^\lambda}, \quad \mathcal{D}^\lambda \in \mathbb{H}_\lambda, \quad \lambda = 1, 2, \dots, \quad (4.32)$$

$$\mathcal{I}^\lambda = \mathcal{D}^{-\lambda} \in \mathbb{H}_\lambda, \quad \lambda = 1, 2, \dots \quad (4.33)$$

With  $\lambda = 1$   $\mathcal{I}^1 = \mathcal{I}$  is defined as

$$\mathcal{I} = \int_{-\infty}^t f(\tau) d\tau \quad (4.34)$$

This class of operators  $\mathbb{H}_\lambda$  is particularly characterised by the following permutability relations:

$$\mathcal{K} T(\tau) = T(\tau) \mathcal{K}, \quad (4.35)$$

$$\mathcal{K} D(s) = s^\lambda D(s) \mathcal{K}. \quad (4.36)$$

With equations (4.23) and (4.36) one obeys for any  $\mathcal{K} \in \mathbb{H}_\lambda$

$$\langle \mathcal{K} D(s_1, \tau_1) f, D(s_2, \tau_2) g \rangle = s_1^\lambda \left\langle \mathcal{K} f, D\left(\frac{s_2}{s_1}, \tau_2 - \frac{s_2}{s_1} \tau_1\right) g \right\rangle. \quad (4.37)$$

From equation (4.14) and with  $D(1, \tau) = D(1) T(\tau) = T(\tau)$  one can conclude

$$\langle \mathcal{K} D(s, \tau_1) f, D(s, \tau_2) g \rangle = s^\lambda \langle \mathcal{K} f, T(\tau_2 - \tau_1) g \rangle. \quad (4.38)$$

If a linear operator  $\mathcal{K} \in \mathbb{H}_\lambda$  is applied to a dilated and translated version of the scaling function  $\phi$ , one obtains with equation (4.26)

$$\begin{aligned} \mathcal{K} D(s, \tau) \phi &= \mathcal{K} D(s, \tau) \sum_{n=0}^{2g-1} h_n D(2, n) \phi \\ &= \sum_{n=0}^{2g-1} h_n \mathcal{K} D(s, \tau) D(2, n) \phi \\ &= \sum_{n=0}^{2g-1} h_n \mathcal{K} D(s) T(\tau) D(2) T(n) \phi. \end{aligned}$$

Applying equations (4.14), (4.16), (4.35) and (4.36) yields

$$\begin{aligned} \mathcal{K} D(s, \tau) \phi &= \sum_{n=0}^{2g-1} h_n \mathcal{K} D(s) D(2) T(2\tau) T(n) \phi \\ &= \sum_{n=0}^{2g-1} h_n \mathcal{K} D(2s) T(2\tau + n) \phi \\ &= \sum_{n=0}^{2g-1} h_n (2s)^\lambda D(2s) \mathcal{K} T(2\tau + n) \phi \\ &= \sum_{n=0}^{2g-1} h_n (2s)^\lambda D(2s) T(2\tau + n) \mathcal{K} \phi \\ \mathcal{K} D(s, \tau) \phi &= (2s)^\lambda \sum_{n=0}^{2g-1} h_n D(2s, 2\tau + n) \mathcal{K} \phi. \end{aligned} \quad (4.39)$$

This means that the derivative or the integral of a translated and dilated version of the scaling function  $\phi$  can be calculated based on the dilations and translations of the respective derivative or integral of the scaling function. A very similar expression can be derived for the wavelet  $\psi$ :

$$\mathcal{K} D(s, \tau) \psi = (2s)^\lambda \sum_{n=0}^{2g-1} g_n D(2s, 2\tau + n) \mathcal{K} \psi . \quad (4.40)$$

### 4.2.2 Connection Coefficients

Provided that there is a signal given that can be decomposed by a multi-scale analysis, the wavelet coefficients of a derivative or an integral of the signal can be determined by means of so-called connection coefficients. It is assumed that the translated and dilated versions of the scaling function and the wavelet, respectively,  $\phi_{m,n} = D(2^{-m}, n) \phi$  and  $\psi_{m,n} = D(2^{-m}, n) \psi$ , as given in equations (4.24) and (4.25), are known. Then one can define the following connection coefficients of a linear operator  $\mathcal{K} \in \mathbb{H}_\lambda$  as:

$$\Gamma_{i,j}^{k,l}(\phi, \phi) = \langle \mathcal{K} \phi_{i,j}, \phi_{k,l} \rangle , \quad (4.41)$$

$$\Gamma_{i,j}^{k,l}(\psi, \psi) = \langle \mathcal{K} \psi_{i,j}, \psi_{k,l} \rangle , \quad (4.42)$$

$$\Gamma_{i,j}^{k,l}(\phi, \psi) = \langle \mathcal{K} \phi_{i,j}, \psi_{k,l} \rangle , \quad (4.43)$$

$$\Gamma_{i,j}^{k,l}(\psi, \phi) = \langle \mathcal{K} \psi_{i,j}, \phi_{k,l} \rangle . \quad (4.44)$$

The connection coefficients in equation (4.41) at the basic scale, i.e.  $i = k = 0$ , can be denoted in compact form:

$$\Gamma_j^l = \Gamma_{0,j}^{0,l}(\phi, \phi) . \quad (4.45)$$

With  $j = 0$  one gets the coefficients  $\Gamma_0^l$  that are called the fundamental connection coefficients of the operator  $\mathcal{K}$ .

For a linear operator  $\mathcal{K} \in \mathbb{H}_\lambda$ , the respective connection coefficients satisfy the relations:

$$\Gamma_{i,j}^{k,l}(f, g) = 2^{i\lambda} \Gamma_{0,0}^{k-i, l-2^{(k-l)}j}(f, g) , \quad (4.46)$$

$$\Gamma_{i,j}^{k,l}(f, g) = 2^{i\lambda} \Gamma_{0,0}^{0, l-j}(f, g) = 2^{i\lambda} \Gamma_0^{l-j}(f, g) , \quad (4.47)$$

$$\Gamma_{i,j+n}^{k,l+n}(f,g) = \Gamma_{i,j}^{i,l}(f,g) = \Gamma_{i,0}^{i,l-j}(f,g) , \quad (4.48)$$

$$\Gamma_{j+n}^{l+n}(f,g) = \Gamma_j^l(f,g) = \Gamma_0^{l-j}(f,g) , \quad (4.49)$$

$$\Gamma_{i,j}^{k,l}(f,g) = 2^{n\lambda} \Gamma_{i-n,j}^{k-n,l}(f,g) . \quad (4.50)$$

In equations (4.46) to (4.50) for  $f$  and  $g$ , the functions  $\phi$  and  $\psi$  can be inserted in any combination.

All connection coefficients of an operator  $\mathcal{K}$  with respect to a wavelet  $\psi$  can be calculated if the respective fundamental coefficients  $\Gamma_0^l$  are known. The fundamental coefficients of a differential operator  $\mathcal{D}^\lambda$  or an integral operator  $\mathcal{I}^\lambda$  are determined by solving the system of linear equations

$$\sum_{\nu=0}^{2g-2} \beta_{k,\nu} \Gamma_{0,0}^{0,\nu} = - \sum_{\nu \in \mathbb{N}_+} \alpha_{\nu+2k} G_\nu , \quad (4.51)$$

with the normalised autocorrelation coefficients  $\alpha_\nu$  of the real normalised scaling function's coefficients  $\tilde{h}_k$  (equation (1.61))

$$\alpha_\nu = \frac{1}{2} \sum_k \tilde{h}_k \tilde{h}_{k+\nu} . \quad (4.52)$$

From equation (1.65) follows

$$\alpha_0 = 1 . \quad (4.53)$$

For orthogonal wavelet systems, the autocorrelation coefficients with even subscripts vanish:

$$\alpha_{2n} = 0 , n \in \mathbb{N}_+ . \quad (4.54)$$

The values  $\beta_{k,\nu}$  in equation (4.51) are obtained from

$$\beta_{k,\nu} = \alpha_{2k-\nu} + (1 - \delta_{0,\nu}) (-1)^\lambda \alpha_{2k+\nu} 2^{-\lambda} \delta_{k,\nu} . \quad (4.55)$$

The coefficients  $G_\nu$  in equation (4.51) depend on the operator  $\mathcal{K}$ , i.e. on  $\lambda$ . They are listed in table 4.2 for the operators  $\mathcal{D}^1$ ,  $\mathcal{D}^2$ ,  $\mathcal{I}^1$  and  $\mathcal{I}^2$ .

Since  $G_\nu$  is zero for all differential operators, the respective right hand sides of the system of equations (4.51) vanish. Consequently, an additional non-homogeneous condition is



operator:	$\mathcal{D}^2$	$\mathcal{D}^1$	$\mathcal{I}^1$	$\mathcal{I}^2$
$G_\nu$	0	0	1	$\nu$

Table 4.2: Values of the coefficients  $G_\nu$  with respect to differential and integral operators of first and second order

required for the calculation of the respective fundamental coefficients of the operators  $\mathcal{D}^\lambda$ .

This condition is given by:

$$\sum_{\nu} \nu^\lambda \Gamma_0^\nu = (-1)^\lambda \lambda!, \quad \nu = 2 - 2g, \dots, 0, \dots, 2g - 2. \quad (4.56)$$

Furthermore, the fundamental connection coefficients of the operators  $\mathcal{D}^\lambda$  and  $\mathcal{I}^\lambda$  satisfy the relation

$$\Gamma_0^\nu = (-1)^\lambda \Gamma_0^{-\nu} + G_\nu. \quad (4.57)$$

With equation (4.57), the introduction of negative superscripts  $\nu$  in equation (4.56) can be avoided.

The fundamental connection coefficients  $\Gamma_0^\nu$  of the operators  $\mathcal{D}^1$ ,  $\mathcal{D}^2$ ,  $\mathcal{I}^1$  and  $\mathcal{I}^2$  are given in appendix B. If the connection coefficients of a differential operator should be applied, it must be ensured that the respective scaling function and wavelet are differentiable at the respective order. That means, a solution of the system of equations (4.51) and (4.56) may exist but must not be applied if the respective wavelet is not differentiable. Therefore, e.g. tables B.1 and B.3 do not contain any  $\Gamma_0^\nu$  for the Daubechies wavelet  $D2$ .

### 4.2.3 Application of Connection Coefficients

Recalling equation (1.77), a signal  $f(t)$  can be described by its wavelet decomposition as follows:

$$f(t) = \sum_k a_{M,k} \phi_{M,k}(t) + \sum_{m=1}^M \sum_k d_{m,k} \psi_{m,k}(t). \quad (4.58)$$

The application of a linear operator  $\mathcal{K} \in \mathbb{H}_\lambda$  gives

$$\mathcal{K} f(t) = \sum_k a_{M,k} \mathcal{K} \phi_{M,k}(t) + \sum_{m=1}^M \sum_k d_{m,k} \mathcal{K} \psi_{m,k}(t). \quad (4.59)$$

The scaling coefficients of equation (4.59) are obtained as the inner product with the scaling function at the basic level:

$$\langle \mathcal{K} f(t), \phi_{0,l}(t) \rangle = \sum_k a_{M,k} \langle \mathcal{K} \phi_{M,k}(t), \phi_{0,l}(t) \rangle + \sum_{m=1}^M \sum_k d_{m,k} \langle \mathcal{K} \psi_{m,k}(t), \phi_{0,l}(t) \rangle . \quad (4.60)$$

Deploying equations (4.41) and (4.44), this relation becomes

$$\langle \mathcal{K} f(t), \phi_{0,l}(t) \rangle = \sum_k a_{M,k} \Gamma_{M,k}^{0,l}(\phi, \phi) + \sum_{m=1}^M \sum_k d_{m,k} \Gamma_{m,k}^{0,l}(\psi, \phi) . \quad (4.61)$$

Consequently, the scaling coefficients of a signal's derivative or integral can be described by an orthogonal wavelet decomposition of the original signal and the appropriate wavelet connection coefficients.

According to equation (1.77), a signal can be interpreted as an approximation at the basic decomposition scale:

$$f(t) = \sum_k a_{0,k} \phi_{0,k}(t) . \quad (4.62)$$

Hence

$$\mathcal{K} f(t) = \sum_k a_{0,k} \mathcal{K} \phi_{0,k}(t) . \quad (4.63)$$

Therefore

$$\langle \mathcal{K} f(t), \phi_{0,l}(t) \rangle = \sum_k a_{0,k} \Gamma_{0,k}^{0,l}(\phi, \phi) . \quad (4.64)$$

With the relations in equations (4.49) and (4.57) it can be deduced that only the original signal and the fundamental connection coefficients  $\Gamma_0^l$  are required for the approximation of an integral or a derivative of the signal. The respective algorithm can be summarised by two steps:

1. calculate an approximation of the derivative or integral of the given signal at the basic level utilising the fundamental connection coefficients  $\Gamma_0^l$  of the respective linear operator and
2. subsequent wavelet decomposition of this approximation.

The principle of this approach is illustrated in figure 4.1, where the approximations and details of the respective decompositions at a level  $m$  are denoted by  $A_m$  and  $D_m$ , respectively (see section 1.4.2).

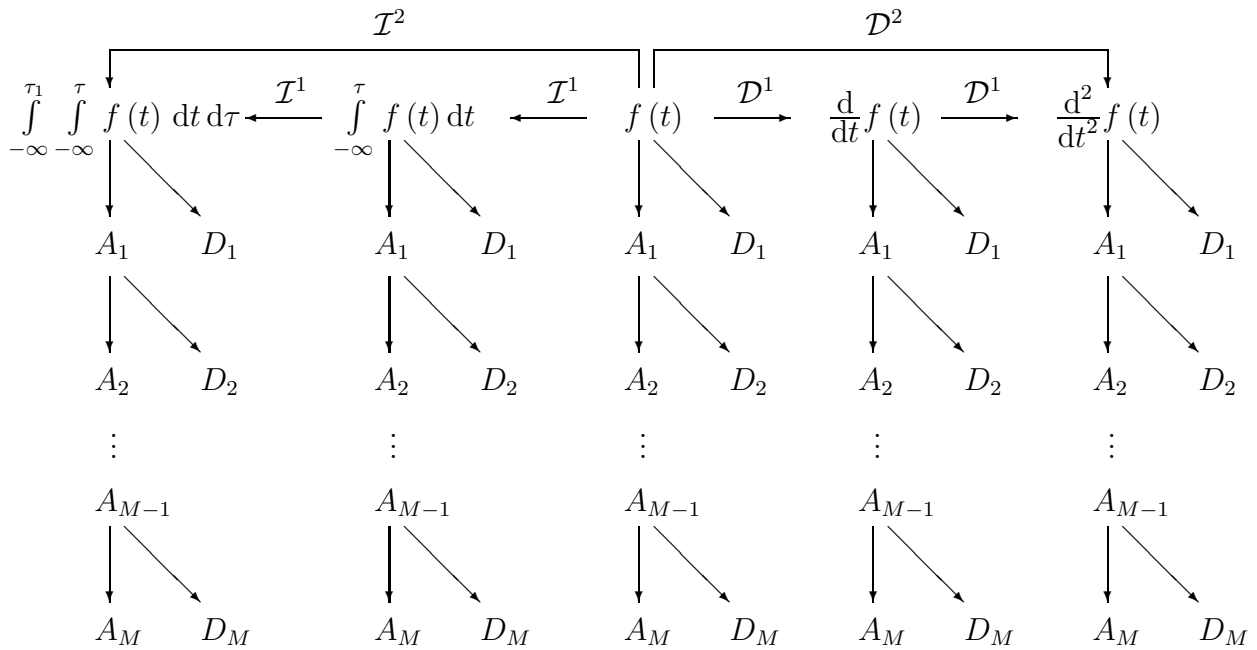


Figure 4.1: Flow diagram of the application of differential and integral operators (fundamental connection coefficients) and wavelet decomposition

The accuracy of the proposed approach depends on the properties of the signal and the applied mother wavelet. Border distortions may occur as well as deviations from the theoretical results at the coarsest scales.

If the proposed concept is applied for the estimation of a signal's derivative, the differentiability of the respective mother wavelet has to be considered. As mentioned earlier, e.g. the second order derivative of the Daubechies wavelet  $D2$  is not defined.

#### 4.2.4 Implementation of the Concept of Connection Coefficients

The fundamental connection coefficients for both the first and second order differentiation and integration with respect to the Daubechies wavelets of genus 2 to 10 were calculated and are listed in appendix B. The operators  $\mathcal{D}^1$ ,  $\mathcal{D}^2$ ,  $\mathcal{I}^1$  and  $\mathcal{I}^2$  based on wavelets of the Daubechies family were implemented into the SLang software package ("wavelet derivative" and "wavelet integrate" commands) [5]. The examples in appendix C demonstrate the performance of the implemented algorithms.

## Chapter 5

# Direct Parameter Estimation

The dynamic behaviour of a linear viscously damped system is governed by the system of differential equations

$$[M] \{\ddot{x}(t)\} + [C] \{\dot{x}(t)\} + [K] \{x(t)\} = \{f(t)\} , \quad (5.1)$$

where  $[M]$ ,  $[C]$  and  $[K]$  refer to the system's mass, damping and stiffness matrices, respectively, while the displacements, velocities and accelerations at a time instant  $t$  are given by the vectors  $\{x(t)\}$ ,  $\{\dot{x}(t)\}$  and  $\{\ddot{x}(t)\}$ . The vector  $\{f(t)\}$  denotes the excitation of the system.

The inverse problem is dedicated to the identification of the system's parameter matrices from measured structural response and excitation. For linear time-invariant systems, the matrices  $[M]$ ,  $[C]$  and  $[K]$  are constant throughout the whole test.

Usually, the structural response of a civil engineering structure is measured in dynamic tests as accelerations or as velocities. The numerical integration of measured data, that almost always incorporates noisy contributions, causes problems. Therefore, the formulation of equation (5.1) based on measured data seems to be impractical for the solution of the inverse problem. However, in conjunction with the concepts developed in chapter 4, a wavelet-based representation of the equation of motion (5.1) provides an expedient base in this context, as shown in this chapter.

In section 5.1 it is shown how the complete equation of motion for a linear time-invariant system can be represented in the time-scale domain utilising continuous wavelet transforms of measured accelerations. A related approach, that is based on discrete wavelet analysis, is described in section 5.2. The performance of the derived technique is verified by means of examples.

## 5.1 Continuous Wavelet Analysis Approach

For linear time-invariant systems the transformation of the equation of motion (5.1) into the time-scale domain with respect to a wavelet  $\psi''$  results in

$$[M] \{W_{\psi''}^{\ddot{x}}(a, b)\} + [C] \{W_{\psi''}^{\dot{x}}(a, b)\} + [K] \{W_{\psi''}^x(a, b)\} = \{W_{\psi''}^f(a, b)\} . \quad (5.2)$$

Employing the relations derived in section 4.1, equation (5.2) can be re-written as

$$[M] \{W_{\psi''}^{\ddot{x}}(a, b)\} - a [C] \frac{z_{\psi'}}{z_{\psi''}} \{W_{\psi'}^{\ddot{x}}(a, b)\} + a^2 [K] \frac{z_{\psi}}{z_{\psi''}} \{W_{\psi}^{\ddot{x}}(a, b)\} = \{W_{\psi''}^f(a, b)\} . \quad (5.3)$$

According to equation (5.3), a complete set of equations of motion in the time-scale domain can be formulated based on wavelet transforms of accelerations and excitations.

Assuming that both the accelerations and the excitations are known from a dynamic test, equation (5.3) can be re-arranged for a single-degree-of-freedom (SDOF) system in the form

$$\left\{ W_{\psi''}^{\ddot{x}}(a, b), a \frac{z_{\psi'}}{z_{\psi''}} W_{\psi'}^{\ddot{x}}(a, b), a^2 \frac{z_{\psi}}{z_{\psi''}} W_{\psi}^{\ddot{x}}(a, b) \right\} \begin{Bmatrix} m \\ c \\ k \end{Bmatrix} = W_{\psi''}^f(a, b) . \quad (5.4)$$

The parameters  $m$ ,  $c$  and  $k$  can be obtained by solving a system of equations that is based on the wavelet transforms of both measured accelerations and excitation at three coordinate pairs  $(a, b)$ .

If the measured data is noise corrupted, equation (5.4) should be set up for more than three coordinate pairs  $(a, b)$ . This results in an overdetermined system of equations that can be solved for the parameter vector by a least-squares method.

Equation (5.4) can be easily adapted to multi-degree-of-freedom (MDOF) systems. One obtains

$$[W^{\ddot{x}}(a, b)] \{p\} = \left\{ W_{\psi''}^f(a, b) \right\}. \quad (5.5)$$

The vector  $\{p\}$  refers to the collection of system parameters, the matrix  $[W^{\ddot{x}}(a, b)]$  contains the respective wavelet transforms of the measured accelerations. The structure of the matrix  $[W^{\ddot{x}}(a, b)]$  is shown a for five-degree-of-freedom system in example 5.1.

### Example 5.1. Linear 5-DOF system

*The identification approach described in this section was verified by means of a numerical simulation. The considered system is the 5-DOF system shown in figure 5.1. The system's parameters are listed in table 5.1. A resonance test was simulated by numerically exciting the system at DOF 2 with the sweep force given in figure 5.2. As analysing functions, the*

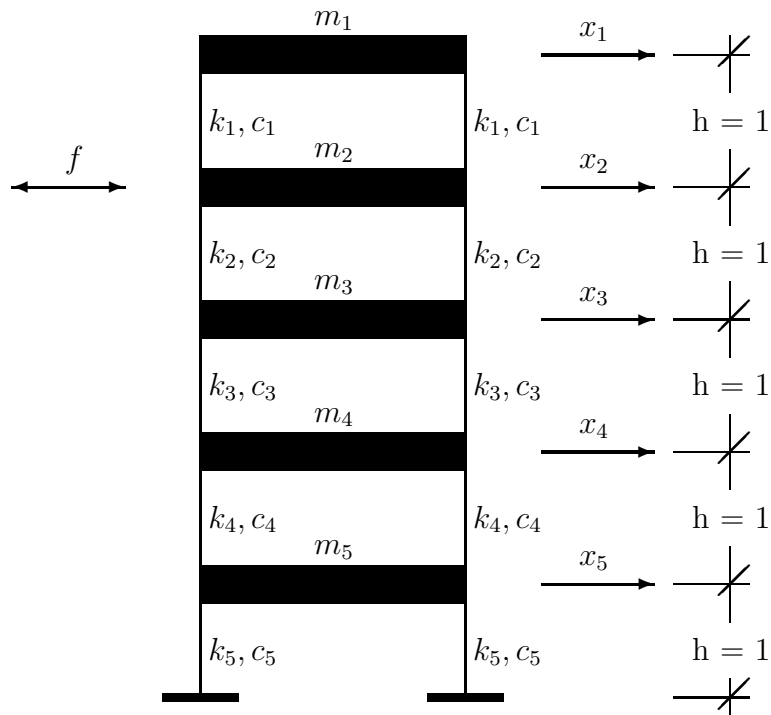


Figure 5.1: Five-degree-of-freedom system

first three wavelets of the Gaussian function's derivatives family were chosen:

$$\psi = t e^{-\frac{t^2}{2}}, \quad \psi' = (t^2 - 1) e^{-\frac{t^2}{2}}, \quad \psi'' = (t^3 - 3t) e^{-\frac{t^2}{2}}.$$

The respective wavelet transforms were calculated using the MATLAB Wavelet Toolbox. Assuming that the lumped masses  $m_i$  were known, equation (5.5) becomes, for any coordinate pair  $(a, b)$

$$[W^{\ddot{x}}(a, b)] \{p\} = \left\{ W_{\psi''}^f(a, b) \right\} - [M] \left\{ W_{\psi''}^{\ddot{x}}(a, b) \right\}. \quad (5.6)$$

For a single coordinate pair  $(a, b)$  the matrix  $[W^{\ddot{x}}(a, b)]$  is constructed as

$$[W^{\ddot{x}}(a, b)] = \begin{bmatrix} (W_{\psi'}^{\ddot{x}_1} - W_{\psi'}^{\ddot{x}_2}) & (W_{\psi'}^{\ddot{x}_2} - W_{\psi'}^{\ddot{x}_1}) & 0 & 0 & 0 \\ 0 & (W_{\psi'}^{\ddot{x}_2} - W_{\psi'}^{\ddot{x}_3}) & (W_{\psi'}^{\ddot{x}_3} - W_{\psi'}^{\ddot{x}_2}) & 0 & 0 \\ 0 & 0 & (W_{\psi'}^{\ddot{x}_3} - W_{\psi'}^{\ddot{x}_4}) & (W_{\psi'}^{\ddot{x}_4} - W_{\psi'}^{\ddot{x}_3}) & 0 \\ 0 & 0 & 0 & (W_{\psi'}^{\ddot{x}_4} - W_{\psi'}^{\ddot{x}_5}) & (W_{\psi'}^{\ddot{x}_5} - W_{\psi'}^{\ddot{x}_4}) \\ 0 & 0 & 0 & 0 & W_{\psi'}^{\ddot{x}_5} \\ (W_{\psi}^{\ddot{x}_1} - W_{\psi}^{\ddot{x}_2}) & (W_{\psi}^{\ddot{x}_2} - W_{\psi}^{\ddot{x}_1}) & 0 & 0 & 0 \\ 0 & (W_{\psi}^{\ddot{x}_2} - W_{\psi}^{\ddot{x}_3}) & (W_{\psi}^{\ddot{x}_3} - W_{\psi}^{\ddot{x}_2}) & 0 & 0 \\ 0 & 0 & (W_{\psi}^{\ddot{x}_3} - W_{\psi}^{\ddot{x}_4}) & (W_{\psi}^{\ddot{x}_4} - W_{\psi}^{\ddot{x}_3}) & 0 \\ 0 & 0 & 0 & (W_{\psi}^{\ddot{x}_4} - W_{\psi}^{\ddot{x}_5}) & (W_{\psi}^{\ddot{x}_5} - W_{\psi}^{\ddot{x}_4}) \\ 0 & 0 & 0 & 0 & W_{\psi}^{\ddot{x}_5} \end{bmatrix}^T, \quad (5.7)$$

where  $W_{\psi'}^{\ddot{x}_i} = a \frac{z_{\psi'}}{z_{\psi''}} W_{\psi'}^{\ddot{x}_i}(a, b)$  and  $W_{\psi}^{\ddot{x}_i} = a^2 \frac{z_{\psi}}{z_{\psi''}} W_{\psi}^{\ddot{x}_i}(a, b)$ . The parameter vector  $\{p\}$  contains the system's stiffness and damping parameters

$$\{p\} = \{c_1, c_2, c_3, c_4, c_5, k_1, k_2, k_3, k_4, k_5\}^T \quad (5.8)$$

The influence of noise within the data on the identification's accuracy was investigated by adding Gaussian white noise to both the accelerations and the excitation. Three levels of noise intensity were considered: 1 %, 2 % and 5 %, where the percentage indicates the standard deviation of the respective random vector in relation to the "clean" data's



mass parameter	value	stiffness parameter	value	damping parameter	value
$m_1$	1.00	$k_1$	300.00	$c_1$	10.00
$m_2$	1.25	$k_2$	600.00	$c_2$	9.00
$m_3$	1.50	$k_3$	900.00	$c_3$	8.00
$m_4$	1.75	$k_4$	1200.00	$c_4$	9.00
$m_5$	2.00	$k_5$	1500.00	$c_5$	10.00

Table 5.1: Lumped masses  $m_j$ , stiffness parameters  $k_j$  and damping coefficients  $c_j$  of the 5-DOF system

maximum. Figure 5.2 shows details of the excitation and the accelerations at DOF 2 near resonance with a noise contamination of 2 %. The respective wavelet transforms are given in figure 5.4. The frequency contents of the two series are illustrated in figure 5.3.

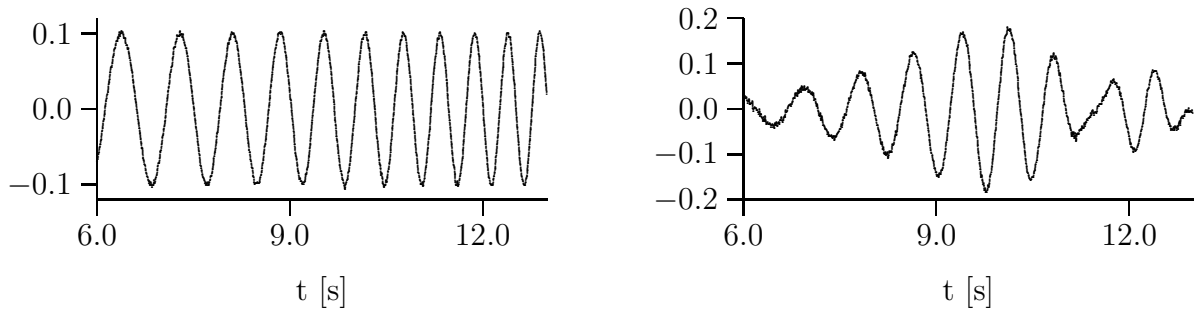


Figure 5.2: Details of the time series of the exciting force (left) and the accelerations at DOF 2 (right) – noise level 2 %

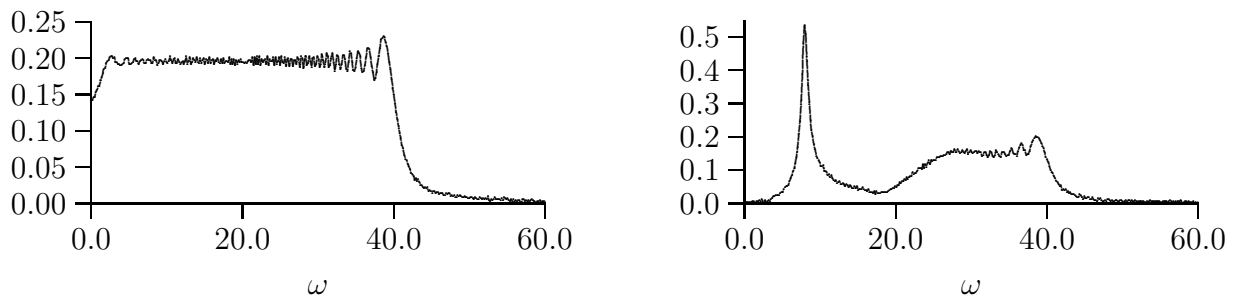


Figure 5.3: Magnitudes of the Fourier transforms of the exciting force (left) and the accelerations at DOF 2 (right) – noise level 2 %

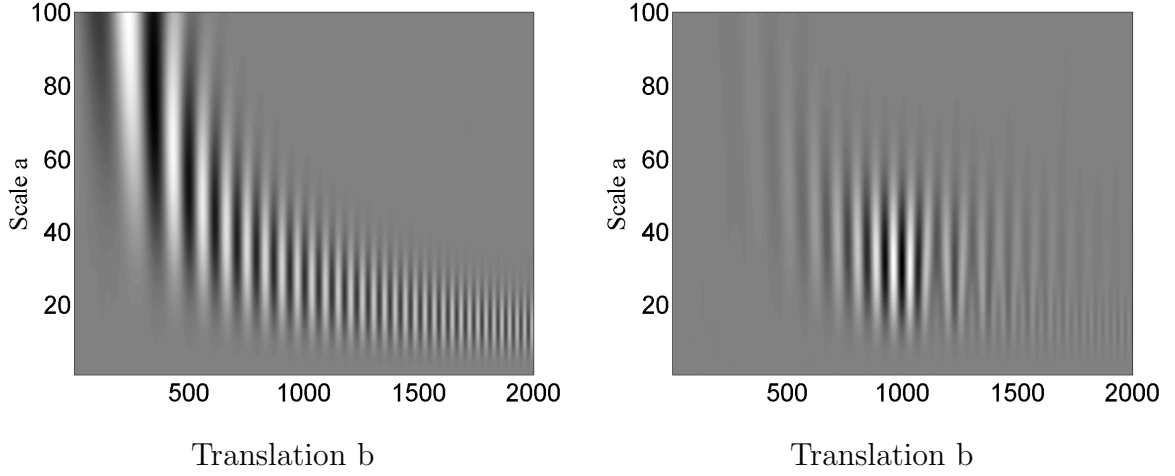


Figure 5.4: Wavelet transforms with respect to the wavelet  $\psi''$  of the exciting force (left) and the accelerations at DOF 2 (right) – noise level 2.0 %

*In order to validate the performance of the identification based on continuous wavelet transforms, the results were compared with those obtained from a related procedure that can be derived from applying the Fourier transformation to the equation of motion:*

$$[M] \left\{ \hat{x}(\omega) \right\} + [C] \left\{ \frac{\hat{x}(\omega)}{i\omega} \right\} + [K] \left\{ \frac{\hat{x}(\omega)}{\omega^2} \right\} = \left\{ \hat{f}(\omega) \right\} . \quad (5.9)$$

*For the identification, both Fourier coefficients and wavelet transforms were selected in the vicinity of the first resonance ( $6.136 \leq \omega \leq 12.272$ ;  $8 \leq a \leq 64$ ,  $750 \leq b \leq 1250$ ). For the wavelet-based approach each parameter set was calculated on the base of the wavelet transforms at seven coordinate pairs  $(a, b)$  taken at a dyadic grid such that redundancy was reduced. This means, each system of equations that was solved by means of a least squares method contained the wavelet transforms at the coordinates  $(a_j, b_j)$ ,  $(a_j, b_j + a_j)$ ,  $(a_j, b_j + 2a_j)$ ,  $(a_j, b_j + 3a_j)$ ,  $(2a_j, b_j + \frac{a_j}{2})$ ,  $(2a_j, b_j + \frac{5a_j}{2})$  and  $(4a_j, b_j + \frac{3a_j}{2})$ . In total 164 sets of parameters were calculated. It became obvious from a statistical analysis that the results were not normally distributed. Therefore, it was decided to consider the histograms' peak values as identified parameters rather than the mean values. The identified*

	orig. value	ident. no noise	error [%]	ident. 1 % noise	error [%]	ident. 2 % noise	error [%]	ident. 5 % noise	error [%]
$k_1$	300.00	299.61	0.13	304.66	1.55	292.44	2.67	283.26	5.58
$k_2$	600.00	599.26	0.12	601.77	0.29	597.05	0.49	606.93	1.16
$k_3$	900.00	899.03	0.11	895.77	0.47	886.57	1.49	908.36	0.93
$k_4$	1200.0	1198.6	0.12	1193.5	0.54	1191.7	0.69	1155.9	3.67
$k_5$	1500.0	1498.3	0.11	1493.9	0.41	1494.8	0.35	1502.7	0.18
$c_1$	10.00	9.998	0.02	10.027	0.27	9.543	4.57	10.252	2.52
$c_2$	9.00	8.989	0.12	8.714	3.18	9.253	2.81	6.204	31.07
$c_3$	8.00	8.007	0.09	8.632	7.90	8.086	1.08	8.736	9.20
$c_4$	9.00	9.007	0.08	8.568	4.80	7.573	15.85	8.588	4.58
$c_5$	10.00	10.009	0.09	10.190	1.90	10.060	0.60	8.769	12.31

Table 5.2: Identified parameters  $k_j$  and  $c_j$  with respect to the level of noise contamination – wavelet-based approach

parameters  $k_j$ ,  $c_j$  and the respective errors

$$err(k_j) = \frac{|k_{j,orig} - k_{j,ID}|}{k_{j,orig}} \times 100\%, \quad (5.10)$$

$$err(c_j) = \frac{|c_{j,orig} - c_{j,ID}|}{c_{j,orig}} \times 100\% \quad (5.11)$$

are summarised in tables 5.2 and 5.3. For the wavelet-based technique the listed parameters are the central values of the respective histogram's class. The histograms of the results from the wavelet-based approach, collected in appendix D.1, were computed for 41 classes.

The results of the investigations in example 5.1 suggest that the method presented in this section leads to acceptable results that are of slightly higher or similar accuracy to those that were obtained by means of a related approach based on the Fourier transforms of the measured data. The quality of the results depends considerably on the choice of the coordinates  $(a, b)$  at which the wavelet transforms are extracted for the identification. Generally, the best results were achieved when the wavelet transforms that represent the highest contributions to the system's response energy were included into the analysis.

	orig. value	ident. no noise	error [%]	ident. 1 % noise	error [%]	ident. 2 % noise	error [%]	ident. 5 % noise	error [%]
$k_1$	300.00	297.82	0.73	293.79	2.07	277.81	7.40	201.07	32.98
$k_2$	600.00	595.62	0.73	586.6	2.23	578.03	3.66	428.79	28.53
$k_3$	900.00	894.06	0.66	886.64	1.48	854.14	5.10	646.71	28.14
$k_4$	1200.0	1193.3	0.56	1180.2	1.67	1147.3	4.39	913.79	23.85
$k_5$	1500.0	1492.1	0.53	1474.8	1.68	1438.3	4.11	1169.3	22.05
$c_1$	10.00	9.9124	0.88	9.7836	2.16	9.2774	7.23	6.569	34.31
$c_2$	9.00	8.9922	0.87	8.5874	4.58	8.8914	1.21	9.341	3.79
$c_3$	8.00	8.0483	0.60	9.0213	12.77	7.4633	6.71	7.625	4.69
$c_4$	9.00	9.0012	0.01	8.7648	2.61	7.5661	15.93	6.636	26.26
$c_5$	10.00	10.006	0.06	9.9233	0.77	9.301	6.99	8.769	6.75

Table 5.3: Identified parameters  $k_j$  and  $c_j$  with respect to the level of noise contamination – Fourier transform-based approach

## 5.2 Discrete Wavelet Analysis Approach

It has to be mentioned that a considerable drawback is inherent in the method described in section 5.1. The calculation of continuous wavelet transforms involves a large number of numerical integrations and is thus relatively time consuming. Therefore, an approach that is based on discrete wavelet calculus and multi-scale analysis is given in this section.

### 5.2.1 Derivation of the Approach

Any one-dimensional discrete signal can be represented by an orthogonal wavelet decomposition (equation (1.77))

$$f(t) = \sum_k a_{M,k} \phi_{M,k}(t) + \sum_k \sum_{m=1}^M d_{m,k} \psi_{m,k}(t) .$$

Since the wavelet transformation is a linear transformation, the equation of motion for a linear time-invariant system (5.1) can be re-written, for any instant  $k$ , at decomposition

level  $m$  (rather than time  $t$ ) as:

$$[M] \{d_{m,k}^{\ddot{x}}\} + [C] \{d_{m,k}^{\dot{x}}\} + [K] \{d_{m,k}^x\} = \{d_{m,k}^f\}, \quad (5.12)$$

where the vectors  $\{d_{m,k}^{\ddot{x}}\}$ ,  $\{d_{m,k}^{\dot{x}}\}$ ,  $\{d_{m,k}^x\}$  and  $\{d_{m,k}^f\}$  respectively contain the wavelet coefficients of the accelerations, velocities, displacements and excitation at level  $m$  and instant  $k$ . This means, the equation of motion can be transposed from the time domain to the discrete time-scale domain. With respect to practical application, the wavelet coefficients in equation (5.12) should be multiplied by weighting coefficients  $u_m$  that have to be chosen by the analyst for each considered scale  $m$ .

Equation (5.12) uses the wavelet coefficients of accelerations, velocities and displacements. However, from dynamic tests, usually only accelerations are available. For the estimation of velocities and displacements in the sense of integrals of accelerations the concept of connection coefficients (section 4.2) is suggested. The same approach can be employed if displacements or velocities were measured. However, when utilising connection coefficients of differential operators, the differentiability properties of the respective basic wavelet have to be taken into account.

Assuming that the excitation is known and interpreting a measured discrete series of accelerations  $\ddot{x}(k)$  as a series of scaling coefficients at the basic decomposition scale, the following algorithm can be developed:

1. Calculate approximations of displacements and velocities using the respective connection coefficients.
2. Decompose the respective approximations into its wavelet coefficients by means of a multi-scale analysis (scheme in figure 4.1).
3. Select coordinates  $m$ ,  $k$  of wavelet coefficients that are to be included into the identification.

4. set up the system of equations for the identification of the system matrices' elements:

$$[[d_{m,k}^{\ddot{x}}], [d_{m,k}^{\dot{x}}], [d_{m,k}^x]] \left\{ \begin{array}{c} m_{1,1} \\ m_{1,2} \\ \vdots \\ m_{n,n} \\ c_{1,1} \\ c_{1,2} \\ \vdots \\ c_{n,n} \\ k_{1,1} \\ k_{1,2} \\ \vdots \\ k_{n,n} \end{array} \right\} = \{d_{m,k}^f\}. \quad (5.13)$$

If the mass matrix is assumed to be known, the contributions of the inertia forces in equation (5.13) can be shifted to the right hand side by subtraction. The matrix on the left hand side of equation (5.13) should have more rows than the parameter vector which is obtained by considering a sufficient number of coordinates  $(m, k)$ .

5. Solve the system of equations (5.13) for the parameter vector and re-arrange the solution in the respective system matrices.

It should be mentioned that an approach which is related to the method presented in this section is described in [28]. However, there the estimation of the response is limited to the base of measured displacements. The accelerations and velocities are approximated by means of the connection coefficients of differential operators given in [53]. Furthermore, the scaling coefficients rather than the wavelet coefficients are used in the system of equations. This means, only high-frequency components are omitted, all low-frequency contributions remain within the selected coefficients. In the case of approximating the accelerations and velocities by differentiating displacements, this concept might be practicable. But using scaling (rather than wavelet) coefficients obtained by decomposition

of an approximation that was estimated by integration of measured accelerations usually incorporates considerable errors.

## 5.2.2 Solution Methods

It seems to be self-evident to solve the problem (5.13) by means of a least squares approach:

$$\{p\} = \left[ [d_{m,k}^x]^T [d_{m,k}^{\ddot{x}}]^T \right]^{-1} \left\{ \{d_{m,k}^f\} - [M] [d_{m,k}^{\ddot{x}}] \right\} . \quad (5.14)$$

In equation (5.14) the mass matrix is considered to be known. If the matrices  $[C]$  and  $[K]$  are assumed to be symmetric, one can always force the result of equation (5.14) to be elements of symmetric matrices by respective arrangement of the matrices' and vectors' elements that form the system of equations.

Another possibility to obtain symmetric matrices  $[C]$  and  $[K]$  by means of matrix operations can be derived as follows. Provided that the matrix  $[M]$  is known, equation (5.12) can be written as

$$[K]_{n \times n} [d_{m,k}^x]_{n \times j} + [C]_{n \times n} [d_{m,k}^{\ddot{x}}]_{n \times j} = [d_{m,k}^f]_{n \times j} - [M]_{n \times n} [d_{m,k}^{\ddot{x}}]_{n \times j} , \quad (5.15)$$

where the matrices  $[d_{m,k}^y]$ ,  $y = x, \dot{x}, \ddot{x}, f$  contain  $j$  wavelet coefficients with respect to  $n$  degrees of freedom. Accordingly, equation (5.15) can be re-written as

$$\left[ [d_{m,k}^x]^T [d_{m,k}^{\ddot{x}}]^T \right] \begin{bmatrix} [K] \\ [C] \end{bmatrix} = [RHS] \quad (5.16)$$

with

$$[RHS] = [d_{m,k}^f] - [M] [d_{m,k}^{\ddot{x}}] . \quad (5.17)$$

Post-multiplying equation (5.16) by its transposed yields

$$[D] \begin{bmatrix} [K] \\ [C] \end{bmatrix} \begin{bmatrix} [K]^T & [C]^T \end{bmatrix} [D]^T = [RHS] [RHS]^T , \quad (5.18)$$

where  $[D] = \begin{bmatrix} [d_{m,k}^x]^T & [d_{m,k}^i]^T \end{bmatrix}$ . If  $[D]^+$  denotes the pseudo inverse of  $[D]$ , obeys

$$\begin{aligned} \begin{bmatrix} [K] \\ [C] \end{bmatrix} \begin{bmatrix} [K]^T & [C]^T \end{bmatrix} &= \begin{bmatrix} [K][K]^T & [K][C]^T \\ [C][K]^T & [C][C]^T \end{bmatrix} \\ &= [D]^+ [RHS] [RHS]^T [D]^{+T} = \begin{bmatrix} [A] & [B] \\ [G] & [H] \end{bmatrix}. \end{aligned} \quad (5.19)$$

Provided that the upper left and the lower right  $n \times n$  submatrices  $[A]$ ,  $[H]$  in equation (5.19) are positive definite, the symmetric matrices  $[K]$  and  $[C]$  can be deduced as

$$[K] = [A]^{\frac{1}{2}} = [\Phi_A]^T \left[ \text{diag} \sqrt{\lambda_A} \right] [\Phi_A], \quad (5.20)$$

$$[C] = [H]^{\frac{1}{2}} = [\Phi_H]^T \left[ \text{diag} \sqrt{\lambda_H} \right] [\Phi_H], \quad (5.21)$$

$$[C] = [K]^{-1} [B], \quad (5.22)$$

$$[C] = [G] [K]^{-1}, \quad (5.23)$$

$$[K] = [B] [C]^{-1}, \quad (5.24)$$

$$[K] = [C]^{-1} [G]. \quad (5.25)$$

Consequently, equation (5.19) provides a series of several relations for the determination of the matrices  $[K]$  and  $[C]$ . If two of equations (5.20) to (5.25) were used for the estimation of  $[K]$  and  $[C]$ , the remaining relations can be utilised for the assessment of the identified results.

Furthermore, if the considered system satisfies the modal theory, it follows that

$$[K] [C] = [C] [K], \quad (5.26)$$

hence

$$[G] = [G]^T = [B] = [B]^T. \quad (5.27)$$

By means of both the least squares analysis (5.14) and the described matrix relations (5.19) to (5.25), it can be ensured that the identified matrices are symmetric. However, if the right hand side in equation (5.14) is ill-conditioned, the least squares method may



lead to negative parameters or negative diagonal elements in  $[K]$  and  $[C]$ . Similarly, one might obtain negative eigenvalues for the submatrices  $[A]$  and  $[H]$  in equation (5.19) if the right hand side is ill-posed. In that case, it is not possible to identify positive definite system matrices  $[K]$  and  $[C]$ .

A third alternative for the identification of the matrices  $[K]$  and  $[C]$  is the formulation of an optimisation problem with the objective function

$$\left\| [M] [d_{m,k}^{\ddot{x}}] + [C] [d_{m,k}^{\dot{x}}] + [K] [d_{m,k}^x] - [d_{m,k}^f] \right\| \rightarrow \min . \quad (5.28)$$

Basically, this is a least square error minimisation, i.e. the result should be the same as that obtained from equation (5.14). However, the mathematical procedure is different from the matrix calculus in the approach described by equation (5.14). It can be ensured that the resulting matrices are symmetric and have no negative diagonal elements, by arranging the optimisation variables appropriately and by definition of respective boundary values for the variables. Moreover, parameters of finite elements of a more complex system can be identified using the optimisation approach if the algorithm is connected to a structural analysis program. With the approaches based on matrix operations, this is only possible for very simple systems.

All three methodologies for the solution of the inverse problem were tested in examples that are described in the following section.

### 5.2.3 Verification

The performance of the algorithm presented in section 5.2.1 is illustrated in this section. Both the identification of linear time-invariant MDOF systems and the detection and quantitative identification of damage during an observation interval are shown in numerical examples. The robustness of the proposed technique, with respect to noise contamination of the measured data, is investigated.

For the verification of the proposed method's capability to identify models of existing systems based on experimental data, tests were carried out with a locally damaged steel

beam.

### Example 5.2. 5-DOF system, sweep excitation

As in example 5.1, the response of the 5-DOF system shown in figure 5.1, due to a sweep force acting at DOF 2, was numerically simulated for 4096 time instants sampled at a rate of  $\Delta t = 0.01$  s. The time series and the respective wavelet decompositions of the excitation and of the response at DOF 1 are given in figure 5.5. The system's parameters were identified utilising the wavelet coefficients at the 690 coordinate pairs listed in table 5.4.

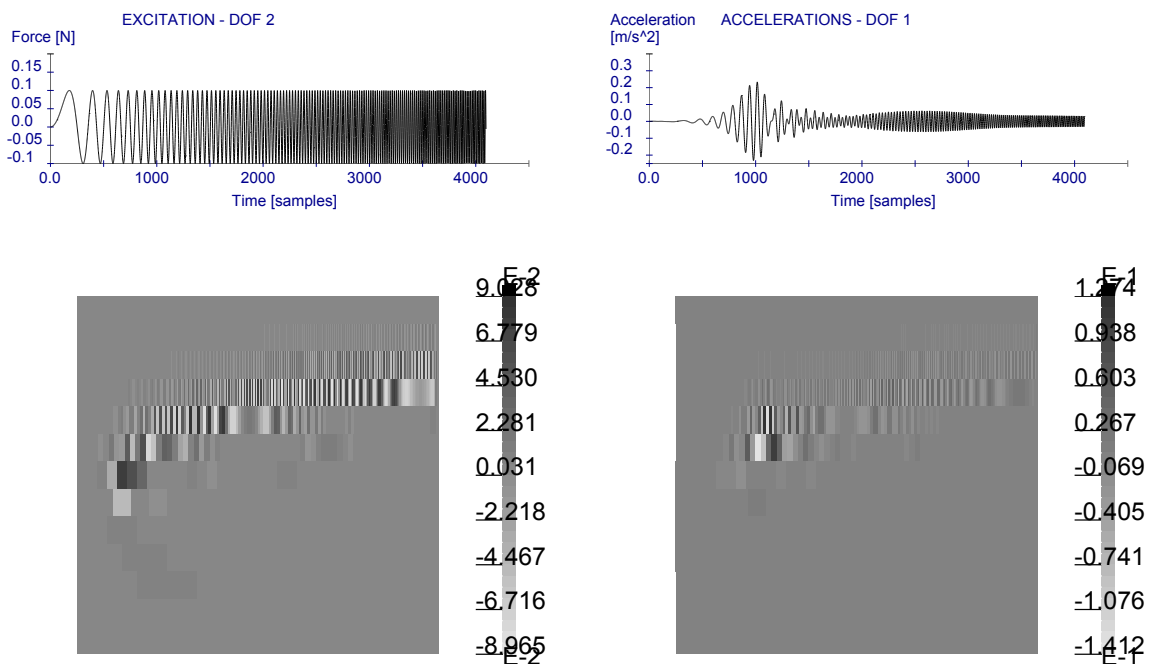


Figure 5.5: Time series (top) and wavelet coefficients (bottom) of the excitation (left) and the accelerations at DOF 1 (right), analysing wavelet  $D_3$

Two of the three solution methods presented in section 5.2.2 were applied to this example, the least squares solution approach and the optimisation technique. The results of the matrix calculus procedure are not reported. A disadvantage of this method is that a priori knowledge about the matrices structures cannot be incorporated into the identification. Not

level	begin sample	number of samples
3	100	400
4	40	190
5	20	80
6	10	20
		$\Sigma = 690$

Table 5.4: Coordinates of wavelet coefficients selected for the identification

*only is the number of unknowns larger than necessary, but also considerable defects can occur in the off-diagonal terms that should be zero.*

*In a first step, all selected coefficients were included into the system of equations to be solved. The respective results are summarised in table 5.5. The identified parameters are very similar for both the least squares method and the optimisation. A decrease in accuracy can be observed with increasing noise contamination of the simulated data. However, with respect to the level of noise contamination, the quality of the results can be considered as comparatively close to the true values.*

*In a second attempt, the wavelet coefficients at 690 coordinates were selected for each system of equations according to the scheme in figure 5.6. By moving a 590 samples wide window along the selected coefficients vector, 100 systems of equations and resulting parameter sets were obtained. Figure 5.7 illustrates the identified results for the parameters  $k_3$  and  $c_3$ . The respective diagrams for all parameters are collected in appendix D.2.*

*Figures D.5, D.6 and tables D.1, D.2 in appendix D.2 show that the results vary only slightly for the different systems of equations. The respective mean values are very close to the solutions summarised in table 5.5. Both solution methods applied resulted in nearly identical parameter sets.*

*In order to assess the confidence in the results obtained, a statistic investigation was carried out. The identification was repeated 300 times with different sets of random vectors for the case of a signal-to-noise ratio  $SNR = 5$ . A comparison of the mean values and*

	orig. value	least squares approach			optimisation		
		no noise	$SNR = 10$	$SNR = 5$	no noise	$SNR = 10$	$SNR = 5$
$k_1$	300.00	296.86	295.89	296.07	296.86	295.90	296.09
$k_2$	600.00	591.48	590.48	583.09	591.43	590.42	582.99
$k_3$	900.00	886.69	874.48	850.04	886.60	874.36	849.87
$k_4$	1200.00	1183.9	1173.6	1141.8	1183.8	1173.5	1141.6
$k_5$	1500.00	1481.0	1478.5	1464.8	1480.9	1478.4	1464.7
$c_1$	10.00	9.923	9.850	9.691	9.922	9.849	9.690
$c_2$	9.00	8.913	9.027	9.215	8.913	9.028	9.215
$c_3$	8.00	7.937	8.194	8.366	7.936	8.193	8.361
$c_4$	9.00	8.884	8.376	7.529	8.884	8.371	7.512
$c_5$	10.00	9.939	9.487	8.831	9.938	9.485	8.829

Table 5.5: Identified parameters obtained as solutions of systems of equations including all selected parameters

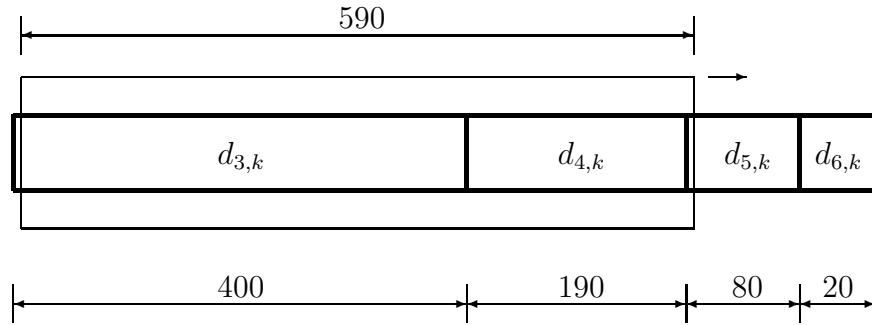


Figure 5.6: Scheme of the wavelet coefficients' selection for the identification

standard deviations of  $k_3$ , obtained from the least squares identifications with the respective results of the optimisation is given in figure 5.8. The black curves mark the identified mean values. The grey curves, that are almost identical with the black lines, refer to the standard deviations of the respective identifications. A collection of diagrams, such as shown in figure 5.8, can be found for all parameters in appendix D.2. It can be observed, that the parameters obeyed from the identifications using different noise vectors, scatter

more strongly than the solutions of one single identification. The standard deviations of the single identifications obtained as optimisation results are slightly higher than those of the least squares solutions, but still very small.

	orig. value	least squares approach			optimisation		
		$\overline{(k_i)}$	$\frac{\sigma(k_i)}{\overline{(k_i)}}$	$\frac{\sigma(\overline{k_i})}{\overline{(k_i)}}$	$\overline{(k_i)}$	$\frac{\sigma(k_i)}{\overline{(k_i)}}$	$\frac{\sigma(\overline{k_i})}{\overline{(k_i)}}$
$k_1$	300.00	299.39	0.00050562	0.011241	299.16	0.00094018	0.011663
$k_2$	600.00	578.83	0.00033073	0.010629	577.92	0.0010942	0.011084
$k_3$	900.00	864.57	0.0001925	0.010055	863.45	0.0012511	0.0087392
$k_4$	1200.00	1142.1	0.00035861	0.014296	1144.6	0.0018707	0.013605
$k_5$	1500.00	1465.5	0.00016878	0.0075187	1462.6	0.0010011	0.0070201

Table 5.6: Mean values of the identified mean stiffness parameters, mean levels of confidence of the single identifications and levels of confidence of a series of identified parameters

If the series of all identified parameter sets, i.e. using different noise vectors, are considered, one can observe that the levels of confidence in the results obtained by the two

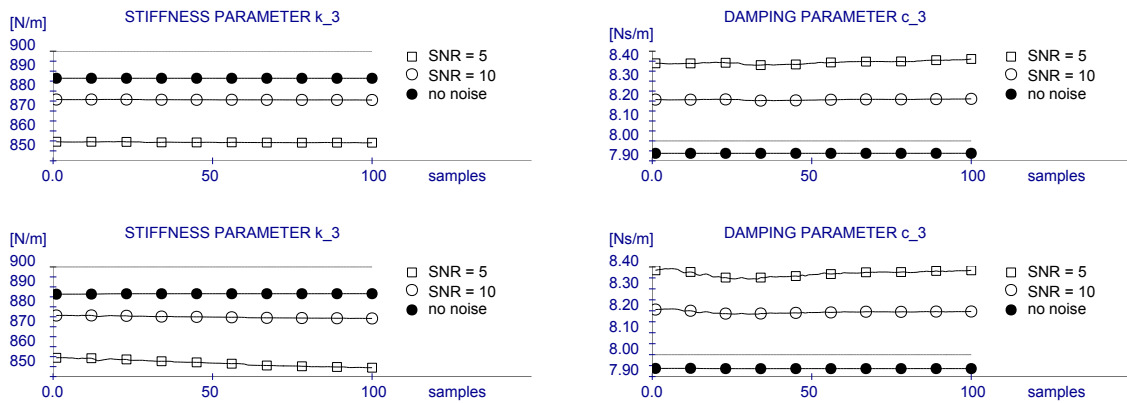


Figure 5.7: Identified parameters  $k_3$  (left) and  $c_3$  (right), 590 coefficients per system of equation, least squares solution (top) and optimised values(bottom)

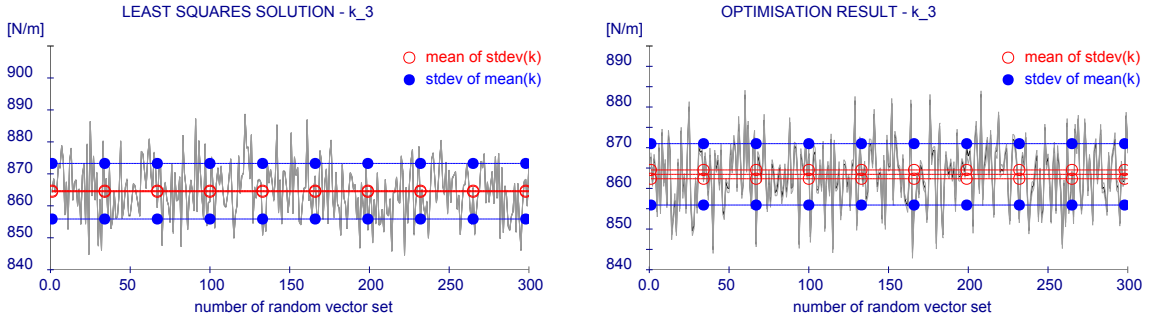


Figure 5.8: Statistical analysis of  $k_3$  stiffness parameters identified, mean values (black curves), standard deviations of the single identifications (grey curves), comparison between least squares solutions (left) and optimisation results (right)

	orig. value	least squares approach			optimisation		
		$\overline{(\bar{c}_i)}$	$\frac{\sigma(c_i)}{\overline{(\bar{c}_i)}}$	$\frac{\sigma(\bar{c}_i)}{\overline{(\bar{c}_i)}}$	$\overline{(\bar{c}_i)}$	$\frac{\sigma(c_i)}{\overline{(\bar{c}_i)}}$	$\frac{\sigma(\bar{c}_i)}{\overline{(\bar{c}_i)}}$
$c_1$	10.00	9.7757	0.00035307	0.011565	9.7589	0.00048669	0.011699
$c_2$	9.00	9.0223	0.00073089	0.021792	9.0200	0.0017958	0.022537
$c_3$	8.00	7.7554	0.0013243	0.039384	7.7492	0.0017341	0.038581
$c_4$	9.00	8.1401	0.0032149	0.090316	8.1148	0.0056418	0.090012
$c_5$	10.00	9.5352	0.00060757	0.052998	9.5593	0.0023767	0.052553

Table 5.7: Mean values of the identified mean damping parameters, mean levels of confidence of the single identifications and levels of confidence of a series of identified parameters

methods employed are approximately identical. It has to be noted that the results are influenced by the choice of the weighting coefficients  $u_m$ . An indicator for inappropriate weighting is e.g. if the curves in diagrams such as in figure 5.7 show strong irregularities at positions where wavelet coefficients at another scale enter into the system of equations.

### Example 5.3. 5-DOF system, base excitation

This example is focused on the detection of damage occurrence during an observation

interval. A horizontal random base acceleration was applied to the 5-DOF system that is illustrated in figure 5.1. The excitation and the response at the structure's top are given in figure 5.9. Damage was simulated as an abrupt 10 % drop of the stiffness parameter  $k_4$  in conjunction with an increase of the damping parameter  $c_4$  by 10 %.

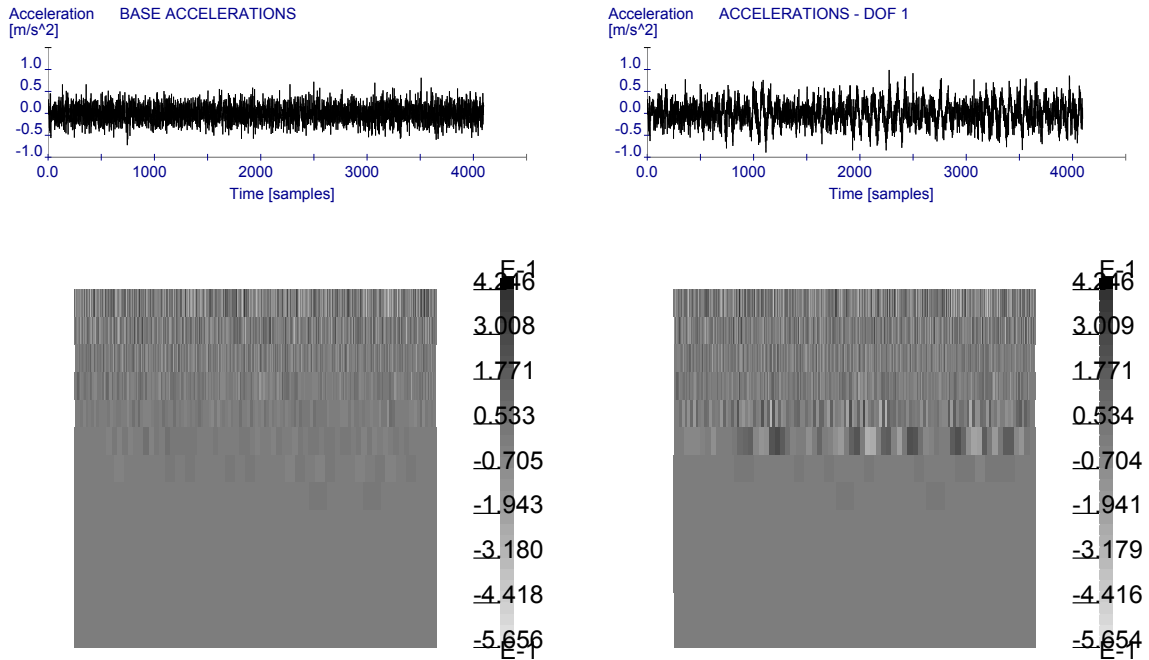


Figure 5.9: Time series (top) and wavelet coefficients (bottom) of the base accelerations (left) and the accelerations at DOF 1 (right), analysing wavelet  $D_3$

It was decided to include the wavelet coefficients at the first six decomposition levels into the analyses. Consequently, the resolution in time was determined by the resolution at the coarsest level, i.e. at level 6. Accordingly, 50 sets of wavelet coefficients at coordinates on a dyadic grid, as shown in figure 5.10, were formed for the identification.

The identified parameters  $k_4$  and  $c_4$  are shown in figure 5.11 for both the situation of non-noisy data and of a noise corruption with an  $SNR = 50$ . For stronger noise contamination levels, the abrupt parameter changes could not clearly be deduced from the diagrams. Slightly better results were obtained for an SDOF system, where a 5 % change in both stiffness and damping could still be detected from data with a signal-to-noise ratio

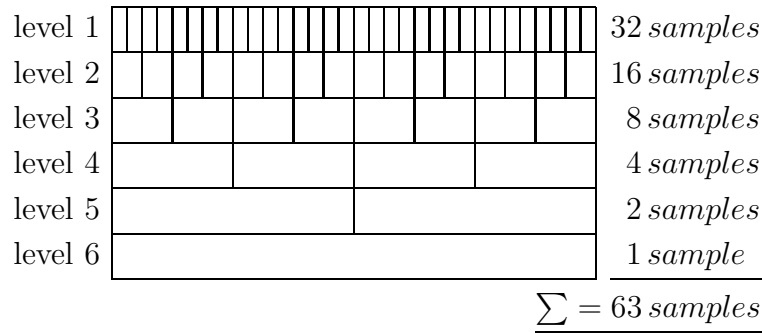


Figure 5.10: Scheme of the wavelet coefficients' selection for the identification of 20. The results presented were calculated by means of the least squares approach. It was observed that the parameters obtained from an optimisation varied too strong for a clear identification of the parameter's changes.

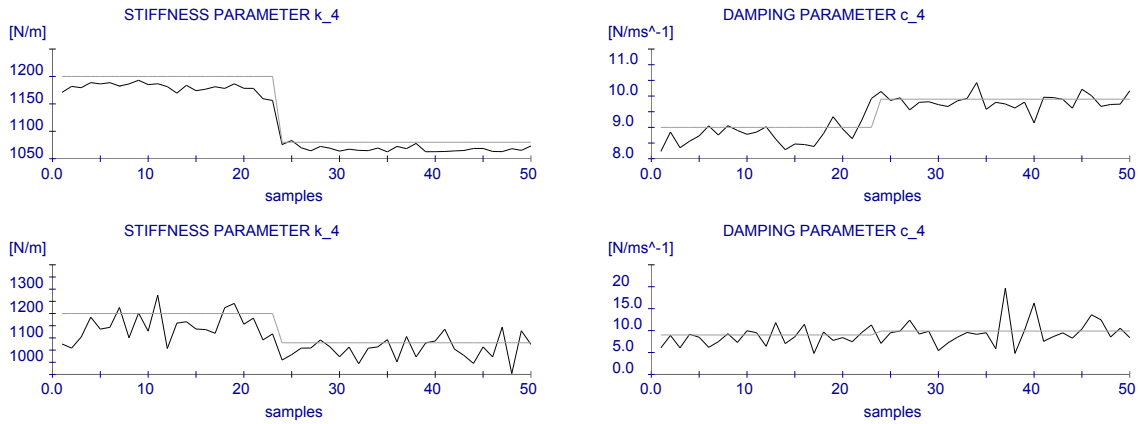


Figure 5.11: Parameters  $k_4$  (left) and  $c_4$  (right), identified using non-noisy data (top) and noise contaminated data with  $SNR = 50$  (bottom), grey lines mark the original values

**Example 5.4. Simply supported beam, impulse load**

For the system in examples 5.2 and 5.3, complete information about both accelerations and excitations at all degrees of freedom was assumed. However, the structural response can be measured only at a limited number of points in a test. Usually, sensors that measure translational accelerations are used. As an example for an application to a typical structural member, a free vibration test of a simply supported beam, as shown in figure



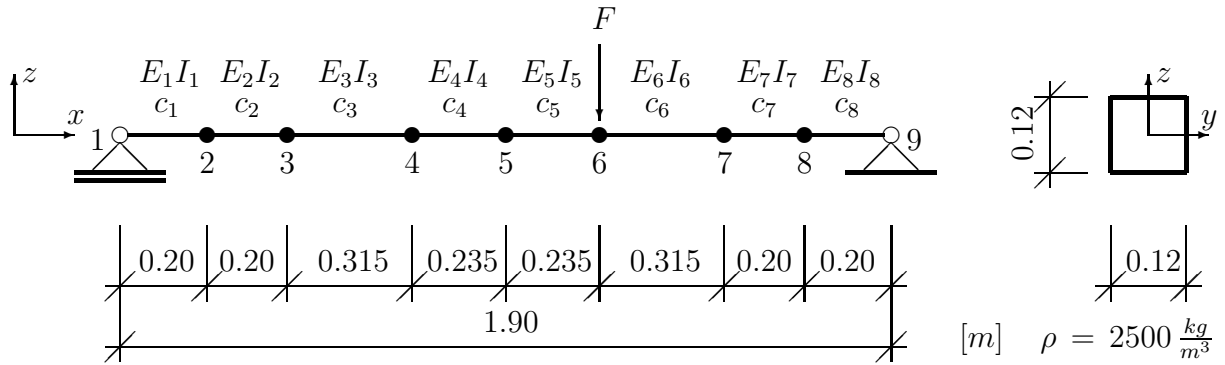


Figure 5.12: Simply supported beam, structural system and cross section

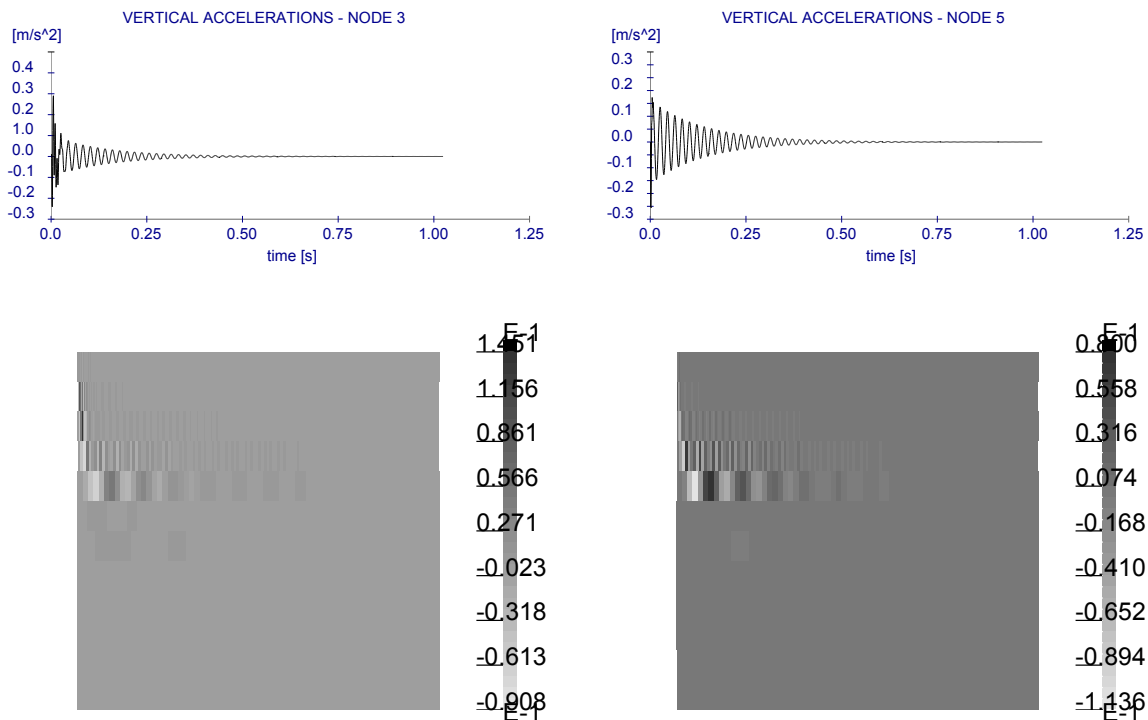


Figure 5.13: Time series (top) and wavelet coefficients (bottom) of the accelerations at DOF 3 (left) and the accelerations at DOF 5 (right), undamaged structure, analysing wavelet  $D3$

5.12, was simulated numerically. A vertical impulse load was applied at node 6.

The vertical accelerations at nodes 3, 5 and their wavelet decompositions with respect to the wavelet  $D3$  are given in figure 5.13.

Since the measured response data refers to a reduced model, a direct solution method cannot be applied for the identification of the elements' stiffness and damping parameters. Therefore, only the optimisation routine was used in this case. In each optimisation step, the complete system matrices were created, based on a selected set of parameters. Then the system matrices were reduced to the dimension of the measured degrees of freedom utilising the procedure for an improved reduced system model (IRS), developed in [50].

Successive damage, occurring between subsequent tests, was simulated by reducing element stiffness values and increasing the respective damping parameters simultaneously. Four stages of simulated damage were considered. The identified values of the Young's moduli and material damping coefficients are summarised in table 5.8. These results were obtained based on data that was not contaminated by noise.

The values in tables 5.8 and 5.9 suggest a comparatively good performance of the proposed method. However, it became evident that the algorithm behaved very sensitively with respect to noise in the data.

state	$E_1$ [ $\frac{N}{m^2}$ ]	$E_2$ [ $\frac{N}{m^2}$ ]	$E_3$ [ $\frac{N}{m^2}$ ]	$E_4$ [ $\frac{N}{m^2}$ ]	$E_5$ [ $\frac{N}{m^2}$ ]	$E_6$ [ $\frac{N}{m^2}$ ]	$E_7$ [ $\frac{N}{m^2}$ ]	$E_8$ [ $\frac{N}{m^2}$ ]
0	2.984e10 (3.0e10)	2.982e10 (3.0e10)	2.982e10 (3.0e10)	2.981e10 (3.0e10)	2.981e10 (3.0e10)	2.981e10 (3.0e10)	2.982e10 (3.0e10)	2.984e10 (3.0e10)
1	2.989e10 (3.0e10)	2.955e10 (3.0e10)	2.973e10 (3.0e10)	2.665e10 (2.7e10)	2.675e10 (2.7e10)	2.962e10 (3.0e10)	2.979e10 (3.0e10)	2.942e10 (3.0e10)
2	2.963e10 (3.0e10)	2.968e10 (3.0e10)	2.670e10 (2.7e10)	2.670e10 (2.7e10)	2.670e10 (2.7e10)	2.670e10 (2.7e10)	2.966e10 (3.0e10)	2.966e10 (3.0e10)
3	2.970e10 (3.0e10)	2.670e10 (2.7e10)	2.672e10 (2.7e10)	2.672e10 (2.7e10)	2.672e10 (2.7e10)	2.672e10 (2.7e10)	2.671e10 (2.7e10)	2.966e10 (3.0e10)

Table 5.8: Identified Young's moduli (original values in brackets)

### Example 5.5. Damage localisation, experimental verification

Similar tests to that numerically simulated in example 5.5 were performed for a steel

state	$c_1$ [ $\frac{Ns}{m^2}$ ]	$c_2$ [ $\frac{Ns}{m^2}$ ]	$c_3$ [ $\frac{Ns}{m^2}$ ]	$c_4$ [ $\frac{Ns}{m^2}$ ]	$c_5$ [ $\frac{Ns}{m^2}$ ]	$c_6$ [ $\frac{Ns}{m^2}$ ]	$c_7$ [ $\frac{Ns}{m^2}$ ]	$c_8$ [ $\frac{Ns}{m^2}$ ]
0	4.000e6 (4.0e6)	4.000e6 (4.0e6)	3.999e6 (4.0e6)	4.000e6 (4.0e6)	4.000e6 (4.0e6)	3.999e6 (4.0e6)	4.000e6 (4.0e6)	4.000e6 (4.0e6)
1	3.973e6 (4.0e6)	3.821e6 (4.0e6)	3.964e6 (4.0e6)	4.281e6 (4.4e6)	4.291e6 (4.4e6)	3.960e6 (4.0e6)	3.825e6 (4.0e6)	3.974e6 (4.0e6)
2	3.808e6 (4.0e6)	3.851e6 (4.0e6)	4.194e6 (4.4e6)	4.225e6 (4.4e6)	4.225e6 (4.4e6)	4.194e6 (4.4e6)	3.852e6 (4.0e6)	3.808e6 (4.0e6)
3	3.756e6 (4.0e6)	4.067e6 (4.4e6)	4.126e6 (4.4e6)	4.131e6 (4.4e6)	4.127e6 (4.4e6)	4.121e6 (4.4e6)	4.070e6 (4.4e6)	3.757e6 (4.0e6)

Table 5.9: Identified damping coefficients (original values in brackets)

beam. Figures 5.14 and 5.15 show the test set-up. Local structural damage was simulated by cutting the beam's lower flange five times at two positions, respectively (figure 5.15).

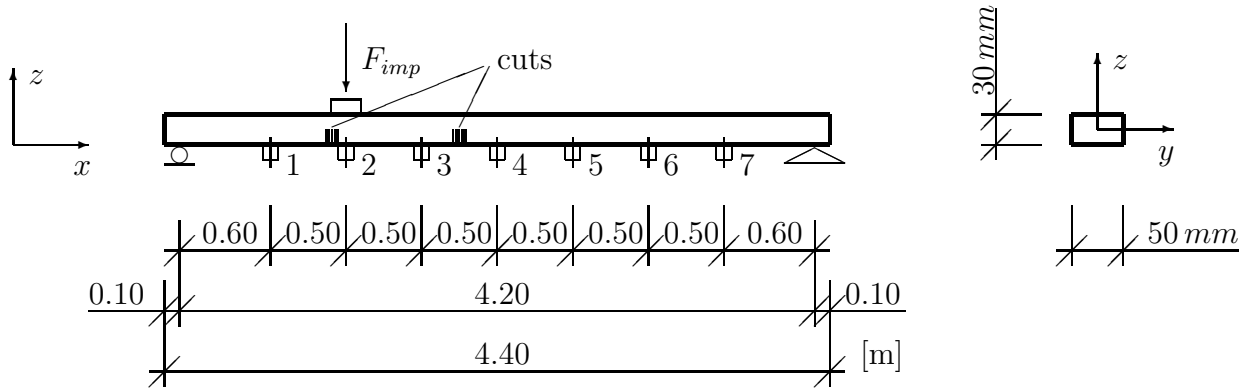


Figure 5.14: Tested steel beam – test set-up

The beam was excited to free vibration by a vertical hammer impact. The response was measured in the vertical direction by means of accelerometers at seven positions. Simultaneously, the impulse force generated by the hammer was recorded. Examples for the time series and wavelet decompositions of the exciting force and of the respective response are given in figures 5.16 and 5.17.

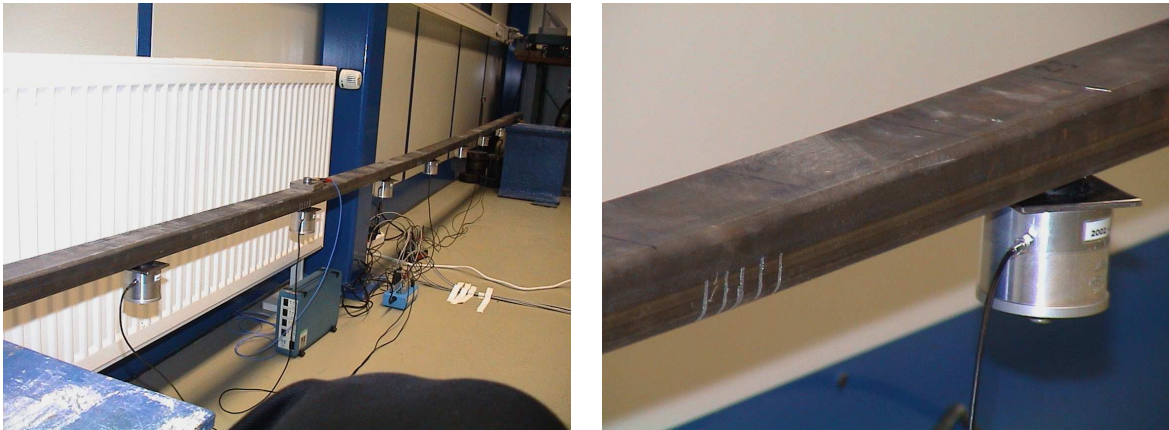


Figure 5.15: Tested steel beam – test set-up (left), cuts between accelerometers 3 and 4 (right)

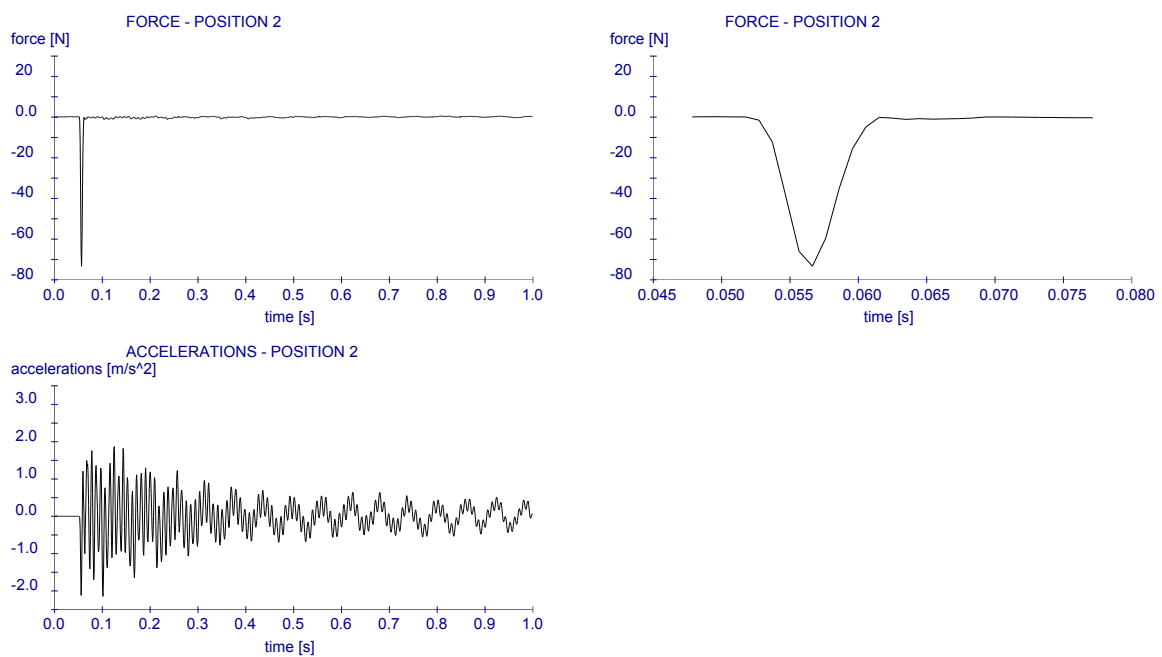


Figure 5.16: Measured time series of impulse force (top, left), detail of impulse force (top, right), measured time series of accelerations at position 2 (bottom)

*The tests were repeated ten times. From each set of measured data, one set of parameters was identified. These parameters were based on a finite element model consisting of ten beam elements and additional masses at the nodes that were located at the accelerometers' positions.*

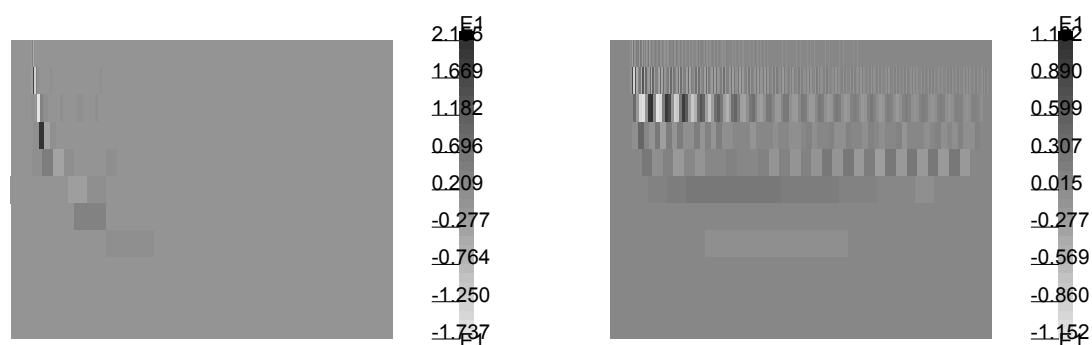


Figure 5.17: Wavelet decompositions of the measured impulse force (left) and of the measured accelerations at position 2 (right), analysing wavelet - *DaubechiesD3*

*As described in example 5.5, the optimisation scheme was employed for the identification of the elements' stiffness and damping. It was assumed, that the system parameters were constant along the length of each element. The stiffness was estimated by optimising for the Young's modulus rather than geometry of the elements' cross sections. Similarly, viscous damping parameters were considered as unknowns that determined the elements' damping properties. The mass was considered as known. All parameters were identified based on wavelet coefficients at scales 2, 3, 4 and 5.*

*The identified parameters, as obtained from all ten data sets, are illustrated in figure 5.18. The grey lines in the plot of the Young's moduli mark the lower and upper bounds and the start values for the optimisation, respectively. One can clearly detect significant stiffness reductions for the elements that correspond to the damage positions in the test specimen. For the elements adjacent to the damaged zones, stiffness values were obtained that are far beyond realistic parameters for a steel beam. However, this effect is due to the simplified modelling of local damage by homogeneous finite elements of considerably larger extension than the size of the damaged zone.*

*With respect to the identified damping parameters, it has to be intimated that the estimated results barely differed from the initial values, regardless which values were chosen at the beginning of the optimisation. This observation indicates a negligible influence of the*

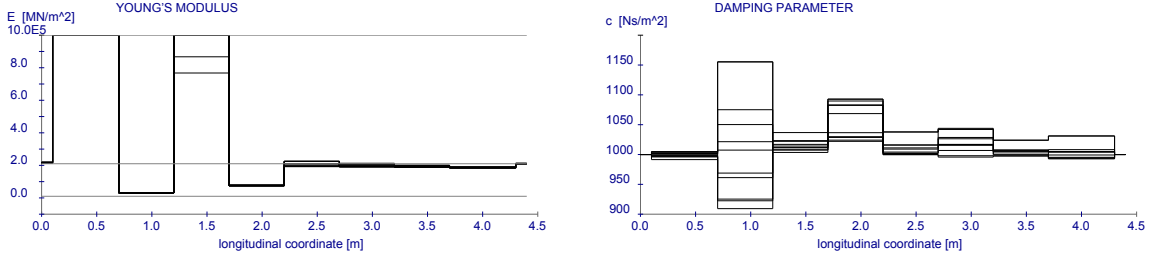


Figure 5.18: Identified sets of Young's moduli (left) and damping parameters (right) with respect to the beam's longitudinal axis

*damping if viscous damping that is proportional to the element stiffness is assumed. The very weak damping was already obvious during the tests.*

*In table 5.10 the average natural frequencies of the estimated models' first five bending modes are compared with those identified from the measured data. The average MAC values (e.g. [26])*

$$MAC_i(\text{ident}, \text{model}) = \frac{\left| \sum_{j=1}^n (\phi_{i,\text{model}})_j (\phi_{i,\text{ident}})_j^* \right|^2}{\left( \sum_{j=1}^n (\phi_{i,\text{model}})_j (\phi_{i,\text{model}})_j^* \right) \left( \sum_{j=1}^n (\phi_{i,\text{ident}})_j (\phi_{i,\text{ident}})_j^* \right)}, \quad (5.29)$$

*for the corresponding mode shapes are summarised in table 5.11. The identified natural frequencies and mode shapes were determined by means of the Ibrahim time domain method (ITD) [33].*

*It can be deduced from this example, that the proposed method of wavelet-based direct parameter estimation is an appropriate tool for the identification of a finite element model that represents a tested structural element. Local damage could be identified, even based on a very simplified model. The modal parameters of the identified model agree relatively good with those of the tested system.*

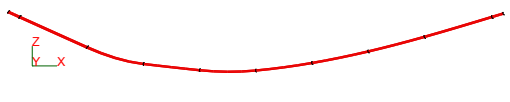


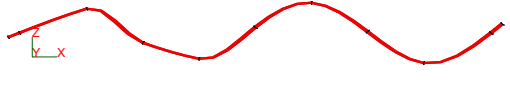

$f_{n,model} [Hz]$	$f_{n,meas} [Hz]$	error [%]	mode shape of the model
3.6565	3.8274	4.465	
14.156	16.483	14.118	
32.171	35.453	9.257	
71.209	72.207	1.382	
104.60	106.35	1.646	

Table 5.10: Average natural frequencies of the estimated models and identified from measured data

0.96441	0.00013946	1.4692e-05	5.0824e-06	8.6054e-05
9.0692e-06	0.93744	0.00075311	4.6988e-05	2.3042e-06
4.045e-07	0.00047522	0.91086	7.1701e-05	3.4854e-05
1.0774e-07	5.9969e-06	7.8325e-06	0.88111	0.00019247
3.3422e-07	4.1914e-06	2.6346e-05	0.001211	0.97829

Table 5.11: Average MAC values

# Chapter 6

## Assessment of Progressive Damage

Damage detection and structural health monitoring have become fields of increasing interest to civil engineers in recent years. Among numerous methods, approaches that are based on the observation of the dynamic behaviour of a structure were developed (e.g. [9], [18], [42], [36], [11]). Many of these techniques use identified modal parameters in some way for the detection and localisation of structural damage.

As pointed out in section 2.3, techniques that utilise wavelet analysis in context with damage detection were suggested by several researchers. Inspired by one of these proposals, investigations about the characterisation of a structural element's damage state, based on the energy components of free response signal's wavelet decompositions, were carried out.

### 6.1 Signal Energy-Based Damage Assessment

The assessment of a structure's damage state, by means of free vibration response signal's energy, is suggested in [63] (see section 2.3). It is proposed to calculate a complete wavelet packet decomposition of response signals that were obtained from free vibration tests of the structure at different stages of damage. The excitation is assumed to be identical in all tests. The damage indices developed in [63] are based on the comparison of the energy



components of wavelet packet decompositions of response signals, measured at certain stages of damage, with a set of reference energy components. The degree of the sum of these absolute differences, or their squares, are interpreted as a measure for structural damage. The indices presented in [63] do not consider whether the respective differences of energy components are positive or negative. Furthermore, these damage indices were directly calculated from measured response data. This means an exact repetition of the test, i.e. the excitation, is required.

The two latter remarks gave reason to investigate how the system's response energy components change with progressive structural damage and if the restriction of ensuring an exactly repeated excitation for each test can be avoided. With respect to continuous structural health monitoring, particularly the dependence on performing identical tests has to be considered as being difficult in practice. Accordingly, an appropriate normalisation of the response data would be beneficial.

If the excitation of the system is known, an obvious normalisation of the response is that with respect to the exciting force. This results in the impulse response function or its wavelet decomposition. Another possibility is to normalise the response at one location in the structure to that, measured at another position, which leads to a transmissibility function. The consideration of transmissibility functions and their wavelet decompositions seems to be rather suitable in the context of continuous structural health monitoring.

The investigations presented in this chapter comprised the following steps:

1. Calculation of the wavelet coefficients of the impulse response or the transmissibility functions by means of data obtained from dynamic tests with a known impulse excitation according to [49].
2. Selection of wavelet coefficients that significantly contribute to the characteristics of the respective function (definition of scales and number of wavelet coefficients at these scales).

3. Calculation of the energy components  $E_{i,j}$  for the selected wavelet coefficients

$$E_{i,j} = d_{i,j}^2 2^i, \quad (6.1)$$

where  $i$  is the index of the respective decomposition level.

4. Calculation of the total energies at the respective scales  $E_i$  and of all considered components  $tot.E$ :

$$E_i = \sum_j E_{i,j}, \quad (6.2)$$

$$tot.E = \sum_i E_i = \sum_i \sum_j E_{i,j}. \quad (6.3)$$

5. Comparison of the respective energy components and their sums at different stages of structural damage.

## 6.2 Description of the Tests

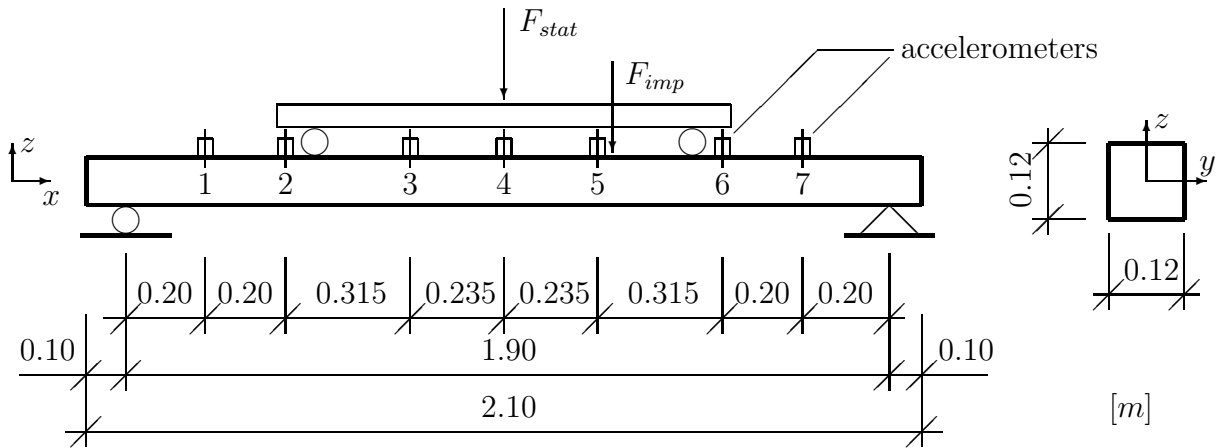


Figure 6.1: Test set-up, simply supported reinforced concrete beam

The data that was analysed, as described in the previous section, was collected in tests of a progressively damaged reinforced concrete beam. The structural damage was caused by incrementally increased static loading. The test set-up and the specimen's dimensions are illustrated in figures 6.1 and 6.2.



Figure 6.2: Test specimen in the laboratory

The tests were carried out within a series of tests on 20 identically designed reinforced concrete elements. A detailed description of this test series is given in [24] and [25].

The history of the static load increments and a description of the respective damage features are summarised in table E.1 and in figures E.1 and E.2 in appendix E.1. Dynamic tests were carried out on the unloaded structure in the virgin state and after each static load step. The system was excited to a free vibration by imposing a vertical impact force  $F_{imp}$  at position 5. Both the accelerations at seven positions and the excitation force were measured simultaneously at a sampling rate of  $0.9766\text{ ms}$ .

The collected data was analysed according to the scheme developed in section 6.1. The results of the data analysis and respective conclusions are described in the following section.

### 6.3 Assessment of the Test Results

In this section, the most significant results of the energy component analysis for the tests described in section 6.2 are summarised. The diagrams, tables and figures that are given

here are a selection obtained from the experimental data for specific measurement points. There were several measurement locations for which similar results were obtained. Nevertheless, it should be noted that it was deduced from the investigation, that the sensor's location is of considerable importance with respect to structural health monitoring.

Often, the change of the system's natural frequencies is considered as an indicator of structural damage, as suggested for example in [36]. The natural frequencies of the first mode identified for the investigated reinforced concrete beam are shown in figure 6.3.

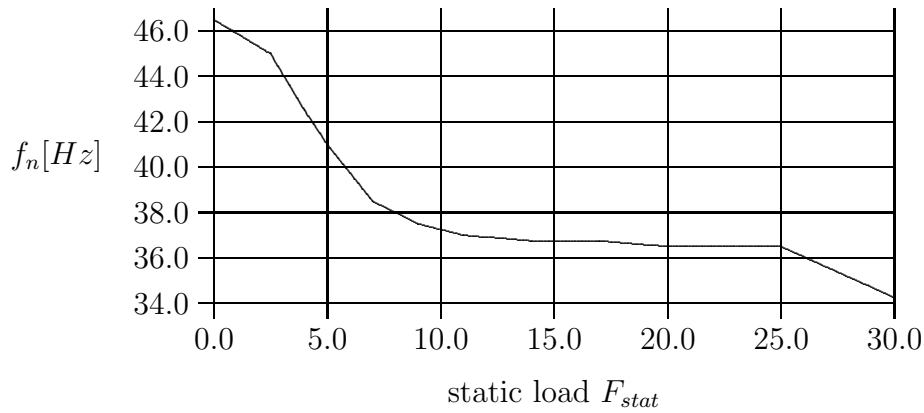


Figure 6.3: Identified first natural frequencies of the beam

For the investigations of the energy components according to the descriptions in section 6.1, the five finest scales of the impulse response and transmissibility functions, respectively, were taken into account. The coordinates considered are collected in table 6.1.

Decomposition level:	1	2	3	4	5
sample numbers:	1 ... 40	1 ... 40	1 ... 40	1 ... 16	1 ... 6

Table 6.1: Coordinates of the considered wavelet coefficients' energy components

At the selected coordinates, the energy components  $E_{i,j}$  were determined according to equation 6.1. The sums of these energy components at each considered scale and their total sum were calculated. Figures 6.4 and 6.5 show examples for the developments of the energy component sums with progressive damage.

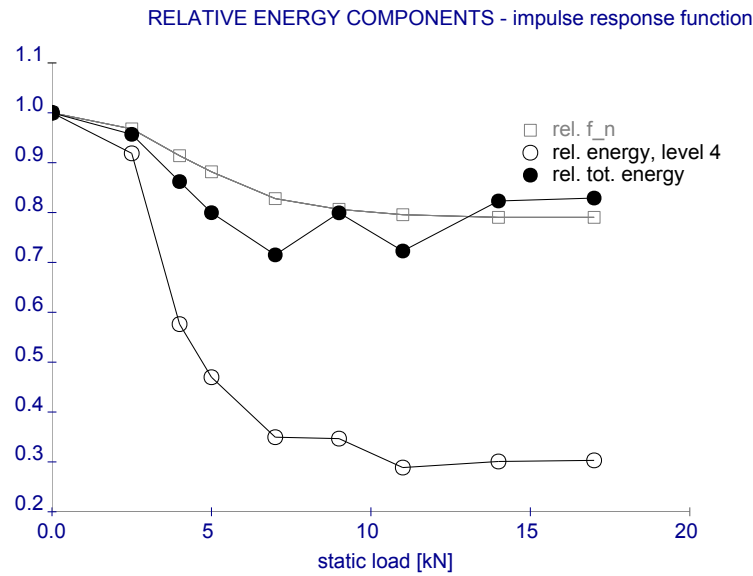


Figure 6.4: Relative energy components, impulse response function, channel 2

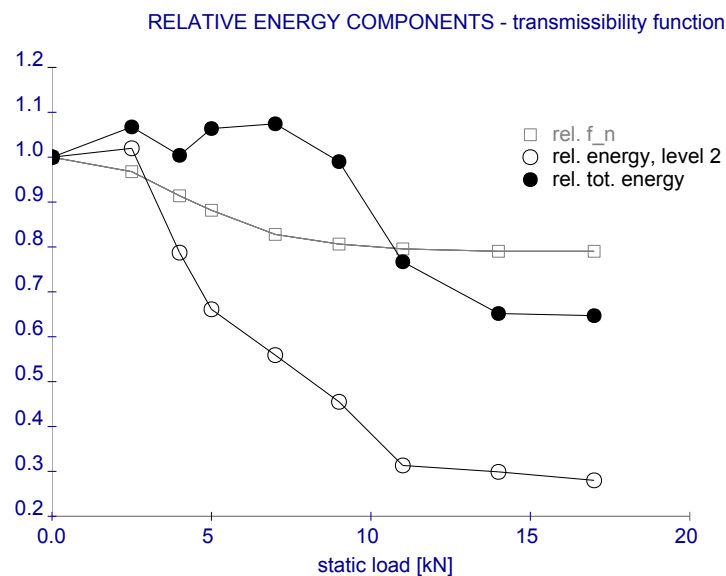


Figure 6.5: Relative energy components, transmissibility function channel 5 → channel 2

From the diagrams in figures 6.4 and 6.5, it can be deduced that the application of the total energy component sums might not necessarily provide clear information concerning the assessment of structural damage. However, the curves that were obtained for the energy component sums at selected levels suggest a considerable decrease with progressing damage. The respective degradation is considerably more significant than that of the first

natural frequency.

The energy decrease at specific scales is caused by increasing damping due to cracks in the beam and by a reduction of the natural frequency, which results in a shift of the signal energy components to coarser scales. These conclusions can be drawn from figures 6.6 and 6.7 that give an overview about the energy component distributions at the selected scales with respect to the state of damage.

By studying the diagrams in figures 6.6 and 6.7, it can be observed that the pattern of the energy components' distributions changes with progressive damage. The energy at specific levels is increasingly concentrated in fewer components. This feature becomes more obvious if the relative energy components are considered (figures 6.8 and 6.9). These values were obtained by dividing the individual energy components by the sum of the components at the respective scale. Both the 4th level's energy components of the impulse response function of DOF 2 with respect to an excitation at DOF 5 and the 2nd level's energy components of the transmissibility function of DOF 2 with reference to DOF 5 show a high energy concentration in very few components after the cracks became wider than  $0.05 \dots 0.1 \text{ mm}$ .

The observations described in this section suggest, that wavelet-based energy components of normalised response signals can be utilised as an indicator of structural damage detection, provided that the monitoring set-up is appropriately calibrated. Calibration means in this context the choice of appropriate sensor locations and the selection of energy component coordinates. Nevertheless, further analyses of data collected from tests of progressively damaged structures is required in order to draw more general conclusions. In particular, the research should be concentrated on the investigation of correlations between the degree of damage and both the energy component degradation and patterns of the wavelet-based energy components.

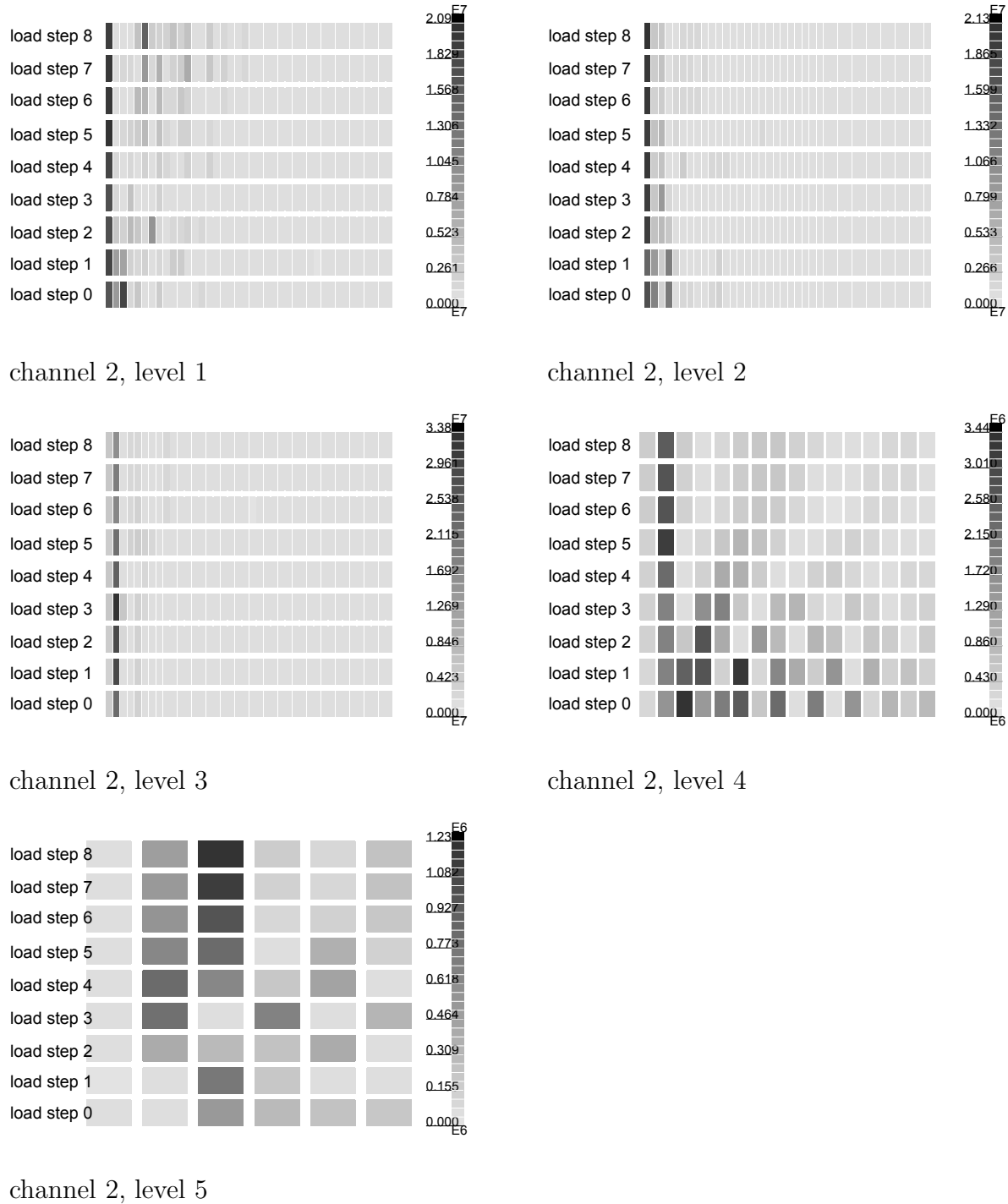
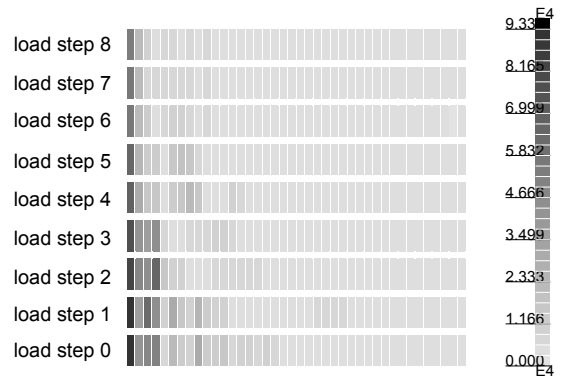
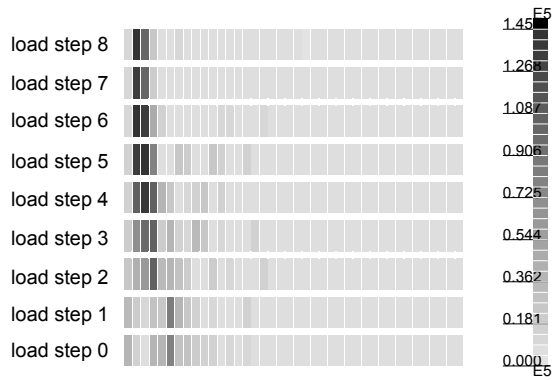
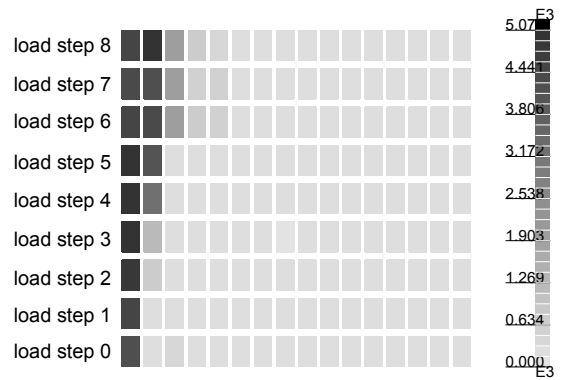
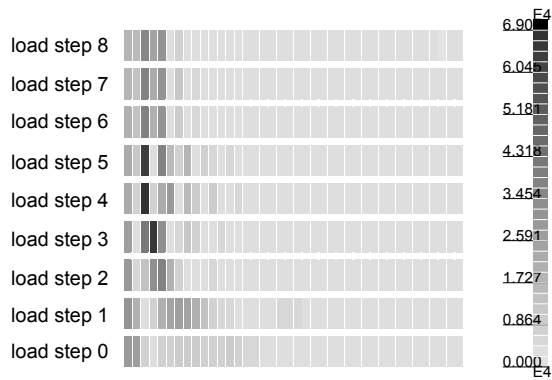


Figure 6.6: Absolute energy components, impulse response function, excitation DOF 5, response DOF 2



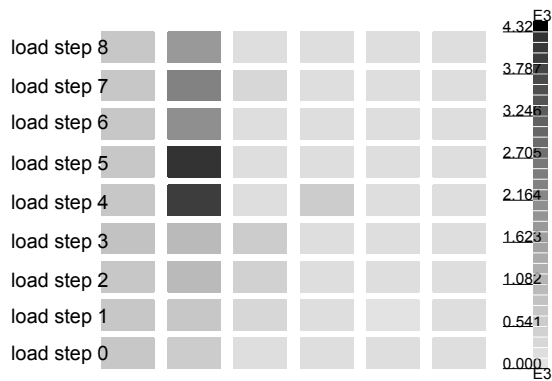
channel 2, level 1

channel 2, level 2



channel 2, level 3

channel 2, level 4



channel 2, level 5

Figure 6.7: Absolute energy components, transmissibility function, reference DOF 5, response DOF 2



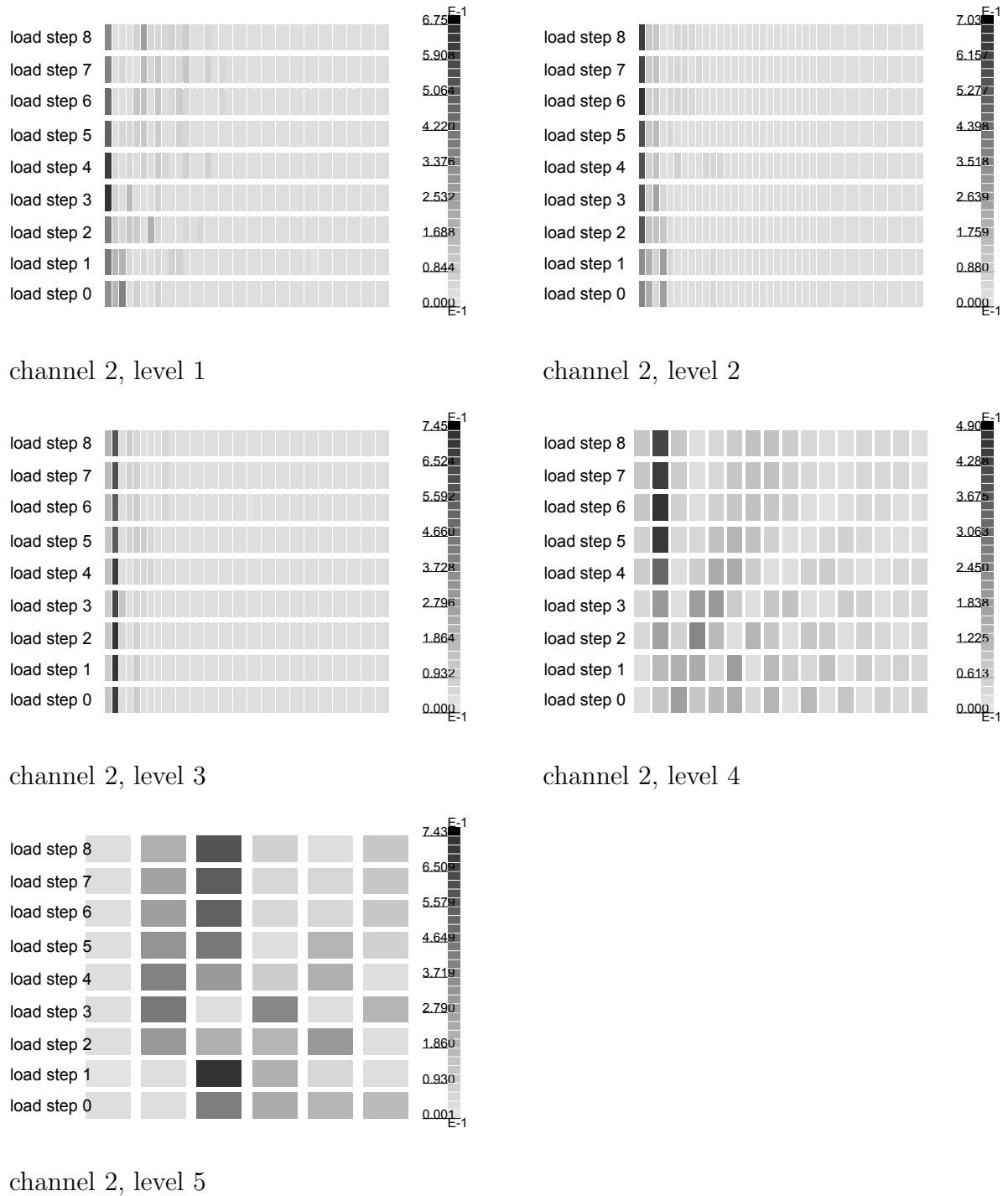
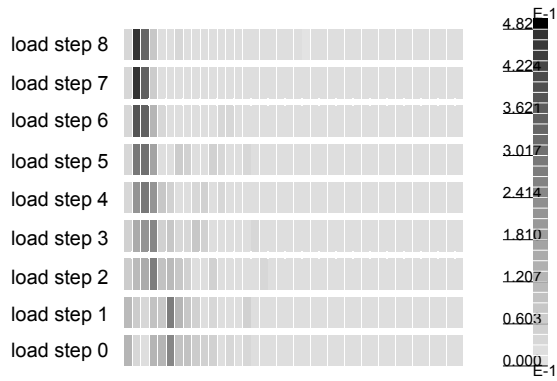
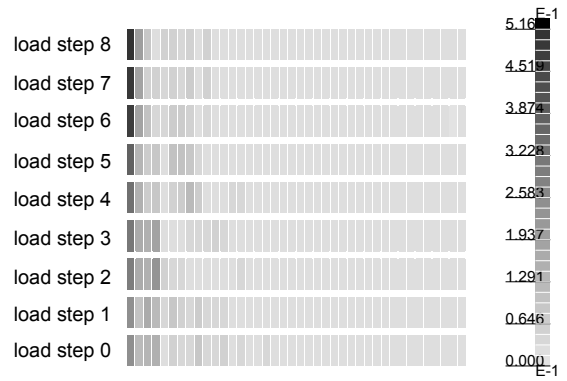


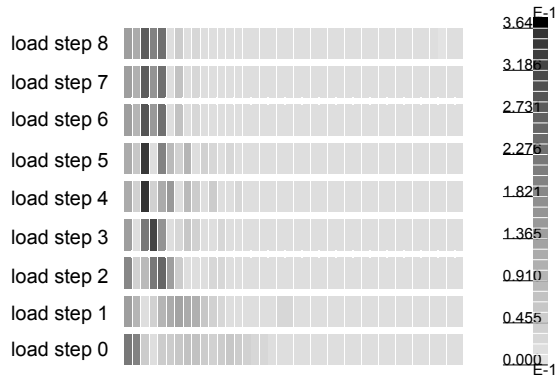
Figure 6.8: Relative energy components, impulse response function, excitation DOF 5, response DOF 2



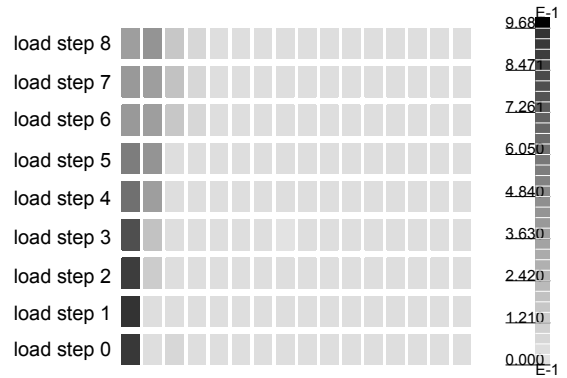
channel 2, level 1



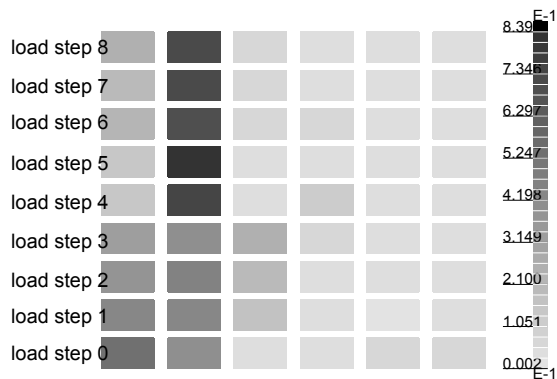
channel 2, level 2



channel 2, level 3



channel 2, level 4



channel 2, level 5

Figure 6.9: Relative energy components, transmissibility function, reference DOF 5, response DOF 2

## Conclusions

The research described in this dissertation attempted to develop a wavelet-based method that allows the direct identification of a system's parameters from data generated in dynamic tests of a structure. Of specific interest was the application of fast algorithms and the need for an algorithm that requires the response data solely in the form of accelerations. It was intended that the method is applicable to multi-degree-of-freedom systems and to existing structural elements and structures that are typically found in civil engineering.

Approaches were derived that are based on representations of the equation of motion in both continuous and discrete time-scale domain. Special emphasis was put on an algorithm that uses the orthogonal wavelet transformation and the concept of connection coefficients. It was found in numerical simulations that the parameters of linear time-invariant systems can be identified with a relatively high accuracy, even if the simulated data was contaminated by noise. In the examples, the stiffness terms identified agreed better with the original values than the viscous damping parameters. Difficulties became apparent when the occurrence of relatively weak parameter changes during the test (abrupt damage) should have been identified from noise-corrupted data. The correct identification of a simply supported beam's parameters based on simulated and noise-contaminated translational accelerations due to an impulse force also occurred to be problematic.

The applicability of the proposed method to experimental data was demonstrated for laboratory tests of a steel beam. It was possible to identify a finite element model of this

system that reflected the damage of the structure at two locations comparatively well.

A possible explanation for the relatively good performance of the proposed method is that the time-scale representation of a structure's dynamic response gives a more detailed description of the system's characteristic properties than the information that can be derived from either a time series or its Fourier transform.

The method's performance seems to be better in cases where the signal's energy is distributed to a larger number of time-scale coordinates. The solution of the respective system of equations then implies an averaging of more samples, which is beneficial with respect to noise-corrupted data. Regarding the detection of damage occurrence during the measurement, it should be noted that a more accurate time localisation is only obtained if fewer wavelet coefficients are taken into account. However, that consequently means that the solution is an average of very few samples and is accordingly less reliable if noise is present in the measured data.

A prerequisite for satisfactory results seems to be, that the significance of the secondary degrees of freedom, i.e. those for which no response measurements are available (e.g. rotations), is considerably smaller than that of the primary degrees of freedom. This condition has an influence on the accuracy of the reduced system, that the system of equations to be solved is based on.

All systems considered were weakly damped, as is typical for civil engineering structures. Accordingly, the damping's influence on the system's dynamic behaviour is less significant than that of the stiffness parameters. Therefore the identification of realistic damping coefficients becomes very problematic as soon as the measured data is erroneous and contaminated by noise.

The proposed parameter estimation method is based on simultaneous measurements of both the excitation and the structural response during a dynamic test. Consequently, it cannot be directly applied to situations where only information about the structural response is available. The method's performance depends on the choice of the degrees of freedom, for which the structural response can be measured, on the selection of the

wavelet coefficients to be taken into account and on their respective weighting in the analysis.

The second focus of this dissertation was on investigations regarding progressive damage of a reinforced concrete beam and the derivation of a sensitive, wavelet-based first level damage detection indicator. The analysis of experimental data, as obtained from free vibration laboratory tests, has shown a relationship between the structure's damage condition and the wavelet-based signal energy components of impulse response and transmissibility functions, respectively.

It was found, that an appropriate selection of observed energy components can result in an indicator that is considerably more sensitive than the structure's first natural frequency.

These promising results are probably caused by two phenomena:

1. Compared to an undamaged condition, a higher dissipation of initial kinetic energy takes place due to friction between reinforcement and concrete and within the cracked zones of the concrete.
2. A decrease of the structure's natural frequencies results in a shift of free vibration signal's energy contributions to coarser scales.

These observations were made by assessing data that was obtained from laboratory tests on a single specimen. In order to draw more general conclusions, data from both other in-situ and laboratory tests should be analysed. In this context, the calibration (i.e. the selection of the energy components' coordinates) has to be investigated in more detail.

Generally, one can conclude that the described investigations led to promising and encouraging results. Future research should include the application of wavelet analysis to system identification methods that are solely based on structural response measurements (output-only methods). Furthermore a sensitivity investigation concerning the choice of the analysing wavelet could be of interest. It is recommended to continue the investigations with respect to the proposed first level damage indicator using data from in-situ tests and from long term structural health monitoring.

# Bibliography

- [1] A. Al-Khalidy, M. Noori, Z. Hou, S. Yamamoto, A. Masuda, and A. Sone. Health monitoring systems of linear structures using wavelet analysis. In F.-K. Chang, editor, *Structural Health Monitoring – Current Status and Perspectives, Proceedings of the International Workshop on Structural Health Monitoring*, pages 164–175, Stanford University, Stanford, CA, USA, 18-20 September 1997. Technomic, Lancaster, Basel.
- [2] R. J. Alonso, M. Noori, L. D. Duval, A. Masuda, and Z. Hou. Damage detection for a nonlinear SDOF system under deterministic and random load. In *Proceedings of the 8th International Conference on Structural Safety and Reliability (ICOSSAR 2001) – CD-ROM*, Newport Beach, CA, USA, 17-21 June 2001. A.A. Balkema, Rotterdam.
- [3] K. F. Alvin. *Second-Order Structural Identification via State Space-Based System Realizations*. PhD thesis, Center for Aerospace Structures, University of Colorado, Boulder, CO, USA, April 1993. Report No. CU-CSSC-93-09.
- [4] P. Argoul, H. P. Yin, and B. Guillermin. Use of the wavelet transform for the processing of mechanical data. In *Proceedings of ISMA23*, volume I, pages 329–337, Leuven, Belgium, September 1998. Katholieke Universiteit Leuven - Departement Werktuigkunde.
- [5] V. Bayer, C. Bucher, M. Ebert, E. Herz, O. Huth, G. Purkert, J. Riedel, D. Roos, Y. Schorling, and V. Zabel. *SLang – the Structural Language*. Bauhaus-Universität, Inst. of Struct. Mech., Weimar, 2002.

- [6] G. Beylkin and B. Torr sani. Implementation of operators via filter banks, autocorrelation shell and hardy wavelets. In *PAM Report 185 – Applied and Computational Harmonic Analysis*, volume 3, pages 164–185, 1996.
- [7] P. Bodin and B. Wahlberg. A frequency response estimation method based on smoothing and thresholding. *International Journal of Adaptive Control and Signal Processing*, 12(5):407–416, August 1998.
- [8] P. Bodin and B. Wahlberg. A wavelet shrinkage approach for frequency response estimation. In *IFAC Symposium on System Identification (SYSID 1994)*, volume Postprint volume, pages 737–742, Copenhagen, 1998. Pergamon Press, New York.
- [9] S. W. Boebling, C. R. Farrar, M. B. Prime, and D. W. Schevitz. Damage identification and health monitoring of structural and mechanical systems from changes in their vibration characteristics: A literature review. Technical Report LA-13070-MS, Los Alamos National Laboratory, Los Alamos, 1996.
- [10] C. Boller, W. Staszewski, F.-K. Chang, J.-B. Ihn, and H. Speckmann. Smart systems for in-service crack monitoring of aircraft components. In T. Seeger and S. Klee, editors, *25 Jahre Fachgebiet Werkstoffmechanik an der TU Darmstadt, Vortr ge des Festkolloquiums am 28. 09. 2001*, volume Heft 65 of *Ver ffentlichungen des Instituts f r Stahlbau und Werkstoffmechanik der Technischen Universit t Darmstadt*, pages 184–194, Darmstadt, September 2001. Technische Universit t Darmstadt.
- [11] R. Brincker, P. Andersen, and R. Cantieni. Identification and level I damage detection of the Z24 highway bridge. *Experimental Techniques*, 25(6):51–57, 2001.
- [12] R. A. Carmona, W. L. Hwang, and B. Torr sani. Characterization of signals by the ridges of their wavelet transforms. *IEEE Transactions on Signal Processing*, 45(10):2586–2590, October 1997.
- [13] Y. T. Chan. *Wavelet Basics*. Kluwer Academic Publishers, Boston, Dordrecht, London, 1995.

- [14] C. K. Chui. *An Introduction to Wavelets*. Wavelet Analysis and its Applications. Academic Press, Boston, San Diego, New York, London, Sydney, Tokyo, Toronto, 1992.
- [15] A. Cohen, I. Daubechies, B. Jawerth, and P. Vial. Multiresolution analysis, wavelets and fast algorithms on an interval. *Comptes Rendus de l'Académie des Sciences*, 316(Séries I):417–421, 1993.
- [16] R. R. Coifman and D. L. Donoho. Translation-invariant de-noising. In A. Antoniadis and G. Oppenheim, editors, *Wavelets and Statistics*, pages 125–150, New York, 1995. Springer-Verlag.
- [17] I. Daubechies. *Ten Lectures on Wavelets*. Society for Industrial and Applied Mathematics (SIAM), Philadelphia, 1992.
- [18] G. De Roeck, M. Abdel Wahab, J. Maeck, and B. Peeters. Localisation of damage in reinforced concrete structures by dynamic system identification. In K. Meskouris, editor, *Baustatik - Baupraxis 7, Berichte der 7. Fachtagung "Baustatik- Baupraxis"*, pages 347–355, Aachen, 18-19 March 1999. A.A.Balkema/Rotterdam/Brookfield.
- [19] D. L. Donoho. De-noising by soft-thresholding. 1992.
- [20] D. L. Donoho and I. M. Johnstone. Ideal spatial adaption by wavelet shrinkage. Research report, Department of Statistics, Stanford University, Stanford, CA, U.S.A, 1993.
- [21] D. L. Donoho and I. M. Johnstone. Adapting to unknown smoothness via wavelet shrinkage. Research report, Department of Statistics, Stanford University, Stanford, CA, U.S.A, July 1994.
- [22] D. L. Donoho, I. M. Johnstone, G. Kerkyacharian, and D. Picard. Wavelet shrinkage: Asymptopia? In *AMS Annual Meeting*, January 1993.



- [23] O. Døssing. Detection and tracking of rubbing phenomena in seals and journal bearings using filter banks and wavelets applied in continuous machine health monitoring. In *Noise and Vibration Engineering, Proc. ISMA23*, volume 3, pages 1337–1344, Leuven, Belgium, September 1998. Katholieke Universiteit Leuven - Departement Werktuigkunde.
- [24] M. Ebert. *Experimentelle und numerische Untersuchung des dynamischen Verhaltens von Stahlbetontragwerken unter Berücksichtigung stochastischer Eigenschaften*. Ph.d. diss., Fakultät Bauingenieurwesen der Bauhaus-Universität Weimar, Weimar, 2002.
- [25] M. Ebert and C. Bucher. Damage effects on the dynamic properties of r/c beams - experimental and numerical investigations. In H. Grundmann and G. I. Schuëller, editors, *Structural Dynamics – EUROODYN 2002, Proceedings of the 5th European Conference on Structural Dynamics*, volume II, pages 1433–1438, Munich, Germany, 2-5 September 2002. A.A. Balkema, Lisse / Abingdon / Exton (PA) / Tokyo.
- [26] D. J. Ewins. *Modal Testing: Theory, Practice and Application*. Engineering Dynamics Series. Research Studies Press Ltd., Baldock, Hertfordshire, England, second edition, 2000.
- [27] D. Gabor. Theory of communication. *Journal Inst. of Electr. Engineering*, 93(III):429–457, 1946.
- [28] R. Ghanem and F. Romes. A wavelet-based approach for the identification of linear time-varying dynamical systems. *Journal of Sound and Vibration*, 234(4):555–576, 2000.
- [29] R. Ghanem and F. Romes. A wavelet-based approach for model and parameter identification of non-linear systems. *International Journal of Non-Linear Mechanics*, 36(5):835–859, 2001.
- [30] S. Hans, E. Ibraim, S. Pernot, C. Boutin, and C.-H. Lamarque. Damping identification in multi-degree-of-freedom systems via a wavelet-logarithmic decrement

- part 1: study of a civil engineering building. *Journal of Sound and Vibration*, 235(3):375–403, 2000.
- [31] W. Heylen, S. Lammens, and P. Sas. *Modal Analysis Theory and Testing*. Katholieke Universiteit Leuven - Departement Werktuigkunde, Leuven, Belgium, 1997.
- [32] Z. Hou, M. Noori, R. S. Amand, J. Hu, A. Al-Khalidy, M. Baker, S. Yamamoto, A. Masuda, and A. Sone. Damage detection using wavelet approach and its application for on-line health monitoring. In T. Kobori, Y. Inoue, K. Seto, H. Iemura, and A. Nishitani, editors, *Proceedings of the Second World Conference on Structural Control*, volume 3, pages 2351–2358, Kyoto, Japan, 1999. John Wiley & Sons.
- [33] S. R. Ibrahim and E. C. Mikulcik. A method for the direct identification of vibration parameters from the free response. *Shock and Vibration Bulletin*, 47(4):183–198, 1977.
- [34] G. Kaiser. *A Friendly Guide to Wavelets*. Birkhäuser, Boston, Basel, Berlin, 1994.
- [35] Y. Kitada. Identification of nonlinear structural dynamic systems using wavelets. *Journal of Engineering Mechanics*, 124(10):1059–1066, October 1998.
- [36] W. B. Krätzig and S. Y. Noh. Über nichtlinear-progressive Schädigungsprozesse von Tragwerken. *Bauingenieur*, 73(6):267–273, Juni 1998.
- [37] A. Kyprianou and W. J. Staszewski. On the cross wavelet analysis of duffing oscillator. *Journal of Sound and Vibration*, 228(1):199–210, 1999.
- [38] C.-H. Lamarque, S. Pernot, and A. Cuer. Damping identification in multi-degree-of-freedom systems via a wavelet-logarithmic decrement – part 1: theory. *Journal of Sound and Vibration*, 235(3):361–374, 2000.
- [39] K. M. Liew and Q. Wang. Application of wavelet theory for crack identification in structures. *Journal of Engineering Mechanics*, 124(2):152–157, February 1998.

- [40] A. K. Louis, P. Maaß, and A. Rieder. *Wavelets: Theorie und Anwendungen*. Teubner, Stuttgart, 2nd edition, 1998.
- [41] G. Y. Luo, D. Osypiw, and M. Irle. Real-time condition monitoring by significant and natural frequencies analysis of vibration signal with wavelet filter and autocorrelation enhancement. *Journal of Sound and Vibration*, 236(3):413–430, September 2000.
- [42] J. Maeck and G. De Roeck. Damage assessment of a gradually damaged RC beam using dynamic system identification. In *Proceedings of the 20th International Modal Analysis Conference (IMAC-XX) – CD-ROM*, Los Angeles, California, February 4-7 2002. Society of Experimental Mechanics.
- [43] N. M. M. Maia, J. M. M. a. e Silva, J. He, N. A. J. Lieven, R. M. Lin, G. W. Skingle, W.-M. To, and A. P. V. Urgueira. *Theoretical and Experimental Modal Analysis*. Mechanical engineering research studies. Research Studies Press Ltd., 1997.
- [44] S. G. Mallat. A theory for multiresolution signal decomposition: The wavelet representation. *IEEE Transactions on Pattern Analysis and Machine Intelligence*, 11(7):674–693, July 1989.
- [45] K. Markwardt. Systemanalyse und Parameteridentifikation mit Hilfe der schnellen Wavelet-Transformation. unpublished, 2002.
- [46] M. Misiti, Y. Misiti, G. Oppenheim, and J.-M. Poggi. *MATLAB - Wavelet Toolbox User's Guide*. The MathWorks Inc., Natick, MA, USA, version 2 (release 12) edition, 2000.
- [47] A. Morimoto, S. Ozawa, and R. Ashino. An efficient identification method of the structural parameters of MDOF structures using the wavelet transform and neural networks. In T. Kobori, Y. Inoue, K. Seto, H. Iemura, and A. Nishitani, editors, *Proceedings of the Second World Conference on Structural Control*, volume 3, pages 2133–2140, Kyoto, Japan, 1999. John Wiley & Sons.

- [48] F. Murtagh and J.-L. Starck. Noise detection and filtering using multiresolution transform methods. In R. Albrecht, R. N. Hook, and H. A. Bushouse, editors, *Astronomical Data Analysis Software and Systems VII, ASP Conference Series*, volume 145, pages 449–456, 1998.
- [49] D. E. Newland. *An Introduction to Random Vibrations, Spectral and Wavelet Analysis*. Longman, Singapore, 3rd edition, 1993.
- [50] J. O’Callahan. A procedure for an improved reduced system (IRS) model. In *Proceedings of the 7th International Modal Analysis Conference (IMAC-VII)*, pages 17–21, Las Vegas, Nevada, USA, February 1989. Society of Experimental Mechanics.
- [51] R. Ogden. *Essential Wavelets for Statistical Applications and Data Analysis*. Birkhäuser, Boston, Basel, Berlin, 1997.
- [52] B. A. D. Piombo, A. Fasana, S. Marchesiello, and M. Ruzzene. Modelling and identification of the dynamic response of a supported bridge. *Mechanical Systems and Signal Processing*, 14(1):75–89, 2000.
- [53] H. L. Resnikoff and R. O. Wells. *Wavelet analysis: the scalable structure of information*. Springer-Verlag, New York, 1998.
- [54] A. N. Robertson, K. C. Park, and K. F. Alvin. Extraction of impulse response data via wavelet transform for structural system identification. In *Proc. of the Design Engineering Technical Conferences DE-Vol. 84-1, ASME 1995*, volume 3 – Part A, pages 1323–1334, 1995.
- [55] A. N. Robertson, K. C. Park, and K. F. Alvin. Identification of structural dynamics models using wavelet-generated impulse response data. In *Proc. of the Design Engineering Technical Conferences DE-Vol. 84-1, ASME 1995*, volume 3 – Part A, pages 1335–1344, 1995.

- [56] A. Ruzzene, L. Fasana, L. Garibaldi, and B. Piombo. Natural frequencies and dampings identification using wavelet transform: application to real data. *Mechanical Systems and Signal Processing*, 11(2):207–218, March 1997.
- [57] A. Sone, A. Masuda, and A. Nakaoka. Health monitoring system of building by using wavelet analysis. In *Proc. of the Eleventh World Conference on Earthquake Engineering, paper No. 235*, 1996.
- [58] W. J. Staszewski. Identification of non-linear systems using multi-scale ridges and skeletons of the wavelet transform. *Journal of Sound and Vibration*, 214(4):639–658, 1998.
- [59] W. J. Staszewski. Cross-wavelet analysis of MDOF nonlinear systems. In P. Sas and D. Moens, editors, *Noise and Vibration Engineering, Proc. ISMA25*, volume II, pages 703–707, Leuven, Belgium, September 2000. Katholieke Universiteit Leuven - Departement Werktuigkunde.
- [60] W. J. Staszewski. *Wavelets for Mechanical and Structural Damage Identification*. Monograph Series: Studia i Materiały, No. 510/1469/2000. Polish Academy of Science Press, Gdańsk, 2000.
- [61] W. J. Staszewski and J. E. Cooper. Flutter data analysis using the wavelet transform. In L. Jezequel, editor, *New Advances in Modal Synthesis of Large Structures – Proceedings of the International Conference MV2, Lyon, France, 5-6 October 1995*, pages 203–214, Rotterdam/Brookfield, 1997. A.A. Balkema.
- [62] W. J. Staszewski and J. Giacomini. Application of the wavelet based FRFs to the analysis of nonstationary vehicle data. In *Proc. of the International Modal Analysis Conference IMAC–XV*, volume 1, pages 425–431, Orlando, Florida, February 1997.
- [63] Z. Sun and C. C. Chang. A wavelet packet based method for structural damage assessment. In *Proceedings of the 3rd World Conference on Structural Control*, Como, Italy, 7-12 April 2002. Wiley.

- [64] C. Taswell and K. McGill. Wavelet transform algorithms for finite– duration discrete– time signals. Numerical Analysis Project Manuscript NA–91–07, Department of Computer Science, Stanford University, Stanford, 1993.
  
- [65] P. Tchamitchian and B. Torr sani. Ridge and skeleton extraction from the wavelet transform. In M. B. Ruskai, G. Beylkin, R. Coifman, I. Daubechies, S. Mallat, Y. Meyer, and L. Raphael, editors, *Wavelets and their Applications*, pages 123–151, Boston, London, 1992. Jones and Bartlett Publishers.

# Appendix A

## SLang Commands Related to Wavelet Analysis

The following table gives an overview of the commands within the SLang software system that are related to wavelet analysis. The algorithms implemented use the wavelets  $D2 \dots D10$  as basis functions. For more detailed descriptions refer to [5].

Command	Short description
<code>wavelet derivative</code>	Calculation of the scaling coefficients of the first- or second-order derivative of a given series of scaling coefficients (approximation) at the same decomposition level; the algorithm is based on the concept of connection coefficients (section 4.2)
<code>wavelet extract</code>	Extraction of the scaling or wavelet coefficients, respectively, at one particular level from the results of an orthogonal wavelet decomposition
<code>wavelet integrate</code>	Calculation of the scaling coefficients of the first- or second-order integral of a given series of scaling coefficients (approximation) at the same decomposition level; the algorithm is based on the concept of connection coefficients (section 4.2)
<code>wavelet reconst</code>	Reconstruction of a data series from its wavelet decomposition; it can be specified whether a complete reconstruction at the basic level is desired or if only an approximation at a certain decomposition level should be obeyed
<code>wavelet shrink</code>	De-noising by wavelet shrinkage (chapter 3); both hard and soft thresholding can be applied to a given series of wavelet coefficients, it can be specified if the coefficients at all available levels should be treated or, rather, a selection
<code>wavelet transform</code>	Wavelet decomposition of a given data series; two options for the treatment of the data at the borders are implemented: zero-padding ( <i>extended filter</i> ) and periodic continuation ( <i>circulant filter</i> , restriction to $2^n$ samples)
<code>wavelet view</code>	Surface plot of either wavelet or scaling coefficients on the decomposition grid

Table A.1: Summary of the SLang commands related to wavelet analysis



## Appendix B

### Wavelet Connection Coefficients

	$D2$	$D3$	$D4$	$D5$	$D6$
$\Gamma_0^0$	0	0	0	0	0
$\Gamma_0^1$	0.6666666666666667	0.745205479452055	0.793009504971173	0.82590601185172	0.850136661560152
$\Gamma_0^2$	-0.0833333333333333	-0.145205479452055	-0.191998970797716	-0.22882018706764	-0.258552944142891
$\Gamma_0^3$	0	0.014611872146119	0.033580207051186	0.05335257193322	0.072440589998611
$\Gamma_0^4$	0	0.000342465753425	-0.002224049670590	-0.00746139636627	-0.014545511043685
$\Gamma_0^5$	0	0	-0.000172206190015	0.00023923581976	0.001588561543868
$\Gamma_0^6$	0	0	8.40850522402e-07	5.4047301701e-05	-4.29689145315e-06
$\Gamma_0^7$	0	0	0	2.5241178127e-07	1.20265751913e-05
$\Gamma_0^8$	0	0	0	2.6968610027e-10	-4.20691208857e-07
$\Gamma_0^9$	0	0	0	0	2.89966165561e-09
$\Gamma_0^{10}$	0	0	0	0	-7.02570406758e-13

Table B.1: Fundamental connection coefficients of the  $\mathcal{D}^1$  operator for the Daubechies wavelets

	$D7$	$D8$	$D9$	$D10$
$\Gamma_0^0$	0	0	0	0
$\Gamma_0^1$	0.868743914525375	0.883446046082935	0.89531640583465	0.905071221614378
$\Gamma_0^2$	-0.282965094527508	-0.303259351474408	-0.32031206224778	-0.334784414707492
$\Gamma_0^3$	0.090189066219651	0.106364068289865	0.12095364935918	0.134054665241335
$\Gamma_0^4$	-0.022687411016149	-0.031290147839450	-0.03995272188592	-0.048427300291597
$\Gamma_0^5$	0.003881454657886	0.006958379114893	0.01061693066926	0.014669350195606
$\Gamma_0^6$	-0.000337344047661	-0.001031530212556	-0.00210340281069	-0.003526026907832
$\Gamma_0^7$	-4.23639468409e-06	7.66770694852e-05	0.00027812077691	0.000631219734500
$\Gamma_0^8$	1.65016792303e-06	2.45199290781e-07	-1.9620437693e-05	-7.66834890137e-05
$\Gamma_0^9$	2.18711306275e-07	3.99381276419e-08	4.8782469128e-07	5.49729337265e-06
$\Gamma_0^{10}$	-4.18302068890e-10	-7.20794642299e-08	-1.0361220744e-07	-2.67261853837e-07
$\Gamma_0^{11}$	1.20390290231e-11	-9.69697850826e-10	1.5966863096e-08	3.41578775038e-08
$\Gamma_0^{12}$	4.74101191102e-15	-7.03013516074e-13	8.1373915262e-10	-1.70165941499e-09
$\Gamma_0^{13}$	0	3.65597558140e-14	5.3818998088e-13	-3.69646596092e-10
$\Gamma_0^{14}$	0	2.60393742535e-14	4.5629712928e-14	-3.35929819624e-12
$\Gamma_0^{15}$	0	0	-2.3869629162e-15	-7.24636080721e-14
$\Gamma_0^{16}$	0	0	-2.5337076046e-15	-4.53169522673e-14
$\Gamma_0^{17}$	0	0	0	-4.84319059812e-14
$\Gamma_0^{18}$	0	0	0	-5.14663386064e-14

Table B.2: Fundamental connection coefficients of the  $\mathcal{D}^1$  operator for the Daubechies wavelets (continued)

	$D3$	$D4$	$D5$	$D6$
$\Gamma_0^0$	-5.2678571428571	-4.16597364094082	-3.8349943129026	-3.68606348186489
$\Gamma_0^1$	3.3904761904762	2.64207020826198	2.4147903506376	2.31186656349234
$\Gamma_0^2$	-0.8761904761905	-0.69786910439798	-0.6495021898296	-0.63073324291674
$\Gamma_0^3$	0.1142857142857	0.15097289962331	0.1809535500487	0.20490546941864
$\Gamma_0^4$	0.0053571428571	-0.01057272777808	-0.0299079804265	-0.04936161063956
$\Gamma_0^5$	0	-0.00163037688659	0.0007946205551	0.00647806104529
$\Gamma_0^6$	0	1.5921648176e-05	0.0003671453850	-6.5696290229e-05
$\Gamma_0^7$	0	0	1.656545510e-06	-5.4363378969e-05
$\Gamma_0^8$	0	0	3.540607920e-09	-3.4660860109e-06
$\Gamma_0^9$	0	0	0	2.6299857403e-08
$\Gamma_0^{10}$	0	0	0	-1.2584059863e-11

Table B.3: Fundamental connection coefficients of the  $D^2$  operator for the Daubechies wavelets

	$D7$	$D8$	$D9$	$D10$
$\Gamma_0^0$	-3.604515525832060	-3.55369228990740	-3.518861054971920	-3.49323818665597
$\Gamma_0^1$	2.255045787924190	2.21914659389190	2.194072687181210	2.17521749406950
$\Gamma_0^2$	-0.621497674632171	-0.61561414656071	-0.610929112262259	-0.60668942081749
$\Gamma_0^3$	0.223359102218610	0.23717805822281	0.247332322768392	0.25469743964057
$\Gamma_0^4$	-0.067052362291480	-0.08226639998019	-0.094970844780534	-0.10542969300851
$\Gamma_0^5$	0.013963689191936	0.02207029188649	0.030068613621381	0.03758004182651
$\Gamma_0^6$	-0.001605235463808	-0.00409765688955	-0.007248478692483	-0.01078072257004
$\Gamma_0^7$	4.15664409804e-05	0.00045167920308	0.001230499099979	0.00235727080481
$\Gamma_0^8$	1.40111557812e-06	-2.3982284899e-05	-0.000133610007975	-0.00036938799318
$\Gamma_0^9$	1.48618332204e-06	2.0904233618e-06	9.13093080831e-06	3.8524520380e-05
$\Gamma_0^{10}$	2.06552905366e-09	-3.7230775684e-07	-7.34346861918e-07	-2.5793034928e-06
$\Gamma_0^{11}$	1.63477702421e-10	-1.0585882797e-08	4.75556745436e-08	1.2229721863e-07
$\Gamma_0^{12}$	8.01550715291e-14	-5.8344185255e-11	6.37034472004e-09	6.1143742381e-09
$\Gamma_0^{13}$	0	2.8831888778e-14	4.90890941438e-11	-2.2197506452e-09
$\Gamma_0^{14}$	0	-2.8048472266e-13	5.18159970086e-14	-4.9963249511e-11
$\Gamma_0^{15}$	0	0	-2.60644296851e-13	-1.2504285715e-14
$\Gamma_0^{16}$	0	0	-2.96949513974e-13	2.6084732330e-13
$\Gamma_0^{17}$	0	0	0	2.9114612344e-13
$\Gamma_0^{18}$	0	0	0	3.2637629876e-13

Table B.4: Fundamental connection coefficients of the  $\mathcal{D}^2$  operator for the Daubechies wavelets (continued)

	$D2$	$D3$	$D4$	$D5$	$D6$
$\Gamma_0^0$	0.5	0.5	0.5	0.5	0.5
$\Gamma_0^1$	-0.0444444444444444	-0.058612358989718	-0.065801945369910	-0.070234135008304	-0.073266395252120
$\Gamma_0^2$	0.0013888888888889	0.008967848407707	0.014902834677927	0.019417154580372	0.022924991783950
$\Gamma_0^3$	0	-0.000327443346311	-0.001969668303639	-0.003988251932312	-0.006010399690767
$\Gamma_0^4$	0	-1.91861335731e-06	5.66161558737e-05	0.000434229400092	0.001062833812129
$\Gamma_0^5$	0	0	2.43349185025e-06	-6.54434121813e-06	-9.45371272166e-05
$\Gamma_0^6$	0	0	-2.97057108246e-09	-1.04478691550e-06	4.40679739989e-08
$\Gamma_0^7$	0	0	0	-1.74214455961e-09	2.83278837951e-07
$\Gamma_0^8$	0	0	0	-4.65216948907e-13	5.90884105550e-09
$\Gamma_0^9$	0	0	0	0	-1.70335869034e-11
$\Gamma_0^{10}$	0	0	0	0	1.00525211412e-15

Table B.5: Fundamental connection coefficients of the  $\mathcal{I}^1$  operator for the Daubechies wavelets

	$D7$	$D8$	$D9$	$D10$
$\Gamma_0^0$	0.5	0.5	0.5	0.5
$\Gamma_0^1$	-0.075478591224536	-0.077164879285836	-0.0784924361569140	-0.0795640831493365
$\Gamma_0^2$	0.025714219784524	0.027977006084842	0.0298446184333445	0.0314092492989984
$\Gamma_0^3$	-0.007900403905539	-0.009617279014061	-0.0111585240484624	-0.0125366012048803
$\Gamma_0^4$	0.001840233540706	0.002688282079488	0.0035559754313218	0.0044124636812310
$\Gamma_0^5$	-0.000280123215512	-0.000552988850606	-0.0008933354941876	-0.0012811388644637
$\Gamma_0^6$	2.05726479595e-05	7.34031770243e-05	0.0001635084450405	0.0002901014356903
$\Gamma_0^7$	1.95907284708e-07	-4.60760574241e-06	-1.927308908745e-05	-4.776901768542e-05
$\Gamma_0^8$	-4.91892279168e-08	-4.35037461723e-08	1.092578509252e-06	5.096887515326e-06
$\Gamma_0^9$	-3.90442297871e-09	2.26207024222e-09	-1.594290441931e-09	-2.750409749638e-07
$\Gamma_0^{10}$	3.52324087487e-12	1.51162315189e-09	1.966732393485e-09	4.423519794581e-09
$\Gamma_0^{11}$	-5.37605144262e-14	1.48456307814e-11	-3.909572909594e-10	-8.323470523416e-10
$\Gamma_0^{12}$	-6.09519606940e-18	-6.42046556422e-15	-1.446718115734e-11	5.750230740006e-11
$\Gamma_0^{13}$	0	-4.71498380701e-17	4.452831635012e-15	7.449990778787e-12
$\Gamma_0^{14}$	0	-1.79171262101e-17	-3.015485239851e-16	4.516758455848e-14
$\Gamma_0^{15}$	0	0	-8.000918772060e-18	1.870848909167e-16
$\Gamma_0^{16}$	0	0	1.898362717218e-17	5.317283053141e-18
$\Gamma_0^{17}$	0	0	0	1.986397014814e-18
$\Gamma_0^{18}$	0	0	0	-5.743886735155e-18

Table B.6: Fundamental connection coefficients of the  $\mathcal{I}^1$  operator for the Daubechies wavelets (continued)

	$D2$	$D3$	$D4$	$D5$	$D6$
$\Gamma_0^0$	0.118333333333333	0.110600674207709	0.107639589324152	0.106108055921084	0.105179044087399
$\Gamma_0^1$	-0.0177777777777778	-0.016870315169910	-0.015915686964025	-0.015239216437051	-0.014753079295697
$\Gamma_0^2$	0.0002777777777778	0.003285032930782	0.004432053354856	0.004919792458118	0.005136934500892
$\Gamma_0^3$	0	-4.82468498663e-05	-0.000675569822788	-0.001212154233063	-0.001604701185509
$\Gamma_0^4$	0	-1.41348192970e-07	5.66087445167e-06	0.000144541870607	0.000329813462491
$\Gamma_0^5$	0	0	4.14816297907e-07	-1.63346821844e-07	-3.17369940379e-05
$\Gamma_0^6$	0	0	-2.53183759341e-10	-1.61587875639e-07	-1.22128817332e-07
$\Gamma_0^7$	0	0	0	-2.17755245377e-11	3.52967860371e-08
$\Gamma_0^8$	0	0	0	-2.90468338029e-15	9.67661272750e-10
$\Gamma_0^9$	0	0	0	0	-1.06077443710e-12
$\Gamma_0^{10}$	0	0	0	0	3.00814348026e-17

Table B.7: Fundamental connection coefficients of the  $\mathcal{I}^2$  operator for the Daubechies wavelets



	$D7$	$D8$	$D9$	$D10$
$\Gamma_0^0$	0.104556349220771	0.104109530772902	0.103772797892794	0.103509557117463
$\Gamma_0^1$	-0.014389286137538	-0.014106897542419	-0.013881110559761	-0.013696270486802
$\Gamma_0^2$	0.005228756630471	0.005257932255985	0.005254448632853	0.005233728351440
$\Gamma_0^3$	-0.001882884202806	-0.002079186574136	-0.002218102613877	-0.002316747634179
$\Gamma_0^4$	0.000513729275104	0.000678101187128	0.000818430961948	0.000935707910123
$\Gamma_0^5$	-8.90230060886e-05	-0.000160283050490	-0.000236281190079	-0.000311258007053
$\Gamma_0^6$	7.17271469638e-06	2.39122990529e-05	4.88875004764e-05	7.97454234762e-05
$\Gamma_0^7$	3.09187130751e-08	-1.67645916882e-06	-6.40701177669e-06	-1.46318513146e-05
$\Gamma_0^8$	-3.52034741978e-09	-3.17340151870e-10	4.04015473425e-07	1.71256151613e-06
$\Gamma_0^9$	-6.16612799829e-10	-7.27900305366e-10	-2.41385323895e-09	-9.91067395382e-08
$\Gamma_0^{10}$	2.78066620992e-13	2.09954748202e-10	4.48405303336e-10	1.04858440019e-09
$\Gamma_0^{11}$	-4.24360611385e-15	2.65849376051e-12	-4.24099547619e-11	-1.11719236302e-10
$\Gamma_0^{12}$	1.55237557347e-18	1.24764138121e-15	-2.38526799789e-12	1.93215408993e-12
$\Gamma_0^{13}$	0	-1.48809313597e-18	-6.01672941544e-16	1.11018280547e-12
$\Gamma_0^{14}$	0	1.19466766149e-18	-1.42590234225e-17	8.56313200881e-15
$\Gamma_0^{15}$	0	0	2.85331680282e-20	1.50528067343e-17
$\Gamma_0^{16}$	0	0	-3.91944120452e-20	9.48122262234e-18
$\Gamma_0^{17}$	0	0	0	3.58271754981e-18
$\Gamma_0^{18}$	0	0	0	3.01741040487e-19

Table B.8: Fundamental connection coefficients of the  $\mathcal{I}^2$  operator for the Daubechies wavelets (continued)

# Appendix C

## Examples – Differentiation and Integration

### Example C.1. Continuous wavelet analysis – analytical function

*The relations that were derived in section 4.1 are verified by means of an analytical function. It is shown, how the continuous wavelet transforms of the Gaussian function and its first derivative can be reproduced, based on appropriate wavelet transforms of the Gaussian function's second derivative. Similarly, wavelet transforms of the third and fourth derivatives of the Gaussian function are estimated by wavelet transforms of the Gaussian function's second derivative also. The Gaussian function and its first four derivatives are given by:*

$$g(t) = e^{-\frac{t^2}{2}}, \quad (\text{C.1})$$

$$\frac{dg(t)}{dt} = -t e^{-\frac{t^2}{2}}, \quad (\text{C.2})$$

$$\frac{d^2g(t)}{dt^2} = (t^2 - 1) e^{-\frac{t^2}{2}}, \quad (\text{C.3})$$

$$\frac{d^3g(t)}{dt^3} = (3t - t^3) e^{-\frac{t^2}{2}}, \quad (\text{C.4})$$

$$\frac{d^4g(t)}{dt^4} = (t^4 - 6t^2 + 3) e^{-\frac{t^2}{2}}. \quad (\text{C.5})$$

*The first three wavelets of the Gaussian family were chosen as analysing wavelets.*

For the numerical investigations, the functions described by equations (C.1) to (C.5) were approximated by 250 samples for  $-6 \leq t \leq 6$ . A plot of the second derivative of the Gaussian function is given in figure C.1.

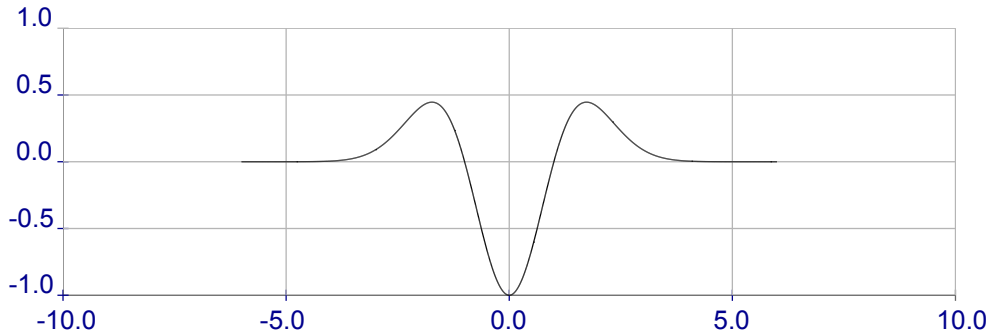


Figure C.1: Second derivative of the Gaussian function  $(t^2 - 1) e^{-\frac{t^2}{2}}$

The wavelet transforms at the first 100 scales were computed by means of the MATLAB Wavelet Toolbox. The results are presented in figures C.2 to C.5, the respective upper diagrams showing the wavelet transform of the analytical function and its estimation based on the Gaussian function's second derivative. The visual appearance suggests a general identity of the two coherent images. Underneath the diagrams of the wavelet transforms in figures C.2 to C.5, a plot of their absolute differences is given. Some relatively small divergences can be observed that mainly occur at scales where the wavelet transforms have only small values.

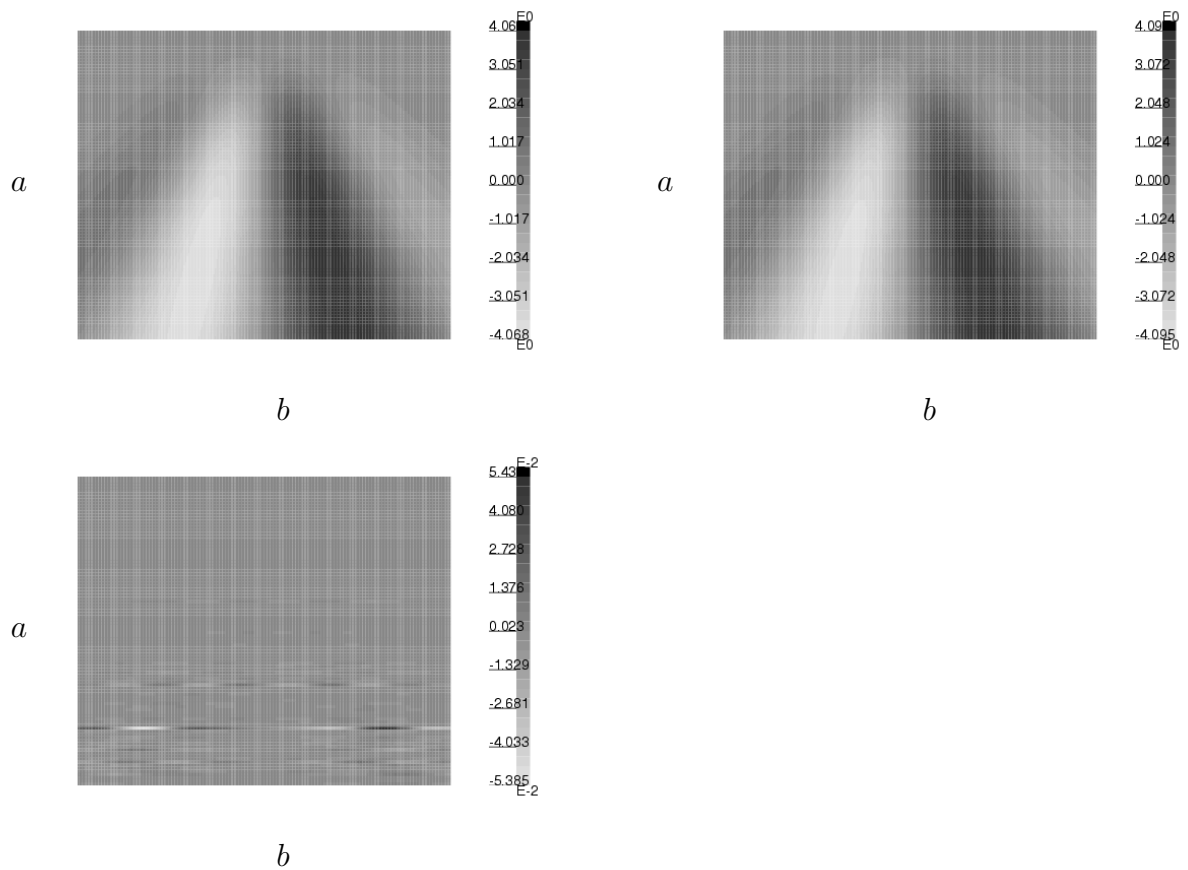


Figure C.2: Wavelet transform of the Gaussian function with respect to the third Gaussian wavelet (top left), scaled wavelet transform of the Gaussian function's second derivative with respect to the first Gaussian wavelet (top right), absolute differences between the two wavelet transforms (bottom left)

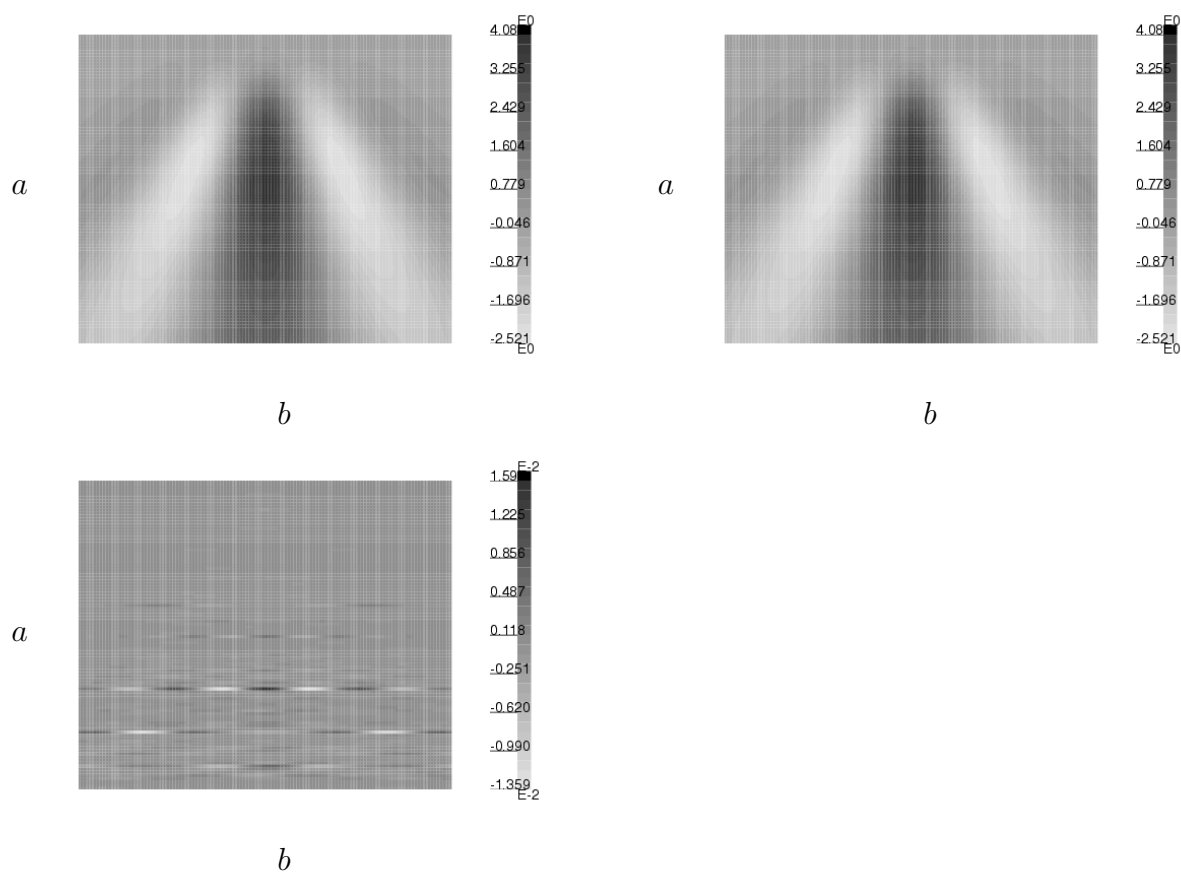


Figure C.3: Wavelet transform of the Gaussian function's first derivative with respect to the third Gaussian wavelet (top left), scaled wavelet transform of the Gaussian function's second derivative with respect to the second Gaussian wavelet (top right), absolute differences between the two wavelet transforms (bottom left)

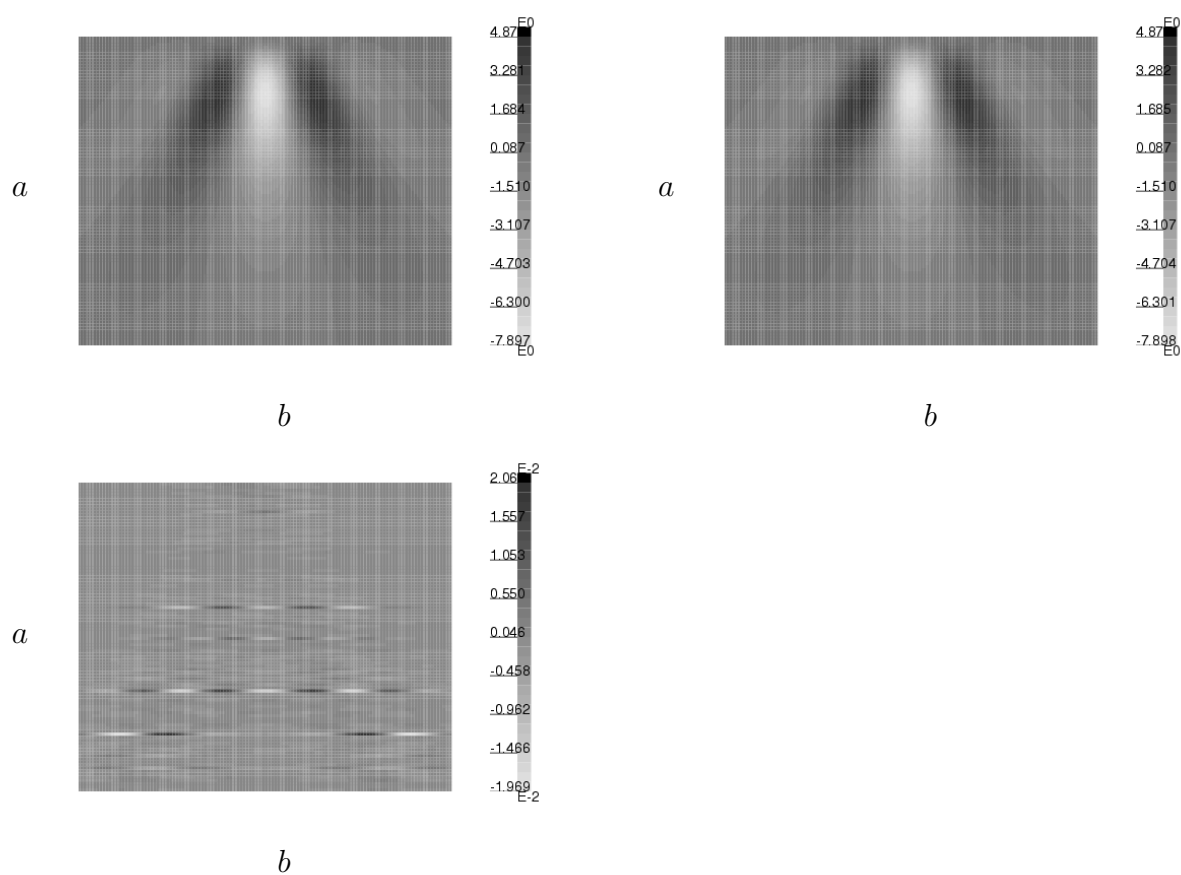


Figure C.4: Wavelet transform of the Gaussian function's third derivative with respect to the first Gaussian wavelet (top left), scaled wavelet transform of the Gaussian function's second derivative with respect to the second Gaussian wavelet (top right), absolute differences between the two wavelet transforms (bottom left)

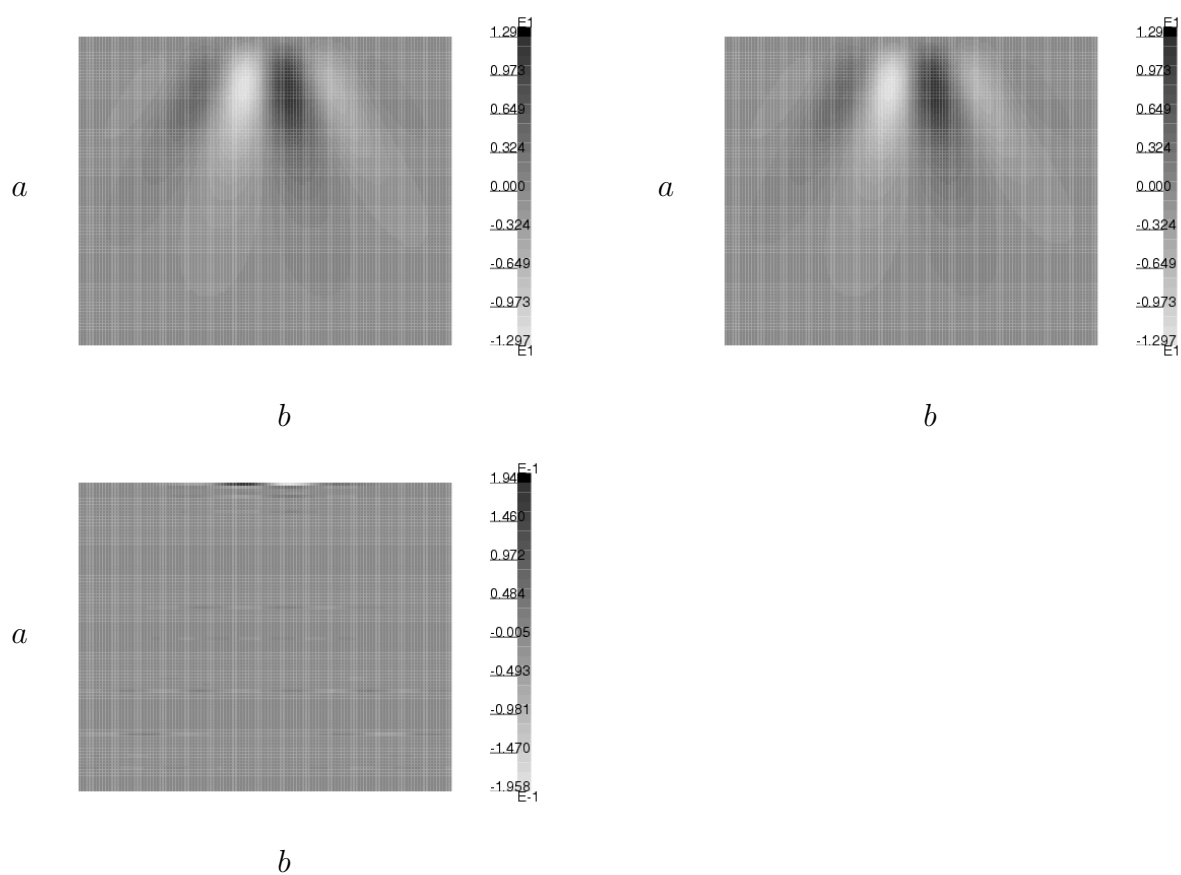


Figure C.5: Wavelet transform of the Gaussian function's fourth derivative with respect to the first Gaussian wavelet (top left), scaled wavelet transform of the Gaussian function's second derivative with respect to the third Gaussian wavelet (top right), absolute differences between the two wavelet transforms (bottom left)

### Example C.2. Continuous wavelet analysis – numerically simulated structural response

The structural response of a single degree of freedom system due to an excitation by a sweep force was simulated numerically. The displacements, velocities and accelerations are shown in figure C.6.

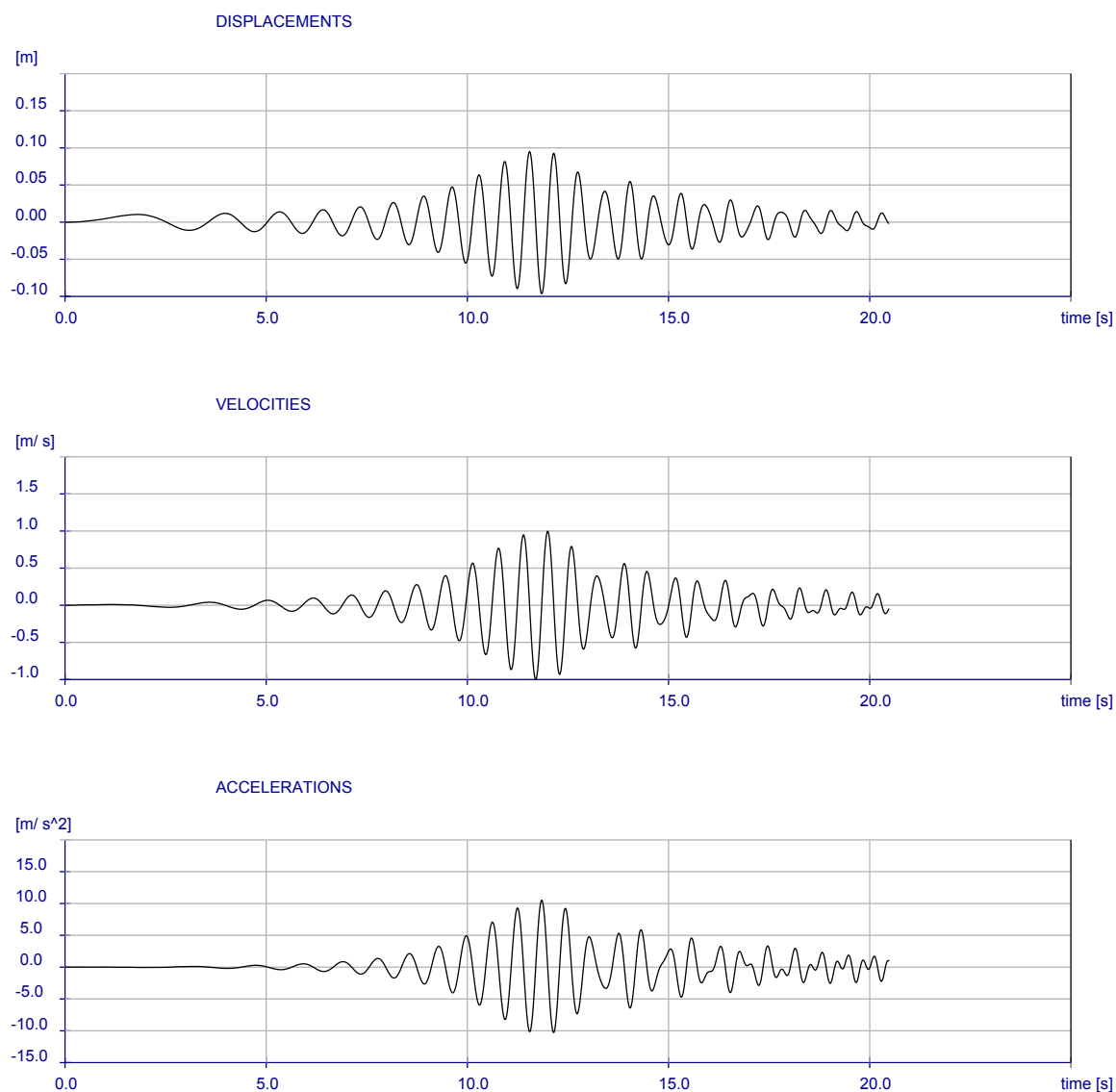


Figure C.6: Numerically simulated structural response of an SDOF system



*Utilising the same approach as described in example C.1, the wavelet transforms of the velocities were approximated by wavelet transforms of the accelerations and displacements, respectively (figures C.7 and C.8). Furthermore, the wavelet transform of the displacements was estimated by a wavelet transform of the accelerations (figure C.9) and vice versa (figure C.10). Again, the plots of the corresponding wavelet transforms appear to be approximately identical. However, from the divergence plots at the bottom of figures C.7 to C.10, one can identify border distortions that are due to the fact that the system's response is not zero end of the observation interval.*

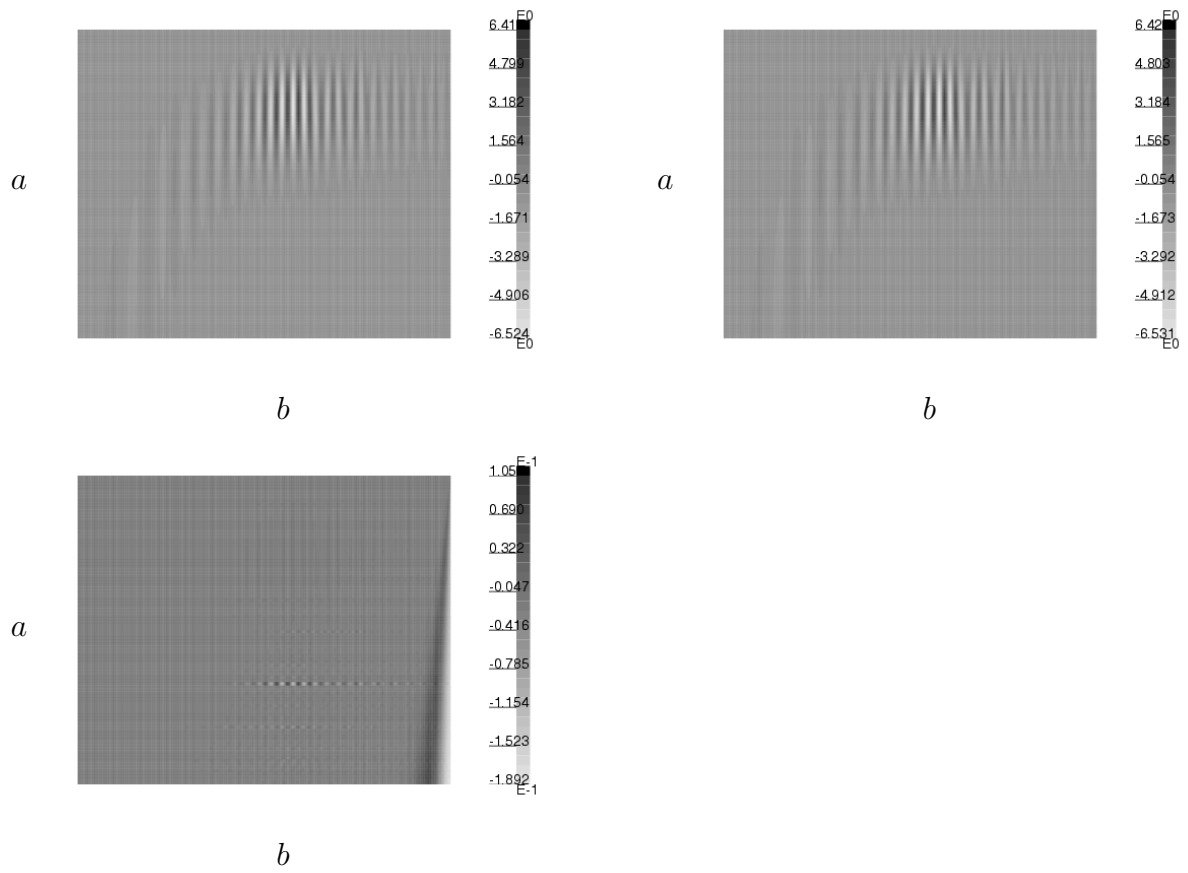


Figure C.7: Wavelet transform of the velocities with respect to the third Gaussian wavelet (top left), scaled wavelet transform of the accelerations with respect to the second Gaussian wavelet (top right), absolute differences between the two wavelet transforms (bottom left)

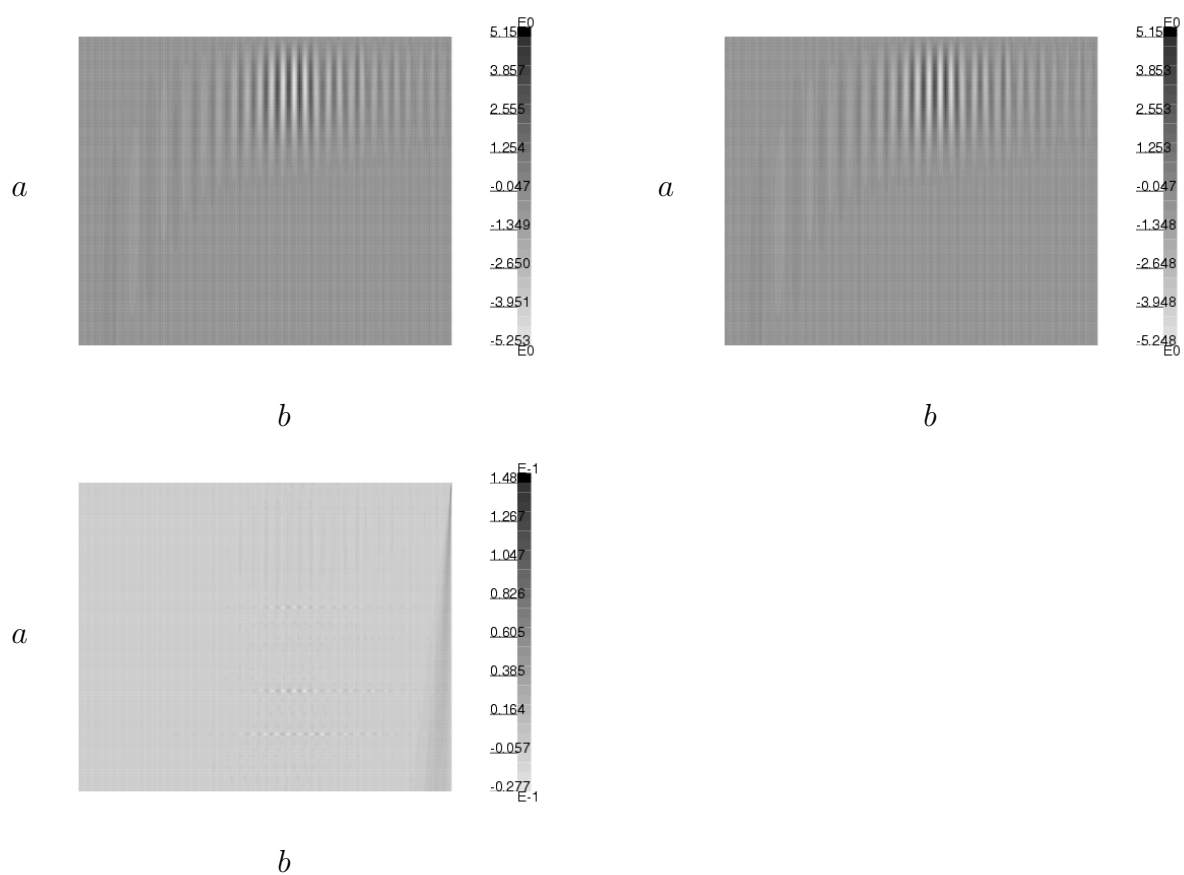


Figure C.8: Wavelet transform of the velocities with respect to the first Gaussian wavelet (top left), scaled wavelet transform of the displacements with respect to the second Gaussian wavelet (top right), absolute differences between the two wavelet transforms (bottom left)

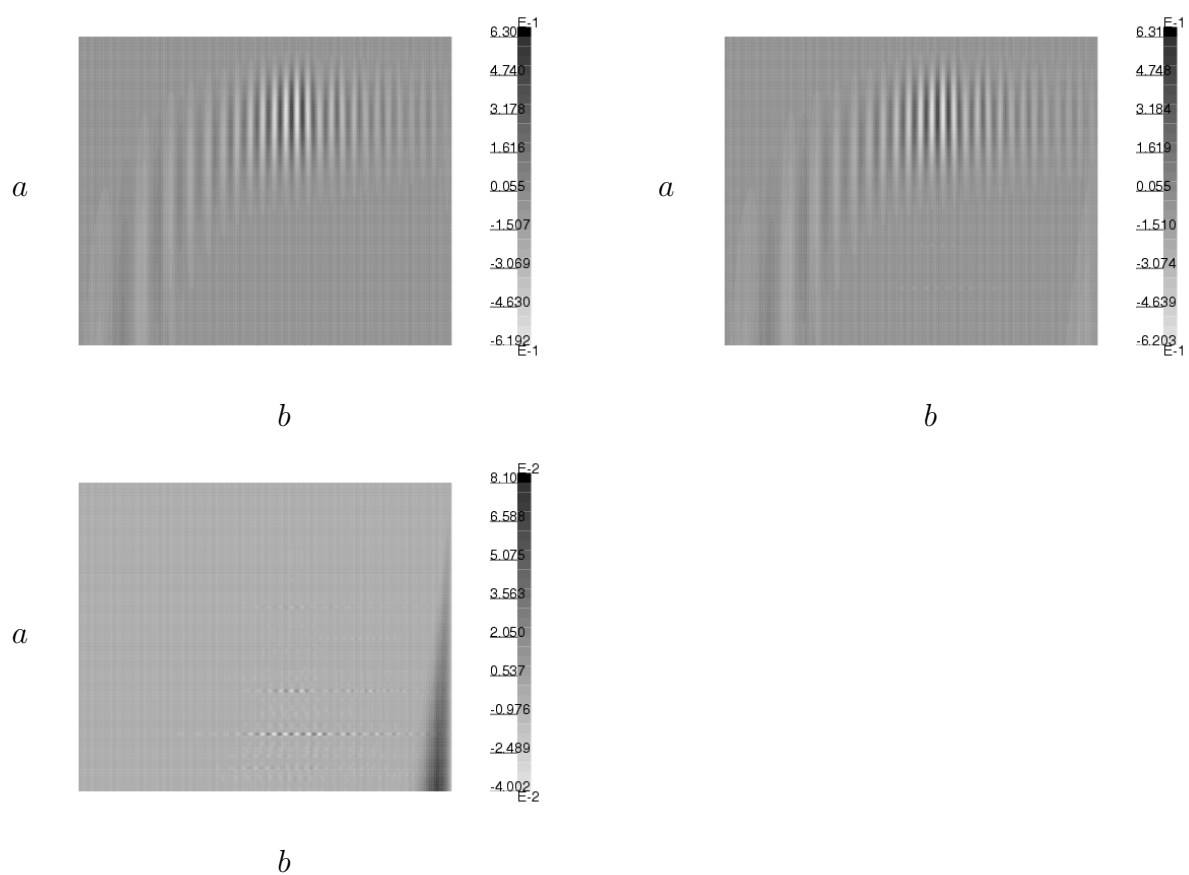


Figure C.9: Wavelet transform of the displacements with respect to the third Gaussian wavelet (top left), scaled wavelet transform of the accelerations with respect to the first Gaussian wavelet (top right), absolute differences between the two wavelet transforms (bottom left)

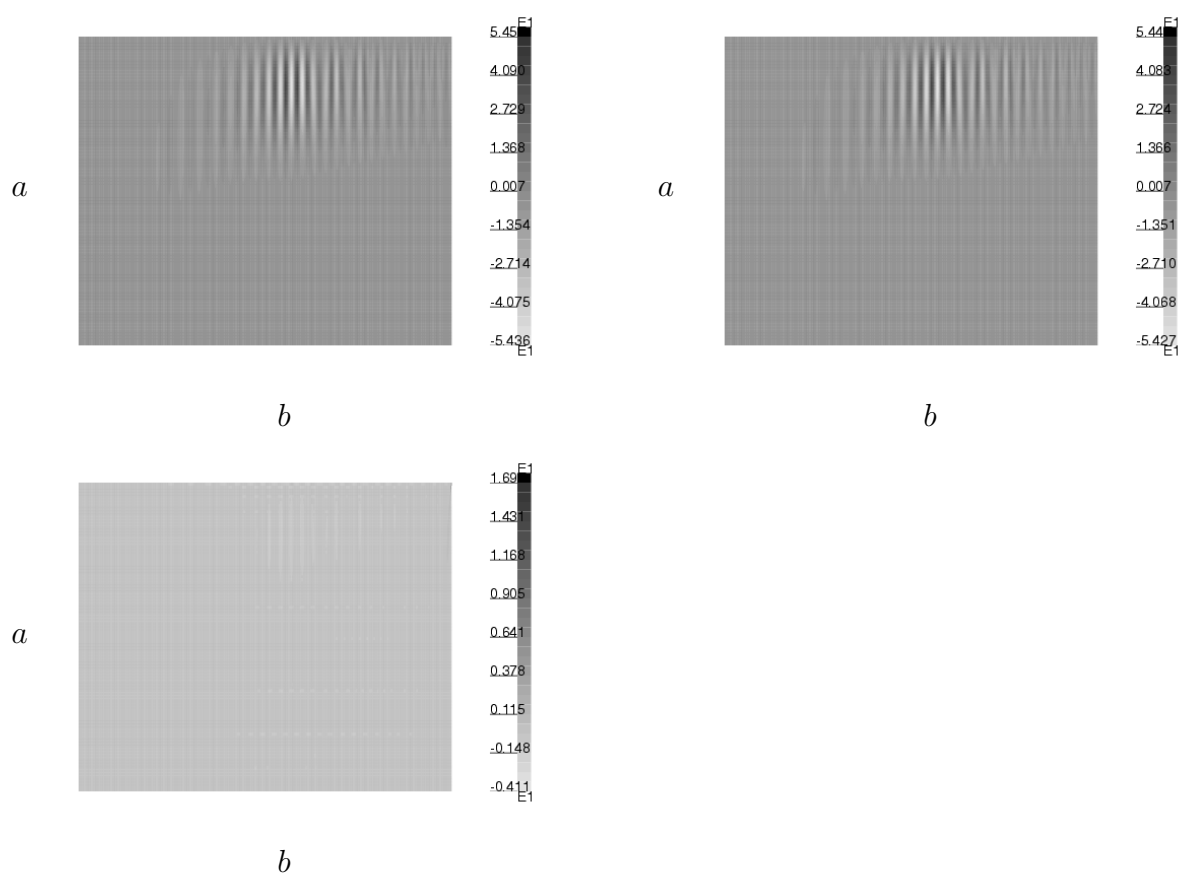


Figure C.10: Wavelet transform of the accelerations with respect to the first Gaussian wavelet (top left), scaled wavelet transform of the displacements with respect to the third Gaussian wavelet (top right), absolute differences between the two wavelet transforms (bottom left)

**Example C.3. Discrete wavelet calculus – analytical function**

*Analogous to example C.1, the relations between the wavelet decompositions of the Gaussian function and its derivatives with respect to the Daubechies wavelet D6 were investigated. Based on the concept of connection coefficients, as explained in section 4.2, the respective wavelet coefficients were estimated from the second derivative of the Gaussian function.*

*Figures C.11 to C.14, that contain the results, have a similar significance to those in examples C.1 and C.2: top left image → wavelet decomposition of the respective analytical function; top right image → wavelet decomposition of the approximation obeyed by the Gaussian function's second derivative; bottom left → difference between the two wavelet decompositions. All plots indicate that the wavelet decompositions of the respective analytical function and that of its approximation are almost identical. The deviations seem to be within a negligible range.*

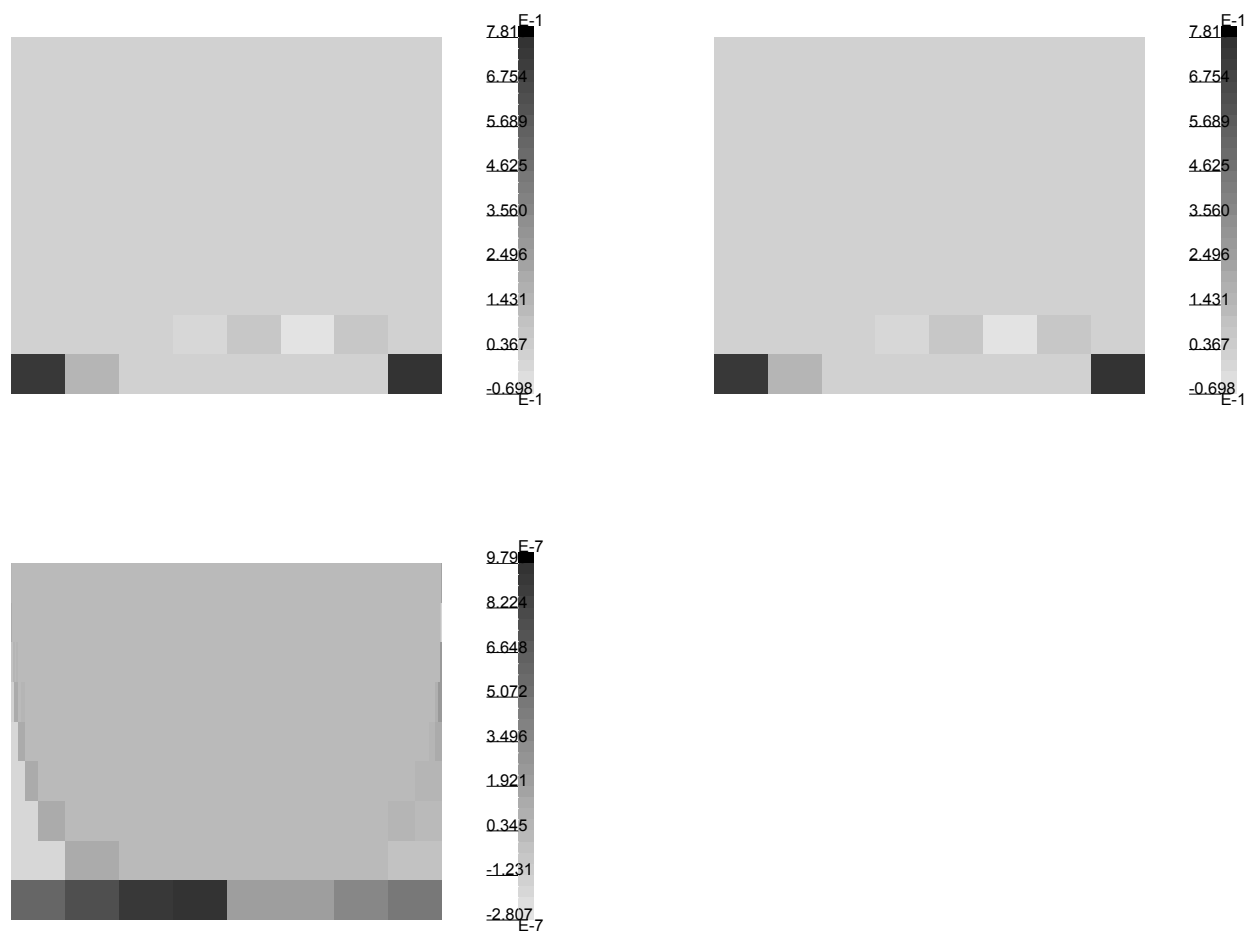


Figure C.11: Wavelet decomposition of the Gaussian function with respect to the  $D6$  wavelet (top left), wavelet decomposition of the estimate of the Gaussian function that was obtained based on the Gaussian function's second derivative (top right), absolute differences between the two wavelet decompositions (bottom left)

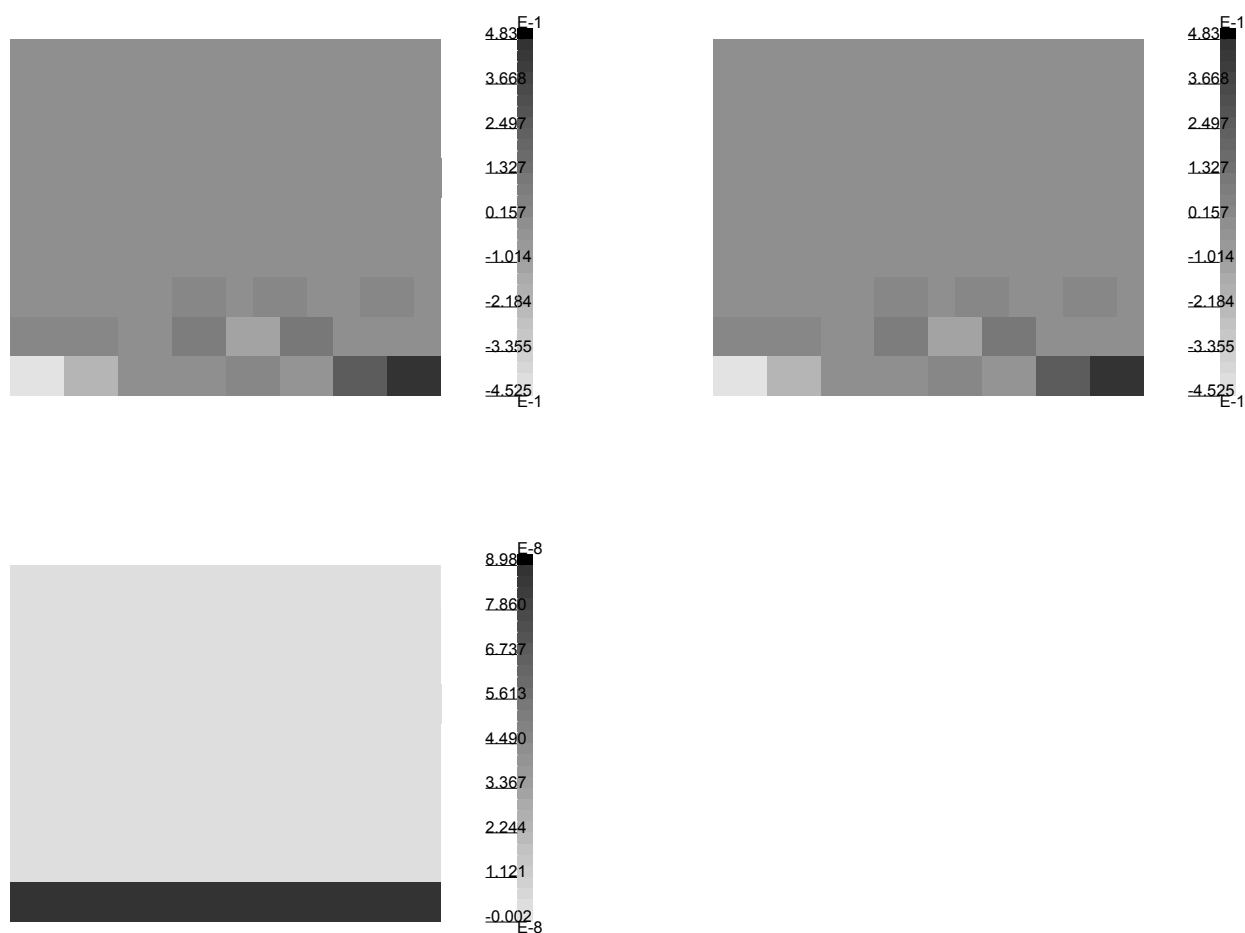


Figure C.12: Wavelet decomposition of the Gaussian function's first derivative with respect to the  $D6$  wavelet (top left), wavelet decomposition of the estimate of the Gaussian function's first derivative that was obtained based on the Gaussian function's second derivative (top right), absolute differences between the two wavelet decompositions (bottom left)



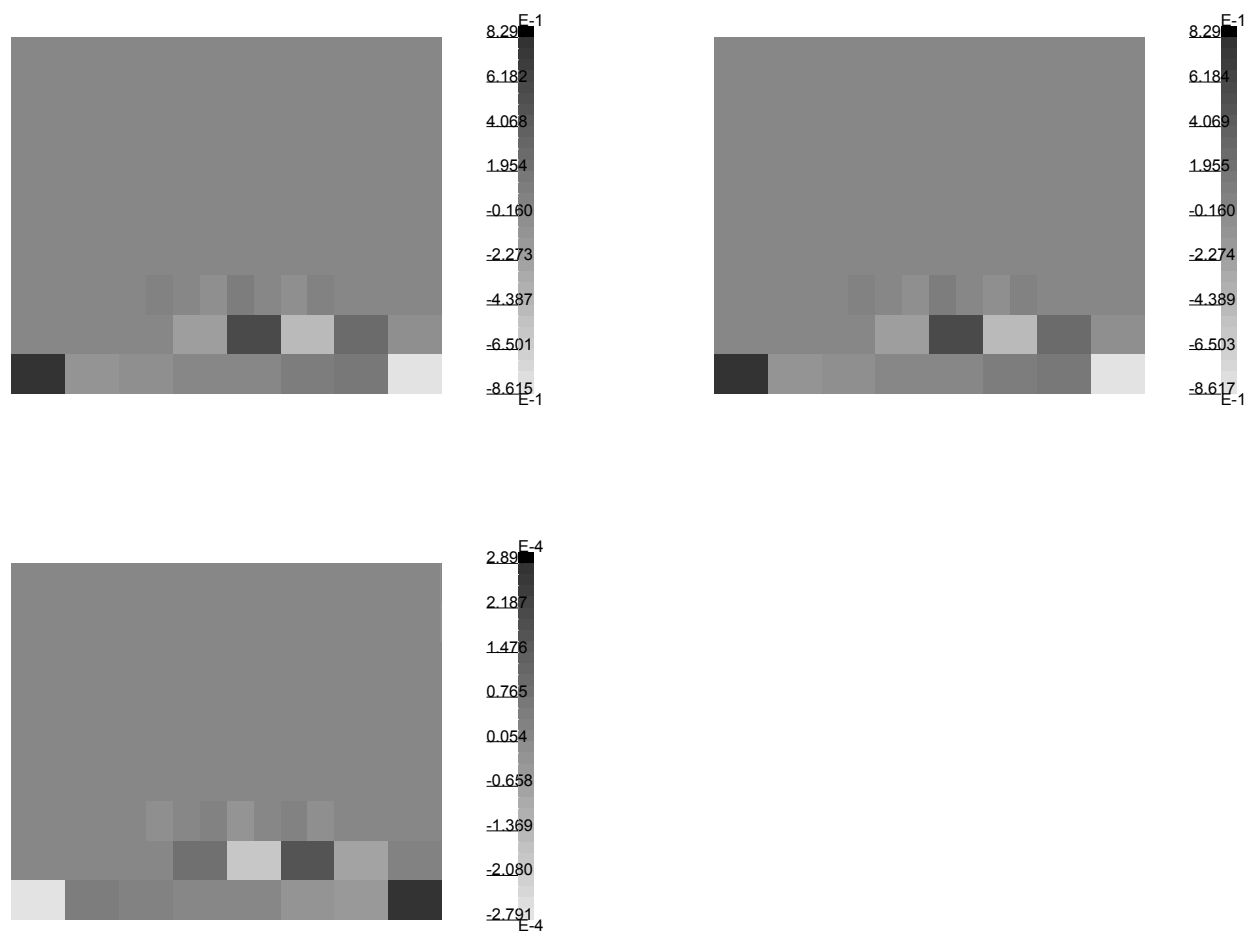


Figure C.13: Wavelet decomposition of the Gaussian function's third derivative with respect to the  $D6$  wavelet (top left), wavelet decomposition of the estimate of the Gaussian function's third derivative that was obtained based on the Gaussian function's second derivative (top right), absolute differences between the two wavelet decompositions (bottom left)

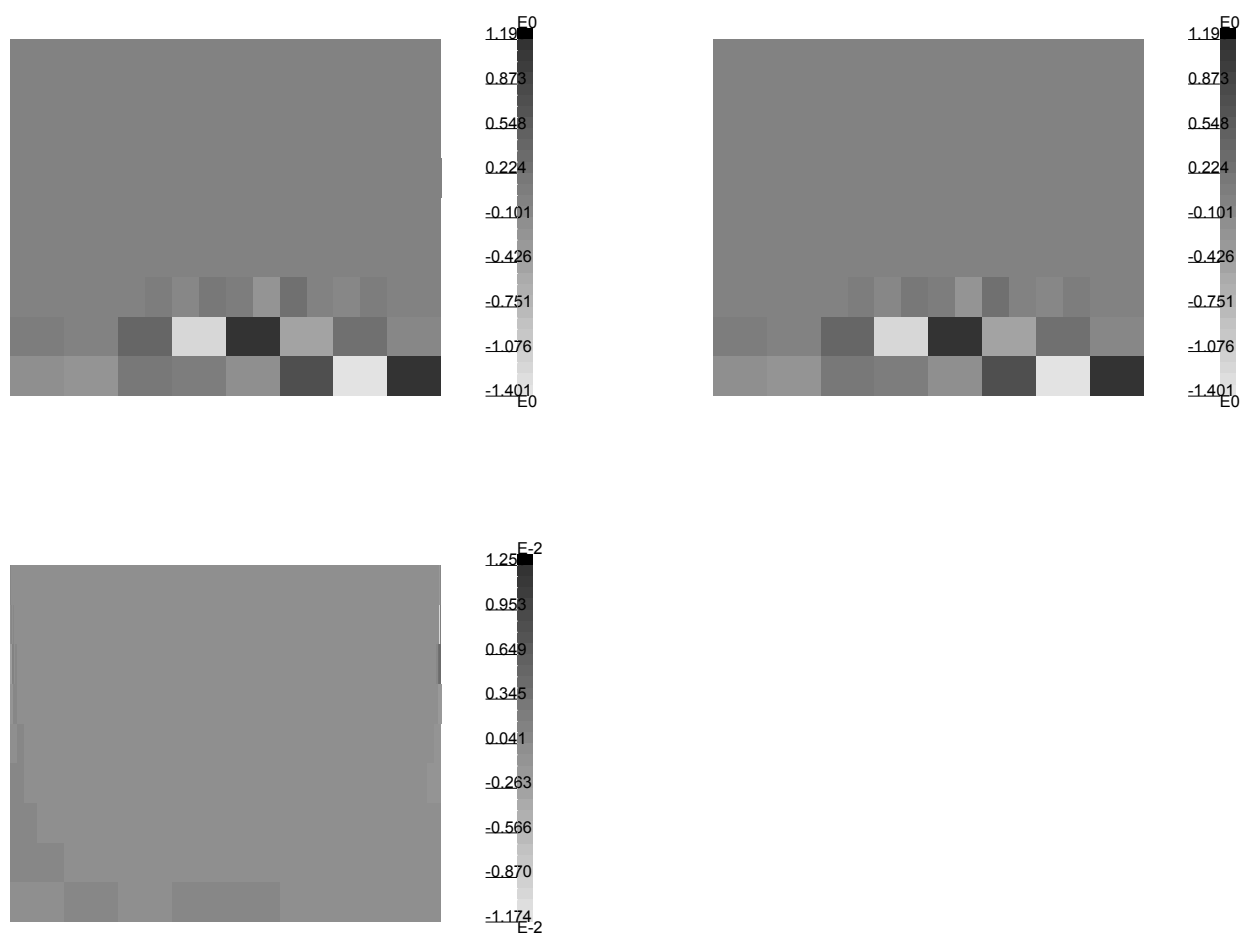


Figure C.14: Wavelet decomposition of the Gaussian function's fourth derivative with respect to the  $D6$  wavelet (top left), wavelet decomposition of the estimate of the Gaussian function's fourth derivative that was obtained based on the Gaussian function's second derivative (top right), absolute differences between the two wavelet decompositions (bottom left)

**Example C.4. Discrete wavelet calculus – numerically simulated structural response**

*The concept of representing wavelet decompositions of integrals or derivatives of a given signal by means of connection coefficients was also applied to the numerically simulated structural response series that are shown in figure C.6 (example C.2). As in example C.3, both the applied connection coefficients and the wavelet decompositions were based on the Daubechies wavelet D6. In figures C.15 to C.18, the respective wavelet coefficients (top diagrams) and the deviations (bottom plots) are mapped. Apparently, in this case the method proposed reproduces integrals of a given function more accurately than its derivatives. This particularly applies to the second derivatives.*

*Figure C.19 gives a closer look at the wavelet coefficients of the acceleration (black curves) and the estimated ones that were obtained from the displacement series (grey curves) at levels 1 to 8. Where the grey curve is interrupted, it exceeds the range of the diagram that was scaled such that the important features of the curves can be observed.*

*From these diagrams, it becomes obvious that border distortions are amplified by applying the connection coefficients. In this case the border distortions mainly occur at the end of the interval. This is due to the artificial extension of the given data by zeros in both directions. In some cases it was observed that better results could be obtained by applying the first-order differential connection coefficients twice, rather than the second-order differential connection coefficients.*

*Additionally, it is observed, that the application of the second-order differential connection coefficients produces some high frequency contents in the estimate that are not contained in the original acceleration series.*

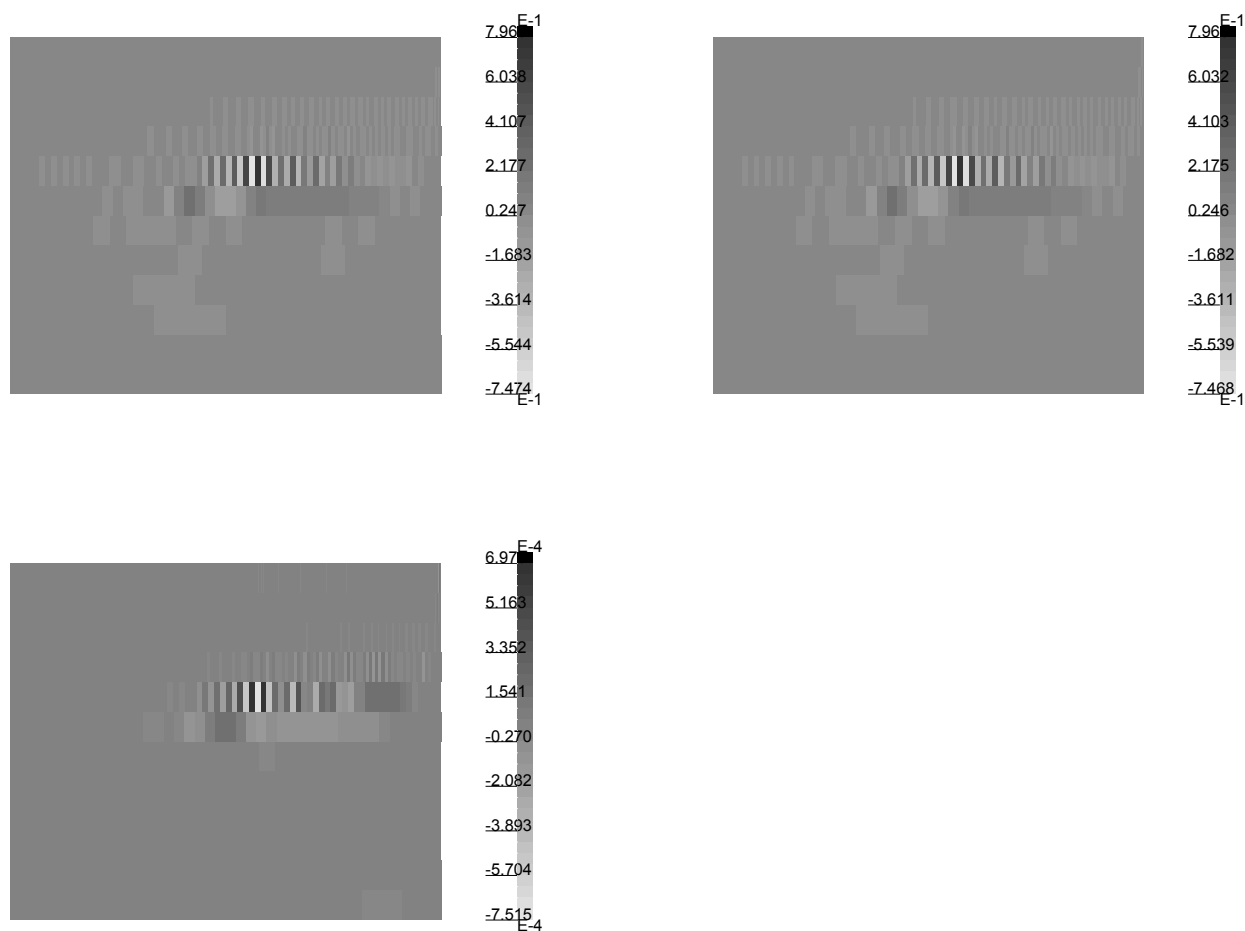


Figure C.15: Wavelet decomposition of the velocities with respect to the  $D6$  wavelet (top left), wavelet decomposition of the estimate of the velocities that was obtained based on the accelerations (top right), absolute differences between the two wavelet decompositions (bottom left)

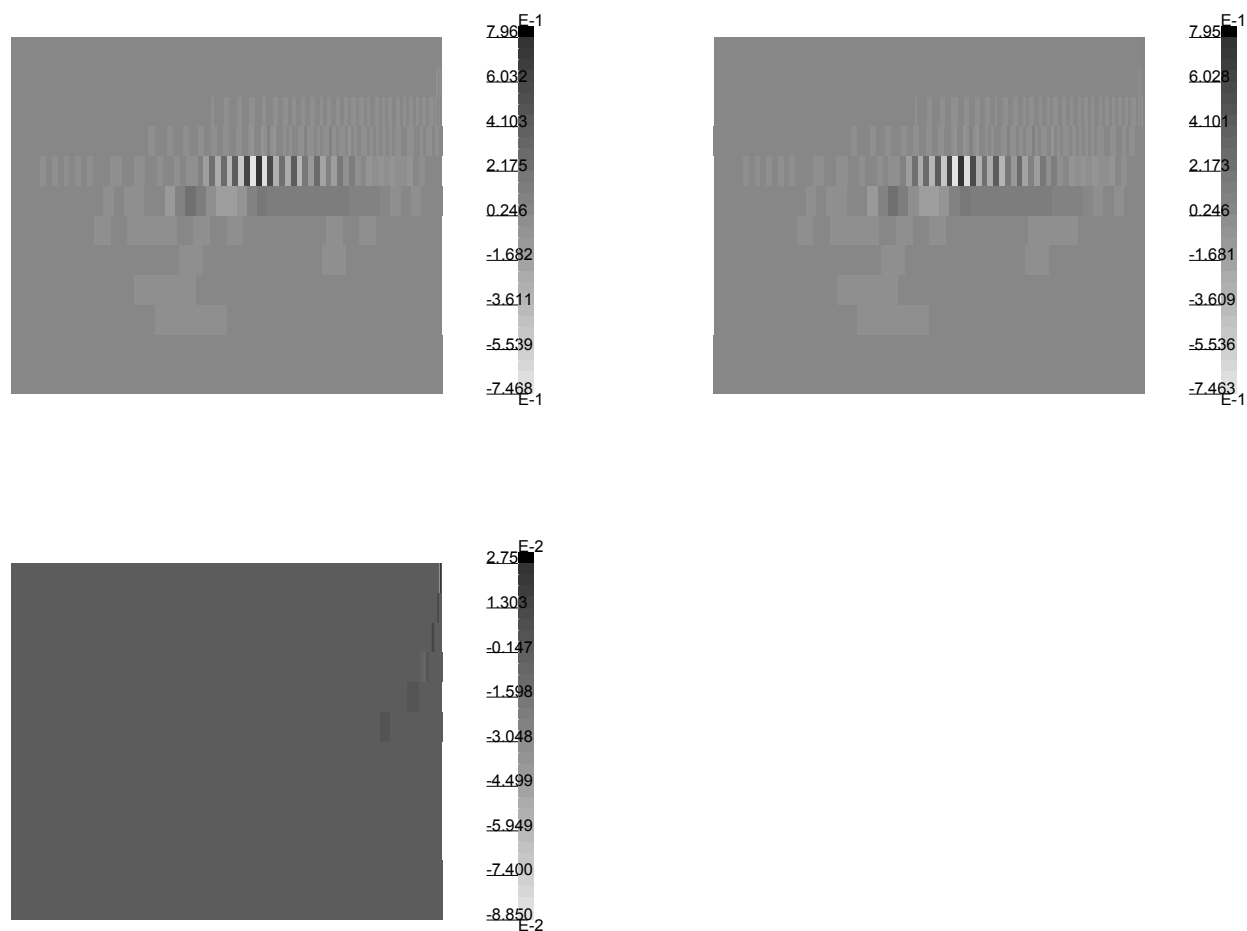


Figure C.16: Wavelet decomposition of the velocities with respect to the  $D6$  wavelet (top left), wavelet decomposition of the estimate of the velocities that was obtained based on the displacements (top right), absolute differences between the two wavelet decompositions (bottom left)

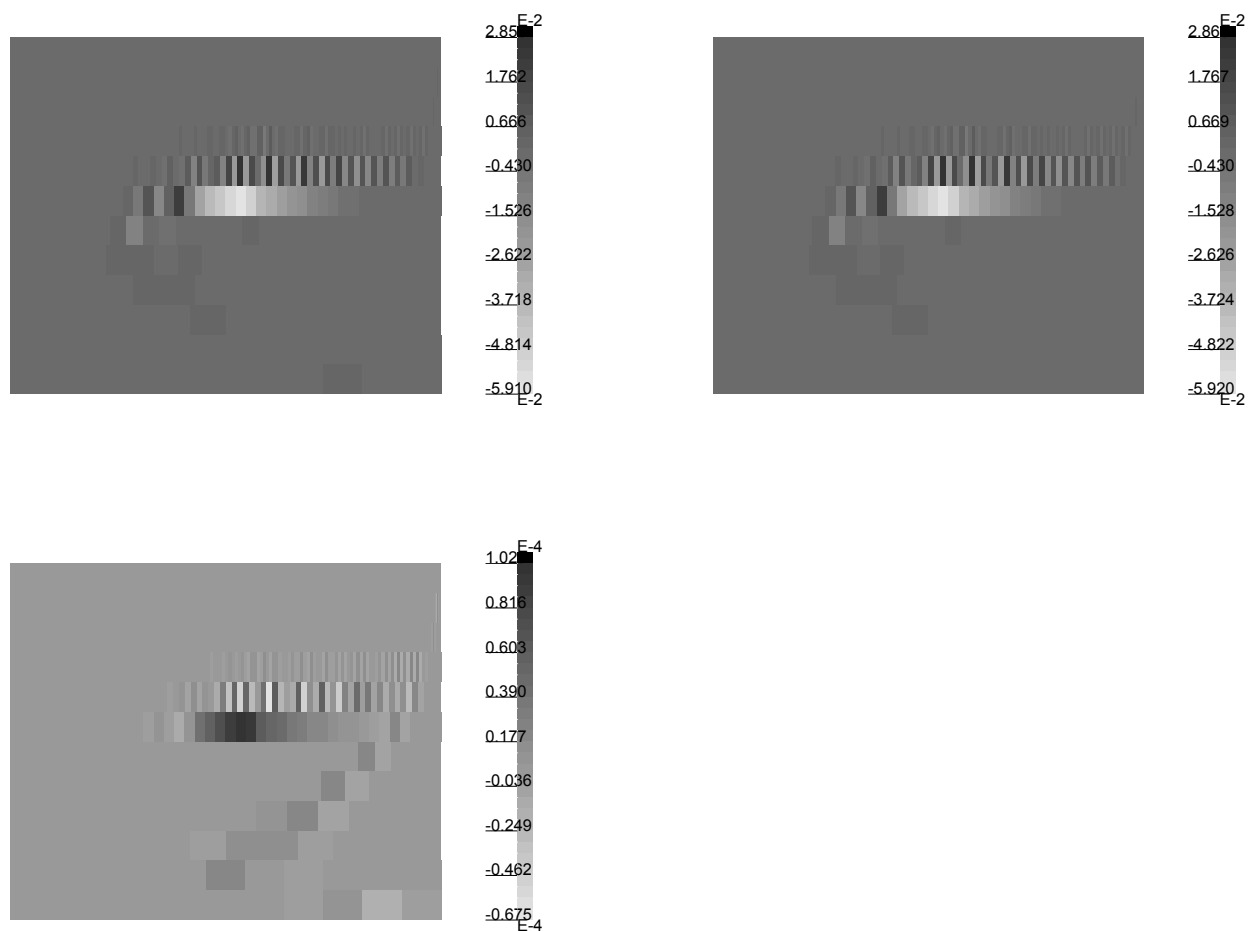


Figure C.17: Wavelet decomposition of the displacements with respect to the  $D6$  wavelet (top left), wavelet decomposition of the estimate of the displacements that was obtained based on the accelerations (top right), absolute differences between the two wavelet decompositions (bottom left)

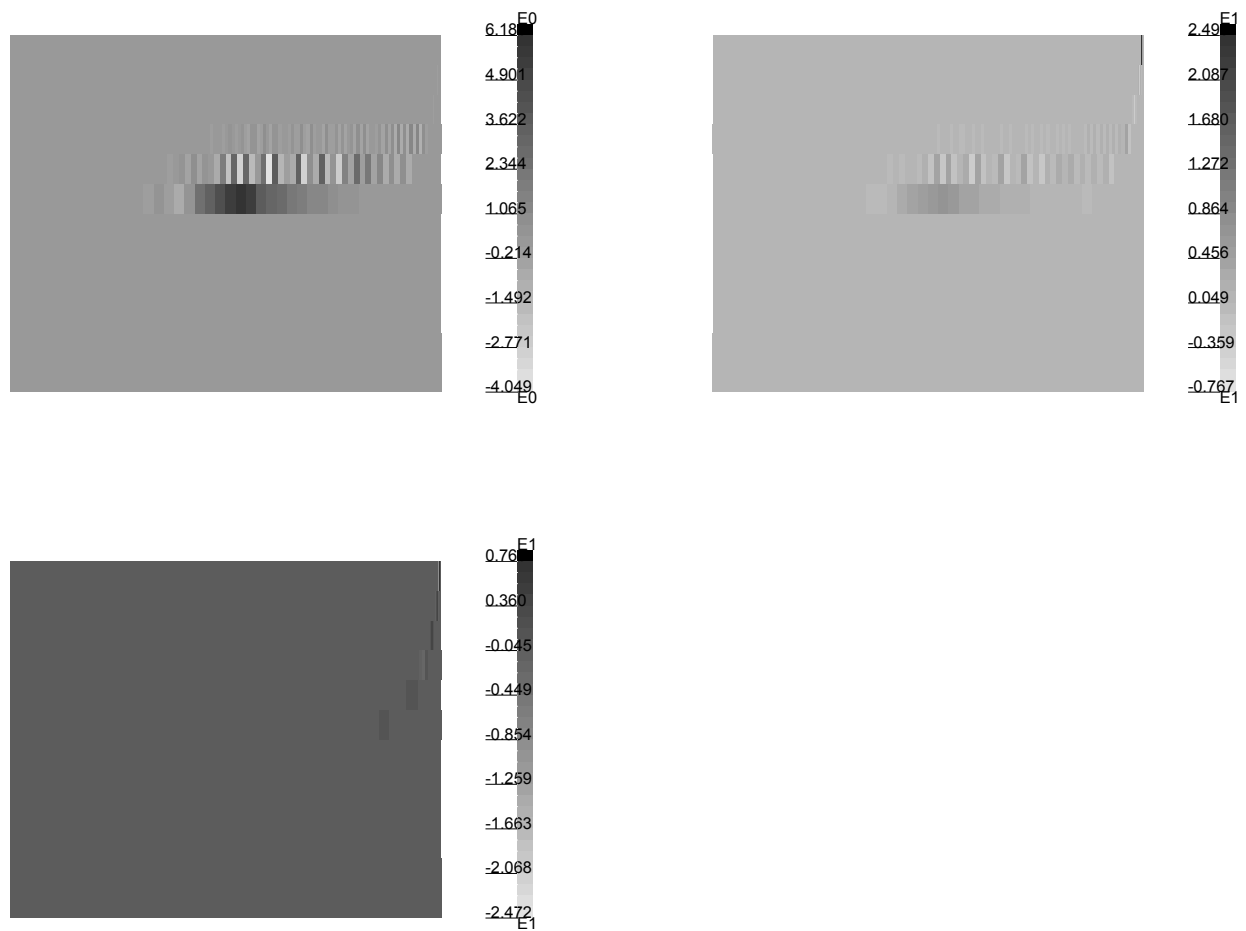


Figure C.18: Wavelet decomposition of the accelerations with respect to the  $D_6$  wavelet (top left), wavelet decomposition of the estimate of the accelerations that was obtained based on the displacements (top right), absolute differences between the two wavelet decompositions (bottom left)

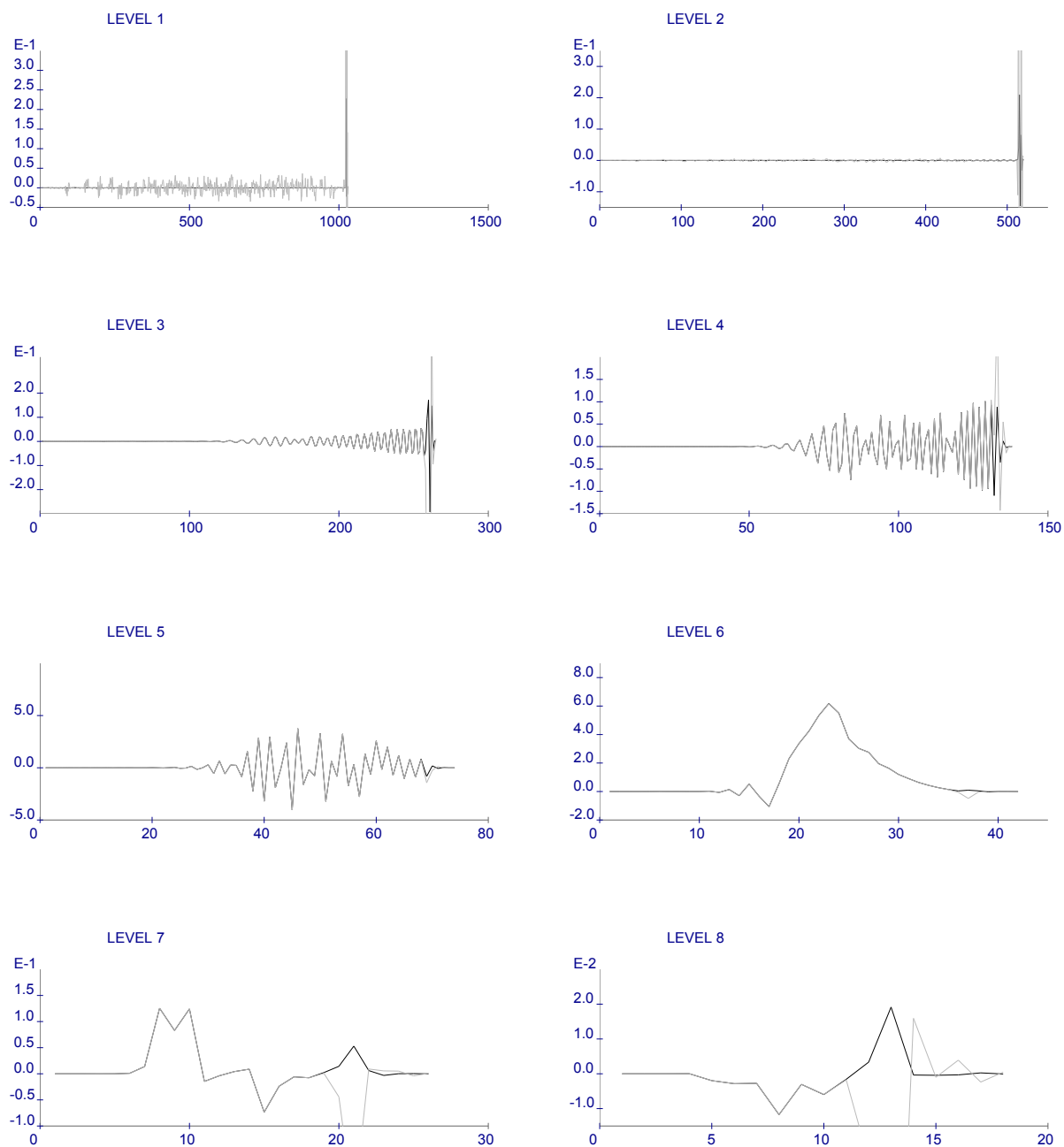


Figure C.19: Wavelet coefficients of the original accelerations (black curves) and of the estimated accelerations, based on displacements (grey curves) at the first eight levels of the decomposition with respect to the  $D_6$  wavelet



# Appendix D

## Examples – Direct Parameter Estimation

### D.1 Example 5.1 – Diagrams

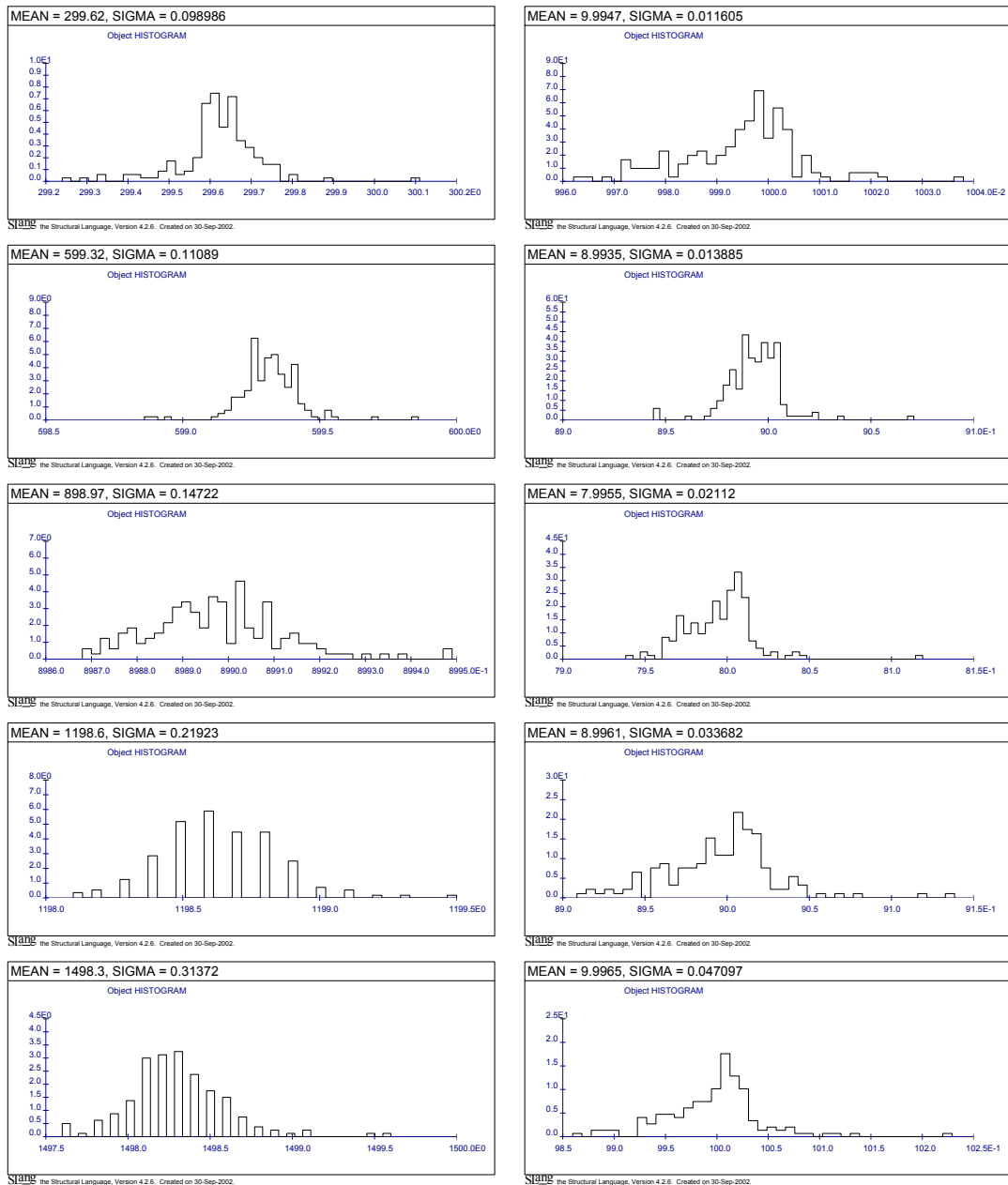


Figure D.1: Histograms of the parameters identified by the wavelet-based method in example 5.1, no noise – stiffness parameters (left) and damping coefficients (right)

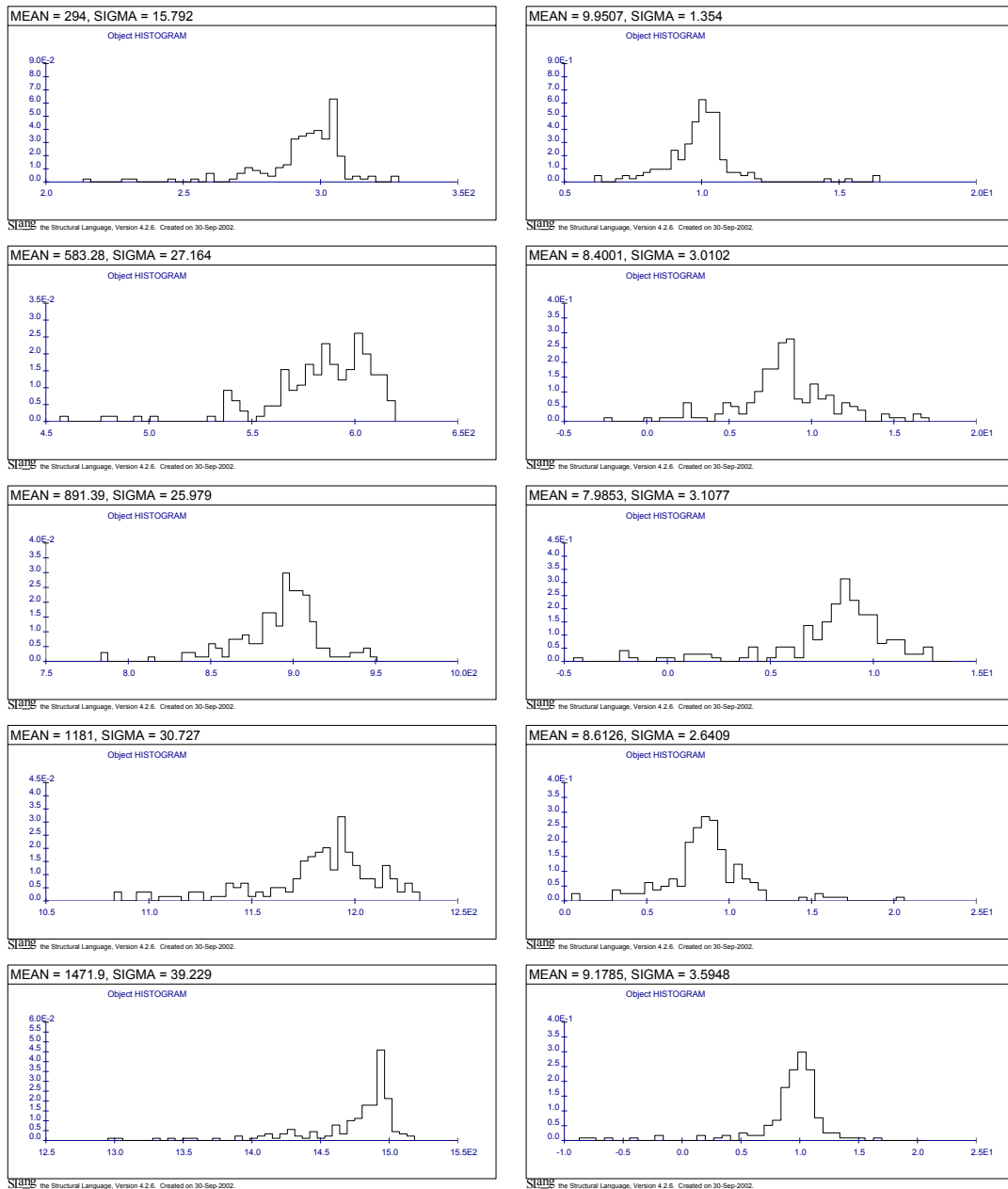


Figure D.2: Histograms of the parameters identified by the wavelet-based method in example 5.1, noise level 1 % – stiffness parameters (left) and damping coefficients (right)

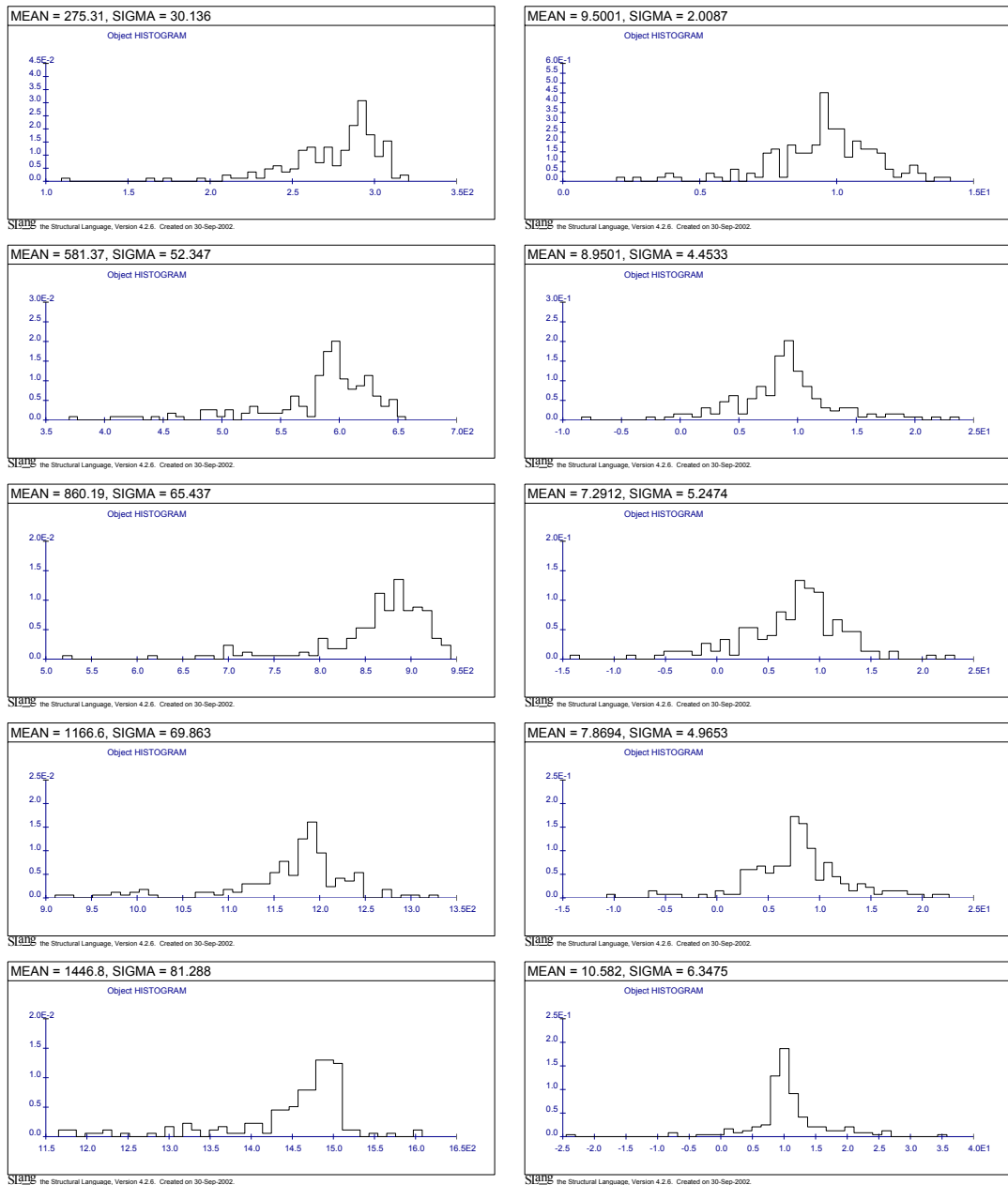


Figure D.3: Histograms of the parameters identified by the wavelet-based method in example 5.1, noise level 2 % – stiffness parameters (left) and damping coefficients (right)

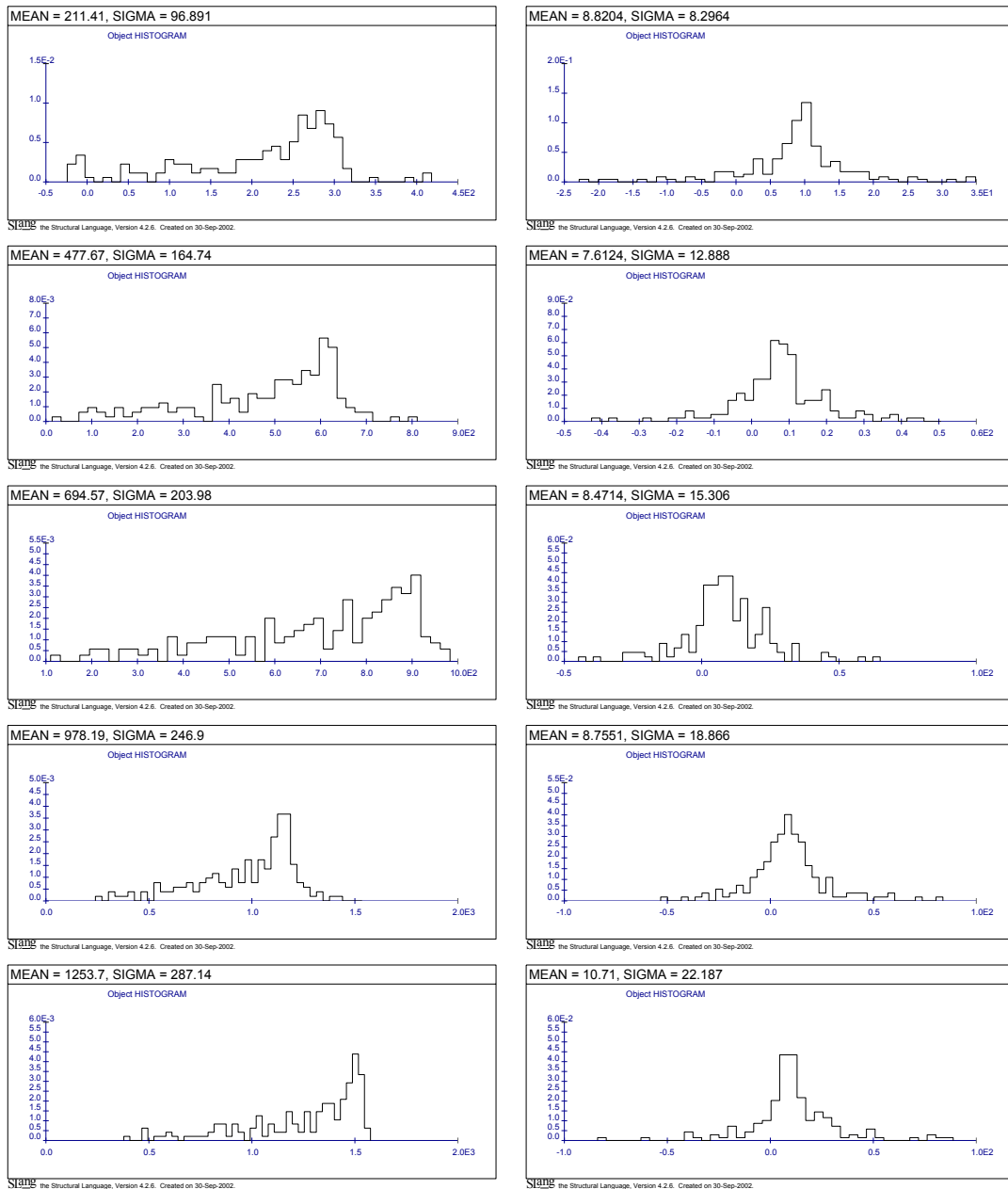


Figure D.4: Histograms of the parameters identified by the wavelet-based method in example 5.1, noise level 5 % – stiffness parameters (left) and damping coefficients (right)

## D.2 Example 5.2 – Diagrams and Tables

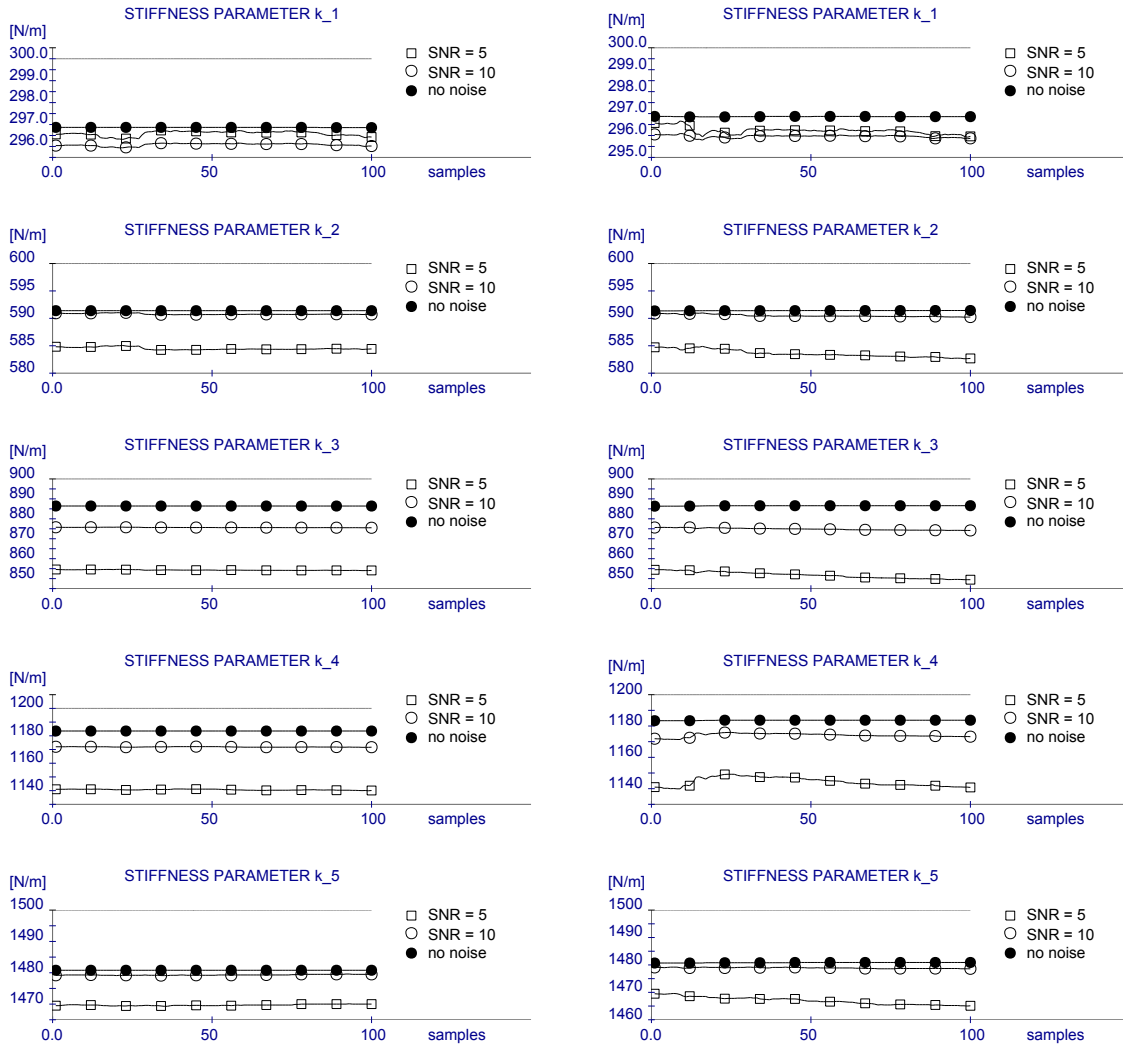


Figure D.5: Example 5.2 – Identified stiffness parameters, least squares solution (left) and results of optimisation (right)

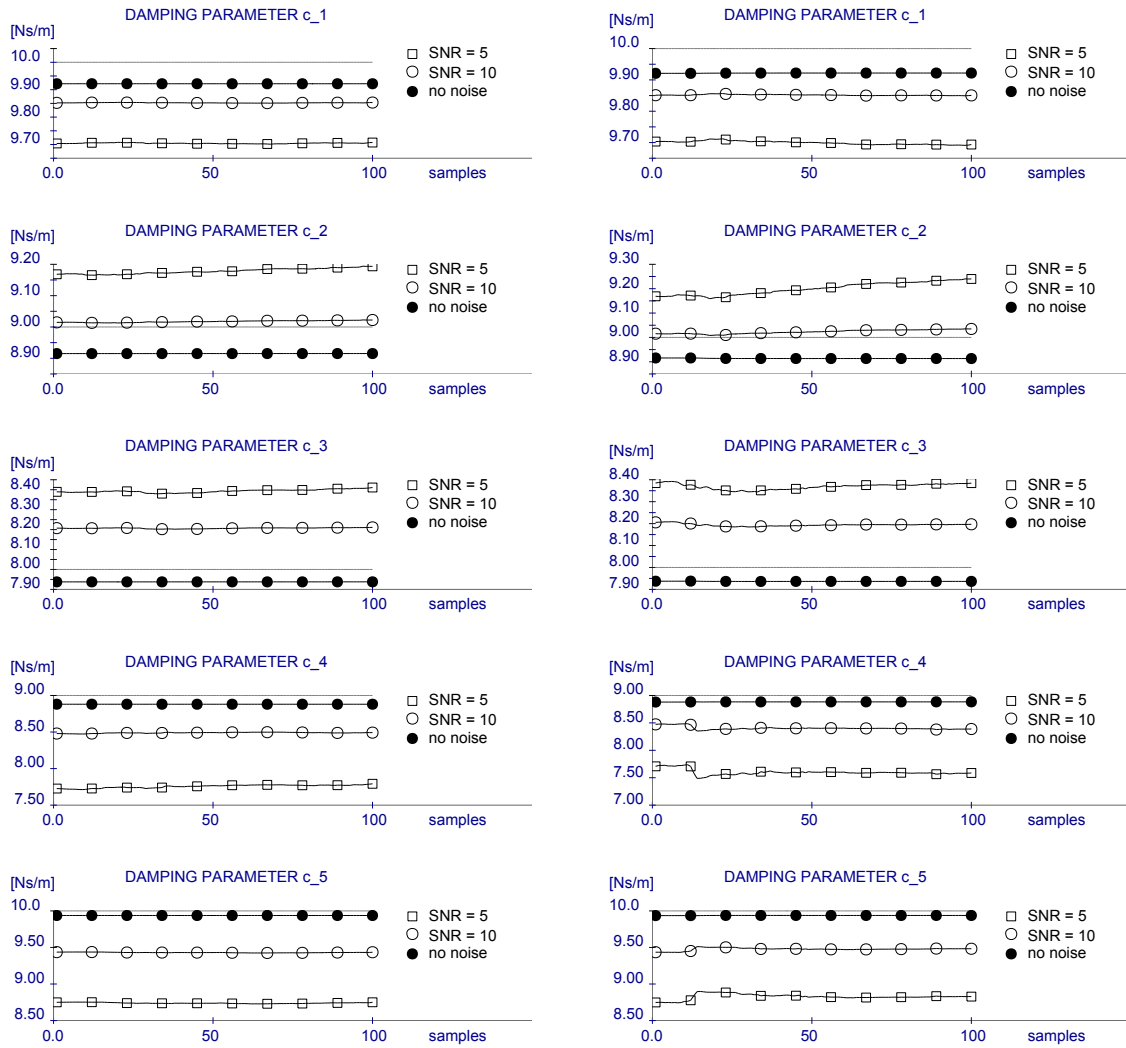


Figure D.6: Example 5.2 – Identified damping parameters, least squares solution (left) and results of optimisation (right)

	orig. value	mean values			standard deviations		
		no noise	$SNR = 10$	$SNR = 5$	no noise	$SNR = 10$	$SNR = 5$
$k_1$	300.00	296.87	296.08	296.59	0.0038	0.0594	0.1112
$k_2$	600.00	591.40	590.78	584.49	9.1e-13	0.1130	0.2338
$k_3$	900.00	886.42	875.64	854.29	0.0067	0.0829	0.1669
$k_4$	1200.00	1183.5	1171.9	1140.7	1.6e-12	0.1567	0.3489
$k_5$	1500.00	1480.8	1479.3	1469.7	4.6e-13	0.1261	0.2062
$c_1$	10.00	9.922	9.852	9.705	3.49e-5	7.06e-4	1.54e-3
$c_2$	9.00	8.915	9.017	9.178	5.02e-5	2.82e-3	8.50e-3
$c_3$	8.00	7.938	8.207	8.393	6.72e-5	2.36e-3	7.86e-3
$c_4$	9.00	8.880	8.490	7.757	8.90e-5	6.52e-3	0.0206
$c_5$	10.00	9.937	9.431	8.739	4.69e-5	3.78e-3	6.97e-3

Table D.1: Example 5.2 – Identified parameters, least squares solution – mean values and standard deviations (figures D.5, D.6)

	orig. value	mean values			standard deviations		
		no noise	$SNR = 10$	$SNR = 5$	no noise	$SNR = 10$	$SNR = 5$
$k_1$	300.00	296.86	295.96	296.21	6.45e-3	0.0574	0.1572
$k_2$	600.00	591.41	590.50	583.58	0.0195	0.2136	0.6619
$k_3$	900.00	886.54	874.86	851.78	0.0746	0.4941	1.5972
$k_4$	1200.00	1183.6	1174.1	1144.4	0.1068	1.1424	2.8230
$k_5$	1500.00	1480.8	1478.9	1466.9	0.0753	0.1938	1.3451
$c_1$	10.00	9.922	9.852	9.699	3.21e-4	1.66e-3	5.54e-3
$c_2$	9.00	8.914	9.023	9.200	7.91e-4	7.91e-3	0.0253
$c_3$	8.00	7.937	8.194	8.369	3.85e-4	5.47e-3	0.0128
$c_4$	9.00	8.883	8.404	7.598	1.03e-3	0.0293	0.0508
$c_5$	10.00	9.938	9.478	8.828	7.85e-4	0.0177	0.0366

Table D.2: Example 5.2 – Identified parameters, optimisation results – mean values and standard deviations (figures D.5, D.6)



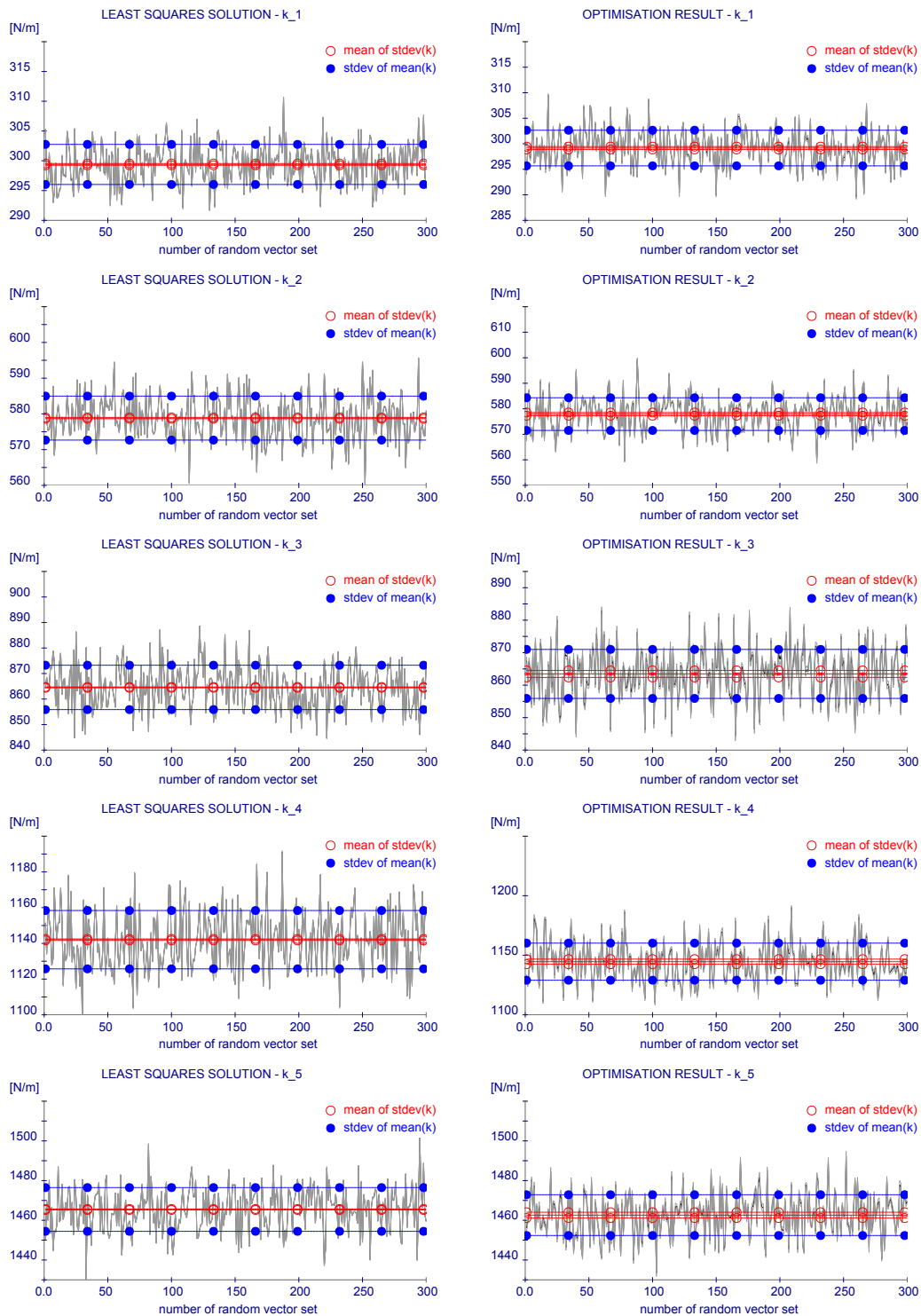


Figure D.7: Example 5.2 – Statistic analysis of identified stiffness parameters, mean values (black curves), standard deviations of the single identifications (grey curves), comparison between least squares solutions (left) and optimisation results (right)

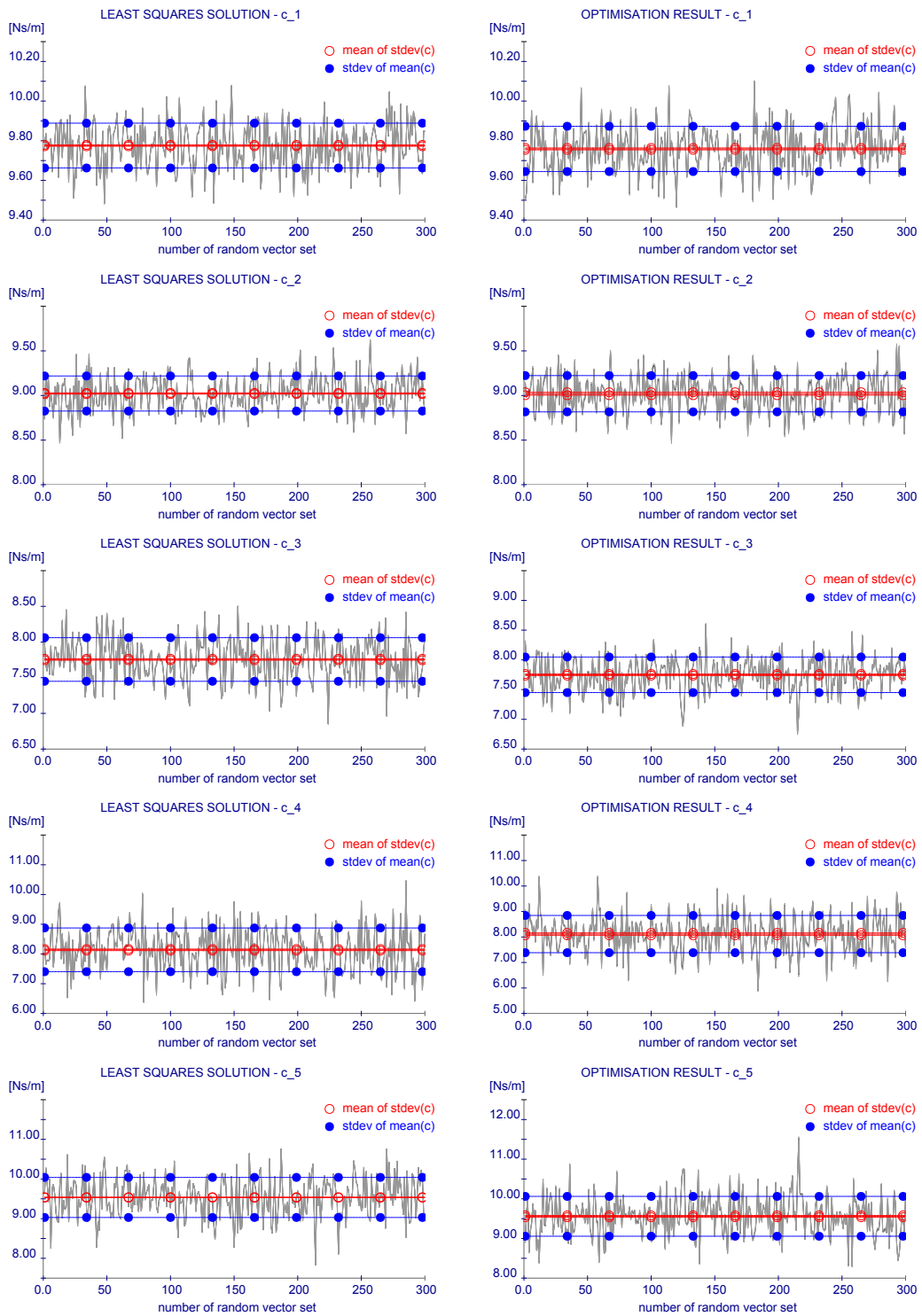


Figure D.8: Example 5.2 – Statistic analysis of identified damping parameters, mean values (black curves), standard deviations of the single identifications (grey curves), comparison between least squares solutions (left) and optimisation results (right)

# Appendix E

## Progressive Damage – Experiments

### E.1 Description of progressive damage

Load step	$F_{stat}$ [kN]	number of visible cracks	Descriptions
0	0.0	–	no visible cracks, system before static loading
1	2.5	–	no visible cracks
2	4.0	7	<ul style="list-style-type: none"><li>• 7 cracks in a 60 cm wide zone around midspan,</li><li>• depth of cracks <math>\approx 3 \dots 4</math> cm,</li><li>• width of cracks <math>&lt; 0.05</math> mm</li></ul>
3	5.0	13	<ul style="list-style-type: none"><li>• 13 cracks in a 90 cm wide zone around midspan,</li><li>• depth of cracks <math>\leq 5</math> cm,</li><li>• width of cracks <math>&lt; 0.05</math> mm</li></ul>
4	7.0	17	<ul style="list-style-type: none"><li>• 17 cracks in a 140 cm wide zone around midspan,</li><li>• depth of cracks <math>\approx 6 \dots 7</math> cm,</li><li>• width of cracks <math>\geq 0.05</math> mm</li></ul>

table continues

Load step	$F_{stat}$ [kN]	number of visible cracks	Descriptions
5	9.0	19	<ul style="list-style-type: none"> <li>• 19 cracks in a 140 cm wide zone around midspan,</li> <li>• depth of cracks <math>\leq 7.5</math> cm,</li> <li>• width of cracks <math>\leq 0.1</math> mm</li> </ul>
6	11.0	21	<ul style="list-style-type: none"> <li>• 21 cracks in a 150 cm wide zone around midspan,</li> <li>• depth of cracks <math>\approx 7 \dots 8</math> cm,</li> <li>• width of cracks <math>\leq 0.15</math> mm</li> </ul>
7	14.0	25	<ul style="list-style-type: none"> <li>• 25 cracks in a 160 cm wide zone around midspan,</li> <li>• depth of cracks <math>\approx 8</math> cm,</li> <li>• width of cracks <math>\approx 0.15 \dots 0.2</math> mm</li> </ul>
8	17.0	26	<ul style="list-style-type: none"> <li>• 26 cracks in a 160 cm wide zone around midspan,</li> <li>• depth of cracks <math>\approx 8</math> cm,</li> <li>• width of cracks <math>\approx 0.25 \dots 0.3</math> mm,</li> <li>• width of some cracks when structure is unloaded <math>\approx 0.05</math> mm</li> </ul>
9	20.0	26	<ul style="list-style-type: none"> <li>• 26 cracks in a 160 cm wide zone around midspan, branching of some cracks,</li> <li>• depth of cracks <math>\approx 8</math> cm,</li> <li>• width of cracks <math>\approx 0.3 \dots 0.35</math> mm,</li> <li>• width of cracks when structure is unloaded <math>\approx 0.05</math> mm</li> </ul>
10	25.0	26	<ul style="list-style-type: none"> <li>• 26 cracks in a 160 cm wide zone around midspan, further branching of cracks,</li> <li>• depth of cracks <math>\approx 8</math> cm,</li> <li>• width of cracks <math>\approx 0.35 \dots 0.4</math> mm,</li> <li>• width of cracks when structure is unloaded <math>\approx 0.05 \dots 0.1</math> mm</li> </ul>

table continues

Load step	$F_{stat}$ [kN]	number of visible cracks	Descriptions
11	30.0	27	<ul style="list-style-type: none"> <li>• initial cracks due to shear stresses near the supports,</li> <li>• depth of cracks <math>\approx 8\text{ cm}</math>,</li> <li>• width of cracks <math>\approx 0.35 \dots 0.4\text{ mm}</math>,</li> <li>• width of cracks when structure is unloaded <math>\approx 0.05 \dots 0.1\text{ mm}</math></li> </ul>
12	33.76		<ul style="list-style-type: none"> <li>• growth of the cracks' lengths around midspan,</li> <li>• structural failure, failure of the beam's compression zone</li> </ul>

Table E.1: Tests of a reinforced concrete beam – Description of progressive damage

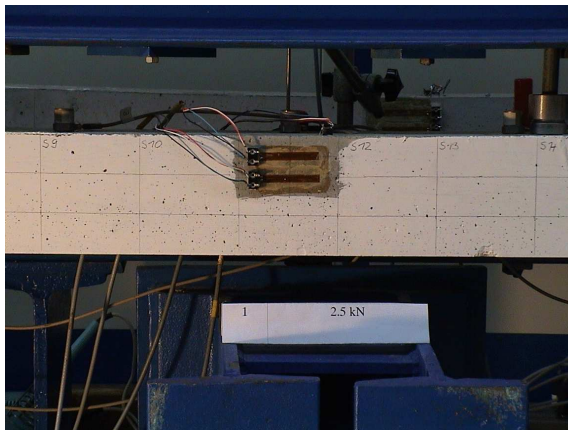
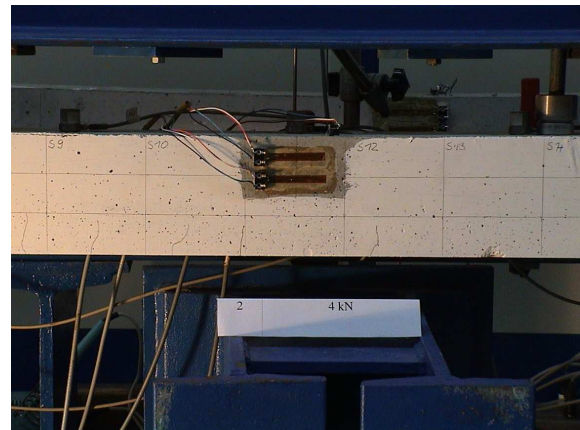
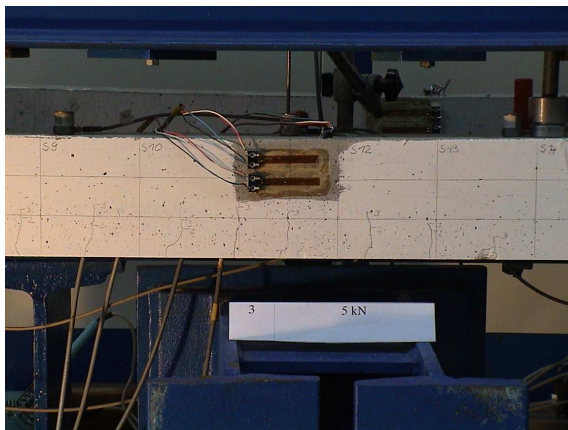
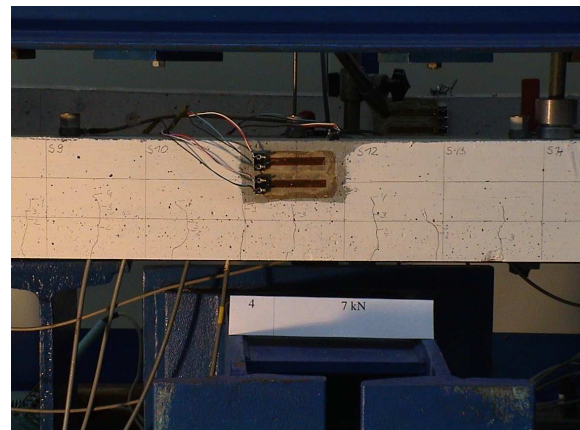
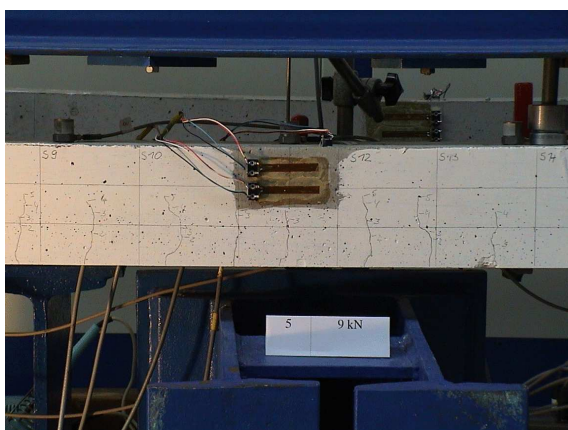
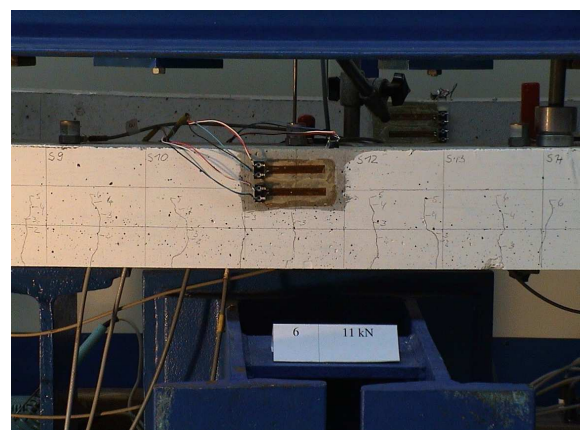
load step 1  $\rightarrow F_{stat} = 2.5kN$ load step 2  $\rightarrow F_{stat} = 4.0kN$ load step 3  $\rightarrow F_{stat} = 5.0kN$ load step 4  $\rightarrow F_{stat} = 7.0kN$ load step 5  $\rightarrow F_{stat} = 9.0kN$ load step 6  $\rightarrow F_{stat} = 11.0kN$ 

Figure E.1: Tests of a reinforced concrete beam – Zone around midspan, progressively damaged (load steps 1 ... 6)



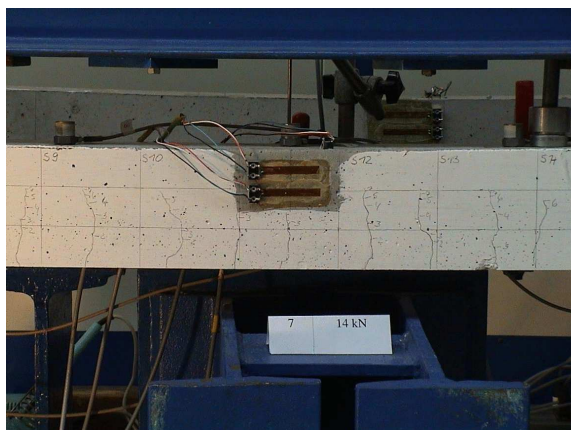
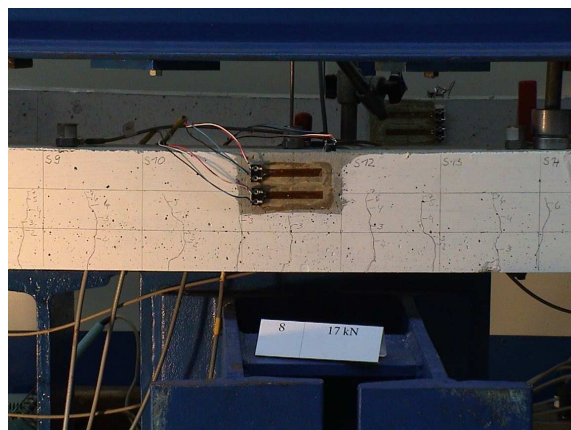
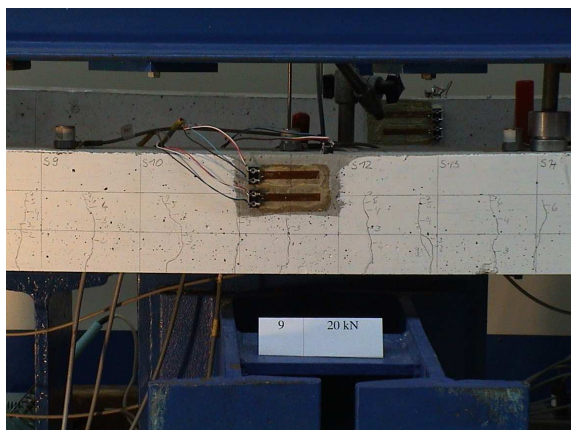
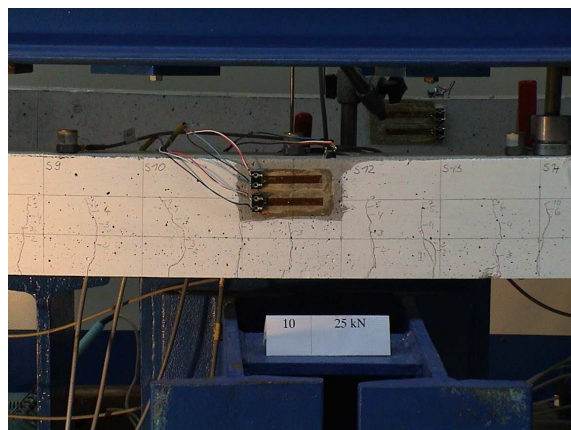
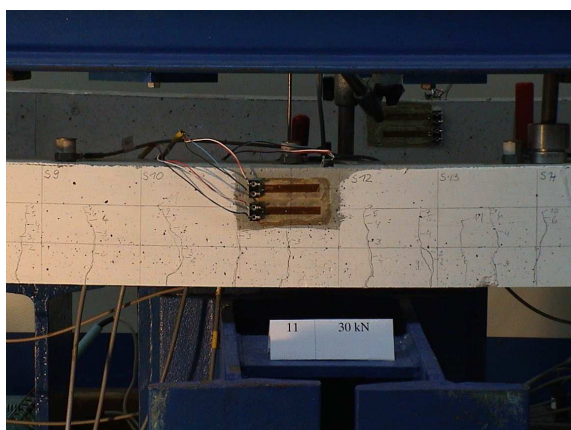
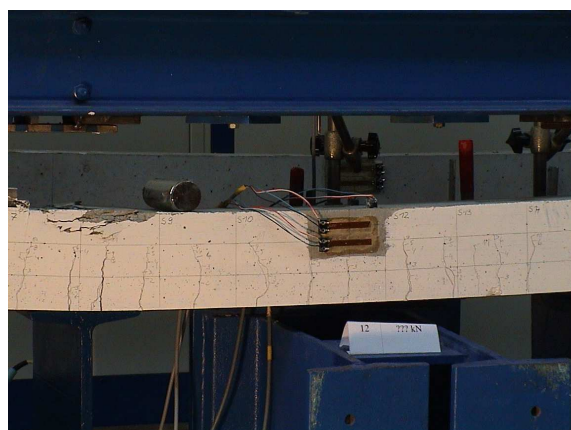
load step 7  $\rightarrow F_{stat} = 14.0kN$ load step 8  $\rightarrow F_{stat} = 17.0kN$ load step 9  $\rightarrow F_{stat} = 20.0kN$ load step 10  $\rightarrow F_{stat} = 25.0kN$ load step 11  $\rightarrow F_{stat} = 30.0kN$ load step 12  $\rightarrow F_{stat} = 33.76kN$  - failure

Figure E.2: Tests of a reinforced concrete beam – Zone around midspan, progressively damaged (load steps 7 ... 12)

# Zusammenfassung in Deutsch

## Einführung

Gegenstand der Systemidentifikation ist die Lösung des inversen Problems der Strukturmechanik. Das bedeutet, es ist ein Modell zu identifizieren, das ein bestehendes mechanisches System (z.B. ein Tragwerk) beschreibt. Die Eigenschaften des Modells werden dabei aus experimentell ermittelten Daten der Einwirkungen (äußere Kräfte) und der Strukturreaktionen abgeleitet. Häufig werden diese Daten aus dynamischen Versuchen gewonnen.

In den meisten bisher entwickelten Methoden der Systemidentifikation werden die gemessenen Daten entweder im Zeitbereich oder im Frequenzbereich analysiert. Erst in jüngerer Zeit wurden Verfahren entwickelt, die auf Darstellungen der Meßreihen im Zeit-Frequenz-Bereich basieren. Bei einer Reihe dieser Ansätze wird die Wavelet-Transformation angewendet.

Die Zielsetzung dieser Arbeit bestand im wesentlichen aus folgenden Punkten:

- Entwicklung einer Methode, die gestattet, Parameter eines Finite-Elemente-Modells direkt aus im Versuch gemessenen äußeren Kräften und daraus resultierender Bauwerksbeschleunigungen zu identifizieren. In Erwartung bestimmter Vorteile wurde für die Datenanalyse die Anwendung der Wavelet-Transformation angestrebt.
- Es sollte untersucht werden, ob die Wavelet-Transformation für die Erarbeitung



eines empfindlichen Indikators zur Erkennung von Schäden in einem Stahlbetontragwerk geeignet ist.

Mit der Arbeit wurde beabsichtigt, einen Beitrag zur Entwicklung von Anwendungen der Wavelet-Transformation auf dem Gebiet der Systemidentifikation zu leisten.

## **Kapitel 1: Grundlagen der Wavelet-Transformation**

Ausgehend von der häufig angewendeten Fourier-Transformation und der gefensterter Fourier-Transformation wird in die kontinuierliche Wavelet-Transformation eingeführt. Die Grundidee wird erläutert und die Definition wird gegeben. An Hand von Beispielen wird gezeigt, welche Eigenschaften Wavelets haben.

Der Übergang von der kontinuierlichen zur diskreten Wavelet-Transformation wird dargestellt. Die der schnellen Wavelet-Transformation zugrunde liegende Multi-Skalen-Analyse wird beschrieben. Am Beispiel der Daubechies-Wavelets wird gezeigt, daß orthogonale Wavelets und die zugehörigen Skalierungsfunktionen durch wenige Koeffizienten beschrieben werden können. Die Ermittlung dieser Koeffizienten wird an einem Beispiel demonstriert.

## **Kapitel 2: Wavelets in der Systemidentifikation – eine Rezension**

In den zurückliegenden zehn Jahren wurde die Wavelet-Transformation in unterschiedlicher Weise für die Bearbeitung von Problemstellungen der Systemidentifikation genutzt. Eine Reihe solcher Entwicklungen verschiedener Autoren sind in Kapitel 2 zusammengefaßt. Einige Methoden basieren auf der kontinuierlichen Wavelet-Transformation, andere auf diskreten Wavelet-Zerlegungen.

Im ersten Abschnitt sind Verfahren beschrieben, die der Identifikation von modalen Parametern und Impulsreaktions- bzw. Frequenzgangfunktionen dienen.

Aus Wavelet-Transformierten lassen sich Informationen über den Frequenzgehalt eines analysierten Signals mit Bezug zur Zeit ablesen. Daher ist es naheliegend, die Wavelet-Transformation im Zusammenhang mit zeitlich veränderlichen Systemen einzusetzen. Die Bandbreite der vorgeschlagenen Methoden reicht von der Erkennung nichtlinearen Systemverhaltens bis hin zur Identifikation von Systemparametern nichtlinearer oder zeitlich veränderlicher linearer Systeme. Die Qualität der vorgestellten Ergebnisse ist sehr unterschiedlich. Meist sind die Anwendungen auf sehr einfache Systeme beschränkt. Die Verfahren, in denen die diskrete Wavelet-Transformation zur Anwendung kommt, bauen auf der Beschreibung des Systemverhaltens durch Skalierungskoeffizienten (Approximationen) auf, das heißt auf Tiefpaß-gefilterten Zeitreihen.

Der dritte Abschnitt befaßt sich mit Anwendungen im Zusammenhang mit der Schadenserkennung. Einige der beschriebenen Anwendungen sind darauf gerichtet, aus kontinuierlichen oder diskreten Wavelet-Transformierten gemessener Signale bestimmte Muster abzulesen, die beispielsweise auf Schäden an rotierenden Maschinenteilen hinweisen oder auf den Zeitpunkt, zu dem ein Schaden in einem elasto-mechanischen System (z.B. Bauwerk) eintritt, schließen lassen.

Eine zweite Gruppe von Veröffentlichungen befaßt sich mit der Definition von Indikatoren zur Erfassung einer vorhandenen Schädigung in einem elasto-mechanischen System. Während einige Methoden auf einem zu identifizierenden Strukturmodell beruhen, werden in anderen Herangehensweisen alleine Eigenschaften der gemessenen Signale ausgewertet.

### **Kapitel 3: Selektive Wavelet-Rekonstruktion**

Bestandteil einiger der in Kapitel 2 beschriebenen Techniken ist eine selektive Wavelet-Rekonstruktion. Diese Methode findet in vielen technischen Disziplinen Anwendung. Häufig wird sie genutzt, um Rauschanteile aus Signalen zu entfernen. Deshalb wird auch

oft vom Entrauschen (*De-noising*) gesprochen.

Der Algorithmus besteht aus drei Schritten:

1. Wavelet-Zerlegung des ursprünglichen Signals,
2. Schwellwertbehandlung der Wavelet-Koeffizienten,
3. Rekonstruktion eines gefilterten Signals aus den modifizierten Wavelet-Koeffizienten.

Eine Reihe von Ansätzen für die Schwellwertermittlung, die der Literatur entnommen sind, wird vorgestellt. Die Vorgehensweise wird auf ein numerisch erzeugtes Signal und im Zusammenhang mit der experimentellen Ermittlung des Übertragungsverhaltens eines Beschleunigungsaufnehmers getestet.

## **Kapitel 4: Ableitungen und Integrale von Wavelet-Transformierten**

Zunächst wird hergeleitet, wie Ableitungen und Integrale eines Signals im Zeit-Skalen-Bereich einer kontinuierlichen Wavelet-Transformation dargestellt werden können, ohne das ursprüngliche Signal im Zeitbereich zu differenzieren beziehungsweise zu integrieren. Die Voraussetzung für die beschriebene Vorgehensweise ist die Existenz eines zweifach differenzierbaren Wavelets, dessen erste beiden Ableitungen ebenfalls Wavelets sind.

Anschließend wird in das Konzept der Verbindungskoeffizienten eingeführt, auf dessen Grundlage Wavelet-Zerlegungen von Ableitungen oder Integralen eines Signals berechnet werden können. Es wird erläutert, wie sich die Verbindungskoeffizienten für die Differentiations- und Integrationsoperatoren erster und zweiter Ordnung bestimmen lassen. Für die Daubechies-Wavelets zweiter bis zehnter Ordnung wurden die entsprechenden Grundkoeffizienten berechnet.

An Hand mehrerer Beispiele wird die Genauigkeit der vorgestellten Berechnungsweise untersucht.

## Kapitel 5: Direkte Parameterabschätzung

Die in Kapitel 4 beschriebenen Beziehungen werden für die Abschätzung von Systemparametern eingesetzt. Es wird angenommen, daß im Versuch die Systemreaktion an wesentlichen Freiheitsgraden sowie die dynamische Anregung gemessen werden. Bei baudynamischen Untersuchungen werden die Systemreaktionen in der Regel in Form von Beschleunigungen gemessen. Für den vorgeschlagenen Algorithmus können diese Informationen allerdings auch als Geschwindigkeiten oder Verschiebungen vorliegen.

Die Systemparameter werden durch Lösen eines Gleichungssystems, das man durch entsprechendes Umstellen der Bewegungsgleichungen im Zeit-Skalen-Bereich einer kontinuierlichen oder diskreten Wavelet-Transformation erhält, bestimmt. Die Leistungsfähigkeit der entwickelten Vorgehensweise wurde in numerischen Beispielen untersucht. Für die Lösung des Gleichungssystems, das sich auf der Grundlage der diskreten Wavelet-Koeffizienten ergibt, werden zwei verschiedene Ansätze angewendet.

Die Untersuchungen ergaben, daß die Parameter eines linearen Systems auch bei verhältnismäßig hohen Störanteilen in den Meßwerten relativ genau bestimmt werden können. Die Genauigkeit der Ergebnisse läßt sich durch eine geeignete Auswahl und Gewichtung der in die Rechnung einfließenden Wavelet-Koeffizienten erhöhen. Können im Versuch die Reaktionen nicht an allen für das Systemverhalten wesentlichen Freiheitsgraden aufgezeichnet werden, sinkt die erzielbare Genauigkeit der Resultate mit zunehmenden Störanteilen in den Signalen.

Untersuchungen hinsichtlich der Identifikation plötzlich auftretender Systemparameteränderungen ergaben ebenfalls zunehmende Probleme mit steigendem Rauschanteil in den Meßreihen.

Für die praktische Anwendung der Identifikationsmethode wurden Ausschwingversuche mit einer Impulsanregung an einem Stahlträger durchgeführt. Der Querschnitt des Trägers war an zwei Stellen durch Einschnitte reduziert. Durch die Auswertung der aufgezeichneten Daten mit dem vorgestellten Verfahren ließen sich diese Unregelmäßigkeiten im System lokalisieren.

## Kapitel 6: Erfassung fortschreitender Schädigung

Zur Einschätzung des Zustands eines zunehmend geschädigten Stahlbetontragwerks wird vorgeschlagen, die Energie-Komponenten der Wavelet-Zerlegungen von relativen Ausschwingensignalen zu untersuchen. Die Vorgehensweise beinhaltet die folgenden Schritte:

1. Ermittlung der Wavelet-Koeffizienten der Impulsreaktions- bzw. der Impulsübertragungsfunktionen aus den Meßwerten,
2. Auswahl der die jeweilige Funktion im wesentlichen charakterisierenden Wavelet-Koeffizienten,
3. Berechnung der Energie-Komponenten aus den ausgewählten Wavelet-Koeffizienten,
4. Bestimmung der Gesamtenergie auf den ausgewählten Skalen,
5. Vergleich der Energie-Komponenten der Signale bzw. ihrer Summen, die aus Versuchen an der Struktur in verschiedenen Schädigungszuständen ermittelt wurden.

Ein Stahlbetonbalken wurde im Labor experimentell untersucht. Die schrittweise gesteigerte statische Belastung führte zu einer zunehmenden Schädigung des Systems. Zwischen den einzelnen Belastungsstufen wurden Ausschwingversuche durchgeführt.

Durch Auswertung der im Versuch aufgezeichneten Daten wurde festgestellt, daß sich bei geeigneter Auswahl der Wavelet-Koeffizienten mit zunehmender Schädigung wesentlich stärkere Veränderungen aus den Energie-Komponenten ablesen lassen als aus den Eigenfrequenzen. Um allgemeine Schlußfolgerungen zu einem praktisch anwendbaren Schadensindex treffen zu können, sind allerdings die Ergebnisse weiterer Versuchsreihen auszuwerten.

## Schlußfolgerungen

Ausgangspunkt für diese Arbeit war die Annahme, daß die Wavelet-Transformation Vorteile bei der Bearbeitung von Aufgaben auf dem Gebiet der Systemidentifikation bietet.

Auf der Grundlage theoretischer Grundlagen wurde eine Methode entwickelt, die ermöglicht, Parameter eines Finite-Elemente-Modells aus im Versuch gemessenen Anregungen und sich daraus ergebenden Bauwerksbeschleunigungen zu ermitteln. Als besonders effizient hat sich dabei die Anwendung der diskreten Wavelet-Transformation und der in diesem Zusammenhang verwendeten schnellen Algorithmen erwiesen. Durch die Einbindung entsprechender Routinen in das Programm SLang wurde eine gute Verbindung zwischen Datenanalyse und Strukturberechnungen hergestellt.

In numerischen Untersuchungen wurde eine verhältnismäßig niedrige Anfälligkeit des Verfahrens in Hinsicht auf Störanteile in den gemessenen Signalen festgestellt. Die Genauigkeit der Ergebnisse nimmt ab, wenn nur wenige Meßwerte in die Analyse einbezogen werden und wenn die Systemreaktion an für das Strukturverhalten wesentlichen Freiheitsgraden nicht gemessen werden kann. Mit der vorgeschlagenen Vorgehensweise konnte ein Modell eines experimentell untersuchten Stahlträgers identifiziert werden, das sowohl die modalen Eigenschaften als auch lokale Querschnittsreduzierungen erfaßt.

Die diskrete Wavelet-Transformation wurde weiterhin für die Beurteilung des Schädigungszustands eines experimentell untersuchten Stahlbetonbalkens angewendet. Dabei hat sich gezeigt, daß aus den Energie-Komponenten der Wavelet-Zerlegungen von Ausschwingensignalen ein relativ empfindlicher Schädigungsindikator abgeleitet werden kann.

Aufbauend auf die im Rahmen dieser Arbeit erzielten Ergebnisse wird empfohlen, weitere Untersuchungen durchzuführen:

- hinsichtlich des vorgeschlagenen Schädigungsindikators,
- zur Anwendung der Wavelet-Transformation auf Verfahren, die keine gemessenen Einwirkungen erfordern und
- in Hinblick auf den Einfluß der Auswahl des jeweils verwendeten Wavelets auf die Qualität der Ergebnisse.